WILEY

Edited by Ashutosh K. Shukla

Analytical Characterization Methods for Crude Oil and Related Products

Analytical Characterization Methods for Crude Oil and Related Products

Analytical Characterization Methods for Crude Oil and Related Products

Edited by
Ashutosh K. Shukla
Physics Department
Ewing Christian College, India

WILEY

This edition first published 2018

Registered Office(s)
John Wiley & Sons, Inc., 111 River Street, Hoboken, NJ 07030, USA
John Wiley & Sons Ltd, The Atrium, Southern Gate, Chichester, West Sussex, PO19 8SQ, UK

Editorial Office
The Atrium, Southern Gate, Chichester, West Sussex, PO19 8SQ, UK

For details of our global editorial offices, customer services, and more information about Wiley products visit us at www.wiley.com.

Wiley also publishes its books in a variety of electronic formats and by print-on-demand. Some content that appears in standard print versions of this book may not be available in other formats.

Library of Congress Cataloging-in-Publication Data applied for
ISBN : 9781119286318

Cover Design: Wiley
Cover Image: © mmmx / Shutterstock

Set in 10/12pt WarnockPro by SPi Global, Chennai, India

10 9 8 7 6 5 4 3 2 1

To my teachers

Contents

List of Contributors

T. Biktagirov
Kazan Federal University
Kremlevskaya
Kazan
Russia

Jonathan L. Bryan
Department of Chemical and
Petroleum Engineering
Schulich School of Engineering
University of Calgary
Canada

and

PERM Inc.
Calgary
Canada

Stella Corsetti
College of Life Sciences
University of Dundee
United Kingdom

Eduardo Di Mauro
Universidade Estadual de Londrina
(UEL)/Laboratório
de Fluorescência e Ressonância
Paramagnética Eletrônica
(LAFLURPE), Brazil

Igor N. Evdokimov
Department of Physics
Gubkin Russian State University of
Oil and Gas
Moscow
Russia

Marat Gafurov
Kazan Federal University
Kremlevskaya
Kazan
Russia

Carmen Luisa Barbosa Guedes
Universidade Estadual de Londrina
(UEL)/Laboratório
de Fluorescência e Ressonância
Paramagnética Eletrônica
(LAFLURPE), Brazil

Siavash Iravani
Faculty of Pharmacy and
Pharmaceutical Sciences
Isfahan University of Medical
Sciences
Iran

Apostolos Kantzas
Department of Chemical and Petroleum Engineering
Schulich School of Engineering
University of Calgary
Canada

and

PERM Inc.,
Calgary
Canada

Johannes Kiefer
Technische Thermodynamik
Universität Bremen
Germany

Galo Antonio Carrillo Le Roux
Departamento de Engenharia Química
Escola Politécnica da Universidade de São Paulo
Brasil

Juan López-Gejo
SICPA SA
Prilly
Switzerland

G. Mamin
Kazan Federal University
Kremlevskaya
Kazan
Russia

Flavio H. Marchesini
Department of Mechanical Engineering
Pontifical Catholic University of Rio de Janeiro
Brazil

Claudio Augusto Oller do Nascimento
Departamento de Engenharia Química
Escola Politécnica da Universidade de São Paulo
Brasil

S. B. Orlinskii
Kazan Federal University
Kremlevskaya
Kazan
Russia

Patricia Araujo Pantoja
Universidad de Ingeniería y Tecnología (UTEC)
Lima
Peru

Marilene Turini Piccinato
Universidade Tecnológica Federal do Paraná – Campus Londrina (UTFPR-LD)
Brasil

Inês Portugal
Department of Chemistry
CICECO
Aveiro Institute of Materials
University of Aveiro
Portugal

Jorge Ribeiro
Galp Energia
Refinaria de Matosinhos
Leça da Palmeira
Portugal

Artur M. S. Silva
Department of Chemistry
QOPNA
University of Aveiro
Portugal

Carlos M. Silva
Department of Chemistry
CICECO
Aveiro Institute of Materials
University of Aveiro
Portugal

Catarina Varanda
Department of Chemistry
CICECO
Aveiro Institute of Materials
University of Aveiro
Portugal

and

Department of Chemistry
QOPNA
University of Aveiro
Portugal

M. Volodin
Kazan Federal University
Kremlevskaya
Kazan
Russia

and

Sakhalin Energy Investment
Company Ltd.
Yuzhno-Sakhalinsk
Russia

Preface

The characterization of crude oil and related products is of increasing interest to the scientific community as well as the petroleum industry because the property and composition of samples from different oilfields are different. This present collection of writings intends to describe the potential applications of a variety of spectroscopic techniques in this field. This volume contains nine chapters which include ESR, NMR, IR, UV-Vis, and Raman spectroscopic techniques. In addition, a chapter on rheological characterization is included to bring a sense of completeness. Contributors to this volume are from a variety of disciplines and hence lend this volume a multidisciplinary character. Mathematical details have been kept to a minimum. All the authors are experts of eminence in their field and I learned many things from their chapters. I hope that readers will also enjoy reading it in a meaningful way.

I sincerely thank Jenny Cossham, commissioning editor, Natural Sciences, John Wiley & Sons, Ltd for giving me an opportunity to present this book to readers. I wish to thank Emma Strickland, assistant editor, Natural Sciences, John Wiley & Sons, Ltd for extending all the support during the development of this project. It is the prompt response of the project editor, Elsie Merlin, which allowed me to present this work in such a short time. I thank the authors for taking time out of their busy academic schedules to contribute to this volume. I offer my special thanks to anonymous reviewers for their comments, which helped me to cover a wide range of spectroscopic tools.

I am grateful to Prof. Ram Kripal and Prof. Raja Ram Yadav, Department of Physics, University of Allahabad for their suggestions and comments. My sincere thanks are also due to Dr. M. Massey, Principal, Ewing Christian College, Allahabad and my colleagues for their constant encouraging remarks during the development of this book.

Gratitude to my parents cannot be expressed in words. I could complete this task with their blessings only. My brother Dr. Arun K. Shukla, Department of Biological Sciences and Bioengineering, Indian Institute of Technology, Kanpur has always supported my endeavors. My special thanks are also due to my wife

1

Rheological Characterization of Crude Oil and Related Products

Flávio H. Marchesini

Pontifical Catholic University of Rio de Janeiro

1.1 Introduction

Crude oil and related products undergo different transport processes from extraction to end use. For example, crude oils may be transported through pipelines before the refining process (Petrellis and Flumerfelt, 1973; Smith and Ramsden, 1978; Rønningsen *et al.*, 1991; Wardhaugh and Boger, 1991a), fuel oils are injected into combustion engines to produce mechanical work (Graboski and McCormick, 1998, Ramadhas *et al.*, 2004; Agarwal, 2007; Joshi and Pegg, 2007), and lubricant oils are used to reduce friction between mechanical parts in contact (Dyson, 1965; Webber, 1999, 2001).

The design of each of these processes requires the rheological properties of the oils, as the pumping power and the dimensions of the lines, connections, and mechanical parts are defined assuming that the oil has a viscosity within a specific range. If this range is not properly set during the design stage and the process starts running with an oil having a viscosity out of the appropriate range, different issues can arise. For example, severe flow assurance issues can be faced during the restart flow of crude oils in pipelines (Petrellis and Flumerfelt, 1973; Smith and Ramsden, 1978; Wardhaugh and Boger, 1991a; Rønningsen *et al.*, 1991), and filters and lines can be plugged, preventing an engine from starting (Graboski and McCormick, 1998; Ramadhas *et al.*, 2004; Agarwal, 2007; Joshi and Pegg, 2007). Therefore, to guarantee that the process works properly, the rheological properties of these oils must be known as accurately as possible, in representative process conditions.

In general, at high enough temperatures, crude oil and related products behave as simple Newtonian liquids, whose viscosities depend solely on temperature. However, at low enough temperatures, the rheological behavior of these oils usually becomes quite complex due to precipitation of higher-molecular-weight compounds, which gives rise to a gelation

Analytical Characterization Methods for Crude Oil and Related Products, First Edition.
Edited by Ashutosh K. Shukla.

phenomenon when a certain amount of crystals is present. At this low temperature range, the oil viscosity increases significantly and depends not only on temperature but also on time, shear, and thermal and shear histories (Petrellis and Flumerfelt, 1973; Smith and Ramsden, 1978; Wardhaugh and Boger, 1987, 1991b; Rønningsen *et al.*, 1991; Rønningsen, 1992; Chang *et al.*, 1998, 2000; Webber, 1999, 2001; Venkatesan *et al.*, 2005).

This complex rheological behavior at low temperatures may introduce difficulties in performing the rheological characterization of these oils. A number of precautions must be taken to get accurate properties during rheological measurements with these oils (Wardhaugh and Boger, 1987, 1991a; Marchesini *et al.*, 2012; Alicke *et al.*, 2015). Thus, we discuss in this chapter how to prepare samples for rheological measurements (in Section 1.2), the most common rheological tests performed with these oils and how to interpret the data (in Section 1.3), and the potential sources of errors in rheological measurements and how to avoid them (in Section 1.4).

1.2 Sample Preparation for Rheological Characterization

As described in this section, the sample preparation procedure for rheological characterization can be divided into four main steps: (i) ensuring the chemical stability (Section 1.2.1), (ii) choosing the rheometer geometry (Section 1.2.2), (iii) erasing the thermal memory (Section 1.2.3), and (iv) performing the cooling process (Section 1.2.4).

1.2.1 Ensuring the Chemical Stability

The first step of the sample preparation procedure is to make sure that the crude oil or related product is not going to evaporate or lose significant amounts of lightweight compounds under the temperature and pressure conditions in which the rheological test is going to be performed. This step is intended to guarantee the chemical stability of the sample during the test, thus avoiding evaporation effects on the time-dependent rheological properties being measured (Wardhaugh and Boger, 1987).

If the oil is not stable enough at the test conditions, a pretreatment can be applied to the oil to evaporate light ends before loading a sample into the rheometer or viscometer used. The pretreatment usually consists of heating the oil at a temperature within the temperature range of the process of interest (Smith and Ramsden, 1978; Wardhaugh and Boger, 1987; Marchesini *et al.*, 2012).

It is important noting that a difference between the rheological properties of the pretreated oil and the untreated oil can be observed, and higher viscosity values are usually obtained for the samples after applying a pretreatment to

evaporate light ends (Wardhaugh and Boger, 1987). However, with regard to many applications, the rheological tests with the pretreated oil provide conservative data for the transport process design (Wardhaugh and Boger, 1991a). If this is not the case or if more accurate data is needed, the rheological properties of the pretreated oil can be corrected by estimating the increase in viscosity due to evaporation of light ends (Wardhaugh and Boger, 1987; Rønningsen *et al.*, 1991).

1.2.2 Choosing the Rheometer Geometry

The second step is to choose the appropriate rheometer geometry in which the sample is going to be loaded for rheological characterization. The classical geometries used to perform the rheological characterization of materials in rotational rheometers are: (i) cone and plate, (ii) parallel plates, and (iii) concentric cylinders (also known as the Couette geometry). To decide which is the best geometry for the rheological characterization of a given oil used for a particular application, some points must be addressed.

If the rheological tests are going to be performed in a temperature range in which no crystals appear in the sample, the oil may present a Newtonian behavior. In this case, any classical geometry is expected to give the same results, so any of the three geometries can be chosen. However, if crystals are expected to appear during the test and if the oil presents the complex rheological behavior expected at low temperatures, the rheometer geometry must be carefully chosen to obtain reliable data of the bulk rheological behavior (Marchesini *et al.*, 2012).

Even though the cone and plate geometry is widely used for the rheological characterization of crude oil and related products, this geometry may not be the best choice depending on the oil at hand and test conditions (Marchesini *et al.*, 2012). In favor of the cone and plate there is the argument that it is the only geometry in which all parts of the sample are submitted to exactly the same shear rate (Wardhaugh and Boger, 1987). In addition, as the cone and plate geometry requires a small amount of sample, it may be easy to control the temperature inside the sample. However, the cone and plate geometry is not suitable for the rheological characterization of samples having large enough crystals suspended, as it may violate the continuum hypothesis used in the rheometer theory. In addition, there is evidence in the literature that very small gaps—as the ones of commercial cone and plate geometries—cause the precipitation of crystals at higher temperatures (Davenport and Somper, 1971; Rønningsen *et al.*, 1991). Thus, to obtain the bulk rheological properties of these oils at low temperatures, large enough gaps are required (Marchesini *et al.*, 2012).

In this case, the parallel plates or the concentric cylinders can be chosen. The parallel-plate geometry has the advantage of being the best geometry

to vary the gap, thus making easy the task of finding the large enough gap above which the rheological data stop changing with the gap. Moreover, the parallel-plate geometry is also a convenient choice for preventing apparent wall slip during rheological measurements, as it is easy to vary the gap and roughen its surfaces (e.g. by using sandpaper). However, the parallel-plate geometry has the disadvantage of having a shear rate dependence on the radius inside the sample, which might complicate the control of the shear history in some cases. It is important to note that as the highest shear rates occur at the highest radii—the regions that contribute most to the torque being measured—the non-homogeneous flow field in the parallel-plate geometry should not be a serious issue, at least in some cases. Corrections are available in the literature to end up with more accurate data when using the parallel-plate geometry (de Souza Mendes *et al.*, 2014).

The concentric cylinders geometry presents the advantage of having a much less significant shear rate gradient inside the sample when compared to the parallel-plate geometry, allowing for a better control of the shear history in some cases. However, the concentric cylinders require larger sample volumes, which can lead to errors in the measurements due to contraction of the sample during the test (Wardhaugh and Boger, 1987, 1991a). Besides that, to obtain gap-independent results with the concentric cylinders geometry, cylinders with different diameters ratio are needed to vary the geometry gap, which may not be available. So, the best choice of rheometer geometry to get accurate data may depend on each case (Marchesini *et al.*, 2012).

1.2.3 Erasing the Thermal Memory

The third step is to load the oil sample into the rheometer geometry and apply an isothermal holding time at an initial temperature within the temperature range of the process of interest (Smith and Ramsden, 1978; Wardhaugh and Boger, 1987; Marchesini *et al.*, 2012). This initial temperature is usually a high enough temperature to dissolve the crystals suspended in the oil sample, thus "erasing the thermal memory" of the oil (Wardhaugh and Boger, 1987, 1991b). This step is intended to ensure that each sample loaded into the rheometer geometry is going to have the same microstructure configuration in the beginning, so that repeatable results can be obtained. It is important to note that the initial temperature should not be higher than the highest temperature observed in the process of interest to avoid introducing effects in the measurements that are not observed in the process (Marchesini *et al.*, 2012).

1.2.4 Performing the Cooling Process

The fourth and last step of the sample preparation procedure is the cooling process, in which the sample is cooled from the initial temperature to the measurement temperature under controlled shear and cooling rate (Wardhaugh

and Boger, 1987, 1991b; Marchesini *et al.*, 2012). This fourth step is intended to reproduce in the sample the thermal and shear histories experienced by the oil in the process of interest. After achieving the measurement temperature under controlled thermal and shear histories, the rheological characterization of the oil can be performed and the post-cooling rheological properties investigated.

1.3 Rheological Tests

Some of the most common rheological tests performed with crude oil and related products are: (i) temperature ramps, (ii) flow curves, and (iii) oscillatory stress amplitude sweep tests. From these tests it is possible to obtain the most important rheological properties required for the design and operation of transport processes involving these oils.

Temperature ramps consist of applying a cooling or heating rate to a sample under shear, and evaluating how the viscosity evolves as a function of temperature. With regard to crude oil and related products, this kind of test is usually carried out to (i) evaluate the onset temperature below which the viscosity increases significantly, that is marked by a deviation from the Arrhenius temperature dependence, (ii) evaluate the geometry gap above which gap-independent results are obtained (Marchesini *et al.*, 2012), and (iii) perform the cooling process. It is important to note that to evaluate the characteristic temperature below which the viscosity increases significantly, as well as to perform the cooling process, the temperature ramp must be carried out with the appropriate geometry, gap, and temperature range for the oil at hand (Marchesini *et al.*, 2012). Besides that, it is important to point out that the cooling process can be conducted by either applying shear to the sample, in the case of performing a temperature ramp, or by simply cooling the sample statically.

An example of temperature ramp can be found in Figure 1.1. This temperature ramp starts at an initial temperature T_i. A constant shear rate $\dot{\gamma}$ and a constant cooling rate $\dot{T}$ are then applied to the sample and the viscosity is measured as a function of temperature. As the temperature decreases, an Arrhenius viscosity temperature dependence is observed up to the gelation temperature T_{gel}, below which the viscosity increases significantly and a gelation process takes place. It is interesting to note that in this temperature range below the T_{gel} the typical complex rheological behavior of these oils can be observed. As the temperature decreases further below the T_{gel}, more crystals precipitate and start to interact with each other, building up a microstructure. At the same time, however, the shear applied to the sample during cooling breaks down the microstructure. So, the microstructure at the measurement temperature T_0, which induces the complex non-Newtonian behavior observed at this temperature, is the result of a competition between the buildup, driven by the cooling

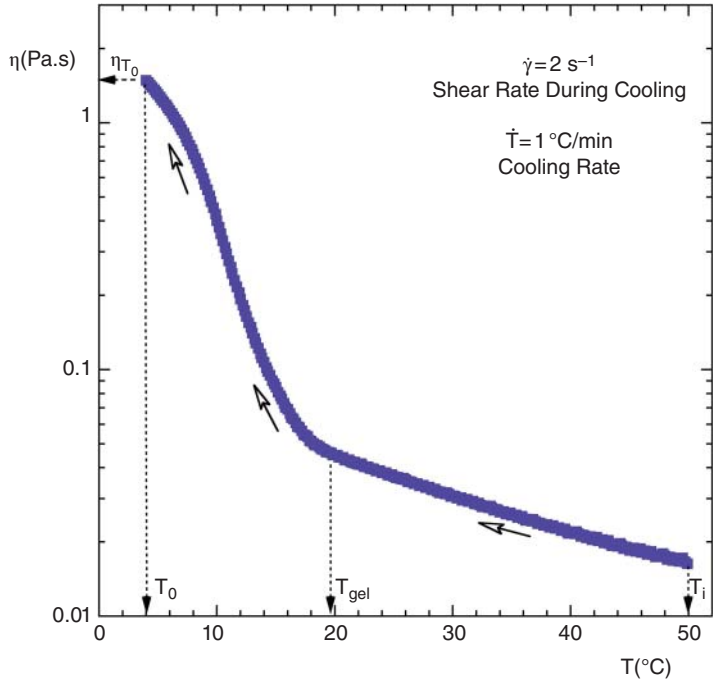

Figure 1.1 A temperature ramp performed with a crude oil sample.

rate, and the breakdown, driven by both the applied shear and cooling rate, as the cooling rate defines the time in which the sample is under shear.

After preparing an oil sample for rheological characterization by completing the cooling process, flow curves, oscillatory stress amplitude sweeps, and other rheological tests can be carried out at the measurement temperature T_0. A flow curve can be obtained by applying either a shear rate or a shear stress to a sample and measuring the resulting shear stress or shear rate, respectively. After achieving the steady state for each measured shear stress or shear rate, the flow curve of a material at a given temperature can be built. A flow curve provides information on the viscosity of a material and can be shown in three different plots, namely viscosity $\eta \times$ shear rate $\dot{\gamma}$, viscosity $\eta \times$ shear stress τ, or shear stress $\tau \times$ shear rate $\dot{\gamma}$. The viscosity is calculated by dividing the shear stress by the shear rate.

Examples of typical flow curves of a crude oil at different temperatures can be found in Figure 1.2. In this figure, the linear relationship between the shear stress τ and the shear rate $\dot{\gamma}$, observed for 25.0 °C, 37.5 °C, and 50.0 °C, indicates that the oil has a constant viscosity at each of these temperatures. This constant-viscosity behavior, typical of Newtonian liquids, is expected at these temperatures, as the T_{gel} of this particular oil is around 20.0 °C. At

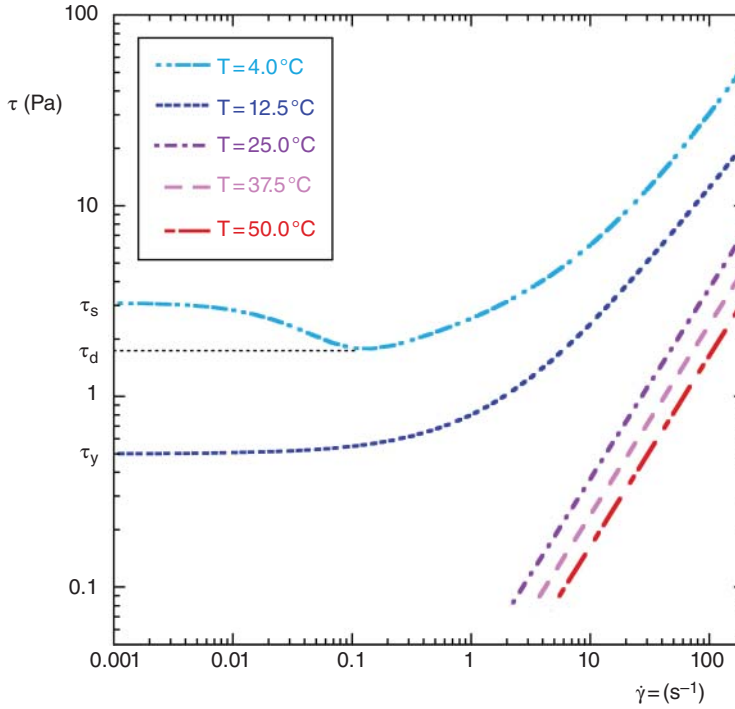

Figure 1.2 Example of the flow curves of a crude oil at different temperatures.

12.5 °C, a sufficient amount of crystals has already been precipitated, so that the oil is gelled and presents the behavior of regular yield-stress materials. In this case, the flow curve of the oil can be described by the Herschel–Bulkley equation with a single yield stress τ_y estimated as 0.5 Pa. At 4 °C, however, the gel structure is formed by a larger number of crystals and the oil presents a non-monotonic flow curve with two yield stresses, a static yield stress τ_s and a dynamic yield stress τ_d. The static yield stress is the minimum stress required to start the flow from rest, while the dynamic yield stress is the minimum stress required to keep the flow once the material is flowing. An equation with the two yield stresses, describing this behavior, can be found in the literature (de Souza Mendes, 2011). It is important to note that, depending on the oil at hand and temperature range investigated, the three different kinds of flow curve presented may not necessarily be observed for a single oil.

Oscillatory stress amplitude sweep tests consist of applying an oscillatory stress at a constant frequency to a sample and measuring the strain response of the material. The stress amplitude is increased in steps after a number of cycles and can be plotted as a function of the measured strain amplitude, as illustrated in Figure 1.3.

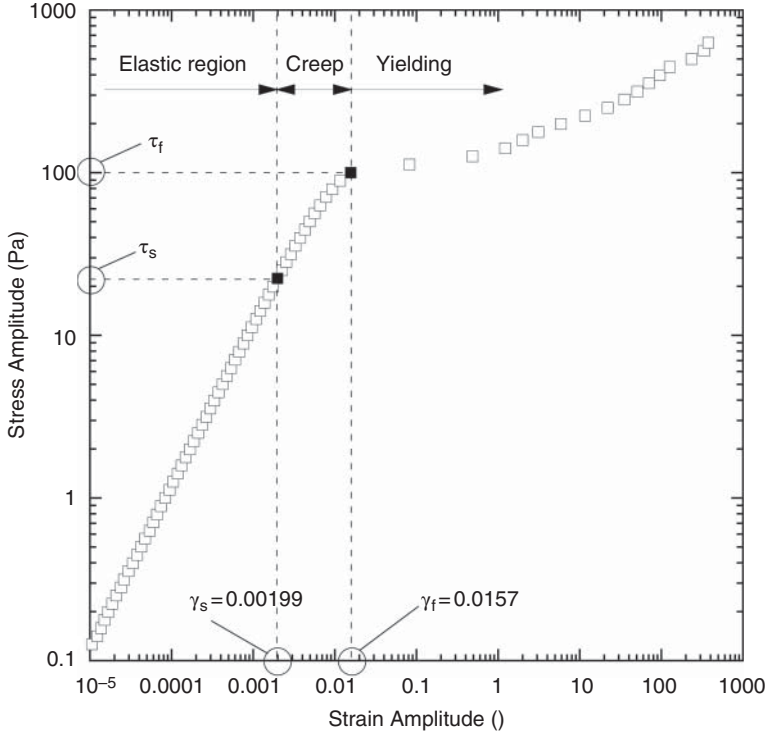

Figure 1.3 A stress amplitude sweep test performed with a crude oil sample.

In this figure, a linear relationship between the stress amplitude and the strain amplitude indicates that the material behaves as a Hookean elastic solid, thus the material does not flow and only elastic deformation is observed in this region. Above a static yield stress τ_s, however, a deviation from this linear relationship is observed and the material starts to creep. A corresponding static yield strain γ_s can be identified at this point. As the stress amplitude increases further above the static yield stress, a fracture yield stress τ_f is achieved, above which the microstructure collapses and an abrupt increase in strain amplitude is seen. Similarly, a corresponding fracture yield strain γ_f can be identified at this point.

It is important noting that, in the literature, the limiting stress above which the material starts to creep is also known as the elastic yield stress τ_e (Chang *et al.*, 1998). However, as this limiting stress marks the start of flow from rest and to keep consistency with the nomenclature used in the flow curve, this limiting stress is referred to as the static yield stress τ_s in this text. Besides that, as described by Chang *et al.* (1998), this limiting stress, measured in oscillatory

stress amplitude sweep tests, does not depend on the frequency used in the test, indicating that this is an accurate measurement of a true material property, the static yield stress τ_s. However, the fracture yield stress τ_f measured in stress amplitude sweep tests depends on the frequency used in the test. Thus, as highlighted by Chang *et al.* (1998), the τ_f can only be used in the design of transport processes of these oils if the timescale of the measurement—related to the frequency used in this case—is of the same order of the timescale of the process to be designed.

In summary, from the above-mentioned rheological tests it is possible to obtain the gelation temperature T_{gel}, the viscosity of the oil at different temperatures, described by the flow curves, the static and dynamic yield stresses of gelled oils, and other properties. These are probably the most important rheological properties required to design a transport process involving these oils.

1.4 Potential Sources of Errors

The potential sources of error in rheological measurements of waxy crude oil and related products are discussed in detail in the literature (Wardhaugh and Boger, 1987, 1991b; Marchesini *et al.*, 2012; Alicke *et al.*, 2015). As discussed in this section, particular attention is paid to: (i) evaporation of light ends, (ii) sample contraction, (iii) geometry gap, (iv) inhomogeneous flow, and (v) apparent wall slip.

Evaporation of light ends during rheological tests can introduce errors in the measurements, as discussed in Section 1.2.1. Therefore, it is important to ensure that the sample is chemically stable in the temperature and pressure conditions under which the rheological test is going to be performed. To control this potential source of error, a geometry cover and a solvent trap can be used during the test. In addition, a pretreatment to evaporate light ends can be applied during the sample preparation procedure. Alternatively, an enclosed geometry with a pressure cell can be used.

Sample contraction can be an issue depending on the chemical composition of the sample and temperature range of the test. This issue can be identified by visual inspection of the sample at the highest and lowest test temperatures, and can be circumvented by correcting the shear stress and shear rate based on the geometry area in contact with the sample (Wardhaugh and Boger, 1987).

With regard to the geometry gap, large enough gaps must be used to ensure gap-independent results that are representative of the bulk, as discussed in Section 1.2.2. Thus, cone and plate geometries are not recommended for rheological tests with waxy crude oil and related products when temperatures below the T_{gel} are reached.

Inhomogeneous flow is a potential source of error, especially when using parallel plates. Tests with plates and cylinders of different diameters can be performed to identify whether this is an important source of error in the measurements performed with the oil at hand. However, as far as the present authors know, there is no clear evidence that this is a serious problem in rheological measurements performed with these oils (Wardhaugh and Boger, 1987; Marchesini *et al.*, 2012). Future measurements can shed light on this point.

Apparent wall slip is another potential source of error that might require attention, as it is observed in rheological measurements of structured materials, especially when using small gaps and low shear rates. A roughened surface can be used to prevent this phenomenon effect. However, the fact that gap-independent results are obtained is strong evidence that apparent wall slip is not a serious issue in the measurements performed. It is possible to find in the literature evidence to support that (Rønningsen *et al.*, 1991; Marchesini *et al.*, 2012).

References

Agarwal, A. K. (2007) Biofuels (alcohols and biodiesel) applications as fuels for internal combustion engines. *Prog. Energy Combust. Sci.*, 33(3), 233–271.

Alicke, A. A., Leopércio, B. C., Marchesini, F. H., and de Souza Mendes, P. R. (2015) Guidelines for the rheological characterization of biodiesel. *Fuel*, 140, 446–452.

Chang, C., Boger, D. V., and Nguyen, Q. D. (1998) The yielding of waxy crude oils. *Ind. Eng. Chem. Res.*, 37, 1551–1559.

Chang, C., Boger, D. V., and Nguyen, Q. D. (2000) Influence of thermal history on the waxy structure of statically cooled waxy crude oil. *SPE J.*, 5(2), 148–157.

Davenport, T. C. and Somper, R. S. H. (1971) The yield value and breakdown of crude oil gels. *J. Inst. Petrol.*, 57(554), 86–105.

de Souza Mendes, P. R. (2011) Thixotropic elasto-viscoplastic model for structured fluids. *Soft Matter*, 7, 2471–2483.

de Souza Mendes, P. R., Alicke, A. A., and Thompson, R. L. (2014) Parallel-plate geometry correction for transient rheometric experiments. *Appl. Rheol.*, 24(52721).

Dyson, A. (1965) Flow properties of mineral oils in elastohydrodynamic lubrication. *Phil. Trans. R. Soc. A.*, 258(1093), 529–564.

Graboski, M. S. and McCormick, R. L. (1998) Combustion of fat and vegetable oil derived fuels in diesel engines. *Prog. Energy Combust. Sci.*, 24(2), 125–164.

Joshi, R. M. and Pegg, M. J. (2007) Flow properties of biodiesel fuel blends at low temperatures. *Fuel*, 86(1–2), 143–151.

Marchesini, F. H., Alicke, A. A., de Souza Mendes, P. R., and Zıglio, C. M. (2012), Rheological characterization of waxy crude oils: Sample preparation. *Energy Fuels*, 26(5), 2566–2577.

Petrellis, N. C. and Flumerfelt, R. W. (1973) Rheological behaviour of shear degradable oils: Kinetic and equilibrium properties. *Can. J. Chem. Eng.*, 151, 291–301.

Ramadhas, A. S., Jayaraj, S., and Muraleedharan, C. (2004) Use of vegetable oils as IC engine fuels: R review. *Renew. Energy*, 29(5), 727–742.

Rønningsen, H. P. (1992) Rheological behavior of gelled, waxy North Sea crude oils. *J. Petrol. Sci. Eng.*, 7, 177–213.

Rønningsen, H. P., Bjørndal, B., Hansen, A. B., and Pedersen, W. B. (1991) Wax precipitation from North Sea crude oils: 1: Crystallization and dissolution temperatures, and Newtonian and non-Newtonian flow properties. *Energy Fuels*, 5, 895–908.

Smith, P. B. and Ramsden, R. M. J. (1978) The prediction of oil gelation in submarine pipelines and the pressure required for restarting flow. *Eur. Offshore Petrol. Conf.*, 283–290.

Venkatesan, R., Nagarajan, N. R., Paso, K., *et al.* (2005) The strength of paraffin gels formed under static and flow conditions. *Chem. Eng. Sci.*, 60, 3587–3598.

Wardhaugh, L. T. and Boger, D. V. (1987) Measurement of the unique flow properties of waxy crude oils. *Chem. Eng. Res. Des.*, 65, 74–83.

Wardhaugh, L. T. and Boger, D. V. (1991a) Flow characteristics of waxy crude oils: Application to pipeline design. *AIChE Journal*, 37(6), 871–885.

Wardhaugh, L. T. and Boger, D. V. (1991b) The measurement and description of the yielding behavior of waxy crude oil. *J. Rheol.*, 35(6), 1121–1156.

Webber, R. M. (1999) Low temperature rheology of lubricating mineral oils: Effects of cooling rate and wax crystallization on flow properties of base oils. *J. Rheol.*, 43(4), 911–931.

Webber, R. M. (2001) Yield properties of wax crystal structures formed in lubricant mineral oils. *Ind. Eng. Chem. Res.*, 40, 195–203.

2

Optical Interrogation of Petroleum Asphaltenes: Myths and Reality

Igor N. Evdokimov

Department of Physics, Gubkin Russian State University of Oil and Gas, Leninsky Prospekt, 65, Moscow B-296, GSP-1, 119991, Russia

2.1 Introduction

2.1.1 What are Asphaltenes?

As opposed to other well-classified crude oil components—e.g. alkanes and alkenes (McCain, 1990; Pedersen, Fredenslund, and Thomassen, 1989; Speight, 2007)—asphaltenes are an ill-defined solubility class that covers a range of different compounds with differing structures and chemical properties. The operational definition of asphaltenes results from historical observations made by oil industry personnel, and was never intended to offer a rigorous chemical description of these substances (Mullins *et al.*, 2007; Yen and Chilingarian, 1994, 2000). Namely, the term "asphaltene" originated in 1837 when Boussingault defined them as the distillation residue of bitumen: insoluble in alcohol and soluble in turpentine (Boussingault, 1937). More recently, asphaltenes were most often defined as the components of petroleum fluids that are insoluble in light *n*-alkanes such as *n*-pentane (C5 asphaltenes) or *n*-heptane (C7 asphaltenes) but soluble in aromatics such as toluene (Mullins *et al.*, 2007; Speight, 2007; Yen and Chilingarian, 1994, 2000). C5 and C7 solvents provide different amounts of precipitated asphaltenes from the same crude oil; moreover, these precipitates notably differ with respect to their aromaticity (hydrogen/carbon atomic ratio) and average molecular weight (Mitchell and Speight, 1973; Speight, Long, and Trowbridge, 1984). However, the amounts and natures of asphaltenes precipitated with *n*-heptane and with heavier alkanes are very similar (Speight, Long, and Trowbridge, 1984).

Today, the standardized methods of asphaltene separation prescribe the use of normal heptane as the precipitant (ASTM D6560, 2000; ASTM D3279-07, 2007; ASTM D893-05a, 2010; IP 143/84, 1988). Hence, in technical literature the term "asphaltenes" is usually equivalent to "C7-asphaltenes." Typically, 40

Analytical Characterization Methods for Crude Oil and Related Products, First Edition.
Edited by Ashutosh K. Shukla.

volumes of *n*-heptane are added to 1 volume of crude oil. In the Institute of Petroleum Standard (IP 143/84, 1988), asphaltenes are separated from waxy crude oils with *n*-C7 then the precipitated phase is washed for 1 h with a reflux of hot heptane to remove waxes. In the ASTM D-3279 method (ASTM D3279-07, 2007), asphaltenes from petroleum residues are precipitated with *n*-C7 and filtered after 30 min of heating and stirring with a reflux system. In the ASTM D-893 method (ASTM D893-05a, 2010), asphaltenes are precipitated from lubricating oils by centrifugation in *n*-C7. For each separation method, conditions—such as contact time, temperature, filter size, and washing procedure—need to be specified.

Asphaltenes obtained by the standard methods sometimes are referred to as "laboratory asphaltenes" to distinguish them from "field asphaltenes" that precipitate in the field from a depressurization process and may contain different constituents (Joshi *et al.*, 2001).

2.1.2 The Reasons for Intensive Asphaltene Research

The interest for analytical characterization of this ill-defined fraction of crude oil stems mainly from the potential costly damage in various fields of the petroleum industry. In particular, asphaltenes are often referred to as the "cholesterol of petroleum" (Kokal and Sayegh, 1995). While cholesterol promotes clogging of arteries in biological systems, asphaltene can cause clogging of pipes in refining facilities and of pores and channels in geochemical systems such as underground rocks of oilfield reservoirs. Asphaltene precipitation and deposition has been recognized as a significant problem in oil production, transmission, and processing facilities (Mullins *et al.*, 2007; Yen and Chilingarian, 1994, 2000). The precipitation of asphaltenes is caused by a number of factors including changes in pressure, temperature, chemical composition of the crude oil, mixing the oil with diluents or other oils, and during acid stimulation. The precipitated asphaltene reduces the permeability of the reservoir near the wellbore region, causing formation damage and can plug up the well bores and well tubings. Deposition of asphaltenic organic scales leads to operational problems, safety hazards, and an overall decrease in production efficiency, thereby increasing the cost of oil production. Hence, the importance of the molecular structures of asphaltenes to the practicing petroleum engineers is similar to the importance of the knowledge of a cardiologist about the structure of cholesterol present in the arteries of a patient.

Furthermore, the presence of asphaltene causes a marked increase in crude oil viscosity (Werner, Behar, and Behar, 1998), making it difficult to transport and process. Owing to their high resistance to cracking, asphaltene molecules are usually held responsible for decreasing the yield of petroleum distillates. During petroleum refining, the asphaltene constituents are non-distillable and remain in the residua fuels as the distillable fractions are removed. Besides,

owing to the presence of heavy metal components, asphaltenes are very difficult to biodegrade, making them the most undesired compound from a petroleum waste management perspective (Al-Maghrabi *et al.*, 1999). Some other problems associated with asphaltene flocculation include:

- stabilization of water-in-oil emulsions (Evdokimov, 2012; Sjöblom, Hemmingsen, and Kallevik, 2007);
- poisoning of catalysts (Ancheyta, Trejo, and Rana, 2010, and references cited therein);
- fouling of hot metal surfaces (Asomaning and Watkinson, 1999);
- wettability alteration of reservoir rocks (Buckley, 1998).

Owing to the importance of all these industrial problems, asphaltenes have been widely studied. There are several thousands papers on various aspects of asphaltenes, including their chemistry, molecular weight, solubility, phase behavior, and reactivity (see references in Mullins *et al.*, 2007; Speight, 2007; Yen and Chilingarian, 1994, 2000).

2.1.3 No Controversy about the Elemental Composition of Asphaltenes

Asphaltene constituents isolated from different sources are remarkably constant in terms of ultimate elemental composition (Speight, 1994, 2004, 2007). In particular, the amounts of carbon and hydrogen in C7 asphaltenes usually vary within a narrow range. These values correspond to a hydrogen-to-carbon atomic ratio of $1.15 \pm 0.5\%$ (Speight, 2004). Values outside this range are very rarely found (Speight, 2007). Larger variations occur in the proportions of the hetero elements, for example in the proportions of oxygen and sulfur (Speight, 2004). Oxygen contents vary from 0.3 to 4.9% and sulfur contents vary from 0.3 to 10.3%. On the other hand, the nitrogen content of the asphaltene constituents has a somewhat lesser degree of variation: 0.6–3.3% at the extremes (Speight, 1994).

2.1.4 Continuing Debates on the Size and the Structure of Asphaltene Molecules and Aggregates

Largely because of the ill-defined nature of asphaltenes, unresolved controversies surround the basic structure of the material, including debates over the size, weight, and composition of its molecules. As noted by Professor T. F. Yen (Yen, 2000), a common error made by a number of researchers was that they simply studied one or a handful of (three or four) characteristics and drew sweeping conclusions about the general structure of asphaltenes. This tendency toward generalizations really confused the public as well as the experts.

For a long time many scientists believed that asphaltenes existed in petroleum as very large molecules with molecular weights of up to 1,000,000 g/mol. Figure 2.1 shows one of the proposed complex structures (Pokonova, 1980)

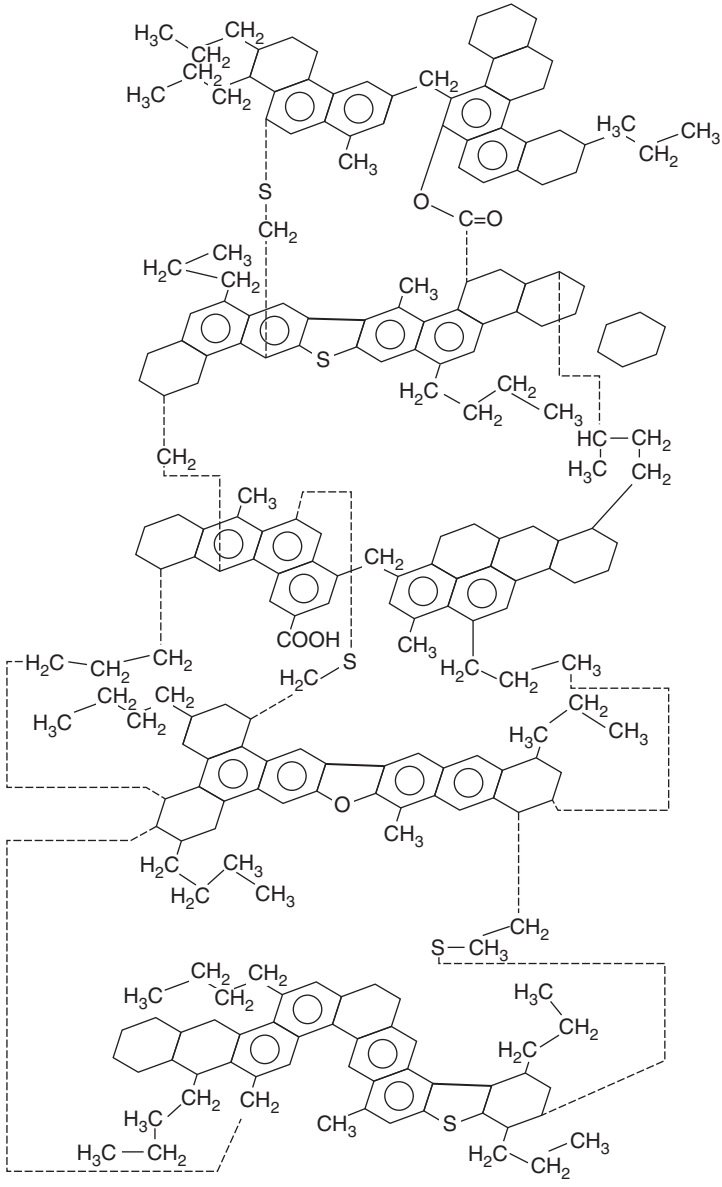

Figure 2.1 Earlier structural model of a typical asphaltene molecule.

of a *single* molecule of asphaltenes in which various structural subunits are covalently linked.

Other scientists argued that the measured high molecular weights belong not to single asphaltene molecules but to molecular aggregates. For several decades, the dominant conceptual model for aggregation of asphaltenes in native petroleum and in solutions has been based on compact clusters (micelles, nanoaggregates) formed by the assembly of some basic molecules, conventionally referred to as "asphaltene monomers" (Mullins *et al.*, 2007; Speight, 2007; Yen and Chilingarian, 1994, 2000). Presumably, the distinctive structural units of these "monomers" are fairly large sheets of 7–10 condensed aromatic rings which facilitate aggregation into parallel stacks via $\pi-\pi$ interactions at asphaltene contents above a specific critical micellar concentration (CMC) of 2–10 g/L (Friberg, 2007; Yen and Chilingarian, 1994, 2000) or a critical nanoaggregate concentration (CNAC) of ca. 100 mg/L (Mullins, 2010; Pomerantz *et al.*, 2015; Ruiz-Morales and Mullins, 2007). These currently popular structural models are illustrated in Figure 2.2.

However, a number of publications by various research teams challenge this dominant paradigm for asphaltene molecular structure (Agrawala and Yarranton, 2001; Alshareef *et al.*, 2011; Evdokimov, Eliseev, and Akhmetov, 2003a, 2003b; Evdokimov and Fesan, 2016; Evdokimov, Fesan, and Losev, 2016; Gray *et al.*, 2011; McKenna *et al.*, 2013; Sheremata *et al.*, 2004; Speight, 2007; Strausz, Mojelsky, and Lown, 1992). In particular, recent steady-state fluorescence emission (SSFE) experiments (Evdokimov and Fesan, 2016; Evdokimov, Fesan, and Losev, 2016) demonstrated that asphaltene "monomers" appear to be much smaller molecular species, predominantly containing 1- to 3-ring aromatic fluorophores, as illustrated at the left of Figure 2.3. Moreover, now there is ample experimental evidence (Evdokimov, Eliseev, and Akhmetov, 2003a, 2003b; Evdokimov and Fesan, 2016; Evdokimov, Fesan, and Losev, 2016; McKenna *et al.*, 2013) that some primary asphaltene aggregates are formed

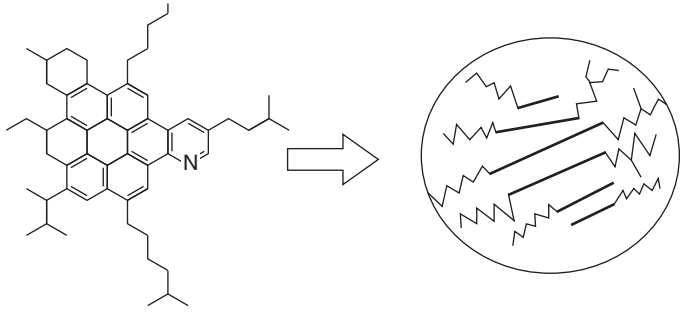

Figure 2.2 Currently popular structural models of a typical asphaltene "monomer" (left) and of an asphaltene "micelle"/"nanoaggregate" (right).

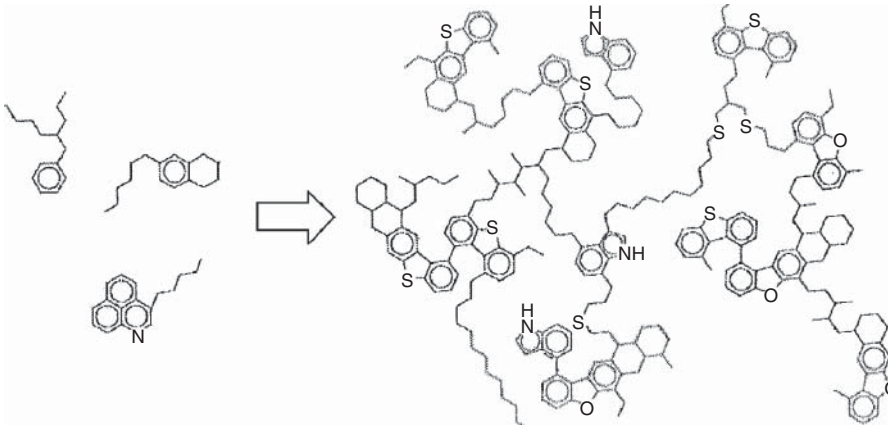

Figure 2.3 Emerging structural models of small asphaltene "monomers" (left) and of asphaltene supramolecular aggregates (right).

at extremely low concentrations of 0.05–0.5 mg/L even in "good" solvents (benzene, toluene, toluene/methanol, etc.). Asphaltene "monomers" aggregate into complex supramolecular entities predominantly not via $\pi-\pi$ stacking but in a head-to-tail manner via hydrogen bonding (Evdokimov, Fesan, and Losev, 2016; Gray *et al.*, 2011). Supramolecular asphaltene aggregates exhibit complex bridged structures, comprising sulfur, nitrogen, aromatic, and naphthenic groups linked by alkyl chains (Gray *et al.*, 2011). These components aggregate in crude oil and "good" solvents over a wide range of concentrations and temperatures, occlude components that are otherwise soluble, are porous to solvents, and are elastic under tension. None of these properties is consistent with the currently popular models of "nanoaggregate" architecture (Figure 2.2) dominated only by $\pi-\pi$ stacking. Supramolecular assemblies of asphaltene molecules combine cooperative binding by Brønsted acid–base interactions, hydrogen bonding, metal coordination complexes, and interactions between cylcoalkyl and alkyl groups to form hydrophobic pockets, with a negligible contribution of aromatic $\pi-\pi$ stacking (Gray *et al.*, 2011). The right part of Figure 2.3 shows a two-dimensional projection of a part of supramolecular asphaltene aggregate, in which small asphaltene "monomers" are linked by various weak non-covalent bonds. An excellent color image of a three-dimensional structure of such aggregate is presented by Gray *et al.* (2011).

2.1.5 Conflicting Paradigms based on Similar Analytical Techniques: Apparent Significance of "Human Factors"

It should be emphasized that the principally different structural schemes of Figure 2.2 and Figure 2.3 were mostly based on the experimental results

of identical optical analytical methods (absorbance and fluorescence spectroscopy, etc.). The authors of the highly publicized model of Figure 2.2 described the respective experiments as an "optical interrogation" of asphaltenes (Mullins, 1998).

Literature analysis shows that the difference in answers to an "optical interrogation" of similar molecular systems with identical analytical instruments most often is a consequence of specific "human factors." Among these factors may be insufficient attention to the limitations of the measuring equipment, limited amount of data points employed for constructing the measured dependencies, inappropriate methods of plotting and approximation of data sets, etc. After such unreliable "optical interrogations," speculations often replace facts and mythical representations of asphaltene properties are constructed.

In the following sections some of these "myths" are discussed and the underlying errors/human factors analyzed.

2.2 Mythical "Characteristic Signatures" of Asphaltenes in Optical Analytical Methods

2.2.1 Nonexistent "Resonance UV Absorption" of Asphaltenes

Over the past few years, a number of authors have reported prominent "characteristic peaks" in UV/Vis absorption spectra for solutions of asphaltenes and of crude oils. For example, in toluene solutions the reported absorption peaks lie in the narrow range of 288–310 nm. In all publications these peaks were regarded as specific fingerprints of asphaltenes that were very useful for their analytical characterization. In some papers (Potapov *et al.*, 2006, 2008) these peaks were also "theoretically" explained by "resonance absorption of pure asphaltene."

Figure 2.4 shows representative examples of such "characteristic peaks," re-plotted from original publications.

a) Absorption spectra for chloroform solutions of asphaltenes from Russian crude oils (Sergienko, Taimova, and Talalajev, 1979). The behavior of "characteristic peak" at 310–320 nm was attributed to specific variations in the structures of asphaltene molecules, e.g. the "red shift" of the peak from 320 to 340 nm was regarded as indicative of increasing asphaltene aromaticity.
b) Absorption spectra for toluene solutions of 50 mg/L asphaltenes from Hamaca crude oil with the maximum of absorbance around 310 nm (Goncalves *et al.*, 2004). On the basis that "the spectral location of the absorption maximum varies considerably and almost continuously for the different crude oils" the authors conclude that "the similarity of the absorption spectra of the asphaltenes studied evidence that the same type of chromophores is present in these fractions."

c) Two absorption spectra for toluene solutions of Athabasca C7-asphaltenes with concentrations in the range from 10 to 200 mg/L (Alboudwarej *et al.*, 2004). The authors emphasize the presence of a common absorption maximum at 288 nm in most dilute solutions and recommend this wavelength as a standard one for the calibration of concentration measurements.
d) "Characteristic absorbance maximum" in the spectra of crude oil solutions (Lai *et al.*, 1993). Values of the intensity and of the wavelength position of this maximum (I_9 and I_8) were regarded as two of the nine "individual" and "most representative" parameters for an analytical characterization of native crude oils. For discriminating between crude oils belonging to different geographic origins the author employed a "pattern recognition method." As illustrated in Figure 2.5, each oil was represented by a circular profile (fingerprint) that consists of nine parameter axes that radiate from the center like spokes on a wheel. Attributes of the discussed "characteristic peaks" (I_8 and I_9) are highlighted by thicker lines.

One more publication (Castillo *et al.*, 2001) reports absorption spectra for toluene solutions of crude oil asphaltenes with concentrations below 100 ppm,

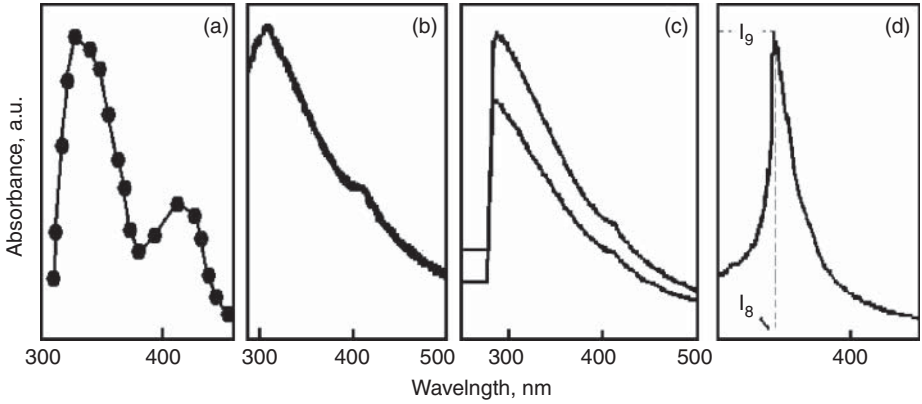

Figure 2.4 Representative examples of published "evidence" for "characteristic peaks" of asphaltenes (see text).

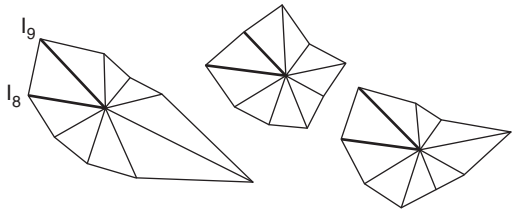

Figure 2.5 Employment of "characteristic absorbance maximum" for analytical characterization of crude oils by "pattern recognition method." *Source:* Adapted from Lai *et al.* (1993).

which exhibit a common absorbance maximum at 305 nm. The authors conclude that the value of this wavelength "hints to the possibility of observing two-photon absorption." A prominent absorbance peak at ca. 300 nm has been also reported for ppm (mg/L) solutions of asphaltenes, derived from coal (Guin and Geelen, 1996). A more recent example of an analytical technique based on "characteristic resonance absorption" in asphaltenes is in a suggested "New Method for Determination of Dispersity in Petroleum Systems" (Potapov *et al.*, 2006, 2008). The authors present experimental circular dichroism (CD) spectra which exhibit "the short-wave band with a maximum near 300 nm" and insist that "there is a correlation between the CD band position of crude oil toluene solutions and resonance absorption of pure asphaltene toluene solutions."

In spite of multiple cases of "experimental evidence," like those in Figure 2.4, our analysis of these results (Evdokimov and Losev, 2007a, 2007b, 2008) has definitely shown that "characteristic resonance absorption" not only cannot be regarded as a "fingerprint attribute" of crude oils/asphaltenes but also is nonexistent, being merely a trivial experimental artifact near the absorption edge of the solvent. This conclusion was arrived at by comparison of published "characteristic peaks" of absorbance, which revealed a striking and highly suspect coincidence of experimental data reported by different research groups for asphaltenes/crude oils of diverse origin. As an illustration, Figure 2.6 shows the data from original publications normalized to equal absorbances at 350 nm. The numbers denote absorbance spectra for the following toluene solutions:

- of a Tatarstan crude with 26 mg/L asphaltenes (Evdokimov and Losev, 2007a);
- of coal asphaltenes, 34.8 mg/L (Guin and Geelen, 1996);

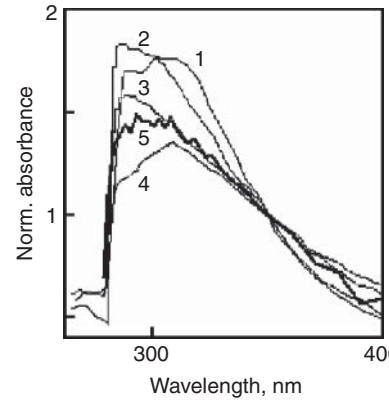

Figure 2.6 Highly suspect coincidence of published absorbance spectra for toluene solutions of asphaltenes and crude oils of diverse origin (see text).

- of asphaltenes from Athabasca bitumens, 100 mg/L (Alboudwarej *et al.*, 2004);
- of asphaltenes from a Hamaca crude, 50 mg/L (Goncalves *et al.*, 2004);
- of an oil solution with 11.2 mg/L asphaltenes (Potapov *et al.*, 2006, 2008).

The apparent origin of "resonance absorption" artifacts is analyzed by Evdokimov and Losev (2008). The spectroscopy specialists may regard the presented arguments as obvious; however, we found it difficult to convey to some petroleum scientists and practitioners the nature of the underlying solvent effects. A typical reaction was: "There cannot be any solvent effects: these are accounted for in modern spectrometers" or, "In spectrometers the solvent absorption is properly subtracted from the sample's signal." In our earlier book (Evdokimov and Losev, 2007b) we regarded such attitudes as "human factors," which we discussed at the end of Section 2.1. Namely, we classified it as a "syndrome of expensive equipment" when one finds it difficult to believe that the newly acquired expensive/modern/sophisticated/multifunctional/sensitive/automated/etc. spectrometer can provide questionable output. In fact, it can, mainly for the reasons that nowadays the details of signal processing and solvent subtraction are buried somewhere deep in the circuits of electronic blocs.

Artifacts due to subtraction rarely appear in concentrated solutions with comparable solvent and solute absorption coefficients. However, owing to extremely high UV/Vis absorptivity of asphaltenes, acceptable absorbances ($A < 2–3$) in conventional (cm length) cuvettes may be achieved only in highly diluted ppm (mg/L) solutions. In this case the ratio of solvent/solute absorption coefficients increases catastrophically near the absorption edge of a solvent. For pure toluene, absorption starts to grow at ca. 282 nm and 1 M absorption coefficient sharply rises to 6596 cm^{-1} at 261.75 nm (Lambert *et al.*, 1976; Berlman, 1971). Quantitative estimates of absorption spectra for 1 ppm and 10 ppm asphaltene concentrations in 1 M toluene are presented in Evdokimov and Losev (2008). Of crucial significance is that calculations predict absorbance values rising above 10^3, while any real spectrometer possesses certain threshold sensitivity to low relative intensities of the light, transmitted by a cuvette I_T/I_0 (where I_0 is incident intensity) and, hence, threshold sensitivity to high absorbances $A = -\log(I_T/I_0)$. For many commercial spectrometers I_T/I_0 thresholds are typically 10^{-4}–10^{-6} ($A_{max} \approx 4$-6). Any transmitted intensity below the threshold is fed into the processing electronic block as a common "noise" signal and, consequently, the processed absorbances for both cuvettes (with the studied solution and with the reference pure solvent) are regarded as being "saturated" at a common maximum level. In the final "solvent subtraction" operation in a spectrometer's electronic block, processed absorbances of the solvent are digitally subtracted from absorbances of solutions. The result is provided as an output signal of a spectrometer. In the vicinity of the solvent's absorption edge, owing to

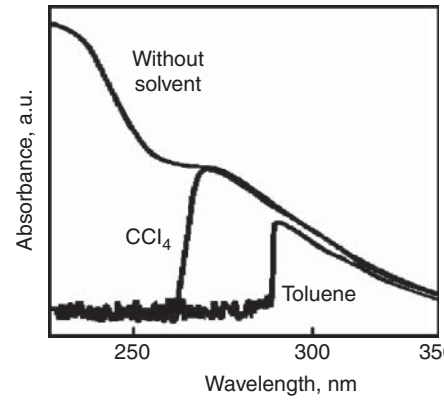

Figure 2.7 UV/Vis absorption spectra of crude oil solutions in toluene, in CCl_4 and of a solvent-free crude oil.

subtraction of equal (saturated) solution and solvent absorbances, the output signal sharply drops to (and remains at) close-to-zero level, an artifact absent in the properly measured absorption spectra. Visually, this artifact for toluene solutions may be classified as a sharp absorption maximum close to 300 nm and, evidently, it is the persistent "resonance absorption peak of asphaltenes," illustrated in Figure 2.4 and Figure 2.6.

The direct experimental verification of the above conclusions was performed by studying absorption spectra of crude oil solutions in solvents with different absorption edges (Evdokimov and Losev, 2007b, 2008). As shown in Figure 2.7, the "characteristic absorption peak" does follow the changes in an absorption edge of a solvent ~282–285 nm for toluene and ~265 nm for carbon tetrachloride. The solvent-free absorbance spectrum of a neat crude oil was obtained by a thin film technique (Evdokimov and Losev, 2007b). This spectrum practically coincides with reliable parts of solution's spectra and does not exhibits any "resonance absorption."

In summary, it may be concluded that many of the previously reported UV/Vis absorption properties of asphaltenes/crude oils may have been noticeably distorted by experimental artifacts. Following the style of a recent critique of other methods for "optical interrogation" of petroleum (Strausz *et al.*, 2008), we may conclude that frequent publications of such artifact as "resonance absorption band of asphaltenes" has caused a measure of confusion that hopefully now has been resolved and this episode in asphaltene studies has been closed for good.

2.2.2 Mythical "Characteristic Monomer Peaks" in Fluorescence Emission Studies

As noted in Section 2.1, even after decades of intensive experimental and theoretical studies, molecular structures of asphaltenes are still not well characterized and are the subjects of ongoing debate.

The most popular structural description of asphaltene molecules in Figure 2.2 are crucially based on the measured parameters of "characteristic" dome-shaped peaks in steady-state fluorescence emission spectra, which were observed at asphaltene concentrations of 10–25 mg/L when, as presumed by experimentalists, asphaltene existed as "monomers" in the studied solutions (Badre *et al.*, 2006; Buenrostro-Gonzalez *et al.*, 2001; Groenzin and Mullins, 1999, 2000, 2007; Mullins, 1998; Ralston, Mitra-Kirtley, and Mullins, 1996; Ruiz-Morales and Mullins, 2007, 2009).

In particular, the position of these peaks at 450–500 nm was regarded as proof of a virtual absence of 1- to 3-ring aromatic molecules in asphaltenes. Furthermore, this position was employed for comparison with a standard wavelength dependence of rotational diffusion correlation times for a set of molecules with well-known properties, as schematically illustrated in Figure 2.8. By such comparison, the average molecular weight of asphaltenes was estimated as ~750 Da.

In addition, the shapes of emission spectra were regarded as indicative of population distribution of asphaltene fluorophores (Mullins, 2010; Ruiz-Morales and Mullins, 2007), as schematically shown in Figure 2.9. On the basis of the peak position in these spectra, it was concluded that non-aggregated asphaltene molecules (monomers) predominantly contain 7–10 fused aromatic rings (FARs) as illustrated in Figure 2.2.

However, our recent re-examination of the above fluorescence experiments revealed that the conclusions about the MW of asphaltenes and the size of their aromatic systems should be regarded as false due to fundamental errors in measurement procedures and in the interpretation of the measured fluorescence spectra.

First, one necessary requirement, which is emphasized in multiple manuals and textbooks on fluorescence measurement (Guilbault, 1990; Lakowicz, 2006;

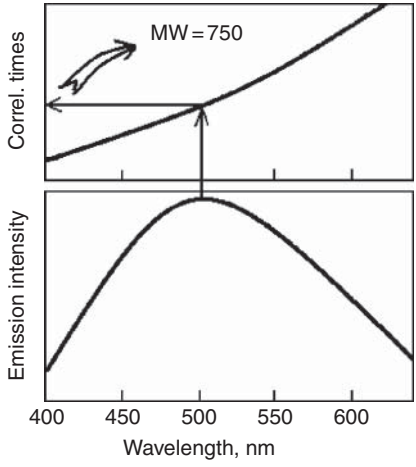

Figure 2.8 A scheme for determining the molecular weight of asphaltenes from the position of "characteristic monomer peaks" in fluorescence emission spectra.

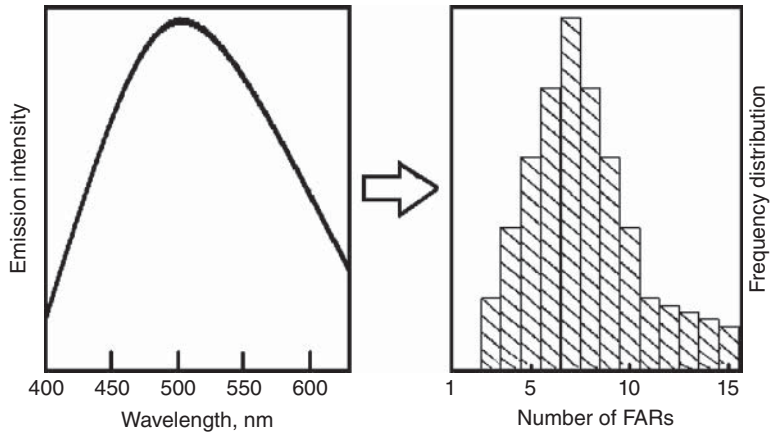

Figure 2.9 A scheme of determination of the predominant fused aromatic systems in asphaltenes from the position of "characteristic monomer peaks" in fluorescence emission spectra.

Miller, 1981; Wehry, 1976; Valeur and Berberan-Santos, 2012), is correcting the "raw" (as-measured) data for inner filter effects (IFEs). IFEs can be segregated into "primary IFEs" from the attenuation of the excitation light with λex and "secondary IFEs" that attenuate the fluorescence emission with λem. Frequently employed is the absorbance-based approach for IFE correction (Lakowicz, 2006), where the observed fluorescence intensity ($I^{obs}_{\lambda ex,\lambda em}$) is converted into the corrected fluorescence intensity ($I^{corr}_{\lambda ex,\lambda em}$) for each pair of excitation and emission wavelengths by the following transformation:

$$I^{corr}_{\lambda ex,\lambda em} = I^{obs}_{\lambda ex,\lambda em} \times 10^{\{0.5\times[A(\lambda ex)+A(\lambda em)]\}} \tag{2.1}$$

The factor 0.5 in the power exponent appears in the 90° geometry because absorbance (excitation) and fluorescence (emission) are assumed to occur at the midpoint of the cuvette.

Such corrections have never been performed in the discussed experiments (Badre *et al.*, 2006; Buenrostro-Gonzalez *et al.*, 2001; Groenzin and Mullins, 1999, 2000, 2007; Mullins, 1998; Ralston, Mitra-Kirtley, and Mullins, 1996; Ruiz-Morales and Mullins, 2007, 2009) in the assumption that "no complications from self-absorption" occur at asphaltene concentrations of 10–25 mg/L because "optical densities OD of all solutions were kept below 0.2." This assumption appears to be unfounded and wrong. First, no direct comparisons of the as-measured "raw" fluorescence emission spectra with those that are corrected for "inner filter"/self-absorption effects are present in the discussed publications. Second, the statement of OD < 0.2 is misleading. The optical densities for 10–25 mg/L asphaltene solutions in standard 10 mm cuvettes do fall below 0.2, but only in the wavelength range that comprises the maxima

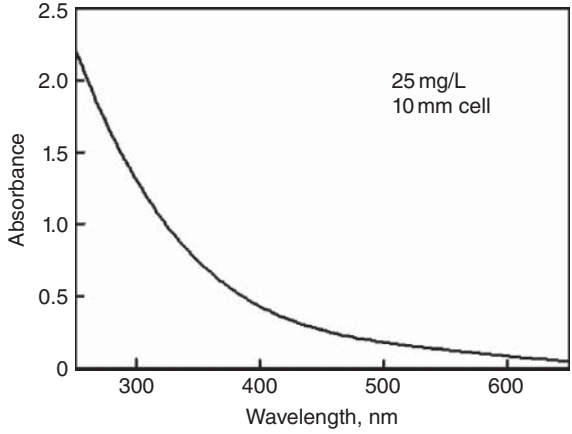

Figure 2.10 Sharp increase of short-wavelength absorbance in asphaltene solutions. *Source:* Adapted from Mullins (2010).

of "raw" spectra. However, optical densities strongly increase at shorter wavelengths. As an example, consider Figure 2.10 with absorbance (optical density) data from Figure 2.14 in Mullins (2010), re-calculated for a standard fluorimeter's 10 mm cell and an asphaltene concentration of 25 mg/L.

Consequently, "inner filter"/self-absorption corrections would notably alter the shape and positioning of the "characteristic monomer peaks" in "raw" fluorescence emission spectra of discussed experiments. To support this conclusion, Figure 2.11 compares one of these "raw" spectra from Mullins (1998, 2010) with the spectrum corrected for "inner filter"/self-absorption effects. The correction was performed by the method of Equation (2.1) with A(λ) dependence from Figure 2.10. Significant changes in the shape and position of the corrected spectrum are clearly seen.

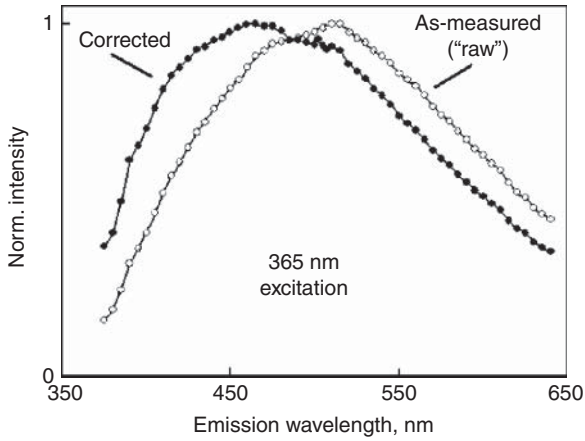

Figure 2.11 Significant shift of "characteristic monomer peak" after proper correction of as-measured (raw) fluorescence emission spectrum for "inner filter"/self-absorption effects.

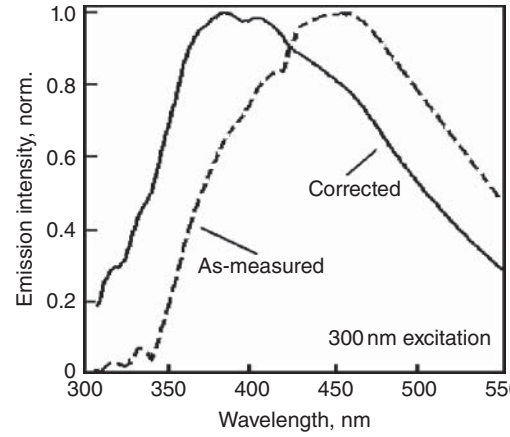

Figure 2.12 Another example of the necessity of "inner filter"/self-absorption corrections in analysis of asphaltenes by fluorescence emission measurements. *Source:* Evdokimov, Fesan, and Losev (2016).

The crucial importance of "inner filter" corrections in fluorescence studies of 10–25 mg/L asphaltene solutions was recently demonstrated by Evdokimov, Fesan, and Losev (2016). As an example, Figure 2.12 shows steady-state fluorescence emission spectra for 15 mg/L asphaltene solution at 300 nm excitation. Significant changes in the corrected spectrum are clearly observed.

Second, the attribution to asphaltene "monomers" of fluorescence emission peaks at 450–500 nm in 10–25 mg/L asphaltene solutions is fundamentally wrong. In this attribution, the authors of the popular description of asphaltene "monomers" in Figure 2.2 disregarded multiple experimental evidence of other research teams that asphaltenes start to aggregate at much lower concentrations (see Section 2.1). Moreover, fluorescence emission studies of benzene solutions with a wide range of asphaltene concentrations (Evdokimov, Fesan, and Losev, 2016) definitely proved that the "characteristic" peak at 450–500 nm belongs not to asphaltene "monomers" with 7–10 aromatic rings but to aggregates of much smaller asphaltene molecules. In these studies, non-aggregated asphaltene molecules were registered only in solutions with asphaltene concentrations no higher that 0.7 mg/L. As an illustration, Figure 2.13 shows fluorescence emission spectra for 0.34 mg/L and 15 mg/L solutions, normalized to equal areas. The 0.34 mg/L spectrum is dominated by an emission peak at 290–310 nm with some additional weak structure extending to 390–400 nm. In the original publication, this spectrum was compared with the standard spectra of fluorescence emission from monomers of 1- to 4-ring aromatic compounds (Table 2.1). It was concluded that non-aggregated asphaltene molecules (monomers) predominantly contain small, 1- to 3-ring, aromatic fluorophores. The "characteristic" 450–500 nm peaks appear in the spectra of more concentrated solutions (e.g. 15 mg/L). Following literature analysis, this wavelength range is typical for emission from aggregates of small aromatic molecules (see

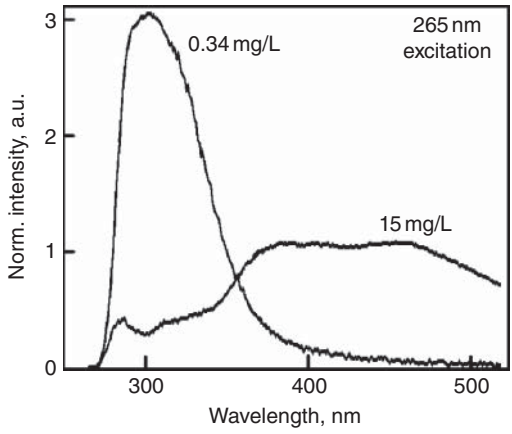

Figure 2.13 Representative fluorescence emission spectra from benzene solutions with non-aggregated and aggregated asphaltenes. *Source:* Adapted from Evdokimov, Fesan, and Losev (2016).

Table 2.1). Hence, it may be concluded that the above discussed "characteristic monomer peak" is, in fact, a "characteristic aggregate peak" of asphaltenes.

In summary, now there is ample experimental evidence that individual asphaltene molecules, which are prone to aggregation at higher concentrations, are relatively small species with predominant 1- to 3-aromatic ring chromophores, in contrast to the widely publicized misconception of the structure in Figure 2.2, which describes much larger 7- to 10-ring "monomers." This misconception appears to originate in multiple publications of a prolific research group (Badre *et al.*, 2006; Buenrostro-Gonzalez *et al.*, 2001; Groenzin and Mullins, 1999, 2000, 2007; Mullins, 1998, 2010; Pomerantz *et al.*, 2015; Ralston, Mitra-Kirtley, and Mullins, 1996; Ruiz-Morales and Mullins, 2007, 2009), which were evidently aimed at designing a simplified "effective" structural description of asphaltenes that is immediately suitable for spectacular practical applications in the Flory–Huggins equations of state and in interpretations of data on "reservoir compartmentalization, connectivity, baffling, tar mat and heavy oil formation, disequilibrium gradients, diffusive gradients in reservoirs, biodegradation, reservoir fluid geodynamics." In a quest for such an effective description, these researchers decided to consider molecular species that are observed at concentrations of up to 10–25 mg/L as individual asphaltene molecules, ignoring available experimental evidence by other research groups that asphaltenes remain aggregated at these and much lower concentrations, below 1 mg/L. Moreover, "experimental proofs" of the 7- to 10-ring model appear to be erroneous. In particular, the fluorescence emission spectra have not been corrected for "inner filter effects." Additionally, multiple flaws were present in the fluorescence depolarization-rotational correlation time experiments, as convincingly demonstrated in Strausz *et al.* (2008), with the conclusion that the 7- to 10-ring results "are egregiously wrong" and the

Table 2.1 Positions of fluorescence emission (FE) peaks in standard spectra of some 1- to 4-ring molecules and their aggregates.

		FE peak from monomers		FE peak from aggregates	
Compound	**No. of rings**	**Position (nm)**	**Reference**	**Position (nm)**	**Reference**
styrene	1	306	Cignoli *et al.* (2012)	335	Kuo (2011)
1,4-Dicyanobenzene	1	290	Zhang and Chen (1988)	378	Zhang and Chen (1988)
thiophene	1	285	Tor *et al.* (2007)	408–522	Yang (2000)
naphthalene	2	320	Dixon, Taniguchi, and Lindsey (2005)	405	Banerjee *et al.* (2012)
benzothiophene	2	300–310	Tor *et al.* (2007)	460–490	Jung *et al.* (2007)
quinoline	2	384	Itoh (2014)	430–480	Ramachandran *et al.* (2014)
phenanthrene	3	365	Cignoli *et al.* (2012)	415	Wang *et al.* (2001)
anthracene	3	389	Cignoli *et al.* (2012)	468	Huang and Feng (2014)
dibenzothiophene	3	328	Zwarich (1968)	400–495	Jung *et al.* (2007); Cho, Woo, and Hwang (2012)
benzoquinoline	3	351–367	Mabuchi *et al.* (2005)	440	Mabuchi *et al.* (2005)
pyrene	4	391	Cignoli *et al.* (2012)	483	Pope and Swenberg (1999)

"inferences postulated with respect to the molecular architecture of asphaltene … should in their entirety be disregarded."

2.3 Misconceptions about the Properties of UV/Vis Absorption Spectra of Asphaltenes

In publications on "optical interrogation of asphaltenes" studies of light intensity attenuation in asphaltene solutions are conventionally described as

"absorption studies" (Mullins, 1998, 2010). In these experiments the measured quantities are intensities of light I and I_0 passing through the cell with investigated solution and through the identical reference cell with pure solvent. The calculated quantity $\log_{10}(I_0/I)$ is a function of light wavelength. It is usually called "absorbance" $A(\lambda)$ and is described by a Beer-Lambert law

$$A(\lambda) = \varepsilon(\lambda)Cl, \tag{2.2}$$

where l is the cell's length and C is the asphaltene concentration in the solution. If there are no changes of the molecular state of asphaltenes in different solvents (e.g. in absence of asphaltene aggregation), $\varepsilon(\lambda)$ would be constant and there would be a simple linear dependence of the measured values of A on asphaltene concentration. $\varepsilon(\lambda)$ is called "coefficient of absorption" or "absorptivity" in the assumption that "there is no optical light scattering" by asphaltenes (Mullins, 1990; Mullins, Mitra-Kirtley, and Zhu, 1992; Ruiz-Morales and Mullins, 2007, 2009). As is discussed in Section 2.3.3, recent experiments (Dechaine and Gray, 2011a, 2011b; Derakhshesh, 2012; Derakhshesh, Gray, and Dechaine, 2013; Morimoto, 2015) showed that this assumption may be fundamentally wrong. These studies provided a direct experimental proof that asphaltenes dispersed in toluene showed no absorption in the visible light range and that the measured "absorbance" is due to Rayleigh scattering, which correlated with the size of asphaltene aggregates. Obviously, these results will require serious revision of terminology in the optical interrogation of asphaltenes. However, for convenience, in the following sections the terms "absorption," "absorbance," and "absorptivity" will be used as in original publications without implying any particular mechanisms of light attenuation.

2.3.1 The Myth about the Absence of Asphaltene Aggregation Effects in Optical Absorption Studies

It has been frequently stated that "there is no change in the visible–NIR [near-infrared] spectra of asphaltenes above and below various aggregation concentration thresholds" (Ruiz-Morales and Mullins, 2013; Ruiz-Morales, Wu, and Mullins, 2007); "there is no detectable effect of aggregation on asphaltene absorption spectra" (Mullins, 2010). Without sufficient experimental proof it was concluded that "asphaltene spectra strictly obey the linear Beer–Lambert law; the absorption spectra do not exhibit any appreciable nonlinearities because of aggregation" (Mullins, 2010); "asphaltene electronic absorption is linear in asphaltene concentration over a very wide range – from 5 mg/L to 5 g/L" (Ruiz-Morales and Mullins, 2009).

However, in optical absorption studies of other molecular systems it is a common practice to study molecular aggregation by observing variations of absorptivity $\varepsilon(\lambda)$ with concentration, i.e. deviations from the linear Beer–Lambert law implying constant absorptivity (Carroll *et al.*, 1999; Haswell, 1991; Rao, 1975).

Hence, there is no reason why aggregating asphaltenes in solution would be a unique example of constant absorptivity. Indeed, a literature survey of publications on optical absorption of asphaltenes revealed quite a number of experimental results which, subjected to a proper analysis, show specific effects that may be attributed to asphaltene aggregation. These effects, however, have not been noticed by the authors, because of inappropriate methods of data presentation, namely on plots of absorbance versus concentration comparatively weak variations of $\varepsilon(\lambda)$ are masked by the strong linear dependence on C. As a representative example, consider the studies of asphaltene aggregation in toluene (Castillo *et al.*, 2001). The authors present a "calibration curve," i.e. a plot of absorbance at 532 nm (optical path length $l = 0.1$ cm) vs. asphaltene concentration in the range of C = 10–600 mg/l. They state that absorption "is rather insensitive to aggregation processes in the observed concentration range" and that "this observation is confirmed by the almost perfectly linear calibration curve." Note that in the original publication this conclusion is not supported by a linear approximation of experimental points. For further analysis, we extracted the numerical absorbance values A(C) from the experimental points in this "calibration curve" and re-plotted the A(C) dependence in Figure 2.14 with an additional best fit of a linear function. Some deviations from "perfect linearity" may be noticed. Furthermore we calculated the respective absorptivities $\varepsilon(C) = A(C)/Cl$ in units of cm^2/mg. The final results of this data analysis are presented in Figure 2.15, where variations of absorptivity with concentration become clearly seen and may be attributed to consecutive aggregation stages (Evdokimov, 2010; Evdokimov, Eliseev, and Akhmetov, 2003b).

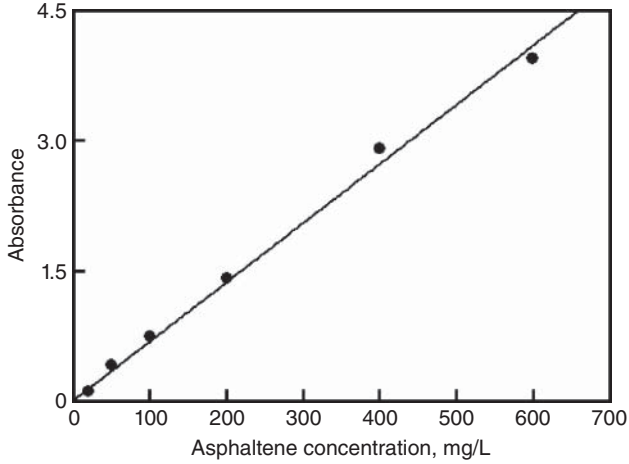

Figure 2.14 The original asphaltene absorbance data (re-plotted from Castillo *et al.*, 2001) with a "perfectly linear" concentration dependence. *Source:* Adapted from Castillo *et al.* (2001).

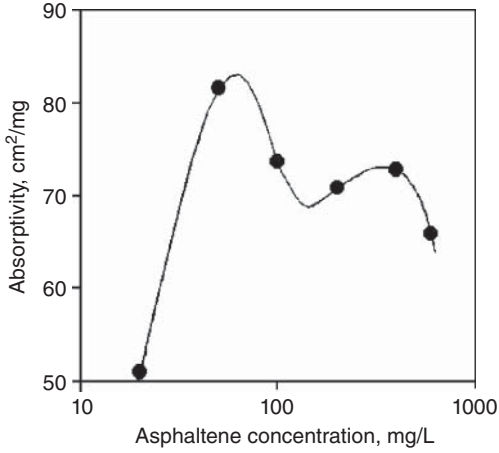

Figure 2.15 The data from Figure 2.14 presented in terms of asphaltene absorptivity. Asphaltene aggregation effects become clearly seen.

Apparently, the first case of intentional use of absorptivity measurements for studying asphaltene aggregation was reported in the rarely cited 1986 publication (Yokota *et al.*, 1986). This paper contains experimental evidence of strong concentration effects on absorption spectra of Athabasca asphaltenes in benzene solutions due to asphaltene aggregation commencing at concentrations of ca. 5 mg/L. As an illustration, Figure 2.16 shows concentration dependence of asphaltene absorptivity, reconstructed from the data in Table 3 of the respective publication.

A detailed investigation of asphaltene aggregation in the wide concentration range (from 1.6 mg/L to 1.5 g/L) was performed by measuring UV/Vis absorption at fixed wavelengths (Akhmetov, Evdokimov, and Eliseev, 2002; Evdokimov, Eliseev, and Akhmetov, 2003a, 2003b). Figure 2.17 shows the dependencies of absorptivity at 670 nm on asphaltene concentration in toluene solutions

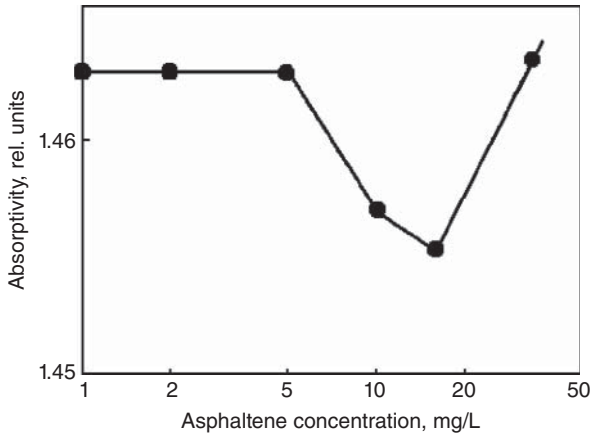

Figure 2.16 The earliest experimental evidence of aggregation-dependent asphaltene absorptivity in highly dilute solutions. *Source:* Adapted from Yokota *et al.* (1986).

of crude oil (data set labelled "O") and of solid asphaltenes (data set labelled "A"). Absorptivity minima were attributed to consecutive formation of various asphaltene oligomers and colloidal particles. Note the virtual coincidence of aggregation stages in both types of solutions. This coincidence indicated that asphaltenes *self-aggregate* in solutions and in crude oils; other crude oil constituents apparently provide only a minor influence on aggregation phenomena. Specifically, in the course of primary aggregation, there appears to be no "stabilizing effect" frequently associated with the presence of resin molecules in oil media (Dickie and Yen, 1967; Yen and Chilingarian, 1994, 2000). The conclusion that resins fail to stabilize asphaltene dispersions has been independently confirmed by other experimental techniques (Gonzalez *et al.*, 2003).

Continuing efforts of some research teams to support the myth about the absence of aggregation effects on asphaltene absorptivities (constancy of $\varepsilon(\lambda)$ in different solutions) may be explained by their "revolutionary" suggestions for simplified analytical characterization of petroleum molecular systems, namely these scientists claim that "the absorption spectral profile … directly gives the population distribution of molecules" in asphaltenes and crude oils (Mullins, 1998; Mullins, Mitra-Kirtley and Zhu, 1992). The respective theoretical model (see Section 2.3.2) was based on "experimental" absorbance spectra in the very wide range of light wavelengths (photon energies), from UV to NIR, like those shown in Figure 2.18 (after Mullins, Mitra-Kirtley, and Zhu, 1992). Note that in these spectra the "measured" absorbances vary by more than three orders of magnitude, while it is not possible to accurately measure absorbances higher than 2–2.5 with commercially available instruments for chemical analysis (Perkampus, 1992). The authors of the original paper recognize that these spectral curves were obtained by splicing absorption spectra of multiple samples with different concentrations. This procedure would be adequate only in case of the constant $\varepsilon(\lambda)$. However, in view of well-proven concentration-dependent absorptivities, such a spliced spectrum appears to be an artificial "chimera" which does not belong to any real substance.

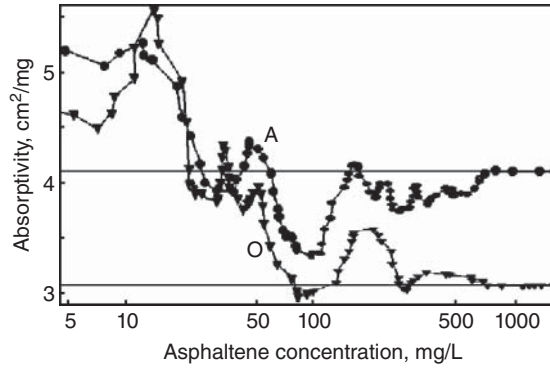

Figure 2.17 Experimental evidence for strong molecular aggregation effects on asphaltene absorptivity in toluene solutions. *Source:* Adapted from Evdokimov, Eliseev and Akhmetov (2003b); Evdokimov (2008).

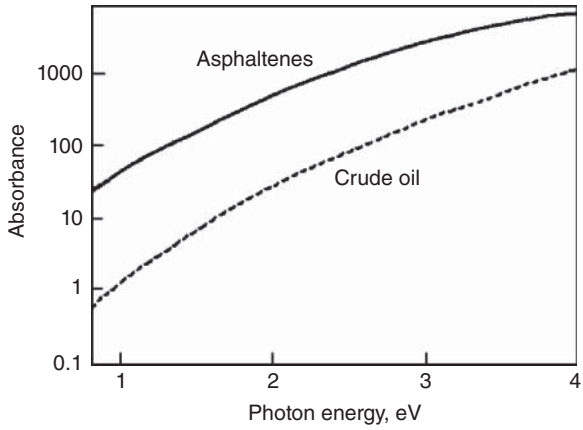

Figure 2.18 "Representative" optical absorption spectra of a crude oil and of asphaltenes (re-plotted from Mullins, Mitra-Kirtley, and Zhu, 1992). Each spectrum is constructed from spliced spectra of multiple samples with various dilutions, an artificial "chimera" which does not belong to any real substance.

2.3.2 The Myth about the "Urbach Tail" in Optical Absorption Spectra of Asphaltenes and Crude Oils

As mentioned above some research teams insist that "the absorption spectral profile … directly gives the population distribution of molecules" in asphaltenes and crude oils (Mullins, 1998; Mullins, Mitra-Kirtley and Zhu, 1992). Above all, this conclusion is derived from erroneous interpretation of the fact that the most apparent feature in absorption spectra of asphaltenes and crude oils is a smooth "continuum." In spite of many suggestions/models, the precise nature of these continuous spectra of crude oils and asphaltenes remains a mystery.

The discussed erroneous interpretations of optical properties of asphaltenes/crude oils utilize some concepts of the so-called amorphous semiconductor (AS) model. The name AS model sounds restrictive and may be misleading. In fact, this model is applicable to descriptions of optical properties of a wide range of molecular systems. The only requirements are the absence of a long-range (crystalline) order, and the presence of some degree of a short-range order in any absorber (chromophore). The latter requirement makes it possible to employ concepts of "densities of states" and of "energy bands" for *individual* molecules/chromophores. It is important that in a liquid phase practically continuous energy bands emerge only in sufficiently large molecules. For example, in so-called conducting polymers initially identical energy levels of monomers split into continuous bands only upon polymerization (Wallace *et al.*, 2003).

The standard AS models consider systems of identical molecules with similar energy bands, as schematically illustrated in Figure 2.19. The main electronic transitions, responsible for different parts of continuous absorption spectra in such AS systems (Figure 2.20), are listed below (Adachi, 1999; Singh and Shimakawa, 2003).

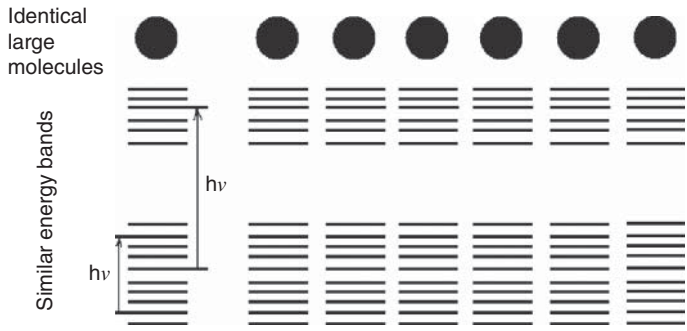

Figure 2.19 Schematic representation of a molecular system described by the standard AS model. All electronic transitions are within energy levels of a specific large molecule (chromophore).

Figure 2.20 The main regions of continuous absorption spectra in the AS model. *Source:* After Adachi (1999) and Singh and Shimakawa (2003).

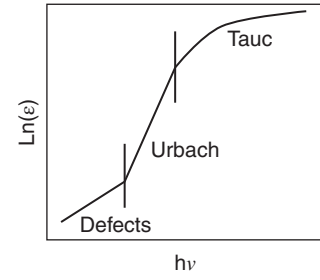

2.3.2.1 Tauc Range

Band-to-band transitions for photon energies in excess of the band gap E_0. In this strong absorption region absorptivity ε can be described by the Tauc relation: $\varepsilon h\nu \sim (h\nu\text{-}E_o)^2$.

2.3.2.2 Urbach Range

Transitions within an energy band involving disorder-related exponential tails (Urbach tails) with $\varepsilon \sim \exp(h\nu/E_U)$, where "Urbach energy" E_U indicates the width of the band tails of localized states.

2.3.2.3 Low Absorption (Defects) Range

Transitions involving defect states within the band gap most frequently are modeled using an error function, which is an integral of a Gaussian energy distribution of defects. As a first approximation, these may be described by another exponential dependence: $\varepsilon \sim \exp(h\nu/E_d)$, where the width of the defect states E_d usually is larger than E_U (Singh and Shimakawa, 2003).

With respect to crude oils and asphaltenes the original AS model has been restricted to the Urbach range and implicitly revised. It has been postulated that "the Urbach phenomenology describes the absorption spectra of crude oils

and asphaltenes when absorption is dominated by lowest energy transitions" (Mullins, 1998).

However, while the original model refers to "population distribution of energy states" in any individual molecule (density of states), the revised AS model suggests that the absorption spectral profile provides a measure of the "population distribution of molecules." It is stated that Urbach slopes of "optical absorption spectra of crude oils give the population distributions of chromophores" (distributions of aromatic molecules) and that "all crude oils, from the heaviest tar to the lightest gas condensate … exhibit the same slope," the reason for similarities of distributions/slopes being "the underlying similarities of the geophysical and geochemical processes which give rise to different crude oils" (all quotes from Mullins, 1998).

Obviously, the above conclusions are fundamentally wrong. As schematically illustrated in Figure 2.21, application of the Urbach law $\varepsilon \sim \exp(h\nu/E_U)$ to systems of molecules without wide energy bands would suggest light absorption by transitions between energy levels of different molecules (!) which is clearly impossible.

The fundamental errors in the revised AS model were also noted by other research groups, for example by Schultze, Lemke, and Löhmansröben (2004). These scientists reported that in their oil samples the long-wavelength absorption tails were formally consistent with the Urbach rule $\varepsilon \sim \exp(h\nu/E_U)$. However, the underlying molecular mechanism they did not discuss in terms of MW distribution. In line with the original AS/Urbach philosophy, Schultze, Lemke, and Löhmansröben (2004) suggest that the observed absorptivity behavior points to the presence in oils of large molecules with high structural disorder, for example of biogenic macromolecules and polymers.

Furthermore, even if "the absorption spectral profile … directly gives the population distribution of molecules" in asphaltenes and crude oils (Mullins,

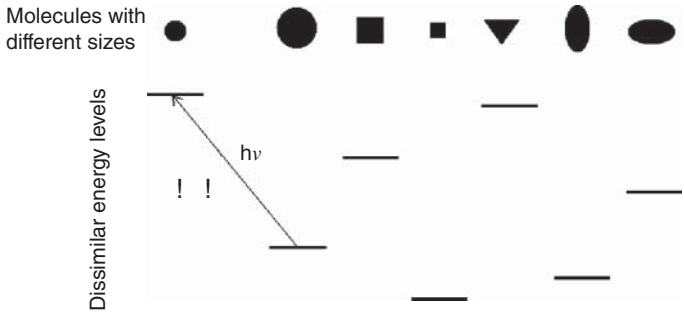

Figure 2.21 Schematic representation of a molecular system implicitly accepted in the revised AS model. Note the impossible electronic transitions between energy levels of different molecules.

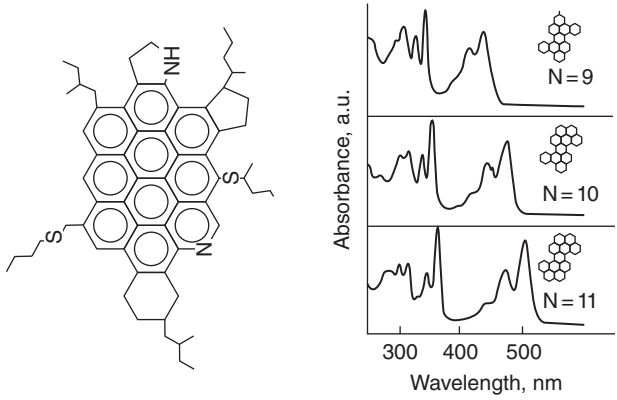

Figure 2.22 Left, a "continental"-type asphaltene molecule with a single large PAH chromophore. *Source:* Rogel (1995). Reproduced with permission of Elsevier. Right, absorption spectra of large PAH molecules. *Source:* Fetzer (2000). Reproduced with permission of John Wiley & Sons, Ltd.

1998; Mullins, Mitra-Kirtley and Zhu, 1992), the authors of the revised AS theory could hardly explain the observed continuum in absorption spectra. The reason is that they assume the multiple-ring "continental" model of an asphaltene molecule (see an example in the left part of Figure 2.22) with the population distribution peaking at the number of pericondensed aromatic rings N = 7–10 (Mullins, 2010; Ruiz-Morales and Mullins, 2007). A literature review shows that superposition of individual spectra of such molecules cannot result in a true absorption continuum. As an illustration, the right part of Figure 2.22 shows representative UV/Vis absorbance spectra for a series of large polycyclic aromatic hydrocarbons (PAHs) with N numbers up to 11 (Fetzer, 2000). It is clear that superposition of the weakly shifting UV bands may be expected to form a peak at 280–360 nm accompanied by a minimum of absorbance, while even such large molecules cannot provide a noticeable absorbance above 500–550 nm. Other authors also pointed out that continuous spectra of petroleum systems cannot belong to PAH series as the superposition of PAH absorption spectra results in well-resolved multiple peak structures (Alfe *et al.*, 2007)

In spite of the above arguments, the authors of the revised AS theory continued their attempts to model continuous absorption spectra by specific population distributions of "continental"-type asphaltene molecules (Ruiz-Morales and Mullins, 2009). For these calculations they employ 523-member population distribution, which they describe as: "The distribution has 7 fused rings as the most probable, with a symmetric distribution falling off to 3 and 11 fused rings, respectively (with no smaller ring systems). We also include a large fused ring 'tail' of up to 15 fused aromatic rings."

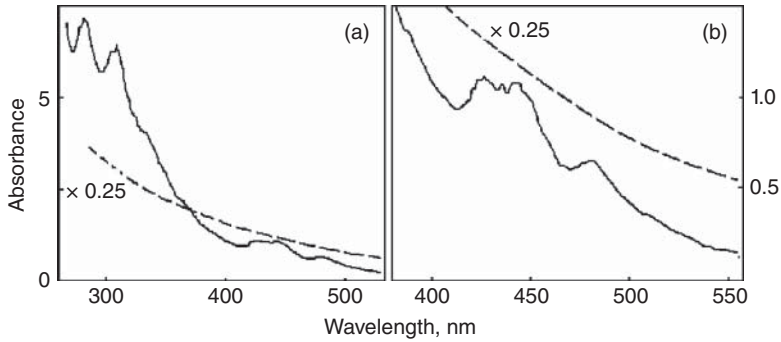

Figure 2.23 (a) Re-plotted simulated and experimental absorption spectra of asphaltenes. (b) The large-wavelength parts of these spectra. *Source:* Adapted from Ruiz-Morales and Mullins (2009).

The authors conclude that their calculated absorption spectra show good agreement with the experimental ones. In particular, they note that an "important similarity between the simulated and measured spectra is the lack of spectral structure." In support, they present plots of logarithm of absorbance vs. photon energy, known to mask/dampen possible peak structures. In fact, after we re-plotted these data in more conventional absorbance vs. wavelength graphs (Figure 2.23), it became clear that the agreement between simulated and experimental spectra is far from satisfactory, as may have been expected. The dashed line in Figure 2.23 represents a perfectly structureless experimental spectrum of "ST3" petroleum asphaltenes (multiplied by a factor of 0.25 for ease of comparison). On the contrary, the simulated spectrum (solid line) does exhibit a well-developed peak structure both at UV wavelengths and in the visible-to-NIR range.

2.3.3 In the UV/Vis Spectral Range Asphaltenes Apparently Act not as Absorbers, but as Scatterers

The previously discussed "Urbach tail" model predicts "the exponential decrease of absorption for asphaltenes" (Mullins, Mitra-Kirtley and Zhu, 1992; Ruiz-Morales and Mullins, 2007) and "the universal exponential decay for crude oil absorption spectra" (Downare and Mullins, 1995) in the visible–NIR wavelength ranges.

However, in depth experimental analysis of multiple crude oil and asphaltene samples of diverse geographical/geological origin revealed that all visible–NIR absorption spectra may be approximated by a power law $A(\lambda) \sim \lambda^{-m}$ with m ranging between 3.14 and 4.33 (Evdokimov, 2010; Evdokimov, Eliseev, and Akhmetov, 2003a). The fact that the observed exponents are centered on a value of 4 suggests that not electronic absorption by individual asphaltene

molecules but Rayleigh scattering from asphaltene aggregates is the dominant mechanism (Derakhshesh, 2012; Derakhshesh, Gray, and Dechaine, 2013).

A direct experimental proof of this suggestion is presented by Dechaine and Gray (2011a, 2011b). The authors studied the diffusion of asphaltenes from several heavy oils and bitumens in dilute toluene solutions using a stirred diffusion cell equipped with ultrafiltration membranes. The pore sizes were varied between 3 and 20 nm to retain aggregates while allowing free molecules to diffuse. The permeate was continuously monitored using an in situ UV/Vis spectroscopy. It was observed that ultrafiltration membranes with pore sizes < 5 nm were able to retain a large portion of the total asphaltenes in toluene solution. Although asphaltenes in solution absorb radiation across the entire UV/Vis spectrum, the permeate from the aforementioned filtration process displayed no absorbance in the visible ($\lambda > 550$ nm) range, as schematically illustrated in Figure 2.24. The fact that the absorbance in the visible region was eliminated by a filtration process indicates that this "absorbance" (light extinction) is likely linked to asphaltenes nano-aggregates, since these species are retained by the membrane if the pores are smaller than the size of the nano-aggregates. Therefore, it is plausible that the interactions of visible light with asphaltenes are affected by a scattering (i.e. a size-dependent) mechanism, and, if so, nano-aggregate size, or more importantly disaggregation phenomena, can be monitored by the UV/Vis spectroscopy. The origin of the asphaltenes (Athabasca, Safaniya, and Venezuela) did not have a significant impact on the observed behavior; therefore, the above observations are widely applicable to all C7 asphaltenes.

Subsequent experiments (Derakhshesh, 2012; Derakhshesh, Gray, and Dechaine, 2013) provided additional evidence for predominance of Rayleigh scattering in visible light attenuation by asphaltenes. Some asphaltenes used in this study were precipitated from an Athabasca bitumen produced by

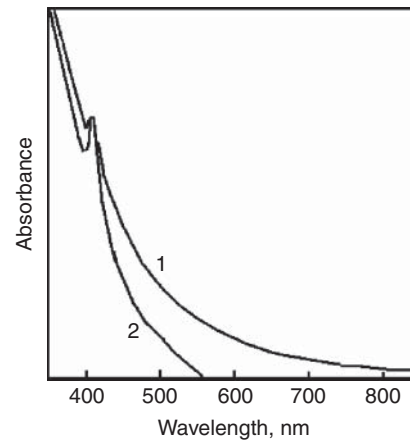

Figure 2.24 Schematic illustration of direct experimental proof that asphaltene "absorbance" in the visible range is due to scattering by molecular aggregates. 1. As-prepared asphaltene solution. 2. Solution with aggregates removed by ultrafiltration. *Source:* Adapted from Dechaine and Gray (2011a).

steam-assisted gravity drainage using n-pentane in an industrial pilot plant. This material had low concentration of mineral solids and was labeled as C5 industrial asphaltenes. The other asphaltene samples used were n-heptane insoluble (C7)—the same as those used in (Dechaine and Gray, 2011a).

In the case of C7 asphaltenes, high concentration stock solutions of asphaltenes in toluene (10 g/L or 2 g/L) were prepared by weighing out the solid asphaltenes on a microbalance (±0.001 mg) and carefully transferring them to a class A 100 mL volumetric flask. The flask was filled to the base of the neck with toluene and sonicated for at least 1 h to accelerate dissolution. Afterward, the flask was allowed to cool, topped to the mark, and the final weight recorded to ±0.0001 g. The stock solutions were then serially diluted to yield solutions with varying concentrations of asphaltenes ranging from 30 mg/L to 10 g/L, spanning three orders of magnitude in concentration. These samples were subjected to UV/Vis spectroscopy measurements using 1 mm and 10 mm cuvettes. Figure 2.25 schematically illustrates typical shapes of the as-measured (raw) UV/Vis spectra for samples with different asphaltene concentrations, in conventional absorbance vs. wavelength plots. The small hump evident at 408 nm of these spectra is evidence of vanadyl porphyrins present in the asphaltenes.

All "raw" spectra were analyzed for the presence of the Rayleigh scattering in the assumption that the measured "absorbance" A may be described by the Beer–Lambert law (Equation (2.2)) where "absorptivity" $\varepsilon(\lambda)$ is dominated by the Rayleigh scattering cross-section $a_R(\lambda)$: $\varepsilon(\lambda) = N_A a_R(\lambda)/2.303$. For a spherical particle of radius r and refractive index n_P, in solvent with refractive index n_S:

$$a_R(\lambda) = \frac{128\pi^5 n_S^4}{3}\left[\frac{(n_P/n_S)^2 - 1}{(n_P/n_S)^2 + 2}\right]^2 \frac{r^6}{\lambda^4} \tag{2.3}$$

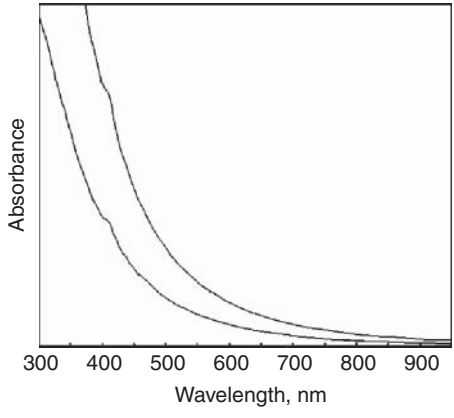

Figure 2.25 Schematic illustration of typical shapes of the as-measured (raw) UV/Vis spectra for samples with different asphaltene concentrations. *Source:* After Derakhshesh (2012) and Derakhshesh, Gray, and Dechaine (2013).

Hence, in the absence of electronic absorption, the measured "absorbance" may be expressed as:

$$A(\lambda) = lC\xi\frac{r^6}{\lambda^4}$$

with the constant factor

$$\xi = \frac{128\pi^5 n_S^4 N_A}{.909}\left[\frac{(n_P/n_S)^2 - 1}{(n_P/n_S)^2 + 2}\right]^2 = const$$

These equations indicate that if Rayleigh scattering is responsible for the measured extinction, then the measured "absorbance," $A(\lambda)$, would vary linearly with the inverse fourth power of the wavelength (λ^{-4}). In contrast, if the observed extinction were due to molecular absorption then the measured absorbance would vary linearly with $1/\lambda$ (Bohren and Huffman, 1983).

Accordingly all "raw" asphaltene spectra (see Figure 2.25) were converted to the Rayleigh scattering form (absorbance vs. λ^{-4}), and the representative results are shown in Figure 2.26.

For all studied samples, the converted spectra were linear within the range of wavelengths from 550 to 950 nm, with a coefficient of determination (R^2) in excess of 0.996 for least-squares regression fits of the data. These results in the visible range were consistent with previously published results in the NIR, which also showed a linear dependence of absorbance on λ^{-4}.

The fact that converted curves are highly linear suggests that the primary mechanism for the observed extinction in the visible–NIR region is indeed Rayleigh scattering. If absorption were significant in this region, it would be expected that the power coefficient for λ would be somewhere between -1 (absorption) and -4 (Rayleigh scattering). However, none of the converted

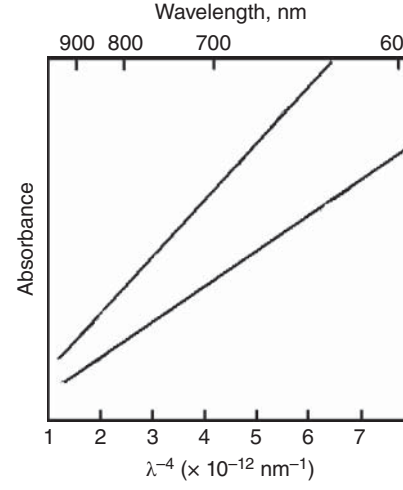

Figure 2.26 Schematic illustration of "raw" spectra from Figure 2.25 converted to the Rayleigh scattering form. *Source:* After Derakhshesh (2012) and Derakhshesh, Gray, and Dechaine (2013).

spectra (like those in Figure 2.26) showed any signs of significant deviations from linearity indicating limited molecular absorption and the predominance of Rayleigh scattering in this region of the UV/Vis spectrum.

The revised mechanisms of light attenuation in asphaltene solutions were concisely described by Dechaine and Gray (2011b) in a conference presentation "Why Are Asphaltene Solutions Black?":

> The apparent absorption of UV-Visible radiation by asphaltenes in solution extends over a very wide range of wavelengths, from the ultraviolet to the infra-red. Recent work with a stirred diaphragm diffusion cell indicates that membranes with pore sizes less than 5 nm are capable of removing the species responsible for the absorption of visible light with wavelengths >550 nm. A further analysis of the spectra of the whole asphaltene samples in toluene indicates that the absorbance of visible light with wavelengths > 600 nm follows a λ^{-4} dependence regardless of concentration or geographical origin. This functional dependence is consistent with Rayleigh scattering, rather than a mixture of colored components or chromophores. The fact that the "chromophores" above 600 nm have sizes > 5 nm and can be filtered out, and the fact that the "absorbance" follows the classical λ^{-4} dependence for Rayleigh scattering provide strong evidence that the apparent absorption of visible light by asphaltenes from 600–850 nm is not a molecular absorption phenomenon but rather a scattering mechanism. A scattering type of mechanism also easily explains the classical sloping tail always present on the UV-Visible spectra of asphaltenes in solution. The black color of the asphaltene solutions therefore arises since the blue/violet/green wavelengths (<600 nm) are absorbed by the aromatic chromophores while the yellow/orange/red wavelengths (>600 nm) are scattered by the colloidal structures in solution, giving rise to the black color we have come to know and love!

2.4 Current State of Knowledge about Asphaltene Monomers and Primary Asphaltene Aggregates

As noted in Section 2.1, asphaltenes impact virtually all aspects of crude oil production and utilization (Speight, 2007). However, in spite of intensive experimental and theoretical studies, association and aggregation properties of petroleum asphaltenes are still not well characterized and are the subject of ongoing debate (Andersen, 2009). In particular, for decades the prevailing aggregation paradigm (now dismissed as erroneous) has been that at a critical micelle concentration (CMC ≈ 2–10 g/L) of asphaltenes in native petroleum, or in "good" solvents, such as toluene, there is a *one-step* transition from single

asphaltene molecules (monomers) to colloidal asphaltene "micelles" of 4–6 molecules (Sheu, 1996).

The development of more accurate experimental techniques provided substantial evidence of asphaltene aggregation at concentrations much lower than previously quoted CMC. Hence, the aggregation paradigm has been changed quantitatively, though not qualitatively. The most popular current model is that at a critical nanoaggregate concentration (CNAC ≈ 100–200 mg/L) of asphaltenes in native crude oils, or in "good" solvents, there is a *one-step* transition from individual asphaltene monomers to colloidal asphaltene "nanoaggregates" of 4–6 monomers (Mullins, 1998, 2010).

$$\text{The dismissed paradigm (Sheu, 1996):}\quad \text{MOLECULE} \xrightarrow{CMC} \text{MICELLE}$$

$$\text{The current paradigm (Mullins, 1998, 2010):}\quad \text{MONOMER} \xrightarrow{CNAC} \text{NANOAGGREGATE}$$

Apparently, owing to their simplicity, the above *one-step* paradigms have been and still are the ones almost exclusively employed to describe asphaltene aggregation phenomena and for interpretation of experimental data. Contradictory evidence of *multi-step* (*multi-state*) asphaltene aggregation commencing at concentrations well below CNAC was largely rejected or ignored.

In fact, for more than four decades, the existence of several structural states/phases of primary asphaltene aggregates at specific concentrations C_{aggr} below CNAC has been repeatedly demonstrated in various experiments, predominantly by analytical methods of "optical interrogation" (see a review in Evdokimov, 2010). It appears that the observed values of C_{aggr} only marginally depend on the geographical/geological origin of asphaltenes or on the type of solvents/crude oils.

In particular, Kazakova and Koretskij (1970) studied luminescence spectra of chloroform solutions of asphaltenes. They attributed maxima of luminescence intensity to aggregation stages of asphaltenes. The maximum at $C_{aggrr} \approx$ 160 mg/L apparently corresponds to the now popular CNAC. At lower concentrations two additional maxima were revealed, a broad one at 15–30 mg/L and a well-resolved one at ca. 5 mg/L.

Yokota *et al.* (1986) studied optical properties of benzene solutions with various concentrations of Athabasca asphaltenes. The authors report "strong concentrations effects" on the profiles of the absorption, excitation, and emission spectra with maxima at concentrations of ca. 5 mg/L and at 25–35 mg/L (see Figure 2.16).

A detailed investigation of primary asphaltene aggregation in toluene was performed by UV/Vis absorption spectroscopy (Evdokimov, Eliseev, and Akhmetov, 2003b); see Figure 2.17. A maximum of absorptivity at 160 mg/L was attributed to aggregation of asphaltenes into "nanocrystallites" (now referred

to as "nanoaggregates"). Maxima at lower asphaltene concentrations—at ca. 45–50 mg/L, at 11–12 mg/L, and at 4–5 mg/L—were attributed to appearance of various primary asphaltene aggregates.

Furthermore, the measured shifts of fluorescence emission bands have shown that self-association of asphaltenes in toluene may start at concentrations of ca. 1.7 mg/L (Juyal, Merino-Garcia, and Andersen, 2005).

However, in spite of all evidence, the concept of *multi-step* (*multi-state*) asphaltene aggregation, commencing at ultra-low concentrations, is still not duly recognized and, hence, requires further experimental verification.

Most recent observations of transition from asphaltene monomers to primary aggregates are reported in Evdokimov and Fesan (2016) and Evdokimov, Fesan, and Losev (2016). In these experiments the authors employed various "optical interrogation" techniques to study aggregation processes of asphaltenes in toluene and benzene at very low concentrations, down to 0.15 mg/L (ca. 0.17 ppm).

2.4.1 Some Requirements for Preparation of Dilute Asphaltene Solutions

In experiments with dilute solutions, to prevent oxidation/deterioration of solid asphaltenes freshly precipitated from crude oils by standard methods (e.g. ASTM D6560, 2000), usually some concentrated (up to several g/L) stock solutions are prepared for further studies. Samples with small contents of asphaltenes are commonly prepared by diluting some portions of the stock sample, for example in "optical interrogation" experiments (Evdokimov and Fesan, 2016; Evdokimov, Fesan, and Losev, 2016) pre-determined volumes of the stock solution were mixed with 50 mL of pure toluene or benzene and concentration of asphaltenes in each dilute solution was verified by weighting each sample before and after mixing (weighting accuracy 0.1 mg). Each prepared solution was intermixed with a glass rod and poured into a dark glass vessel for equilibration.

It should be emphasized that for decades the importance of equilibration time (kinetic effects) in studies of asphaltene solutions has not been recognized. It has been implicitly assumed that changes in the aggregation state of asphaltenes are virtually instantaneous. For example, in studies of refractive index (RI; Wattana *et al.*, 2003), asphaltene solutions of varying compositions were prepared and measurements were performed after a few minutes after mixing.

In studies of steady-state fluorescence emission, discussed in Section 2.2.2 (Badre *et al.*, 2006; Buenrostro-Gonzalez *et al.*, 2001; Groenzin and Mullins, 1999, 2000, 2007; Mullins, 1998; Ralston, Mitra-Kirtley and Mullins, 1996; Ruiz-Morales and Mullins, 2007, 2009), the period between preparations of solutions and collecting the data did not exceed 12 min (Mullins, 1998).

However, recently it has been proved that asphaltene aggregation is a kinetic phenomenon and can take several hours (Sheu and Acevedo, 2006), days, even

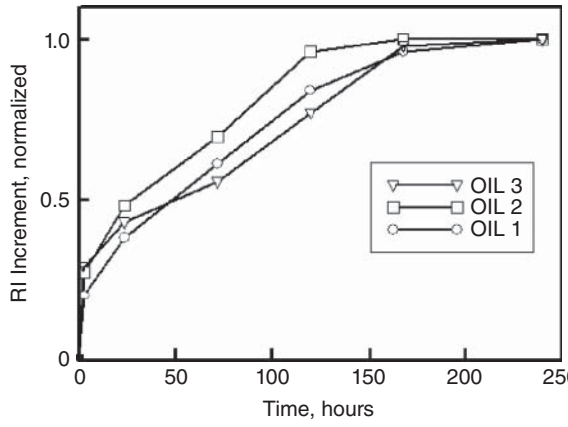

Figure 2.27 Long equilibration times in solutions with asphaltene content 15 mg/L. Data points: the values of RI increments ($RI_{solution}$–$RI_{toluene}$), normalized to their equilibrium values after a period of 10 days. *Source:* Adapted from Evdokimov and Fesan (2016).

or weeks in some cases (Maqbool, Balgoa and Fogler, 2009). Consequently, to ensure that asphaltene aggregates in studied dilute solutions were in their representative equilibrium states, in recent "optical interrogation" experiments (Evdokimov and Fesan, 2016; Evdokimov, Fesan, and Losev, 2016) the measurements were performed at various times after preparation of solutions: 1, 3, 6 h, 1, 3, 5, 7, and 10 days. During the first day after mixing, strong kinetic effects were observed in all studied solutions, as illustrated in Figure 2.27 for increments of RI with respect to pure toluene (Evdokimov and Fesan, 2016). This figure shows that all results stabilized only after a period of 3–7 days; hence only asphaltenes in solutions aged for standard periods of no less than 7 days were regarded to be in their equilibrium states (see also Figure 2.31).

While the crucial importance of kinetic/equilibration effects is most often ignored in performing/discussion of experiments with dilute asphaltene solutions, some critics of such experiments overemphasize possible errors due to absorption of asphaltenes onto the quartz surface of the cuvettes and glass vials used for sample preparation and analysis. Their arguments are usually supported by references to experimental data of Acevedo *et al.* (2003, 2014). In particular, in these studies, as a result of adsorption onto silica surfaces, asphaltene content in studied solutions decreased from 400 to 238 mg/L (Acevedo *et al.*, 2014) and from 20 to 13.5 mg/L (Acevedo *et al.*, 2003), i.e. by ~40% and by ~33%, respectively. However, these large numerical values do not indicate a crucial role of adsorption in conventional experiments with dilute asphaltene solutions. In particular, in their studies Acevedo *et al.* (2003, 2014) employed silica in the form of layers of fine powders on flat substrates, namely commercial "silica 60" with a pore diameter of 60 Å, pore volume of 0.8 mL/g, mean diameter size of 10–12 μm, and very high specific areas of 32–44 m^2/g. Hence, the total area of their silica surfaces approached 10^6 cm^2. On the other hand, in typical "optical interrogation" studies the quartz/glass areas in contact with

any dilute sample (in 1 mL quartz measurement cell and in 50 mL glass vials employed for sample preparation) was ca. 60 cm^2 (Evdokimov and Fesan, 2016; Evdokimov, Fesan, and Losev, 2016). Acevedo *et al.* (2003, 2014) conclude that in extremely dilute asphaltene solutions a monolayer of adsorbed asphaltenes is formed. Hence, the total mass of the absorbed asphaltenes M_A may be estimated with literature data (Groenzin and Mullins, 1999) for a typical radius (~1 nm) and a typical mass (~500 Da = $8 \cdot 10^{-19}$ mg) of a multi-ring asphaltene molecule. For random close packing in a monolayer of such molecules at a 60 cm^2 surface, $M_A \approx 9 \cdot 10^{-4}$ mg. In most dilute samples (~1 mg/L) the initial content of asphaltenes in a 50 mL vial is ca. 0.05 mg and the relative changes due to adsorption would be below 2%. At somewhat higher concentrations of 25–27 mg/L frequently employed in studies of dilute asphaltene solutions (Evdokimov, Fesan, and Losev, 2016; Mullins, 2010; Ruiz-Morales and Mullins, 2007), the estimated effect of adsorption does not exceed 0.07%.

2.4.2 Multiple States/Phases of Primary Asphaltene Aggregates Revealed by Optical Absorption Measurements

As discussed in Section 2.3.1, measurements of UV/Vis absorptivity ε in solutions may be employed to monitor evolution of molecular aggregates at asphaltene concentrations up to several grams per liter (see the concentration dependence of ε in Figure 2.17). A part of this dependence for most dilute asphaltene solutions is reproduced in Figure 2.28.

The maximum of absorptivity at 150–200 mg/L most probably is indicative of the frequently cited critical nanoaggregate concentration (CNAC; Mullins, 1998, 2010). Several structurally different states of asphaltene primary aggregates are revealed by well-resolved extrema of ε at specific C_{aggr} below CNAC, namely minima of absorptivity are observed close to 7, 25–30, and 80 mg/L, while two broad maxima (with a possible presence of a double-peak structure) appear in the ranges of 12–18 and 45–60 mg/L. Note that in the original publication (Evdokimov, Eliseev, and Akhmetov, 2003b) the nature of primary

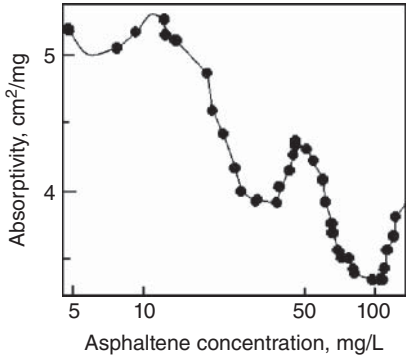

Figure 2.28 Concentration dependence of absorptivity at $\lambda = 670$ nm in dilute toluene solutions of solid asphaltenes. *Source:* Adapted from Evdokimov, Eliseev, and Akhmetov (2003b).

asphaltene aggregates was interpreted in the framework of the then popular model of "consecutive aggregation" in which aggregates of increasing complexity are formed by sequential addition of asphaltene "monomers" with increasing concentration, namely extrema of absorptivity at concentrations ≥7 mg/L were attributed to the sequence of asphaltene dimers, trimers, four-member aggregates, etc. However, most recent results show that the concept of "consecutive aggregation" is outdated (see Section 2.4.7). Apparently, at any concentration there is a polydisperse system of asphaltene primary aggregates in the solution and large-size complex aggregates may exist even at concentrations as low as 1 mg/L.

2.4.3 Multiple States/Phases of Primary Asphaltene Aggregates Revealed by Refractive Index Measurements

As discussed in the previous sections, the experimental methods most suitable for studying molecular structure and the aggregation behavior of asphaltenes in the performed experiments are those of "optical interrogation," in particular of high-precision refractometry (HPR). First, the practice of studying complex asphaltene-containing molecular mixtures of native petroleum and its product revealed that traditional methods of chemical analysis frequently lack the necessary precision, while the newly developed HPR measurements can give the desired information more quickly and much more adequately (Speight, 2007). A number of standard test methods were certified for measuring the RI of complex petroleum liquids (e.g. ASTM D1218, ASTM D1747, ASTM D5006, ASTM D5775) and the respective high-precision "Petroleum Refractometers" have been designed and manufactured (e.g. Koehler K27550, Rudolf J357). Second, it has been repeatedly demonstrated that the investigated problem of asphaltene aggregation in dilute solution may be resolved only by optical experimental techniques (fluorescence, HPR, etc.), as no other methods are sensitive for asphaltene concentration below ~50 mg/L (Mullins, 1998, 2010). Moreover, the HPR technique appears to be especially suited for studies of dilute asphaltene solutions with evolving structural heterogeneity induced by molecular aggregation. Namely, it has been demonstrated that in the HPR instruments with 10^{-5} limiting precision, the effect of even weak changes in the heterogeneity of the dilute sample may lead to RI deviations 10 to 100 times larger than the limiting precision (Meeten, 1997).

Furthermore, high accuracy of the modern HPR equipment allows registering extended "time series" of RI values— RI temporal fluctuations with respect to an equilibrium level. For example, in recent studies of asphaltene aggregation in dilute toluene solutions (Evdokimov and Fesan, 2016) RI measurements were made at 20 °C in a high-precision refractometer Abbemat HP (Anton Paar GmbH). The measuring wavelength was 589±0.2 nm; RI resolution 1×10^{-6}; temperature stability ±0.002 °C. RI "time series" were obtained by registering the values of RI every 2 seconds for periods of ca. 20 min (see Figure 2.29).

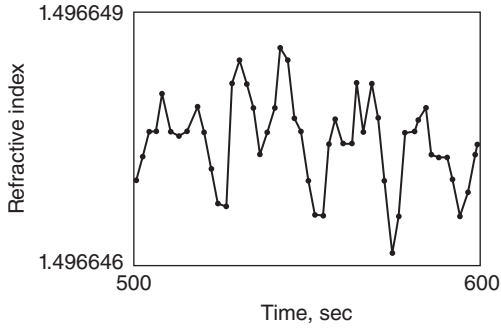

Figure 2.29 A representative part of RI "time series." *Source:* Adapted from Evdokimov and Fesan (2016).

In molecular aggregation studies, the statistical analysis of long-term time series of inherent optical properties proved to be a valuable tool for revealing the details of aggregation mechanisms (Durov, 2004; Elson and Rigler, 2001; Gavrylyak, 2008; Yang and Pearson, 2012). In this analysis some authors employ parameters of modern deterministic chaos theories such as the Hurst exponent, the Lyapunov exponent, the correlation dimension, etc. (Brockwell and Davis, 1996; Grassberger and Procaccia, 1983). However, calculating these parameters required sophisticated specialized software that was not incorporated into publicly available software packages. Hence in experiments of Evdokimov and Fesan (2016) more simple methods of classical statistics (Woodward, Gray, and Elliott, 2012) were used, based on calculating probability density distributions of RI with such parameters as the mean and the standard deviation (for a standard time interval of 800–1000 seconds). A representative experimental distribution (normalized to its maximum value) is shown by dots in Figure 2.30. The solid line is the best fit to experimental data of the Gaussian function:

$$f(n) = \frac{1}{\sigma_n \sqrt{2\pi}} \exp\left[-\frac{(n-\overline{n})^2}{2{\sigma_n}^2}\right]$$

with the mean RI $\overline{n} = 1.496649$ and the standard deviation of RI $\sigma_n = 8{\cdot}10^{-6}$.

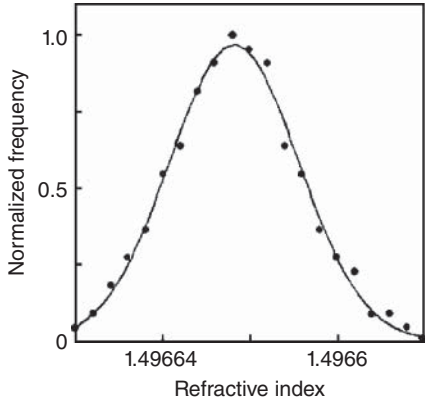

Figure 2.30 Statistical analysis of the measured RI "time series." *Source:* Adapted from Evdokimov and Fesan (2016).

In their publication, Evdokimov and Fesan (2016) note that the values of $\overline{n}$ and of σ_n are sensitive to changes of qualitatively different parameters of molecular aggregates. That is to say, the well-known classical RI theories (Maxwell, Clausius–Mossotti, Lorentz–Lorenz) (see Aspnes, 1982 and Lorentz, 1960) show that in a molecular system the RI is completely determined by molecular polarizability α. In turn, the value of α reflects the dynamical response of a bound system to external fields, and provides insight into an *internal structure* of molecules/molecular aggregates (Lorentz, 1960). On the other hand, the magnitude of RI's fluctuations, here described by σ_n, is directly related to the intensity of light scattering and is primarily determined by the *external dimensions* of molecular aggregates (Elson and Rigler, 2001).

In the discussed experiments, *n*-C7 (heptane insoluble) solid asphaltenes were separated from crude oils according to the standard ASTM method (ASTM D6560, 2000) from samples of various light and heavy crude oils which were collected from the well-heads at several Russian oilfields geographically separated by thousands of kilometers and had a wide diversity in composition and properties (see Table 2.2).

To ensure that asphaltene aggregates in studied dilute solutions were in their representative equilibrium states, RIs of each solution were measured at various times after preparation: from 3 h to 10 days. Strong kinetic

Table 2.2 The diversity in properties of studied crude oils. *Source:* Adapted from Evdokimov and Fesan (2016).

	Oil 1	**Oil 2**	**Oil 3**	**Oil 4**
Region	Samara	Yugra	Yugra	Tatarstan
Oilfield	Kalmayurskoye	Potochnoye	Pogranichnoye	Aznakayevskoye
Well #	238	401	43P	24534
Geographical location	53°12′10″N 50°08′27″E	61°15′15″N 75°12′44″E	63°11′57″N 75°27′02″E	54°32′16″N 52°47′54″E
Density at 20 °C, kg/m^3	991.3	839.5	818.3	893.2
Viscosity at 20 °C, cSt	3732	6.87	2.94	39.3
Asphaltenes, wt%	15.48	0.46	0.13	4.19
Resins, wt%	35.91	2.34	3.82	20.57
Paraffins, wt%	1.53	5.21	2.59	0.89
Sulfur, wt%	2.5	0.56	1.5	2.1
Metals (V + Ni), wt%	0.175	0.0137	0.018	0.076
Solids, wt%	0.587	0.04	0.006	0.07

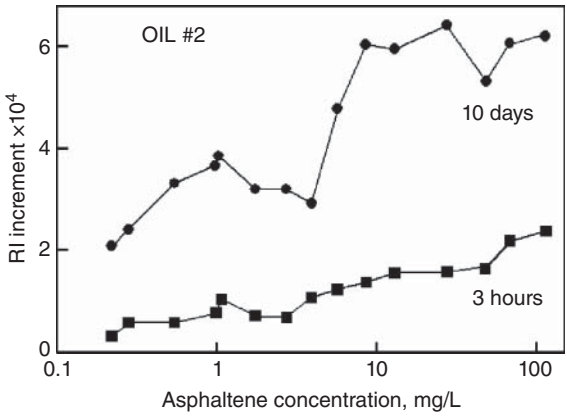

Figure 2.31 Effects of asphaltene concentration on RI increment in non-equilibrated (aged for 3 h) and in equilibrated (aged for 10 days) toluene solutions. *Source:* Based on the original data of Evdokimov and Fesan (2016).

effects were observed in all studied solutions, as discussed in Section 2.4.1. Figure 2.31 illustrates the values of RI increment (with respect to pure toluene) in non-equilibrated and in equilibrated states. It is clear that well-resolved non-monotonic effects of asphaltene concentration may be observed only in solutions aged for a long period (10 days in these experiments).

2.4.3.1 Mean Refractive Index at Concentrations below CNAC

Effects of asphaltene concentration on equilibrium states of asphaltenes from all studied crude oils are compared in Figure 2.32. Non-monotonic concentration dependences of $\overline{n}$, which may be ascribed to changes in the structure of primary asphaltene aggregates, are clearly visible in all data sets. The results suggest a presence of double peak structure in the broad low-concentration maxima of RI in the range of 0.6–1.2 mg/L. At higher concentrations, the next intense maxima of $\overline{n}$ in the range of 9–22 mg/L also demonstrate some dual substructure. In addition, less intense peaks of RI are seen in some data sets at 65–80 mg/L. Finally, well-resolved minima of RI are observed in all samples at asphaltene concentrations of 2–7 and 50–60 mg/L.

In Figure 2.33, all experimental data on different structural states of asphaltene aggregates (RI peak positions) in equilibrated (10 days) solutions of asphaltenes from four crude oils are plotted versus total asphaltene content in native crudes. In spite of the absence of some data points, the existence of common RI peaks (numbered 1 to 5) is clear. Hence, these data reveal a close similarity between aggregation features for asphaltenes from crude oils significantly different in their origin and in their properties.

2.4.3.2 Standard Deviation of Refractive Index at Concentrations below CNAC

As noted above, owing to the absence of publicly available software packages for modern in-depth analysis of RI time series (with such structure-sensitive

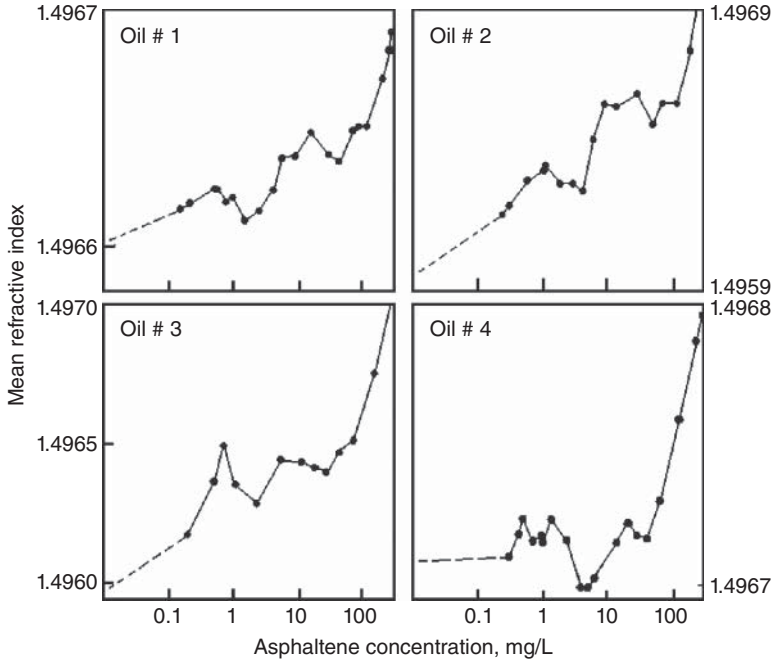

Figure 2.32 Multiple equilibrium structural states of asphaltenes revealed by concentration effects on mean RI in the measured RI "time series." *Source:* Based on the original data of Evdokimov and Fesan (2016).

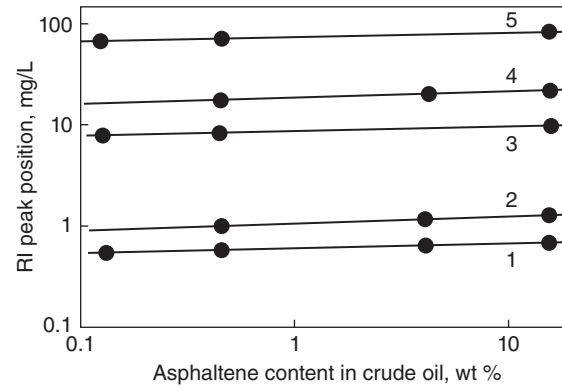

Figure 2.33 Close similarity of structural states in solutions of asphaltenes from crude oils of diverse geographical/geological origin. *Source:* Adapted from Evdokimov and Fesan (2016).

parameters as the Hurst exponent, the Lyapunov exponent, etc.), Evdokimov and Fesan (2016) had to characterize the observed RI variations by the much less sensitive classical parameter of standard deviation σ_n. This may be the principal reason for a noticeable scatter of σ_n data points in experimental results for

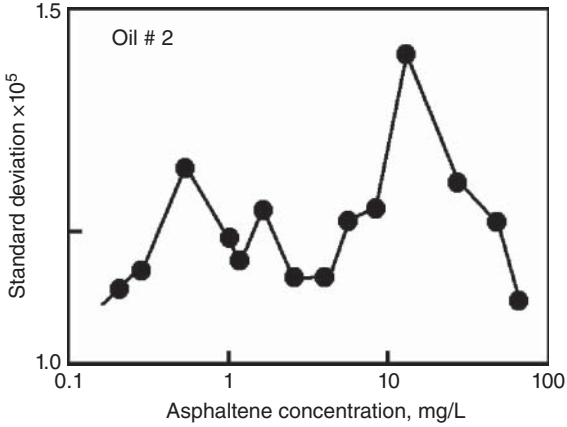

Figure 2.34 Multiple equilibrium structural states of asphaltenes revealed by concentration effects on standard RI deviation in the measured RI "time series." *Source:* Based on the original data of Evdokimov and Fesan (2016).

most dilute solutions of asphaltenes. This scatter was suppressed via smoothing all concentration dependencies of σ_n by three-point sliding data windows.

As a representative example, Figure 2.34 shows the smoothed 10-day data set for solutions of asphaltenes from Oil #2. Peak positions in the concentration dependence of σ_n are fairly close to positions of RI maxima in Figure 2.32. Also, the deep minimum at ca. 4 mg/L is well reproduced.

On the basis of the obtained σ_n results Evdokimov and Fesan (2016) concluded that variations of RI time series should not be regarded merely as instrumental "noise" which disturbs measurements. On the contrary, these variations should be recognized as a source of valuable information about a molecular structure of the studied system. Currently, the method of RI time series measurements may seem to be excessively complicated with respect to both the experimental technique and data analysis. However, it may provide important additional information as compared to conventional measurements of mean RI values. For example, in studies of a critical concentration C_{cr} in aqueous solutions of propylene carbonate/sodium chloride (Fujiwara, Nishimoto, and Arakawa, 1985), the authors observed a perfectly linear dependence of the mean RI on the concentration of NaCl, without any singularities near C_{cr}. On the other hand, the values of σ_n in the RI time series for this solution exhibited sharp peaking at C_{cr}, resembling the data in Figure 2.34.

Furthermore, sharp peaking of RI fluctuations in Figure 2.34 resembles the behavior of critical RI fluctuations (the cause of critical opalescence) resulting from density/concentration fluctuations near critical points and phase transitions of various molecular systems (Stanley, 1971). Analogous behavior is observed in many structurally evolving systems as they are driven away from equilibrium and toward a structural instability (bifurcation) which also may be regarded as a certain phase transition point (Kelso, Scholz, and Schoner, 1986). In particular, in studies of molecular aggregation (Deng, Wang, and Ou-yang,

2012; Fujiwara, Nishimoto and Arakawa, 1985), solutions of monomers and primary molecular aggregates were interpreted as two different phases. A qualitative model was suggested (Deng, Wang, and Ou-yang, 2012) assuming that far from phase transition point the entropy effect tends to make solvent molecules and solute species (monomers or primary aggregates) distribute uniformly in both phases, resulting in small fluctuations. In the vicinity of phase transition, solute–solute interactions compete with entropy effects, the system becomes heterogeneous (different molecular species are distributed non-uniformly) so the magnitude of fluctuations abruptly increases. These mechanisms, however, cannot be quantitatively described by the current theoretical models.

2.4.4 Conditions for Observation of Asphaltene Monomers and Evolution of Primary Asphaltene Aggregates Revealed by Fluorescence Measurements

2.4.4.1 Studies of Steady-State Fluorescence Emission

As discussed in Section 2.2.2, in studies of fluorescence emission from asphaltene solutions in benzene (Evdokimov, Fesan, and Losev, 2016) asphaltene monomers were distinguished from primary molecular aggregates by characteristic peaks in fluorescence emission spectra (see Figure 2.13). Only monomers were observed at asphaltene concentration of 0.34 mg/L, while primary aggregates were registered in solutions with concentrations $\geq$0.68 mg/L. These experiments were supplemented by additional studies of asphaltene solutions in toluene (see representative spectra of fluorescence emission in Figure 2.35 normalized to maximum intensities of the monomer peaks at $\leq$320 nm). With the increase of asphaltene concentration, a broad maximum of emission from primary molecular aggregates appears at larger wavelengths (subdivision to aggregates with smaller/larger fluorophores will be discussed below).

Quantitatively, the effects of asphaltene concentration were characterized by the ratios of integrated emission intensities from all aggregates (in the range 320–550 nm) to the integrated emission intensity from non-aggregated asphaltene monomers (in the range 270–320 nm). The respective data set is presented in Figure 2.36. These results show that in toluene solutions only asphaltene monomers are observed at concentrations of 0.20 and 0.47 mg/L, while asphaltene aggregates appear at concentrations $\geq$0.7 mg/L, in good coincidence with the value of 0.68 mg/L reported for aggregation onset of the same asphaltenes in benzene.

The notable feature of Figure 2.36 is a complicated, non-monotonic character of concentration effects on aggregation of asphaltenes which cannot be accounted for by any of the current aggregation models (see Section 2.4.7). In particular, the relative emission intensities from aggregates sharply increase

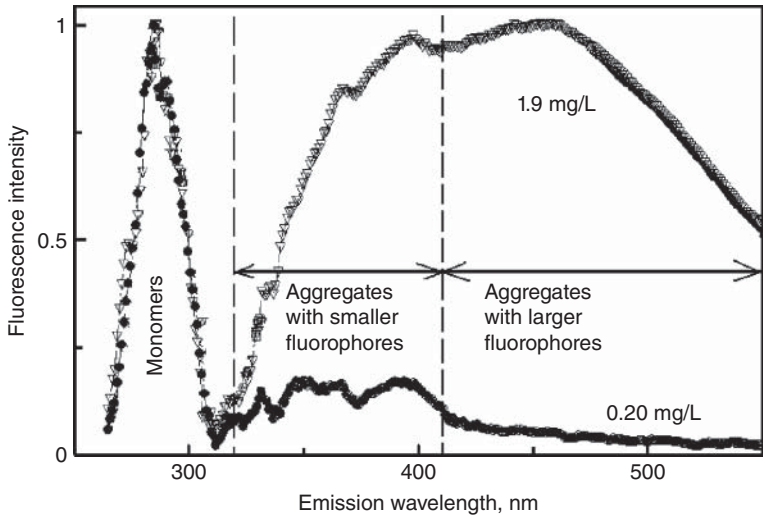

Figure 2.35 Fluorescence emission spectra from asphaltene solutions in toluene, obtained with 265 nm excitation. The vertical dashed lines delimit characteristic ranges of emission wavelengths for monomers and two types of primary aggregates (see text).

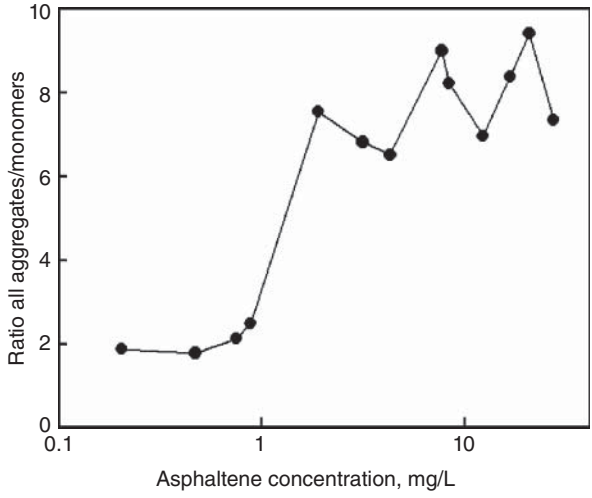

Figure 2.36 Non-monotonic effects of asphaltene concentration on the relative intensity of fluorescence emission from all primary molecular aggregates in toluene solutions of asphaltenes.

with the increase of concentration from 0.7 to 1.9 mg/L, while at higher concentrations there is a much slower overall intensity increase interrupted by two local intensity minima close to 4.3 and 12.3 mg/L. The appearance of minima in the measured data sets may be described as an "apparent re-entrance" in asphaltene solutions (i.e. as a return of the properties in more concentrated samples to the properties of less concentrated ones).

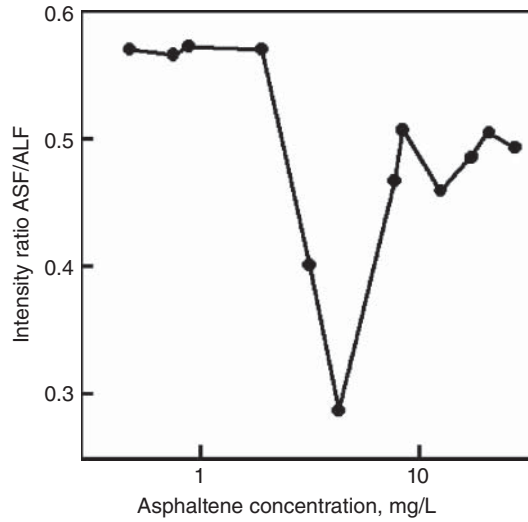

Figure 2.37 The effects of asphaltene concentration on the relative intensity of fluorescence emission from asphaltene aggregates with smaller fluorophores (ASF) with respect to intensity of emission from aggregates with larger fluorophores (ALF).

Furthermore, there is an obvious dissimilarity of concentration effects on fluorescence emission from primary asphaltene aggregates with smaller and larger fluorophores. By literature analysis (some data are shown in Table 2.1), a broad emission maximum from all primary aggregates in Figure 2.35 may be divided into two parts: with predominant emission from aggregates of smaller, 1- to 2-ring, fluorophores (ASF) in the range of 320–410 nm and with predominant emission from aggregates of larger, 3- to 4-ring, fluorophores (ALF) in the range of 410–550 nm. The ratio of integrated intensities from aggregates with smaller (ASF) and larger (ALF) fluorophores at various asphaltene concentrations is plotted in Figure 2.37. These results show that the concurrent evolution of two types of aggregates (constant ASF/ALF ratio) is observed in most dilute solutions with asphaltene concentrations $\leq$1.9 mg/L. In the range of 3.1–7.7 mg/L there is a strong deficiency of emission from aggregates of 1- to 2-ring fluorophores, most notably at 4.3 mg/L. At the present state of knowledge about asphaltene aggregation, the precise molecular nature of this effect is not clear. However, any molecular mechanisms would imply strong restructuring in the ensemble of asphaltene aggregates. Another concentration range of restructuring is indicated by a weaker "re-entrant" minimum of a ASF/ALF ratio close to 12.3 mg/L.

2.4.4.2 Studies of Time-Resolved Fluorescence Emission

In recent experiments (Zhang, 2010; Zhang *et al.*, 2014) fluorescence lifetime measurements were employed to characterize asphaltene toluene solutions. The excitation wavelength was 335 nm and time decay of fluorescence intensity I was measured at the emission wavelength of 420 nm. The decay curves

for various asphaltene concentrations were approximated by sums of four exponents with different amplitudes A_i and relaxation times τ_i:

$$I(t) = I_0 \sum_{i=1}^{i=4} A_i \exp(-t/\tau_i)$$

The authors refrained from attributing particular relaxation times to the specific fluorophores or to the specific aggregates of these fluorophores in the wide concentration range employed in their studies (0.1–10 000 mg/L). However, literature analysis suggests that such attribution may be justified for qualitative discussion of concentration effects in the most dilute solutions. At asphaltene concentrations ≤50 mg/L the following relaxation times were observed: τ_1 = 0.41–0.50 ns, τ_2 = 1.4–1.5 ns, τ_3 = 3.5–4.0 ns, and τ_4 = 9.2–10.0 ns.

Experimental fluorescence lifetimes of various non-aggregated 1- to 5-ring aromatic molecules are reported in a number of publications (Cobb, Nithipatikom, and McGown, 1988; Dawson and Windsor, 1968; Luria, Ofran, and Stein, 1974; Meidinger *et al.*, 1993). Typically, the lifetimes for molecules with smaller (1- and 2-ring) fluorophores are above 8–10 ns. Somewhat shorter lifetimes (down to 3.33 ns) were observed for molecules with larger fluorophores. Furthermore, it has been experimentally proven that fluorescence lifetimes strongly decrease with aggregation (Akins *et al.*, 1996; Fidder and Wiersma, 1995; Obara *et al.*, 2012; Spano and Mukamel, 1989).

In accordance with this information, it may be suggested that the above lifetimes τ_4 and τ_3 (with the respective amplitudes A_4 and A_3) are representative of non-aggregated asphaltene monomers with smaller and larger aromatic fluorophores, while lifetimes τ_2 and τ_1 (with the respective amplitudes A_2 and A_1) reflect emission from primary aggregates of both types of these fluorophores (or emission from two families of aggregates with strongly different sizes).

Hence, in support of the data in Section 2.4.4.1 the results of (Zhang, 2010; Zhang *et al.*, 2014) indicate that even in most dilute solutions primary asphaltene aggregates are complex polydisperse systems. Furthermore, as in Figure 2.36, non-monotonic effects of asphaltene concentration on the composition of primary aggregates in (Zhang, 2010; Zhang *et al.*, 2014) may be revealed by plotting the ratios of emission intensity from aggregated and non-aggregated species. The respective values of $A_1/(A_3 + A_4)$ are presented in Figure 2.38 and show that primary asphaltene aggregates appear at concentrations above 0.5–0.6 mg/L, in good coincidence with the results in Section 2.4.4.1.

2.4.5 Evolution of Primary Asphaltene Aggregates Revealed by Mass Spectrometry

In another recent publication (McKenna *et al.*, 2013), an international group of scientists presented experimental results on molecular aggregation in

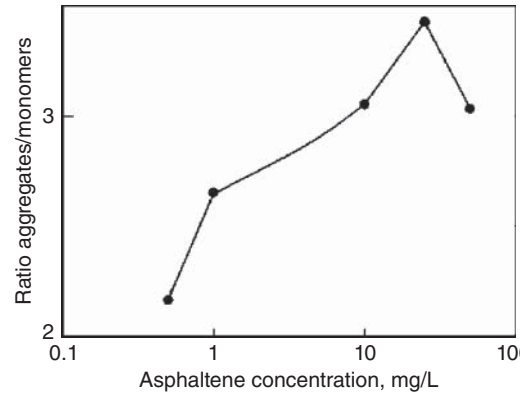

Figure 2.38 Non-monotonic effects of asphaltene concentration on the relative intensity of fluorescence emission from primary asphaltene aggregates. *Source:* Based on original data from Zhang (2010) and Zhang *et al.* (2014).

solutions with asphaltene concentrations down to 5 ng/mL (0.05 mg/L). For a fairly concentrated solution (500 mg/L) in mass spectrum of asphaltenes extending up to ~22 kDa they identified peaks from "monomers" and several peaks from molecular aggregates. The low-mass aggregates they identified as asphaltene dimers and simple multimers. However, the dominant feature of this spectrum was the intense high-molecular-weight peak centered at 9.5 kDa (which corresponds to aggregates of ca. 12 asphaltene "monomers" with MW assumed by McKenna *et al.*, 2013). In detailed studies of concentration effects on the properties of the peak from the largest aggregates, mass spectra were measured in the limited range of m/z = 2500–15000 (see Figure 1 in the original publication).

For quantitative analysis of the effects of asphaltene concentration on the intensity of this peak, we made digital copies of the original graphs and smoothed the curves to suppress random noise. The results of this analysis are presented in Figure 2.39. The insert in this figure schematically illustrates that in original mass spectra the analyzed aggregate peak grows above a sharply falling continuous background. To evaluate the maximum net intensity of this peak I_m, we approximated the underlying part of the background by a fourth-order polynomial (dashed curve in the figure). Finally, the relative peak intensity was calculated as $I_{REL} = I_m/I_c$, where I_c is the continuous background intensity under the peak.

The results of Figure 2.39 show that a massive increase in the content of the high-MW aggregates is observed at asphaltene concentrations between 0.05 and 0.5 mg/L, in good coincidence with primary conditions for the appearance of aggregated asphaltenes (0.5–0.7 mg/L) in fluorescence experiments. Hence, it may be concluded that the above discussed "primary asphaltene aggregates" include large conglomerates of many (apparently >10) basic asphaltene molecules. Furthermore, Figure 2.39 presents additional evidence for complicated non-monotonic effects of asphaltene concentration on the

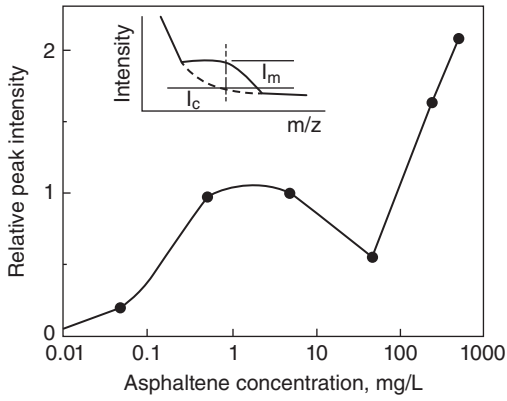

Figure 2.39 Non-monotonic effects of asphaltene concentration on the relative intensity of the peak from the heaviest molecular aggregates in mass spectra of asphaltenes. *Source:* Based on original data from McKenna *et al.* (2013).

properties of aggregates revealed by fluorescence measurements. In particular, the specific significance of ~ 4.3 mg/L (see Figures 2.36 and 2.37) is confirmed by maximum of relative intensity of the high-MW peak.

2.4.6 "Optical Interrogation" Reveals that Primary Asphaltene Aggregates are Porous and Entrap/Occlude Molecules of Metalloporphyrins and other Compounds

Vanadium and nickel are the most abundant and troublesome metal compounds present in petroleum (Zhao, Xu, and Shi, 2015). Metal compounds may cause significant negative impact on refining processes, leading to the deactivation of catalysts. Vanadium and nickel complexes generally are associated with porphyrins. Metalloporphyrins (MPs) are known to concentrate in the heavy, more polar fractions of crude oil and, particularly, in the asphaltene fraction. This association with asphaltenes is probably the reason behind the great difficulties in extracting or separating MPs from crude oils or residues. Although the association of MPs with asphaltenes is well documented, there is no general agreement on the mechanisms of such associations.

For example, the state of MPs in asphaltenes was studied by indirect methods of liquid chromatography coupled to a mass spectrometer with an inductively coupled plasma detector (Acevedo *et al.*, 2012). The authors concluded that no covalent bonds or specific interactions appear to be required to account for the presence of MPs within asphaltene aggregates. The presence of MPs and other physically trapped molecules was related to the fractal structure of asphaltene aggregates in which voids are filled with components coming from the surrounding media.

The above discussed publication (Dechaine and Gray, 2011a) suggests that asphaltene aggregates are porous supramolecular structures that occlude (trap, immobilize) molecules of solvents and other petroleum compounds like MPs. This suggestion was based on indirect experimental evidence from studies of

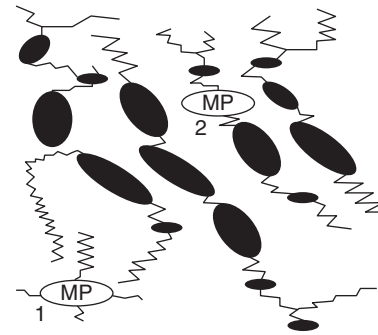

Figure 2.40 Suggested sites of "loosely" bound (1) and "tightly" bound (2) MP molecules in asphaltene supramolecular aggregates. *Source:* Adapted from Dechaine and Gray (2011a).

asphaltene diffusion through ultrafiltration membranes (see Figure 2.24). In particular, the authors concluded that a large fraction of vanadium petroporphyrins present in solutions does not participate in the diffusion process, indicating that these components interact strongly with the asphaltene aggregates, even in a "good" solvent, such as toluene. The proposed mechanisms for inclusion of MPs within the asphaltene aggregate structure are illustrated schematically in Figure 2.40.

1) The first class of bound MPs are "loosely" bound molecules, which are retained in the aggregates by either non-covalent bonds or occlusion as a result of precipitation-type mechanisms. These MPs would be the smallest, simplest structures and would be the easiest to remove from the asphaltenes using simple solvent extraction procedures.
2) The second class of MPs are "tightly" bound molecules. These groups would have peripheral substitutions capable of additional non-covalent bonding with the asphaltene molecules (e.g. fused aromatic groups for $\pi-\pi$ bonding, carboxylic acid groups for hydrogen bonding). They would participate strongly in the aggregation process and, as such, would be the hardest to remove by solvents.

In the above diffusion experiments, reducing the concentration of the asphaltenes to 100 mg/L did not produce any effect on the amount of petroporphyrins bound in asphaltene aggregates. The authors suggested that the petroporphyrins may very well be more mobile at low concentrations, but this effect is not "visible" to the spectrophotometer at $\geq$100 mg/L and, hence, a large portion of the total vanadium in crude oils is unaccounted by conventional methods of UV/Vis spectroscopy.

The main reason for such "invisibility" of MPs trapped in asphaltenes may be the so-called hypochromism, that is the decrease of the absorptivity in the absence of strong molecular interactions (Vekshin, 1999). Mutual "shielding" of chromophores from light due to competition for the incident photon can take place in molecular aggregates and macromolecules. "Shielding" leads to a

decrease in the extinction coefficient. The largest decrease is in the maximum of the absorption band. Strong hypochromism was observed for various porphyrins bound in large biological molecules (Dezhampanah, Bordbar, and Tangestaninejad, 2009), in aggregates of carbon nanotubes (Zarudnev *et al.*, 2012), in CdTe quantum dots (Keane *et al.*, 2012), etc. There is also a possibility of absorbance reduction as a result of porphyrin self-aggregation (Andrade *et al.*, 2008), or aggregation with individual molecules of other compounds (Zhao, Xu, and Shi, 2015).

Direct spectroscopic evidence of petroporphyrin release from asphaltene aggregates at low concentrations was obtained by additional analysis of experimental data from (Evdokimov, Fesan, and Losev, 2016). That is to say in these experiments for correction of fluorescence emission spectra (see Figure 2.12) absorbance vs. wavelength dependencies were measured in a wide asphaltene concentration range, as illustrated in Figure 2.41. These dependencies are perfectly continuous except for absorbance peaks at ca. 410 nm. By literature analysis, these peaks may be reliably ascribed to a specific type of MPs, namely to the Soret band of vanadyl porphyrins (Czernuszewicz, 2000; Doukkali *et al.*, 2001).

For further quantitative analysis, relative maximum intensities of porphyrin Soret absorbance peaks $(A_P - A_B)/A_B$ were evaluated via approximating the continuous backgrounds by fourth-order polynomials, as illustrated in Figure 2.42. Variations of porphyrin Soret peaks in asphaltene solutions with concentrations up to 1 g/L are shown in Figure 2.43.

First, the data of Figure 2.43 show small porphyrin absorbance peaks (i.e. low "visibility" of porphyrins) in asphaltene solutions with concentrations above 100 mg/L, in line with the results of Dechaine and Gray (2011a). As noted above, this may be explained by the effective Soret band hypochromism in porphyrins occluded in asphaltene aggregates.

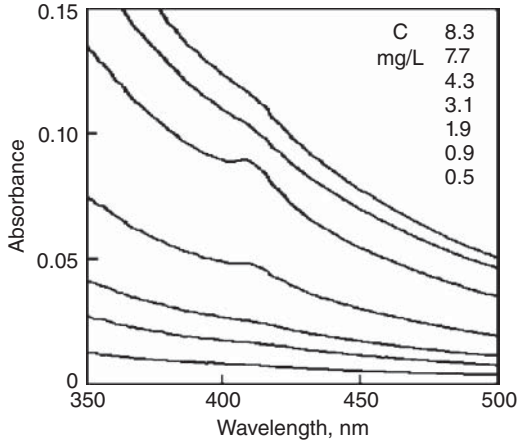

Figure 2.41 Absorbance spectra for asphaltene solutions in benzene with concentrations indicated in the figure. Absorbance peak at ca. 410 nm is from vanadyl petroporphyrins. Additional analysis of experimental data from Evdokimov, Fesan, and Losev (2016).

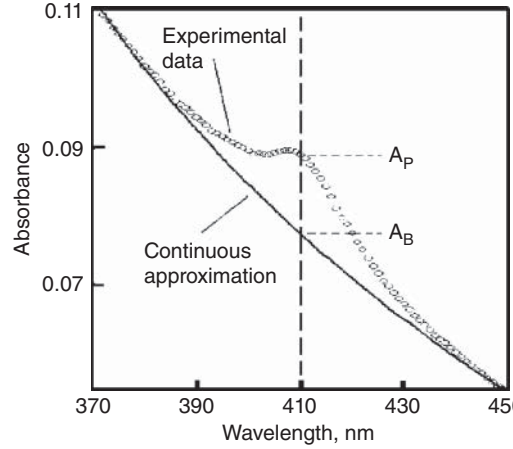

Figure 2.42 Evaluation of the relative intensity of the Soret absorption peak of vanadyl porphyrins in Figure 2.41.

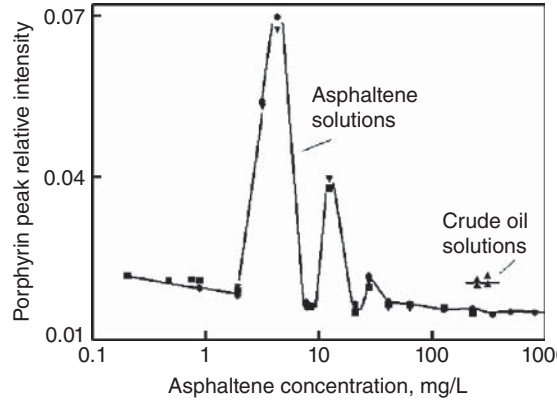

Figure 2.43 Effects of asphaltene concentration on the intensity of porphyrin absorption peak in solutions of solid asphaltenes and in solutions of the parent crude oil. *Source:* Additional analysis of experimental data from Evdokimov, Fesan, and Losev (2016).

Second, porphyrin peaks are more "visible" in crude oil solutions with the same asphaltene concentration. This indicates that some porphyrins initially present in the parent crude oil did not co-precipitate with asphaltenes and, by definition, are not a part of the asphaltene fraction.

Furthermore, Figure 2.43 shows that at some specific concentrations below 100 mg/L several maxima of porphyrin absorbance are observed. In the most prominent maximum, at ca. 4.3 mg/L, Soret absorbance increases almost five-fold with respect to its value in concentrated solutions (100–1000 mg/L). A plausible explanation for this behavior is that at these specific concentrations there are structural rearrangements of asphaltene aggregates, leading to liberation of various types of entrapped porphyrins (see Figure 2.40).

Finally, in the most dilute solutions, Soret absorbance decreases again, which may be the result of complex formation between porphyrin molecules

and asphaltene monomers, predominant at these concentrations (Evdokimov, Fesan, and Losev, 2016).

In summary, the above experiments confirm that there may be two types of vanadyl porphyrins in asphaltene solutions, one free and the other bound, as was recognized previously (Tynan and Yen, 1969) for porphyrins in native crude oils. The data of Figure 2.43 are the first spectrometric evidence that the bound state can undergo transition to the free state upon decreasing asphaltene concentration and, hence, dissolution of supramolecular asphaltene aggregates. Furthermore, these results support earlier suggestions (see Goulon *et al.*, 1984 and references therein) that the UV/Vis spectrophotometric analyses tend systematically to underestimate the porphyrinic content in native crude oils, because a sizeable fraction of porphyrins is not molecularly dispersed but occluded in asphaltene aggregates.

It should also be noted that molecules of other petroleum compounds apparently may be occluded/entrapped in asphaltene aggregates (Gray *et al.*, 2011). In particular, these aggregates can occlude saturated compounds, such as sterane biomarkers (Yang *et al.*, 2009). In the most extreme example, reactive biomarkers were so effectively protected in the asphaltene aggregates that they were stabilized over geological time (Zhao *et al.*, 2010). Moreover, Gray *et al.* (2011) suggest that portions of the asphaltene aggregates are porous enough to enable entrapment of molecules of the surrounding solvents.

2.4.7 Apparent Absence of "Consecutive Aggregation" in Asphaltene Experiments: Revised Description of the Observed Non-monotonic Concentration Effects in Dilute Asphaltene Solutions

In Section 2.4.2, it is noted that, historically, experimental observations of multiple states of primary asphaltene aggregates were interpreted in the framework of "consecutive aggregation" schemes in which aggregates of increasing complexity are formed by sequential addition of asphaltene "monomers" with increasing concentration (Figure 2.44). Such schemes are close to the well-known and mathematically well-developed theories of stepwise molecular aggregation (Beshnova *et al.*, 2009; De Greef *et al.*, 2009; Evstigneev, Buchelnikov, and Evstigneev, 2012; Martin, 1996). These theories are based on the sequential addition of monomer X_1 to oligomer X_{i-1} containing $i-1$ molecules:

$$X_{i-1} + X_1 \overset{K_i}{\longleftrightarrow} X_i$$

In practice, the dependence of equilibrium constant K_i on the number of molecules in an aggregate, referred to as "the profile of equilibrium constant" (Beshnova *et al.*, 2009), is always chosen by an investigator depending on the system under investigation. The two most important cases employed in the majority of applications (De Greef *et al.*, 2009; Martin, 1996; and references

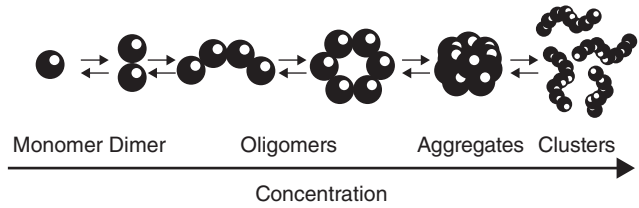

Figure 2.44 "Consecutive aggregation" scheme with parental relationship between asphaltene aggregates formed at increasing concentrations.

therein) are: (1) equal values of K_i at all stages of aggregation (the "EK model" or the "isodesmic model") and (2) the profile $K_i = f(i)$ is introduced empirically as a function of the number of molecules, i, in aggregate.

The important common assumption of all these schemes/theories is a necessary parental relationship between more and more complex states of asphaltene aggregates arising with increasing concentration. Hence, neither of such widely employed descriptions of asphaltene aggregation can account for experimentally observed non-monotonic/re-entrant concentration effects discussed in Sections 2.4.1–2.4.6.

Taking into account the new information on the structure and properties of asphaltene molecules, such inadequacy of "consecutive aggregation" models may be due to the following reasons. First, these models implicitly assume that all types of the species involved in aggregation (monomers, dimers, etc.) are monodisperse. However, it has been experimentally proven that asphaltene "monomers" are polydisperse systems of molecules with different numbers (1–3) of aromatic rings and a variety of different substituents (Evdokimov, Fesan, and Losev, 2016). Hence, any structural state of primary asphaltene aggregates is also bound to be polydisperse. Second, at the onset of asphaltene aggregation (above ca. 0.5 mg L) not only simplest systems of two "monomers" (dimers) are formed, but there appear also very large molecular complexes of asphaltenes (see Section 2.4.5). Finally, a simple, but usually overlooked, reason is that *aggregation* of asphaltenes in solvents of constant composition is *never* observed experimentally. In particular, it is not technically possible to realize the sequential aggregation mechanisms of Figure 2.44. Addition of a very dilute solution of "monomers" to a solution of some aggregates would always *decrease* the net asphaltene concentration.

In practice, as illustrated in Figure 2.45, samples with varying contents of asphaltenes are commonly prepared by independent procedures of diluting some stock sample (concentrated solution or solid asphaltenes). Consequently, there is no direct parental relationship between molecular/aggregate systems in any samples with close asphaltene concentrations. Furthermore, the observed states of asphaltenes in the studied samples obviously are achieved by mechanisms of *dissolution* and not of *aggregation*. Of major importance

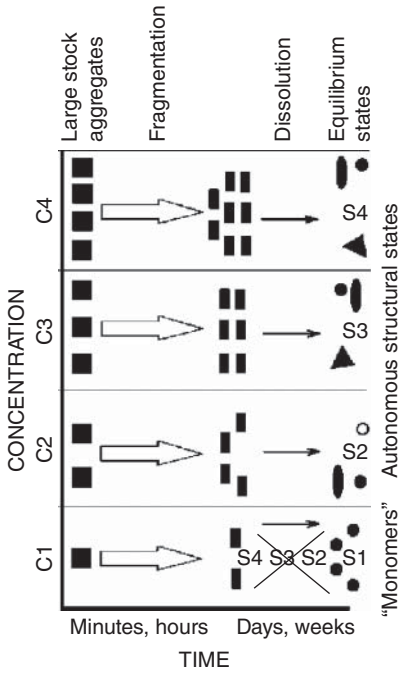

Figure 2.45 Scheme with autonomous routes to independent systems of asphaltene aggregates at different concentrations.

are strong kinetic effects, as noted in Section 2.4.1, equilibrium states of asphaltenes may be observed only after aging the freshly prepared samples for several days. Re-examination of previous experimental results (Evdokimov, 2010; Evdokimov, Eliseev, and Akhmetov, 2003b; Evdokimov and Fesan, 2016; Evdokimov, Fesan, and Losev, 2016) indicates that the aging process may proceed via two different stages, labeled as "fragmentation" and "dissolution" in Figure 2.45.

In the first stage, which lasts for at least several hours, initial large asphaltene aggregates from stock samples are broken into smaller, but still complex, fragments with fairly close individual properties. Hence, in course of this stage there are only quantitative differences (in the numbers of fragments) between various samples and the registered effects of asphaltene concentration would appear fairly continuous. This situation was illustrated in Figure 2.31 by experimental data on RI increments (with respect to pure solvent) in toluene solutions of asphaltenes aged only for 3 h.

Apparently, in the next stage of aging, which lasts for several days, fairly similar fragments of stock asphaltene aggregates in each sample further evolve by the individual successions of dissolution events specific for the particular molecular environment (i.e. for the particular asphaltene concentration). Note that in theoretical models which account for kinetics of aggregation/dissolution (Beshnova *et al.*, 2009; Martin, 1996; and references

therein) constants K_i in specific molecular events were also shown to depend on overall molecular concentration. Eventually in all samples, as schematically illustrated in the right part of Figure 2.45, autonomous structural states S1, S2, etc. of asphaltenes with qualitatively different properties may be formed. In this scheme, there is no reason to expect that the succession of equilibrium states in samples with decreasing concentration S4→S3→S2→S1 would be repeated in the course of any non-equilibrium dissolution route (as illustrated in the lower part of Figure 2.45). Furthermore, in the scheme of Figure 2.45 there is also no ban on the above discussed "apparent re-entrance" (see Figures 2.28, 2.32, 2.34, 2.36–39, and 2.43), that is where the equilibrium properties of solution S4, more concentrated than solution S3, are closer to the properties of the much less concentrated solution S2. As an additional supporting illustration, consider the experimental data set in Figure 2.31 for toluene solutions of asphaltenes equilibrated/aged for 10 days, where non-monotonic concentration effects with well-resolved "re-entrant" minima become clearly seen, in contrast to the non-equilibrium (3 h) data set.

References

Acevedo, S., Castillo, J., and Del Capio, E. H. (2014) Precipitation of asphaltenes and resins at the toluene–silica interface: An example of precipitation promoted by local electrical fields present at the silica–toluene interface. *Energy & Fuels*, 28, 4905–4910.

Acevedo, S., Guzmán, K., Labrador, H., *et al.* (2012) Trapping of metallic porphyrins by asphaltene aggregates: A size exclusion microchromatography with high-resolution inductively coupled plasma mass spectrometric detection study. *Energy & Fuels*, 26, 4968–4977.

Acevedo, S., Ranaudo, M., Garcia, C., *et al.* (2003) Adsorption of asphaltenes at the toluene–silica interface: A kinetic study. *Energy & Fuels*, 17(2), 257–261.

Adachi, S. (1999) *Optical Properties of Crystalline And Amorphous Semiconductors: Materials And Fundamental Principles*, Kluwer Academic Publishers, New York.

Agrawala, M. and Yarranton, H. W. (2001) An asphaltene association model analogous to linear polymerization. *Ind. Eng. Chem. Res.*, 40(21), 4664–4672.

Akhmetov, B. R., Evdokimov, I. N., and Eliseev, N. Y. (2002) Some features of the supramolecular structures in petroleum media. *Chem. Technol. Fuels Oils*, 38(4), 266–270.

Akins, D. L., Ozcelik, S., Zhu, H.-R., and Guo, C. (1996) Fluorescence decay kinetics and structure of aggregated tetrakis(*p*-sulfonatophenyl)porphyrin. *Journal of Physical Chemistry*, 100, 14390–14396.

Alboudwarej, H., Jakher, R. K., Svrcek, W. Y., and Yarranton, H. W. (2004) Spectrophotometric measurement of asphaltene concentration. *Pet. Sci. Technol.*, 22(5–6), 647–664.

Alfe, M., Apicella, B., Barbella, R., *et al.* (2007) Distribution of soot molecular weight/size along premixed flames as inferred by size exclusion chromatography. *Energy & Fuels*, 21(1), 136–140.

Al-Maghrabi, I., Bin-Aqil, A. O., Chaalal, O., and Islam, M. R. (1999) Use of thermophilic bacteria for bioremediation of petroleum contaminants. *Energy Sources*, 21(112), 202–212.

Alshareef, A. H., Scherer, A., Tan, X., *et al.* (2011) Formation of archipelago structures during thermal cracking implicates a chemical mechanism for the formation of petroleum asphaltenes. *Energy & Fuel*, 25(5), 2130–2136.

Ancheyta, J., Trejo, F., and Rana, M. S. (2010) *Asphaltenes: Chemical Transformation during Hydroprocessing of Heavy Oils*, CRC Press, Boca Raton, FL.

Andersen, S. I. (2009) Association of petroleum asphaltenes and the effect on solution properties, in: Birdi, K. S. (ed.), *Handbook of Surface and Colloid Chemistry*, 3rd ed., CRC Press, Boca Raton, FL, 703–718, and multiple references therein.

Andrade, S. M., Teixeira, R., Costa, S. M. B., and Sobral, A. J. F. N. (2008) Self-aggregation of free base porphyrins in aqueous solution and in DMPC vesicles. *Biophysical Chemistry*, 133, 1–10.

Asomaning, S. and Watkinson, A. P. (1999) Deposit formation by asphaltene-rich heavy oil mixtures on heat transfer surfaces, in: Bott, T. R. (ed), *Understanding Heat Exchanger Fouling and its Mitigation*, Begell House, New York, 283–290.

Aspnes, D. E. (1982) Local-field effects and effective-medium theory: A microscopic perspective. *American Journal of Physics*, 50(8), 704–709.

ASTM D6560 (2000) *Standard Test Method for Determination of Asphaltenes (Heptane Insolubles) in Crude Petroleum and Petroleum Products*; American Society for Testing and Materials: West Conshohocken, PA.

ASTM D3279-07. (2007) *Standard Test Method for n-Heptane Insolubles*, Philadelphia, available from http://www.astm.org/Standards/D3279.htm.

ASTM D893-05a (2010) *Standard Test Method for Insolubles in Used Lubricating Oils*, Philadelphia, available from http://www.astm.org/Standards/D893.htm.

Badre, S., Goncalves, C. C., Norinaga, K., *et al.* (2006) Molecular size and weight of asphaltene and asphaltene solubility fractions from coals, crude oils and bitumen. *Fuel*, 85(1), 1–11.

Banerjee, A., Sahana, A., Guha, S., *et al.* (2012) Nickel(II)-induced excimer formation of a naphthalene-based fluorescent probe for living cell imaging. *Inorg. Chem.*, 51(10), 5699–5704.

Berlman, I. B. (1971) *Handbook of Fluorescence Spectra of Aromatic Molecules*, Academic Press, New York.

Beshnova, D. A., Lantushenko, A. O., Davies, D. B., and Evstigneev, M. P. (2009) Profiles of equilibrium constants for self-association of aromatic molecules. *Journal of Chemical Physics*, 130, paper 165105.

Bohren, C. and Huffman, D. (1983) *Absorption and Scattering of Light by Small Particles*, John Wiley & Sons, Ltd, New York.

Boussingault, M. (1937) Memoire sur la Composition des Bitumes, *Annales de Chimie et de Physique*, LXIV, 141–151.

Brockwell, J. P. and Davis, A. R. (1996) *Introduction to Time Series and Forecasting*, Springer-Verlag, New York.

Buckley, J. S. (1998) Wetting alteration of solid surfaces by crude oils and their asphaltenes. *Oil & Gas Science and Technology: Rev. IFP*, 53(3), 303–312.

Buenrostro-Gonzalez, E., Groenzin, H., Lira-Galeana, C., and Mullins, O. C. (2001) The overriding chemical principles that define asphaltenes. *Energy & Fuels*, 15(4), 972–978.

Carroll, M. K., Unger, M. A., Leach, A. M., *et al.* (1999) Interactions between methylene blue and sodium dodecyl sulfate in aqueous solution studied by molecular spectroscopy. *Applied Spectroscopy*, 53(7), 780–784.

Castillo, J., Hung, J., Fernandez, A., and Mujica, V. (2001) Nonlinear optical evidences of aggregation in asphaltene–toluene solutions. *Fuel*, 80(9), 1239–1243.

Cho, H. Y., Woo, S. K., and Hwang, G T. (2012) Synthesis and photophysical study of 2′-deoxyuridines labeled with fluorene derivatives. *Molecules*, 17, 12061–12071.

Cignoli, F., Zizak, G., Benecchi, S., and Tencalla, D. (2012) *Atlas of Fluorescence Spectra of Aromatic Hydrocarbons: 1*, Istituto Tecnologie dei Materiali e dei Processi Energetici: Milano, Italy. Open access to the atlas at: http://www.tempe.mi.cnr.it/zizak/atlas/cld-atlas-eng.html.

Cobb, W. T., Nithipatikom, K., and McGown, L. B. (1988) Multicomponent Detection and determination of polycyclic aromatic hydrocarbons using HPLC and a phase-modulated spectrofluorimeter, in: Eastwood, D. and Chin Love, L. J. (eds), *Progress in Analytical Luminescence, ASTM STP 1009*, American Society for Testing and Materials, Philadelphia, 12–25.

Czernuszewicz, R. S. (2000) Geochemistry of porphyrins: Biological, industrial and environmental aspects. *Journal of Porphyrins and Phthalocyanines*, 4(4), 426–431.

Dawson, W. R. and Windsor, M. W. (1968) Fluorescence yields of aromatic compounds. *Journal of Physical Chemistry*, 72(9), 3251–3260.

Dechaine, G. P. and Gray, M. R. (2011a) Membrane Diffusion Measurements Do Not Detect Exchange between Asphaltene Aggregates and Solution Phase. *Energy & Fuels*, 25, 509–523.

Dechaine, G. P. and Gray, M. R. (2011b) Why are Asphaltene Solutions Black?, in: Proceedings of "Oilsands 2011," Edmonton, Alberta Canada, viewed 26 July

(2016), https://sites.ualberta.ca/dept/chemeng/oilsands/2011_Web_Oilsands/files/Dechaine.pdf.

De Greef, T. F. A., Smulders, M. M. J., Wolffs, M., *et al.* (2009) Supramolecular polymerization. *Chemical Reviews*, 109(11), 5687–5754.

Deng, L., Wang, Y., and. Ou-yang, Z.-C. (2012) Concentration and temperature dependences of polyglutamine aggregation by multiscale coarse-graining molecular dynamics simulations. *Journal of Physical Chemistry*, B 116(34), 10135–10144.

Derakhshesh M. (2012) *Asphaltene aggregation and fouling behavior*. PhD thesis, University of Alberta, Edmonton, Alberta, Canada.

Derakhshesh, M., Gray, M. R., and Dechaine, G. P. (2013) Dispersion of asphaltene nanoaggregates and the role of Rayleigh scattering in the absorption of visible electromagnetic radiation by these nanoaggregates. *Energy & Fuels*, 27, 680–693.

Dezhampanah, H., Bordbar, A.-K., and Tangestaninejad, S. (2009) Aggregation and solution behavior of 5-(1-(4-carboxybutyl) pyridinum-4-yl) 10,15,20–tris (1-methylpyridinium-4-yl) porphyrin: A resonance light scattering, fluorescence and absorption spectroscopic study. *J. Iran. Chem. Soc.*, 6(4), 686–697.

Dickie, J. P. and Yen, T. F. (1967) Macrostructures of the asphaltic fractions by various instrumental methods. *Analytical Chemistry*, 39(14), 1847–1852.

Dixon, J. M., Taniguchi, M., and Lindsey, J. S. (2005) PhotochemCAD: A computer-aided design and research tool in photochemistry and photobiology. *Photochem. Photobiol.*, 81, 212–213. Open access to PhotochemCAD spectra database at: http://omlc.org/spectra/PhotochemCAD/index.html.

Doukkali, A., Saoiabi, A., Zrineh, A., *et al.* (2001) Separation and identification of petroporphyrins extracted from the oil shales of Tarfaya: Geochemical study. *Fuel*, 81(4), 467–472.

Downare, T. D. and Mullins, O. C. (1995) Visible and near-infrared fluorescence of crude oils. *Applied Spectroscopy*, 49(6),754–764.

Durov, V. A. (2004) Models of liquid mixtures: Structure, dynamics, and properties. *Pure and Applied Chemistry*, 76(1), 1–10.

Elson, E. L. and Rigler, R. (eds.) (2001) *Fluorescence Correlation Spectroscopy: Theory and Applications,* Springer, Berlin.

Evdokimov, I. N. (2010) Characterization of asphaltenes and crude oils by near-UV/visible absorption spectroscopy, in: Duncan, J. A. (ed), *Asphaltenes: Characterization, Properties and Applications*, Nova Science Publishers, Inc., New York, 1–46.

Evdokimov, I. N. (2012) *Structural Features of Oilfield W/O Emulsions*, RGU Publishing Centre, Moscow [in Russian].

Evdokimov, I. N., Eliseev, N. Yu., and Akhmetov, B. R. (2003a) Assembly of asphaltene molecular aggregates as studied by near-UV/visible spectroscopy. I. Structure of the absorbance spectrum. *J. Petrol. Sci. Eng.*, 37(3–4), 135–143.

Evdokimov, I. N., Eliseev, N. Yu., and Akhmetov, B. R. (2003b) Assembly of asphaltene molecular aggregates as studied by near-UV/visible spectroscopy: II: Concentration dependencies of absorptivities. *J. Petrol. Sci. Eng.*, 37(3–4), 145–152.

Evdokimov, I. N. and Fesan, A. A. (2016) Multi-step formation of asphaltene colloids in dilute solutions. *Colloid. Surface. A*, 492, 170–180.

Evdokimov, I. N., Fesan, A. A., and Losev, A. P. (2016) New answers to the optical interrogation of asphaltenes: Monomers and primary aggregates from steady state fluorescence studies. *Energy & Fuels*, 30(6), 4494–4503.

Evdokimov, I. N. and Losev, A. P. (2007a) On the nature of UV/Vis absorption spectra of asphaltenes. *Pet. Sci. Technol.*, 25(1–2), 55–66.

Evdokimov, I. N. and Losev, A. P. (2007b) *Potential of Optical Research Methods for Monitoring Oil Field Development*, Neft I Gas, Moscow [in Russian].

Evdokimov, I. N. and Losev, A. P. (2008) Suggested "New Method for Determination of Dispersity in Petroleum Systems" is based on trivial experimental artifacts. *Energy & Fuels*, 22(4), 2470–2473.

Evstigneev, M. P., Buchelnikov, A. S., and Evstigneev, V. P. (2012) Random versus sequential pathway of molecular self-assembly. *Physical Review E*, 85, paper 061405.

Fetzer, J. C. (2000) *Large (C > = 24C) Polycyclic Aromatic Hydrocarbons: Chemistry and Analysis*, Wiley-Interscience, New York.

Fidder, H. and Wiersma, D. A. (1995) Collective optical response of molecular aggregates. *Physica Status Solidi (B)*, 188, 285–295.

Friberg, S. E. (2007) Micellization, in: Mullins, O. C., Sheu, E. Y., Hammami, A., and Marshall, A. G. (eds), *Asphaltenes, Heavy Oils and Petroleomics*, Springer, New York, 189–204.

Fujiwara, S., Nishimoto, Y., and Arakawa, F. (1985) Fluctuation of refractive index of aqueous sodium chloride solution and oxygen effects. *Analytical Science*, 1, 23–27.

Gavrylyak, M. S. (2008) Investigation of dynamic fluctuations of refraction index of water tertiary butanol solutions. *Proc. SPIE* 7008, paper 700816.

Goncalves, S., Castillo, J., Fernandez, A., and Hung, J. (2004) Absorbance and fluorescence spectroscopy on the aggregation behavior of asphaltene–toluene solutions. *Fuel*, 83, 1823–1828.

Gonzalez, G., Neves, G. B. M., Saraiva, S. M., *et al.* (2003) Electrokinetic characterization of asphaltenes and the asphaltenes–resins interaction. *Energy & Fuels*, 17(4), 879–886.

Goulon, J., Retournard, A., Friant, P., *et al.* (1984) Structural characterization by X-ray absorption spectroscopy (EXAFS/XANES) of the vanadium chemical environment in Boscan asphaltenes. *J. Chem. Soc. Dalton Trans.*, 1095–1103.

Grassberger, P. and Procaccia, I. (1983) Characterization of strange attractors. *Physical Review Letters*, 50(25), 346–349.

Gray, M. R., Tykwinski, R. R., Stryker, J. M., and Tan, X. (2011) Supramolecular assembly model for aggregation of petroleum asphaltenes. *Energy & Fuels*, 25(7), 3125–3134.

Groenzin, H. and Mullins, O. C. (1999) Asphaltene molecular size and structure. *J. Phys. Chem. A*, 103(50), 11237–11245.

Groenzin, H. and Mullins, O. C. (2000) Molecular size and structure of asphaltenes from various sources. *Energy & Fuels*, 14(3), 677–684.

Groenzin, H. and Mullins, O. C. (2007) Asphaltene molecular size and weight by time-resolved fluorescence depolarization, in: Mullins, O. C., Sheu, E. Y., Hammami, A., and Marshall, A. G. (eds), *Asphaltenes, Heavy Oils and Petroleomics*, Springer, New York, 17–40.

Guilbault, G. G. (1990) *Practical Fluorescence*, 2nd ed., Marcel Dekker Inc., New York.

Guin, J. A. and Geelen, R. (1996) *Hindered Diffusion of Asphaltenes at Elevated Temperature and Pressure*. Report for Grant No. DE-FG22-95PC95221. Auburn, AL: Auburn University, Chemical Engineering Department.

Haswell, S. J. (1991) *Atomic Absorption Spectrometry: Theory, Design and Applications*. Elsevier, Amsterdam.

Huang, F. and Feng, G. (2014) Highly selective and controllable pyrophosphate induced anthracene-excimer formation in water. *RSC Adv.*, 4(1), 484–487.

IP 143/84 (1988) Asphaltene precipitation with normal heptane, *Standard Methods for Analysis and Testing of Petroleum and Related Products: 1*, Institute of Petroleum, London.

Itoh, T. (2014) Fluorescence and phosphorescence emission of quinoline vapor. *Journal of Molecular Spectroscopy*, 301, 9–12.

Joshi, N B., Mullins, O. C., Jamaluddin, A., *et al.* (2001) Asphaltene precipitation from live crude oil. *Energy & Fuels*, 15(4), 979–986.

Jung, H., Kim, K., Lee, S., *et al.* (2007) Improvement of Luminescence Quantum Efficiency by Intermolecular Interaction, *Bulletin of the Korean Chemical Society*, 28(10), 1807–1810.

Juyal, P., Merino-Garcia, D. and Andersen, S. I. (2005) Effect on molecular interactions of chemical alteration of petroleum asphaltenes: I. *Energy & Fuels*, 19(4), 1272–1281.

Kazakova, V. I. and Koretskij, A. F. (1970) The luminescence of asphaltenes, *Russ. Chem. Bull.*, 19(9), 1855–1858.

Keane, P. M., Gallagher, S. A., Magno, L. M., *et al.* (2012) Photophysical studies of CdTe quantum dots in the presence of a zinc cationic porphyrin. *Dalton Transactions*, 41, 13159–13166.

Kelso, J. A. S., Scholz, J. P., and. Schoner, G. (1986) Nonequilibrium phase transitions in coordinated biological motion: Critical fluctuations. *Physics Letters A*, 118(6), 279–284.

Kokal, S. L. and Sayegh, S. G. (1995) Asphaltenes: The cholesterol of petroleum, in: *Proceedings of the SPE Middle East Oil Show*, Bahrain, paper SPE-29787-MS.

Kuo, A. (2011) Generate rich fluorescence in a simple polystyrene system through solvent removal and molecular interactions. *CheM*, 1(1), 1–8.

Lai, E. P. C., Giroux, R. D., Chen, N., and Guo, R. (1993) Pattern recognition for screening of crude oils using multivariate circular profiles. *Can. J. Chem.*, 73, 968–975.

Lakowicz, J. R. (2006) *Principles of Fluorescence Spectroscopy*, 3rd ed., Springer Science and Business Media, LLC, New York.

Lambert, J. B., Shurvell, H. F., Verbit, L., *et al.* (1976) *Organic Structural Analysis*, Macmillan, New York.

Lorentz, H. A. (1960) *Theory of Electrons*, 2nd ed., Teubner, Leipzig, Germany.

Luria, M., Ofran, M., and Stein, G. (1974) Natural and experimental fluorescence lifetimes of benzene in various solvents. *Journal of Physical Chemistry*, 78(19), 1904–1909.

Mabuchi, T., Nishikiori, H., Tanaka, N., and Fujii, T. (2005) Relationships between fluorescence properties of enzoquinolines and physicochemical changes in the sol–gel–xerogel transitions of silicon alkoxide systems. *Journal of Sol-Gel Science and Technology*, 33(3), 333–340.

Maqbool, T., Balgoa, A. T., and Fogler, H. S. (2009) Revisiting asphaltene precipitation from crude oils: A case of neglected kinetic effects. *Energy & Fuels*, 23(7), 3681–3686.

Martin, R. B. (1996) Comparisons of indefinite self-association models. *Chemical Reviews*, 96(8), 3043–3064.

McCain, W. D., Jr (1990) *The Properties of Petroleum Fluids*, PennWell Publishing Company, Tulsa, OK.

McKenna, A. M., Donald, L. J., Fitzsimmons, J. E., *et al.* (2013) Heavy petroleum composition: 3: Asphaltene aggregation. *Energy & Fuels*, 27(3), 1246–1256.

Meeten, G. H. (1997) Refractive index errors in the critical-angle and the Brewster-angle methods applied to absorbing and heterogeneous materials. *Meas. Sci. Technol.*, 8, 728–733.

Meidinger, R. F., St. Germain, R. W., Dohotariu, V., and Gillispie, G. D. (1993) Fluorescence of aromatic hydrocarbons in aqueous solution, in: *Proceedings of the U.S. EPA/Air and Waste Management Association International Symposium on Field Screening Methods for Hazardous Wastes and Toxic Chemicals*, Las Vegas, NV, 395–403.

Mitchell, D. L. and Speight, J. G. (1973) The solubility of asphaltenes in hydrocarbon solvents, *Fuel*, 52(2), 149–152.

Miller, J. N. (ed) (1981) *Standards in Fluorescence Spectrometry*, Chapman and Hall/Methuen, Inc., New York.

Morimoto, M. (2015) Mapping the degree of asphaltene aggregation, determined using Rayleigh scattering measurements and Hansen solubility parameters. *Energy & Fuels*, 29(5), 288–2812.

Mullins, O. C. (1990) Asphaltenes in crude oil: Absorbers and/or scatterers in the near-infrared region?, *Anal. Chem.*, 62(5), 508–514.

Mullins, O. C. (1998) Optical interrogation of aromatic moieties in crude oils and asphaltenes, in: Mullins, O. C. and Sheu, E. Y. (eds), *Structures and Dynamics of Asphaltenes*. Springer, New York, 21–78.

Mullins, O. C. (2010) The Modified Yen Model. *Energy & Fuels*, 24(4), 2179–2207.

Mullins, O. C., Mitra-Kirtley, S., and Zhu, Y. (1992) Electronic absorption edge of petroleum., *Appl. Spectrosc.*, 46(9), 1405–1411.

Mullins, O. C., Sheu, E. Y., Hammami, A., and Marshall, A. G. (eds) (2007) *Asphaltenes, Heavy Oils and Petroleomics*, Springer, New York.

Obara, Y., Saitoh, K., Oda, M., and Tani, T. (2012) Room-temperature fluorescence lifetime of pseudoisocyanine (PIC) J-excitons with various aggregate morphologies in relation to microcavity polariton formation. *International Journal of Molecular Science*, 13, 5851–5865.

Pedersen, K. S., Fredenslund, A. A., and Thomassen, P. (1989) *Properties of Oils and Natural Gases, Contributions in Petroleum Geology and Engineering*, Gulf Publishing Company, Houston, TX.

Perkampus, H. H. (1992) *UV-VIS Spectroscopy and Its Applications*, Springer, Berlin.

Pokonova, Yu. V. (1980) *Chemistry of High-molecular-weight Petroleum Compounds*, LGU Publ., Leningrad [in Russian].

Pomerantz, A. E., Wu, Q., Mullins, O. C., and Zare, R. N. (2015) Laser-based mass spectrometric assessment of asphaltene molecular weight, molecular architecture and nanoaggregate number. *Energy & Fuels*, 29(5), 2833–2842.

Pope, M. and Swenberg, C. E. (1999) *Electronic Processes in Organic Crystals and Polymers*, 2nd ed., Oxford University Press, New York/Oxford.

Potapov, A. V., Kolyakov, S. F., Krasheninnikov, V. N., and Dumesh, B. S. J. (2006) Circular dichroism of crude oil and its derivatives: Role of permolecular structures. *Colloid Iterf. Sci.*, 303(1), 159–163.

Potapov, A. V., Kolyakov, S. F., Krasheninnikov, V. N., and Syunyaev, R. Z. (2008) Circular dichroism of crude oils: Influence of micelle formation. *Energy & Fuels*, 22, 561–563.

Ralston, C. Y., Mitra-Kirtley, S., and Mullins, O. C. (1996) Small population of one to three fused-aromatic ring moieties in asphaltenes. *Energy & Fuels*, 10(3), 623–630.

Ramachandran, G., Raman, A., Easwaramoorthi, S., *et al.* (2014) Four component domino reaction for the synthesis of highly functionalized dimeric tetracyclic dilactam fluorophores: H-bond Aided Self-Assembly. *RSC Advances*, 4, 29276–29280.

Rao, C. N. R. (1975) *Ultra-Violet and Visible Spectroscopy: Chemical Applications*. Butterworths, London.

Rogel, E. (1995) Studies on asphaltene aggregation via computational chemistry, *Colloid. Surface. A*, 104, 85–93.

Ruiz-Morales, Y. and Mullins, O. C. (2007) Polycyclic aromatic hydrocarbons of asphaltenes analyzed by molecular orbital calculations with optical spectroscopy. *Energy & Fuels*, 21(1), 256–265.

Ruiz-Morales, Y. and Mullins, O. C. (2009) Measured and simulated electronic absorption and emission spectra of asphaltenes. *Energy & Fuels*, 23(3), 1169–1177.

Ruiz-Morales, Y. and Mullins, O. C. (2013) Singlet–triplet and triplet–triplet transitions of asphaltene PAHs by molecular orbital calculations. *Energy & Fuels*, 27(9), 5017–5028.

Ruiz-Morales, Y., Wu, X., and Mullins, O. C. (2007) Electronic absorption edge of crude oils and asphaltenes analyzed by molecular orbital calculations with optical spectroscopy. *Energy & Fuels*, 21(2), 944–952.

Schultze, R. H., Lemke, M., and Löhmansröben, H. G. (2004) Laser-induced fluorescence (LIF) spectroscopy for the in situ analysis of petroleum product-contaminated soils, in: Hering, P., Lay, J. P., and Stry, S. (eds), *Laser in Environmental and Life Sciences*, Springer-Verlag, New York, 79–98.

Sergienko, S. G., Taimova, B. A., and Talalajev, E. I. (1979) *Higher-molecular Non-hydrocarbon Oil Constituents*, Nauka, Moscow [in Russian].

Sheremata, J. M., Gray, M. R., Dettman, H. D., and McCaffrey, W. C. (2004) Quantitative molecular representation and sequential optimization of athabasca asphaltenes. *Energy & Fuels*, 18(5), 1377–1384.

Sheu, E. Y. (1996) Physics of asphaltene micelles and microemulsions: Theory and experiment. *J. Phys.-Condens. Mat.*, 8(25A), A125–A141.

Sheu, E. Y. and Acevedo, S. (2006) A dielectric relaxation study of precipitation and curing of Furrial crude oil. *Fuel*, 85(14–15), 1953–1959.

Singh, J. and Shimakawa, K. (2003) *Advances in Amorphous Semiconductors. Advances in Condensed Matter Science: Volume 5*, Taylor & Francis, New York.

Sjöblom, J., Hemmingsen, P. V. and Kallevik, H. (2007) The role of asphaltenes in stabilizing water-in-crude oil emulsions, in: Mullins, O. C., Sheu, E. Y., Hammami, A., and Marshall, A. G. (eds), *Asphaltenes, Heavy Oils and Petroleomics*, Springer, New York, 549–587.

Spano, F. C. and Mukamel, S. (1989) Superradiance in molecular aggregates. *Journal of Chemical Physics*, 91, 683–700.

Speight, J. G. (1994) Chemical and physical studies of petroleum asphaltenes, in: Yen, T. F. and Chilingarian, G. V. (eds), *Asphaltenes and Asphalts: 1*; Elsevier, Amsterdam, 7–65.

Speight, J. G. (2004) Petroleum asphaltenes: Part 1: Asphaltenes, resins and the structure of petroleum. *Oil & Gas Science and Technology: Rev. IFP*, 59, (5): 467–477.

Speight, J. G. (2007) *The Chemistry and Technology of Petroleum*, CRC Press, Boca Raton, FL.

Speight, J. G., Long, R. B., and Trowbridge, T. D. (1984) Factors influencing the separation of asphaltenes from heavy petroleum feedstocks, *Fuel*, 63, (5), 616–620.

Stanley, H. E. (1971) *Introduction to Phase Transitions and Critical Phenomena*, Oxford University Press, New York.

Strausz, O. P., Mojelsky, T. W., and Lown, E. M. (1992) The molecular structure of asphaltene: An unfolding story. *Fuel*, 71(12), 1355–1363.

Strausz, O. P., Safarik, I., Lown, E. M., and Morales-Izquierdo, A. (2008) A critique of asphaltene fluorescence decay and depolarization-based claims about molecular weight and molecular architecture. *Energy & Fuel*, 22(2), 1156–1166.

Tor, Y., Del Valle, S., Jaramillo, D., *et al.* (2007) Designing new isomorphic fluorescent nucleobase analogues: The thieno[3,2-d]pyrimidine core, *Tetrahedron*, 63, 3608–3614.

Tynan, E. C. and Yen, T. F. (1969) Association of vanadium chelates in petroleum asphaltenes as studied by E.S.R. *Fuel*, 43, 191–208.

Valeur, B. and Berberan-Santos, M. N. (2012) *Molecular Fluorescence: Principles and Applications*, 2nd ed., Wiley-VcHVerlag GmbH, Weinheim/New York.

Vekshin, N. L. (1999) Screening hypochromism in molecular aggregates and biopolymers. *Journal of Biological Physics*, 25, 339–354.

Wallace, G. G., Spinks, G. M., Kane-Maguire, L. A. P., and Teasdale, P. R. (2003) *Conductive Electroactive Polymers: Intelligent Material Systems*, 2nd ed., CRC Press, Boca Raton, FL.

Wang, Z., Friedrich, D. M., Beversluis, M. R., *et al.* (2001) A fluorescence spectroscopic study of phenanthrene sorption on porous silica. *Environmental Science & Technology*, 35(13), 2710–2716.

Wattana, P., Wojciechowski, D. J., Bolanos, G., and Fogler, H. S. (2003) Study of asphaltene precipitation using refractive index measurement. *Petroleum Science & Technology*, 21(3–4), 591–613.

Wehry, E. L. (ed.) (1976) *Modern Fluorescence Spectroscopy: Vols. 1 and 2*, Marcel Dekker Inc., New York.

Werner, A., Behar, F., and Behar, E. (1998) Viscosity and phase behaviour of petroleum fluids with high asphaltene contents. *Fluid Phase Equilibria*, 147(112), 343–349.

Woodward, W. A., Gray, H. L. and Elliott, A. C. (2012) *Applied Time Series Analysis*, CRC Press, Boca Raton, FL.

Yang, C. (2000) *Optical and fluorescent properties of thiophene-based conjugated polymers*. PhD thesis, Department of Chemistry, Simon Fraser University, Canada [and multiple references therein].

Yang, C. P., Liao, Z. W., Zhang, L. H., and Creux, P. (2009) Some biogenic-related compounds occluded inside asphaltene aggregates. *Energy & Fuels*, 23(1), 820–827.

Yang, J. and Pearson, J. E. (2012) Origins of concentration dependence of waiting times for single-molecule fluorescence binding. *Journal of Chemical Physics*, 136(24), paper no. 244506.

Yen, T. F. (2000) The realms and definitions of asphaltenes, in: Yen, T. F. and Chilingarian, G. V. (eds), *Asphaltenes and Asphalts: 2: Developments in Petroleum Science, 40B*, Elsevier Science BV, Amsterdam, 7–28.

Yen, T. F. and Chilingarian, G. V. (eds) (1994) *Asphaltenes and Asphalts: 1*, Elsevier, Amsterdam.

Yen, T. F. and Chilingarian, G. V. (eds) (2000) Asphaltenes and Asphalts: 2. Developments in Petroleum Science, 40B, Elsevier Science BV, *Amsterdam.*

Yokota, T., Scriven, F., Montgomery, D. S., and Strausz, O. P. (1986) Absorption and emission spectra of Athabasca asphaltene in the visible and near ultraviolet regions. *Fuel*, 65(8), 1142–1149.

Zarudnev, E. S., Plokhotnichenko, A. M., Leontiev, V. S., *et al.* (2012) Unusual aggregation of poly(rC)-wrapped carbon nanotubes in aqueous suspension induced by cationic porphyrin. *Journal of Materials Chemistry*, 22, 10795–10804.

Zhang, H. T. (2010) *Probing Asphaltenes Aggregation with Fluorescence Techniques.* MSci thesis, University of Victoria: Victoria, British Columbia, Canada.

Zhang, H. T., Li, R., Yang, Z., *et al.* (2014) Evaluating steady-state and time-resolved fluorescence as a tool to study the behavior of asphaltene in toluene. *Photochemical & Photobiological Sciencies*, 13, 917–928.

Zhang, L. and Chen, S. (1988) Study on exciplexes formed by benzene, naphthalene anthracene and 1,4-dicyanobenzene. *J. Lumin.*, 40–41, 233–234.

Zhao, J., Liao, Z. W., Zhang, L. H., *et al.* (2010) Comparative studies on compounds occluded inside asphaltenes hierarchically released by increasing amounts of H_2O_2/CH_3COOH. *Applied Geochemistry*, 25(9), 1330–1338.

Zhao, X., Xu, C., and Shi, Q. (2015) Porphyrins in heavy petroleums: A review, in: Xu, C. and Shi, Q. (eds), *Structure and Modeling of Complex Petroleum Mixtures*, Springer International Publishing, Switzerland, 39–70.

Zwarich, R. J. (1968) *A study of the spectra of some organic compounds.* PhD thesis, Department of chemistry, The University of British Columbia, Vancouver, BC, Canada.

3

ESR Characterization of Organic Free Radicals in Crude Oil and By-Products

Marilene Turini Piccinato[1], *Carmen Luisa Barbosa Guedes*[2] *and Eduardo Di Mauro*[2]

[1] *Universidade Tecnológica Federal do Paraná – Campus Londrina (UTFPR-LD), Brasil*
[2] *Universidade Estadual de Londrina (UEL)/Laboratório de Fluorescência e Ressonância Paramagnética Eletrônica (LAFLURPE)*

3.1 Introduction

Many kinds of radicals are stable enough to isolate, handle, and store without special precautions. These correspond to a class of free radicals that has been identified as chemical species with unpaired electrons with sufficiently long lifetimes that they can be observed by conventional spectroscopy methods (Hicks, 2007). Since the direct characterization of these radicals is very difficult, ESR (electron spin resonance) or ERP (electron paramagnetic resonance) emerged as the simplest and often most useful tool to detect, monitor, define the location, and characterize the properties of free radicals under different conditions and in different environments (Improta and Barone, 2004). In crude oil and oil by-products, the presence of free radicals allows the ESR technique to assist researchers in their attempts to elucidate the complex chemical composition of these systems.

3.2 Organic-Free Radicals in Crude Oil

Petroleum is formed by the thermal degradation of kerogen and may also contain large amounts of asphaltene (Damsté *et al.*, 1989). Asphaltenes are macromolecular compounds, comprising polyaromatic nuclei linked by aliphatic chains or rings of various lengths and sometimes by functional groups (Yen, Erdman, and Saraceno, 1962; Behar, Pelet, and Roucache, 1984; Pelet, Behar, and Monin, 1986). They appear to differ in size, with a statistically identical distribution of aromatic nuclei and linking units. Recent evidence

Analytical Characterization Methods for Crude Oil and Related Products, First Edition.
Edited by Ashutosh K. Shukla.

suggests that asphaltenes may be considered as small "soluble" fragments of kerogen, as they share comparable structures (Bandurski, 1982; Tissot and Welte, 1984; Behar and Pelet, 1985; Philp and Gilbert, 1985). Asphaltenes from rock extracts, and the corresponding kerogens, contain the same constituent macromolecular units (Pelet *et al.*, 1986). A consequence of this compositional similarity is that asphaltenes and kerogen undergo parallel evolutions during burial heating. Coal may be regarded as a special type of kerogen, derived mainly from terrestrial organic matter (Durand, 1980; Larter, 1984). Each of these materials is comprised mainly of carbon, hydrogen, oxygen, nitrogen, and sulfur (Damsté *et al.*, 1989). An interesting characteristic of the coal and asphaltene fraction of crude oils is the presence of stable free radicals (Uebersfeld Etienne, and Combrisson, 1954). The radical present in petroleum asphaltenes is associated with a non-localized π system of electrons stabilized by resonance. Garif'ianov and Kozyrev (1956) were the first to briefly mention the presence of unpaired electrons in crude oils.

Petroleum and related materials such as heavy oils, asphalt, pitch, coal tar, tar sands, kerogen, and oil shale have been studied by ESR (Ikeya, 1993). ESR is a useful method for the investigation of free radicals.

3.3 ESR of Crude Oil

Electron paramagnetic resonance (EPR) or electron spin resonance (ESR) is a high-resolution spectroscopy that consists in energy absorption of microwave, for electron spin, in the presence of a magnetic field (Ikeya, 1993). As the name itself suggests, ESR is applied in samples containing some paramagnetic species or used as an investigative method, to verify the presence of some paramagnetic species. Paramagnetism is characteristic of species with a total magnetic moment different from zero.

The ESR spectra of crude oils show signals of two different paramagnetic centers, namely the vanadyl group VO^{2+} and free radical (Guedes *et al.*, 2001, 2003). These are overlapped in the same magnetic field range (Figure 3.1), being the very intense central line associated with organic-free radical (Yen, Erdman, and Saraceno, 1962; Montanari *et al.*, 1998; Scott and Montanari, 1998).

The free radical gives rise to a single line corresponding to the transition between the spin $+1/2$ and $-1/2$. The two possible configurations for an unpaired electron in the presence of an external magnetic field (spin up and spin down) have different energies, which are represented by energy level diagrams (Figure 3.2). In the absence of an applied magnetic field, the two spin states are of equal energy (Bunce, 1987).

Energy showed in different spin states in the presence of an external magnetic field is known as the "Zeeman effect" and depends on $\vec{H}$ and the magnetic

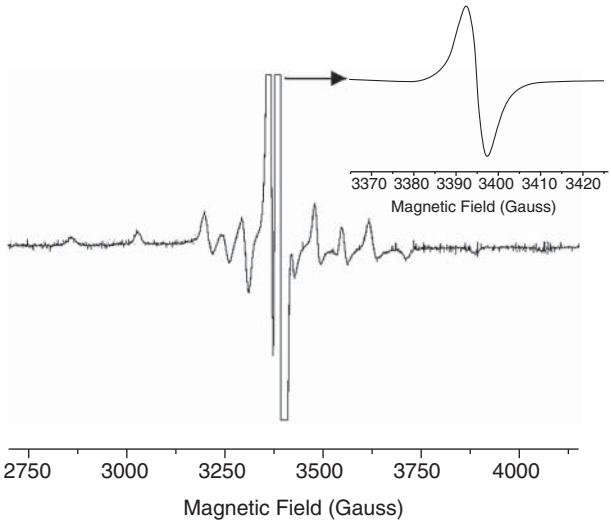

Figure 3.1 ESR spectrum for Kuwait crude oil and signal of the free radical showed in another scale of magnetic field and intensity.

Figure 3.2 Energy levels of a single electron in the presence of an external magnetic field.

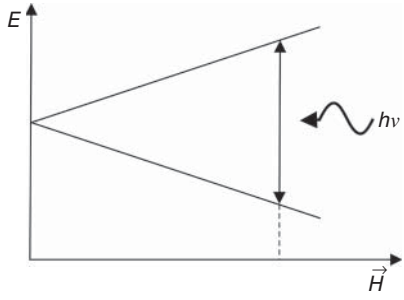

moment ($g\beta M_S$) of the electron (Ikeya, 1993). The Zeeman energy is given by

$$E_z = g\beta H M_s \tag{3.1}$$

According to the equation 3.1, the energy levels to an unpaired electron have energies equal to

$$E_{z+} = +\frac{1}{2} g\beta H \tag{3.2}$$

and

$$E_{z-} = -\frac{1}{2} g\beta H, \tag{3.3}$$

corresponding to spin up ($M_s = +\frac{1}{2}$) and spin down ($M_s = -\frac{1}{2}$) respectively.

If an oscillating field of radiation, in the microwave range, acts on an unpaired electron in the presence of a magnetic field, transitions between two energy states are possible. The transition between energy levels will only occur when the following resonance condition is satisfied:

$$h\nu = g\beta H. \tag{3.4}$$

This happens when the incident radiation is equal to the separation between the Zeeman energy levels. In the equation 3.4 $h\nu$ is the energy of the absorbed photon, β is a constant for the electron (Bohr magneton), H is the external magnetic field, and g (g-factor) is a constant characteristic of spin system (approximately 2.0 for organic-free radicals) (Janzen, 1969). To the ESR experiments, spectrometers work with a fixed microwave radiation and a variable magnetic field to get the resonance condition.

In ESR spectroscopy it is common to record the spectrum as first derivative curve (Figure 3.3, solid curve), as opposed to the direct absorption curve (Figure 3.3, dotted curve), which is the conventional presentation in high-resolution nuclear magnetic resonance (NMR) (Bunce, 1987).

Some parameters are used to identify an ESR signal of free radicals. Among them we can point out the g-factor and the linewidth (ΔH).

The g-factor is obtained from the resonance condition (Equation 3.4) finding the magnetic field at the resonance peak or the magnetic field at the center of line in the first derivative, as demonstrated in Figure 3.3. The g parameter is sensitive to the chemical neighborhood of the unpaired electron, although the asphaltenes (the heavy fraction of oil) have the nature of a mixture of

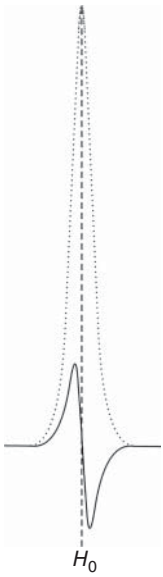

Figure 3.3 ESR spectrum as a first derivative curve (solid line) and absorption curve (dotted line).

free radicals. In a non-localized system an unpaired electron travels over the different atoms, and therefore the *g*-factor tends to increase when heteroatoms are present in the system (Montanari *et al.*, 1998).

The *g*-factor for the free radicals of asphaltenes in some investigated oils range from 2.0028 to 2.0034, being higher than those of the aromatic hydrocarbon radical ions and increasing with the decrease of the aromatic fraction and the related carbon content (Montanari *et al.*, 1998). The relation between the *g*-factor and aromatic fraction can be seen with the Arabian and Colombian oils: the fact that Arabian oil ($g = 2.0033 \pm 0.0001$) presents a heteroatom weight percentage of 2.79%, smaller than Colombian oil (19.77%wt), and the fact that nitrogen and sulfur are located mainly in the aromatic systems in Arabian petroleum, indicate that this oil is less aromatic than the Colombian oil ($g = 2.0030 \pm 0.0001$) (Guedes *et al.*, 2006).

The *g* parameter values for the radicals in petroleum asphaltenes were found to be closest to certain types of neutral carbon and nitrogen radicals (Requejo *et al.*, 1992). To Arabian petroleum (2.0033 ± 0.0001) and Colombian petroleum (2.0030 ± 0.0001) (Guedes *et al.*, 2006), one possible interpretation for the *g*-factor observed likewise corresponds to neutral radicals of carbon or nitrogen (Yen, Erdman, and Saraceno, 1962). To Brazilian petroleum (Campos Basin in the state of Rio de Janeiro), the $g = 2.0045$ suggests the presence of phenoxy radicals, that is radicals partially localized in aromatic systems due to the oxygen (Guedes *et al.*, 2003).

In all crude oils, the signal of free radicals in the ESR spectra consist of an unresolved line with a width of about 5 gauss (G) (Guedes *et al.*, 2001, 2003, 2006; Di Mauro, Guedes, and Nascimento, 2005). No hyperfine (hf) structure is observed. In petroleum asphaltenes, the hf interaction is generally between the electron spin delocalized in an aromatic π orbital and the nuclear magnetic moments of H attached to the aromatic C. When the nucleus has a magnetic moment different from zero, this will interact with the electronic moment, resulting in an hf structure which can be observed in the ESR spectrum (Orton, 1968).

When there is an interaction of the unpaired electron with the nucleus, this splits the electron energy levels, generating a structure called spectral hf structure or hf splitting (Poole, 1967). Each "M_s state" is split into a closely spaced group of $(2I + 1)$ levels (Orton, 1968), being I the nuclear spin quantum number. The way in which these give rise to hf splitting of the resonance lines is illustrated in Figure 3.4.

Transitions are allowed under the following selection rules: $\Delta M = \pm 1$, for electron spin levels spliting, and $\Delta m = 0$, for nuclear spins. For the sample taken, the allowed transitions are indicated by arrows in Figure 3.4. Each of these transitions gives rise to a resonance line in the ESR spectrum at different magnetic fields H_{01} and H_{02} (Figure 3.5). The spacing between the observed lines, usually in gauss, provides the hf coupling constant (A). The

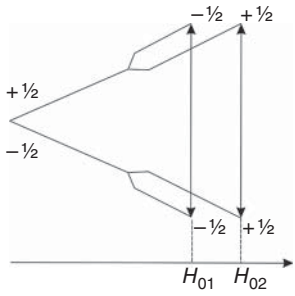

Figure 3.4 Schematic diagram of the hf splitting for unpaired electron interaction with a nucleus of nuclear spin $I = 1/2$.

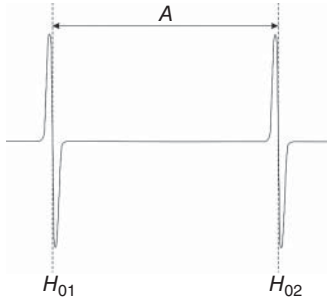

Figure 3.5 Resonance lines at different magnetic fields (H_{01} and H_{02}) for unpaired electron interaction with a nucleus of nuclear spin $I = 1/2$ and indication to the hf coupling constant (A).

spacing between lines is always symmetrically disposed about the center of the spectrum. However, the hf interaction is not always seen in the experimental spectrum, i.e. the experimental lines are unresolved, as identified by free radical ESR spectra in petroleum asphaltenes. Unresolved lines can give rise to linewidth broadening.

The linewidth broadening of the free radical cannot be attributed unequivocally to the unresolved hf structure of the ESR spectrum. The effects of the aromaticity and the different degrees of substitution in the linewidth and the lineshape probably overlap, and a different number of spins could also contribute to the linewidth by dipolar interaction (Scott and Montanari, 1998). There are most likely a number of chemically distinct radicals, and each one of these different radicals also has a range of chemical environments and conformations, in such a manner that the variation in linewidth is not simply due to a variety of radicals but also to the distribution of these radicals in the crude oils (Di Mauro, Guedes, and Nascimento, 2005).

To investigate the resolution possibility of the ESR line corresponding to free radicals in the asphaltenic fraction of crude oil, petroleum of Arabian (Arabian Light Crude Oil) (Figure 3.6) and Colombian (Cusiana crude oil) (Figure 3.7) origin was studied by electron paramagnetic resonance spectroscopy in X- (9 GHz), Q- (34 GHz) and W-bands (94 GHz). Even in the higher band, the ESR spectra were not resolved, but the asymmetry in the lines was observed more intensely in the W-band spectra.

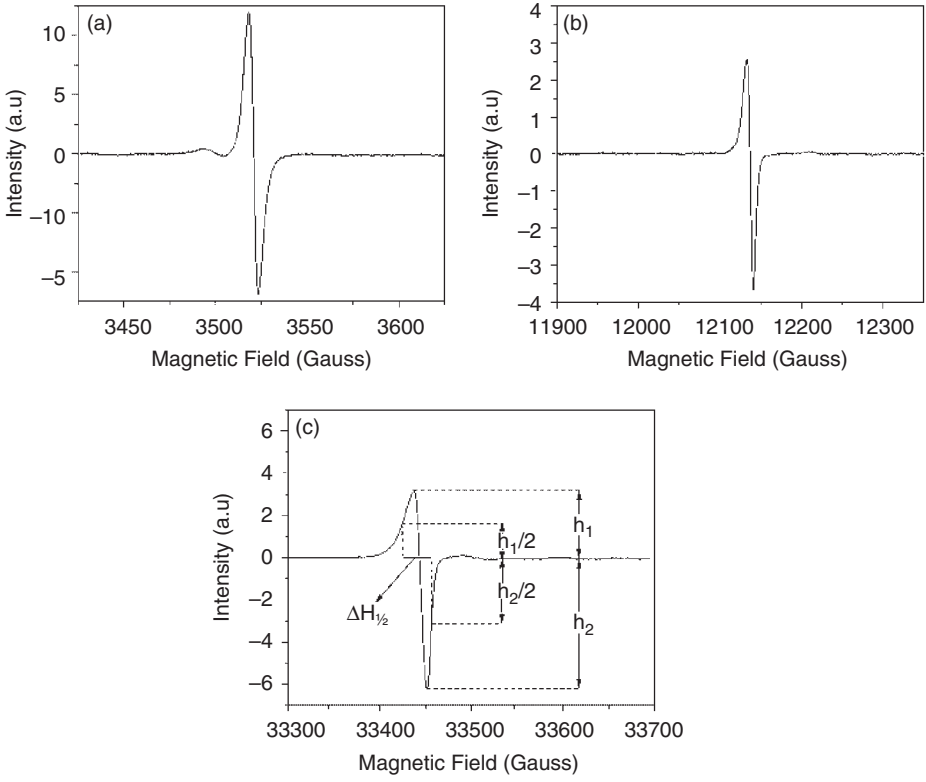

Figure 3.6 Free-radical ESR spectra of Arabian crude oil at room temperature obtained in: (a) X- band, (b) Q- band, (c) W- band; $\Delta H_{1/2}$ is the half height separation of the ESR derivative peak. *Source:* Di Mauro, Guedes, and Nascimento (2005). Reproduced with permission of Springer.

The asymmetry in the line was indicated to be due to the superposition of all the possible orientations of the paramagnetic species in the system and to the contributions of different chemical species that interact with the unpaired electron. Furthermore, the values of the linewidth ΔH in the spectra increased linearly with the microwave frequency utilized in ESR experiments (Figure 3.8).

The increase in values of the linewidth ΔH could be due either to the superposition of all the possible orientations of the paramagnetic species with anisotropic g-factor in the system and/or to the contribution of different chemical species with a different g-factor to the free radical. A mathematical simulation of the free radical signal for the ESR spectra in three bands (X-, Q-, and W-) with a set of parameters corresponding to a single species does not coincide exactly with the experimental signal, signaling that the hf interaction of the unpaired electron with neighborhood correspond to more than one

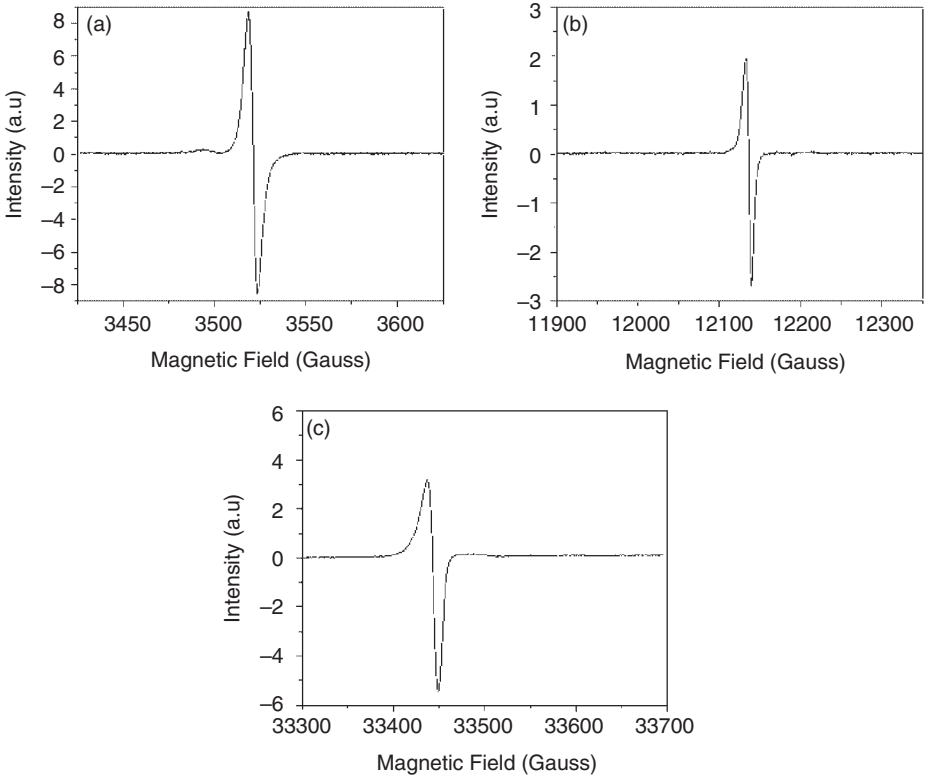

Figure 3.7 Free-radical ESR spectra of Colombian crude oil at room temperature obtained in: (a) X- band, (b) Q- band, (c) W-band. *Source:* Di Mauro, Guedes, and Nascimento (2005). Reproduced with permission of Springer.

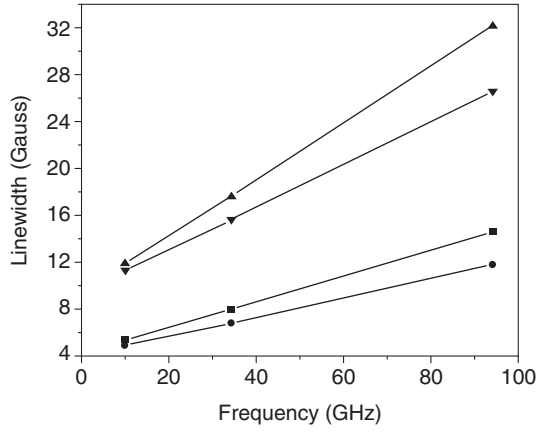

Figure 3.8 Linewidth ΔH of the free-radical signal versus microwave frequency of ESR spectra recorded in the X-, Q- and W-bands at room temperature. ■, ΔH (Arabian petroleum); ●, ΔH (Colombian petroleum); ▲, $\Delta H_{1/2}$ (Arabian petroleum); ▼, $\Delta H_{1/2}$ (Colombian petroleum). *Source:* Di Mauro, Guedes, and Nascimento (2005). Reproduced with permission of Springer.

species of radical in the molecular structure of the crude oil asphaltenes (Di Mauro, Guedes, and Nascimento, 2005).

3.4 By-Product Oil by ESR

The mobility of free radicals in crude oil at room temperature is relatively low, owing to high oil viscosity (Di Mauro, Guedes, and Nascimento, 2005). Many details are lost in high-viscosity liquids, owing to the line broadening caused by anisotropies in the *g*-factor and hf coupling coefficient, plus the exchange and magnetic dipole–dipole interactions between spins of neighboring radicals. In low-viscosity liquids, rapid molecular tumbling averages out these anisotropies and minimizes the exchange and dipole–dipole effects. When stable radicals are dissolved in inert solvents, the spectra can change from single broad lines, for concentrated solutions, to the hf lines as dilution continues. The interest in studying dilute solutions of free radicals is based on the abundant hf structure and the possibility of translating the structure into a map of unpaired electron density throughout the molecule (Alger, 1968).

The intention in studying by-product oil is due to the fact that this low-viscosity, when compared to the crude oil, allows a high mobility of the free radical in its environment. A by-product oil that was studied a great deal by ESR was marine diesel (fluid catalytic cracking diesel, bunker, ship fuel) (Di Mauro, Guedes, and Piccinato, 2007; Piccinato, Guedes, and Di Mauro, 2009). Marine diesel is produced in refineries and integrates mixtures with other products. This kind of diesel is formed through the mixture of several currents from several stages of crude oil processing, such as diesel, heavy naphtha, and light and heavy diesel. Its viscosity at room temperature is $2.5 \cdot 10^{-3}$ kg/m·s, thus less than a thousandth of crude oil's viscosity. The tumbling correlation time for free radicals in marine diesel at room temperature is about 10^{-7}s (Di Mauro, Guedes, and Piccinato, 2007). Although this value is larger than that obtained for nitroxyl radicals (Hwang *et al.*, 1975; Du, Eaton, and Eaton, 1995; Owenius *et al.*, 2004) and tempone (Goldman *et al.*, 1972) in solutions with different viscosity, it is much lower than crude oil values (10^{-4}s) (Di Mauro, Guedes, and Nascimento, 2005) and justifies the high mobility of free radicals in this oil by-product.

The marine diesel spectrum obtained in X-band consists of signal from radicals with a typical hf splitting of protons (Figure 3.9). This spectrum exhibits a septet of lines with intensities proportional to 1, 6, 15, 20, 15, 6, 1. These correspond to different ways of form spins +3, +2, +1, 0, − 1, − 2, − 3 due to the interaction of six equivalent and strong coupled protons [$A(^1H)$]. Each of seven hf lines is split into four lines (quartet), in a second-order interaction, owing to the three weakly coupled protons [A' (^1H)] with intensities proportional to 1, 3, 3, 1, and corresponding to the different ways of form spins +3/2, +1/2, − 1/2, − 3/2 (Di Mauro, Guedes, and Piccinato, 2007).

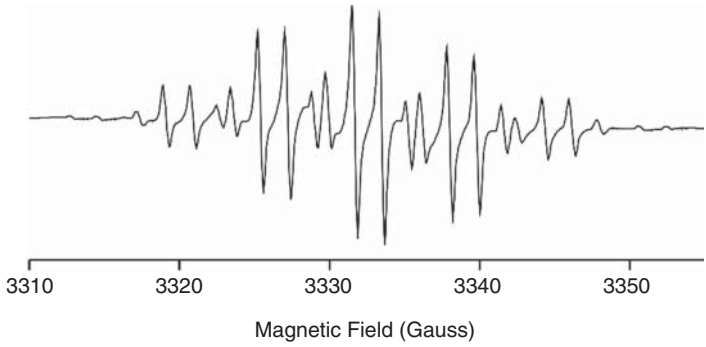

Figure 3.9 ESR spectrum of marine diesel in X-band at room temperature, showing the hf separation into seven lines owing to the interaction between six equivalent strongly coupled protons, and each of the seven lines is resolved into four lines owing to the three weakly coupled protons. *Source:* Di Mauro, Guedes, and Piccinato (2007). Reproduced with permission of Springer.

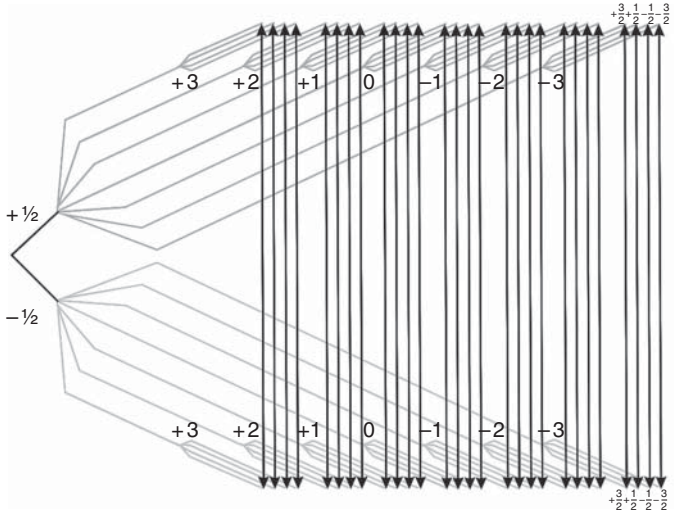

Figure 3.10 Energy diagram of a free radical in marine diesel (bunker).

The analysis suggesting first- and second-order hf splitting, with spin configurations described above, provides the layout of an energy diagram (Figure 3.10). Considering the selection rules, the allowed transitions are indicated by 28 vertical arrows representing each of the spectral lines.

The spectrum shown (Figure 3.9) can be interpreted in terms of the following "isotropic" spin Hamiltonian, since the radical rotates at a short

correlation time:

$$H = g\beta HS + AIS + A'IS. \tag{3.5}$$

The WINEPR SimFonia Version 1.25 software of Bruker® was used in the simulation option for determining g, A, A', and ΔH (peak-to-peak linewith) of the free radical species. The parameter values found were $g = 2.0028 \pm 0.0005$, $A = 6.31 \pm 0.01$ G for six equivalent protons ($I = 1/2$), $A' = 1.80 \pm 0.01$ G for three equivalent protons ($I = 1/2$), and $\Delta H = 0.38 \pm 0.02$ G.

The same septet-quartet signal has been observed in petroleum-rich mudstone and carbonates (Ikeya and Furusawa, 1989). A similar signal observed in flints has been assigned to stable perinaphthenyl radicals (Chandra, Symons, and Griffiths, 1988). Some authors (Ikeya, 1993; Uesugi and Ikeya, 2001) present splitting similar to the pattern mentioned above assigning to *t*-butyl molecules. However, according to Forbes *et al.* (1991) the hf coupling for ^{1}H in *t*-butyl is 22.6 G, which does not fit the spectrum of marine diesel. Sogo, Nakazaki, and Calvin (1957) on the other hand, determined hf parameters for perinaphthene that fit fairly well to the spectrum of marine diesel. Besides, according to Gerson and Huber (2003), perinaphthenyl can be detected in pyrolysis products of petrol fractions. Another chemical evidence favorable to perinaphthenyl is its persistence (Sogo, Nakazaki, and Calvin, 1957) when compared to the not very persistent *t*-butyl.

The results obtained for the hf interaction of free radicals in marine diesel and the discussion regarding the organic molecule models indicate that perinaphthenyl radicals (Figure 3.11) are probably responsible for the septet-quartet EPR spectrum of this oil by-product (Di Mauro, Guedes, and Piccinato, 2007).

According to Figure 3.11, the hf splitting arises from the hf interaction of the unpaired electron with the hydrogen atoms around the molecule. The six hydrogen atoms in positions 1, 2, 4, 5, 7, and 8 are responsible for first-order hf interaction and the other three atoms in positions 3, 6, and 9, the second-order hf interaction.

It has been verified (Piccinato, Guedes, and Di Mauro, 2009) that the signal attributed to the perinaphthenyl radical in marine diesel decreases in intensity and finally disappears with time, depending on the time that samples were

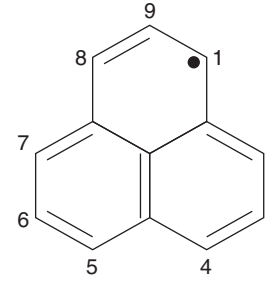

Figure 3.11 Structural representation to perinaphthenyl radical indicating 1 to 9 hydrogen atoms responsible for the hf splitting observed in marine diesel spectrum.

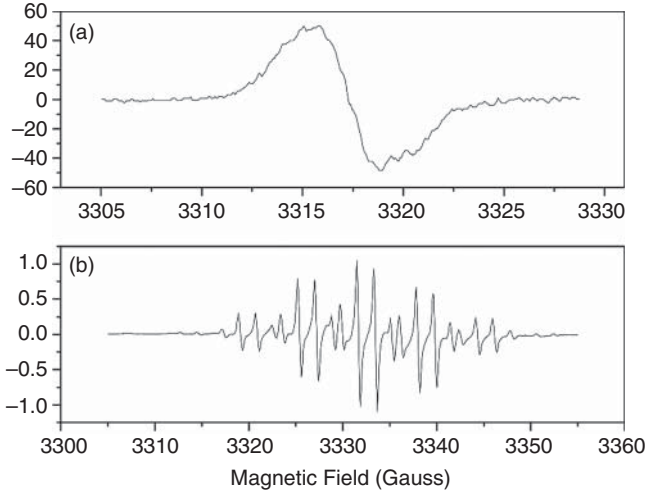

Figure 3.12 Comparison between ESR spectrum of marine diesel. (a) ESR spectrum of marine diesel (older sample) at 9.37 GHz at room temperature. (b) ESR spectrum of marine diesel (fresh sample). *Source:* Piccinato, Guedes, and Di Mauro (2009). Reproduced with permission of Springer.

exposed to air (Figure 3.12a); this suggests that the radical undergoes a chemical reaction, probably with oxygen in air, since phenalenyl is sufficiently persistent in dilute deoxygenated solutions (Gerson, 1966; Hicks, 2007). Senglet *et al.* (1990) observed a weak phenalenyl radical spectra after six months of storage to fuel samples. Another possibility is that the perinaphthenyl radicals form a dimer becoming diamagnetic and, consequently, exhibit no ESR signal.

Studies (Gerson, 1966; Reid, 1958) indicate that the phenalenyl radical and its derivatives show self-association and formation of a diamagnetic dimer. More recently, quantitative ESR studies (Zaitev *et al.*, 2006; Zheng *et al.*, 2003) confirmed that the phenalenyl dimerization occurs reversibly in carbon tetrachloride, toluene, and dichloromethane, resulting in a complete signal loss at low temperatures due to dimer formation. Given that the phenalenyl radical generally exists in equilibrium with its diamagnetic dimer (Gerson, 1966) and taking into account the high mobility of this radical in marine diesel (Di Mauro, Guedes, and Piccinato, 2007), dimerization even at room temperature should be considered.

Concerning this possibility, a marine diesel sample that exhibited no hf resolved lines, labelled "old sample" (Figure 3.12a), was investigated by ESR in the temperature range of 170–400 K. It was expected to obtain the same hf splitting observed in a fresh sample (Figure 3.12b)

The free radical ESR spectrum in marine diesel revealed a progressive appearance of the typical hf of protons with heating (Figure 3.13a). Up to 378 K, it

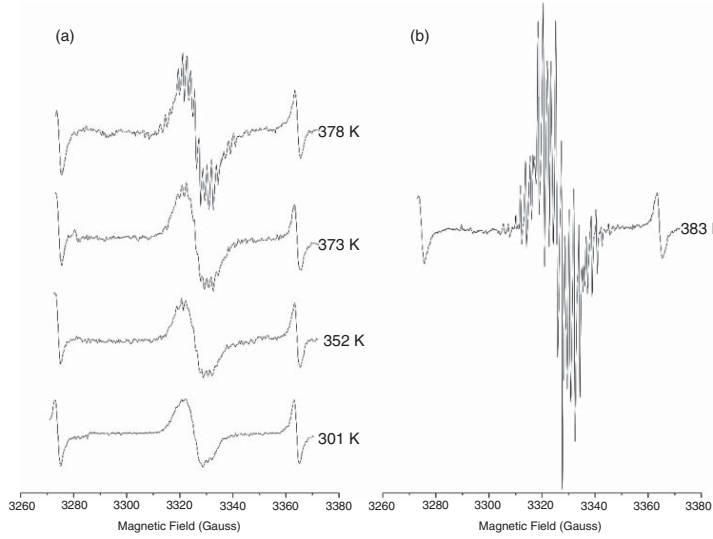

Figure 3.13 (a) ESR spectra of marine diesel (older sample) at 9.37 GHz in the temperature range from 301 to 378 K. (b) Resolved hf lines at 383 K. *Source:* Piccinato, Guedes, and Di Mauro (2009). Reproduced with permission of Springer.

was impossible to determine the interaction of a free electron with hydrogen atoms protons. At 383 K, the spectrum became very intensive (Figure 3.13b) exhibiting resolved lines.

The spectrum at 383 K was analyzed to determine the types of free radicals manifested in this experiment. The hf lines were superimposed over an unresolved line with linewidth of about 9 G, present in all spectra (Figure 3.13a), whose intensity also increased with temperature. In order to investigate only resolved hf lines, a single unresolved line (Figure 3.14a) was subtracted from the spectrum (Figure 3.14b).

The first attempt in the simulation, with WINEPR SimFonia Version 1.25 software of Bruker, was to consider a septet–quartet ESR spectrum attributed to the perinaphthenyl radical ($C_{13}H_9^{\bullet}$). However, this interpretation was not sufficient to reproduce the spectrum presented in Figure 3.14c, indicating the superposition with other groups of less intensive lines which could be due to phenalenyl radicals with different numbers of splitting protons (Zaitev *et al.*, 2006).

The investigation of the remaining lines in the ESR spectrum after subtraction of the first group of lines simulated (Figure 3.15a) revealed the need to add a second group of lines due to the interaction of five equivalent and strongly coupled protons (sextet) and the interaction of three weakly coupled protons (quartet) (Figure 3.15b). The chemical structure corresponding to this interaction is presented in Figure 3.16b. The sum of these two simulated groups (Figure 3.15a and b) reproduced all spectrum lines but not their intensities. The intensity problem was solved by the addition of a third group of lines due

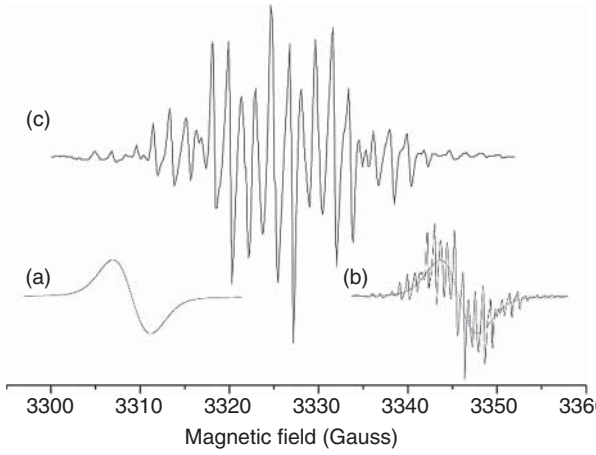

Figure 3.14 Spectra subtraction for analysis of ESR hf lines. (a) Unresolved line simulated by the software WINEPR SimFonia. (b) Overlap of the simulated spectrum and marine diesel spectrum at 383 K for subtraction of the unresolved line. (c) Result of the spectra subtraction.

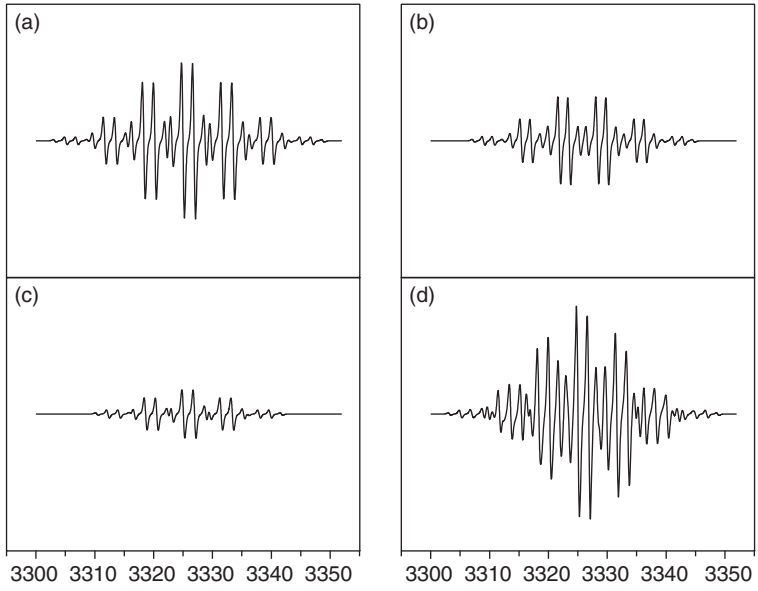

Figure 3.15 (a) Simulation of the septet-quartet ESR spectrum. (b) Simulation of the sextet-quartet ESR spectrum. (c) Simulation of the quintet–quartet spectrum. (d) Superposition of the septet–quartet, sextet–quartet, and quintet–quartet with weight percentages of the 53.5, 30.0, and 16.5%, respectively.

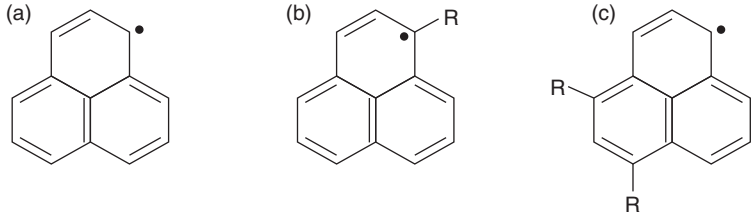

Figure 3.16 Structures of the phenalenyl radical (a) and phenalenyl derivatives (b and c).

to the interaction of four equivalent and strongly coupled protons (quintet) and the interaction of three weakly coupled protons (quartet) (Figure 3.15c) whose structure is presented in Figure 3.16c.

The superimposition of three groups of lines generates a set of lines shown in Figure 3.15d. The hf parameters (A and A') and weight percentages in the intensity of lines, used in the simulation of the three groups of lines, are presented in Table 3.1.

The superposition of experimental spectrum with the simulated spectrum, being this last with three paramagnetic species overlapped, is shown in Figure 3.17.

Table 3.1 hf parameters and weight percentages in intensity of the lines used in the simulation of lines groups.

Simulated spectrum	*A* (G)	*A′* (G)	Intensity (%)
septet-quartet	6.41 ± 0.03	1.82 ± 0.02	53.3
sextet-quartet	6.21 ± 0.03	1.64 ± 0.02	30.0
quintet-quartet	6.16 ± 0.03	1.83 ± 0.02	16.5

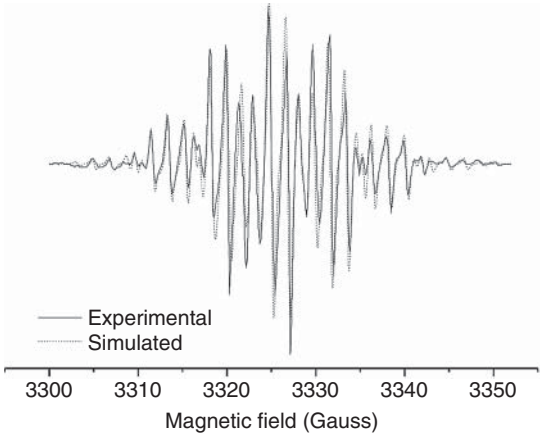

Figure 3.17 Superposition of theoretical model, with three groups of lines (dotted line), and experimental spectrum (solid line). *Source:* Piccinato, Guedes, and Di Mauro (2009). Reproduced with permission of Springer.

The proposed model of three overlapped paramagnetic species accurately reproduced the experimental lines. Three paramagnetic species, phenalenyl plus two of its derivatives, found after heating, indicate that the system (older marine diesel) somehow preserved the phenalenyl structure.

Because the paramagnetic species were overlapped in the same spectrum, apart from the difficulty of obtaining a high-resolution spectrum that allowed the observation of the splitting due to the functional group protons, it was impossible to identify the functional group that substituted the hydrogens atoms.

Spectra to paramagnetic species with different functional groups that substituted one hydrogen atom are presented in the literature (Rabold *et al.*, 1965; Lewis and Singer, 1969; Wain Drouin, and Compton 2006). The calculated hf coupling constants for the second lines group is in strong agreement with the values reported by Rabold *et al.* (1965) to the hydroxyperinaphthenyl radical.

Yamada and Toyoda (1973) observed the formation of the 4,6-dimethylperinaphthenyl radical when acenaphthylene dissolved in an inert solvent was heated up to 440 °C, resulting in the EPR spectrum splitting due to the methyl protons. The two methyl groups occupying two α-positions produce a spectrum similar to that of the third group (Figure 3.15c).

Despite the fact that it is impossible to describe the exact chemical transformations and the mechanisms involved in the appearance of magnetic species in marine diesel due to complexity of this oil by-product, the information provided by ESR spectroscopy, especially the hf coupling, allowed the modifications to be monitored and the type of free radical species observed in this oil during heating to be suggested. Thus, with organic molecule models, perinaphthenyl radicals are probably thermally recuperated by breaking the linkage formed in the dimer, and hydroxyperinaphthenyl and 4,5-dimethylperinaphthenyl radicals are the most likely phenalenyl derivatives yielded upon heating the marine diesel (Piccinato, Guedes, and Di Mauro, 2009).

3.5 ESR and Calculations on the Electronic Structure of Free Radicals in Oil By-Products

The ESR spectra do not provide direct access to the radical structure. Furthermore, the interpretation of the rich indirect information that can be inferred from the analyses of the experimental spectra is seldom straightforward, because of its dependence on the subtle interplay of several different effects (Improta and Barone, 2004). In the light of such findings, theoretical studies can be useful to support and supplement the experimental results.

The model proposed to explain the marine diesel spectrum (Piccinato, Guedes, and Di Mauro, 2009), with three superposed paramagnetic species, generates all lines of the ESR spectrum with great accuracy. However, with three overlapping spectra, it is impossible to observe hf splittings caused by any functional group that replaces the hydrogen of the perinaphthenyl structure. Faced with this difficulty, the density functional theory (DFT) method was used in the calculations on electronic structure of phenalenyl and phenalenyl-derivative radicals responsible for the composition of the ESR spectrum of marine diesel under heating, in order to obtain support for the experimental results. DFT has proven to be an accurate predictive tool not only for calculating the molecular geometries but also for the computation of hf coupling of organic radicals (Atanasov *et al.*, 2004; Munzarová, 2004; Maltar-Strmečki and Rakvin, 2012). The theoretical parameters calculated were the hf coupling constants, which were then used for comparison with the experimental data.

The predominant paramagnetic species in the spectra of marine diesel is the perinaphthenyl radical (Di Mauro, Guedes, and Piccinato, 2007; Piccinato, Guedes, and Di Mauro, 2009). The DFT to this molecule shows high symmetry, and the spin density on the hydrogen atoms, translated by hf coupling, is divided into two different interactions: with the nearest hydrogen atoms named the first-neighbor hf coupling constant (A) and with the farthest hydrogens atoms named the second-neighbor hf coupling constants (A'). The

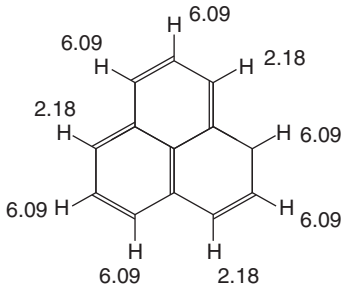

Figure 3.18 hf coupling constants in gauss for the hydrogen atoms of the perinaphthenyl radical obtained using DFT. *Source:* Piccinato *et al.* (2015). Reproduced with permission of John Wiley & Sons, Ltd.

Table 3.2 First- (*A*) and second-order (*A′)* hf coupling constants for the perinaphthenyl radical. *D* is the deviation between experimental and theoretical values.

	A **(G)**	**D (%)**	***A′*** **(G)**	**D (%)**
Theoretical (using UB3LYP/6-311+G(3df,3pd))	6.09 ± 0.00		2.18 ± 0.00	
Experimental: fresh sample	6.31 ± 0.01	3.6	1.80 ± 0.01	17.4
Experimental: after heating	6.41 ± 0.03	5.3	1.82 ± 0.02	16.5

Source: Piccinato *et al.* (2015).

hf coupling constant A is about the same for the six nearest hydrogen atoms and A' has practically the same value to the three farthest hydrogen atoms in the perinaphthenyl radical (Figure 3.18) (Piccinato *et al.*, 2015).

The mean values for the first-order (A) and the second-order (A') hf coupling constants are shown in Table 3.2.

In the table 3.2 there are two sets of ESR experimental parameters A and A' that were obtained for the perinaphthenyl radical in different situations: one for a fresh sample of marine diesel (Di Mauro, Guedes, and Piccinato, 2007) and one for an older sample that had been subjected to temperature variation (Piccinato, Guedes, and Di Mauro, 2009) (rows 3 and 4, Table 3.2). Independent of the experimental conditions, columns two and four of Table 3.2 show that the difference between the experimental and calculated values for A and A' is small, i.e. the experimental values show reasonable agreement with the calculated values. The computational values for A and A' were obtained for a molecule in a vacuum and no variation in temperature was considered. The best experimental values to compare with the calculated values were determined for a fresh experimental sample.

The second paramagnetic species proposed to form the experimental ESR spectrum of marine diesel was the hydroxyperinaphthenyl radical (Piccinato, Guedes, and Di Mauro, 2009). Although the perinaphthenyl radical is only

composed of carbon and hydrogen, in the hydroxyperinaphthenyl radical, one of the hydrogen atoms is replaced by the hydroxyl anion (OH^-). The presence of this functional group changes the molecule's symmetry and the hf interaction. On one side the ESR experimental parameters provide the interaction means between the unpaired electron and hydrogen atoms that compose the radical; however the computational calculations showed the unpaired electron interaction with each of the hydrogen atoms (Figure 3.19a). The presence of this anion also causes redistribution of the spin density on the hydrogen atoms, which modifies the values of the hf coupling constant. In the molecule in question, isotropy was not observed in the interaction of the unpaired electron with the hydrogen atoms, as previously observed for the perinaphthenyl radical (Piccinato *et al.*, 2015).

The last structure submitted to quantum calculus was the dimethylperinaphthenyl radical (Figure 3.19b). The replacement of two hydrogen atoms of the perinaphthenyl radical for two anions (CH_3^-) provides molecule symmetry C_{2v} and a new spin density distribution. The average value to hf coupling constants (A) and (A') to phenalenyl derivative radicals are in Table 3.3.

For all the radical structures, comparisons between the experimental and computational values for A and A' were performed with average values of unpaired electron interaction. The values calculated for the hf parameters using a chemical model (UB3LY/6-311 + G(3df, 3pd)) give results with a high degree of accuracy: the values differ at most 7% for A and 1.6% for A' to phenalenyl derivative radicals. Calculations regarding the electronic structure confirmed that the paramagnetic species proposed to compose the marine diesel ESR spectrum are adequate (Piccinato *et al.*, 2015).

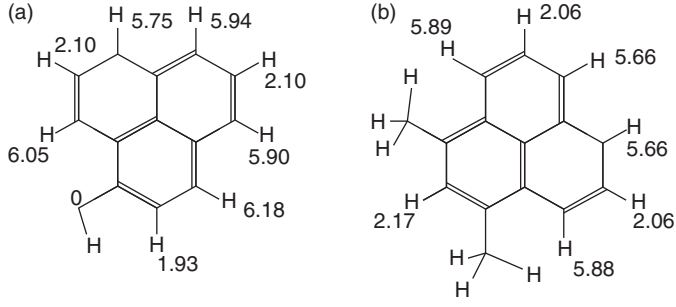

Figure 3.19 Structure optimized via DFT showing the values of the hf coupling constants of the hydrogen atoms. (a) Hydroxyperinaphthenyl radical. (b) Dimethylperinaphthenyl radical. *Source:* Piccinato *et al.* (2015). Reproduced with permission of John Wiley & Sons, Ltd.

Table 3.3 First- (*A*) and second-order (*A′*) hf coupling constants for the hydroxyperinaphthenyl and dimethylperinaphthenyl radicals. *D* is the deviation between experimental and theoretical values.

		A **(G)**	***D*** **(%)**	***A′*** **(G)**	***D*** **(%)**
hydroxyperinaphthenyl radical	Theoretical: UB3LYP/6-311+G(3df,3pd)	5.83 ± 0.05		1.66 ± 0.05	
	Experimental: after heating (older sample)	6.21 ± 0.03	6.5	1.64 ± 0.02	1.2
dimethylperinaphthenyl radical	Theoretical: UB3LYP/6-311+G(3df,3pd)	5.76 ± 0.07		1.80 ± 0.05	
	Experimental: after heating (older sample)	6.16 ± 0.03	6.9	1.83 ± 0.02	1.6

Source: Piccinato *et al.* (2015).

References

Alger, R. S. (1968) *Electron Paramagnetic Resonance: Techniques and Applications*, John Wiley & Sons, Inc, New York.

Atanasov, M., Baerends, E. J., Baettig, P., et al. (2004) The calculation of ESR parameters by density functional theory: the g- and A-tensors of co(acacen). *Chemical Physics Letters*, 399(4–6), 433–439.

Bandurski, E. (1982) Structural similarities between oil-generating kerogens and petroleum asphaltenes. *Energy Sources*, 6(1–2), 47–66.

Behar, F. and Pelet, R. (1985) Characterization of asphaltenes by pyrolysis and chromatography. *Journal of Analytical and Applied Pyrolysis*, 7(1–2), 121–135.

Behar, F., Pelet, R., and Roucache, J. (1984) Geochemistry of asphaltenes. *Organic Geochemistry*, 6, 587–595.

Bunce, N. J. (1987) Introduction to the interpretation of electron spin resonance spectra of organic radicals. *Journal of Chemical Education*, 64(11), 907–914.

Chandra, H., Symons, M. C. R., and Griffiths, D. R. (1988) Stable perinaphthenyl radicals in flints. *Nature*, 332(6164), 526–527.

Damsté, J. S. S., Eglinton, T. I., de Leeuw, J. W., and Schenck, P. A. (1989) Organic sulphur in macromolecular sedimentary organic matter: I: Structure and origin of sulphur-containing moieties in kerogen, asphaltenes and coal as revealed by flash pyrolysis. *Geochimica et Cosmochimica Acta*, 53(4), 873–889.

Di Mauro, E., Guedes, C. L. B., and Nascimento, O. R. (2005) Multifrequency (X-band to W-band) CW EPR of the organic free radical in petroleum asphaltene. *Applied Magnetic Resonance*, 29(4), 569–575.

Di Mauro, E., Guedes, C. L. B., and Piccinato, M. T. (2007) EPR of marine diesel. *Applied Magnetic Resonance*, 32(3), 303–309.

Du, J. L., Eaton, G. R., and Eaton, S. S. (1995) Temperature, orientation, and solvent dependence of electron spin-lattice relaxation rates for nitroxyl radicals in glassy solvents and doped solids. *Journal of Magnetic Resonance A*, 115(2), 213–221.

Durand, B. (1980) Sedimentary organic matter and kerogen. definition and quantitative importance of kerogen, in: *Kerogen: Insoluble Organic Matter from Sedimentary Rocks*, Technip, 13–34, Paris.

Forbes, M. D. E., Dukes, K. E., Myers, T. L., *et al.* (1991) Time-resolved electron-paramagnetic resonance spectroscopy of organic free-radicals anchored to SiO2 surfaces. *Journal of Physical Chemistry*, 95(26), 10547–10549.

Garif'ianov, N. S. and Kozyrev, B. M. (1956) Relaxation times T1 and T2 in anthracite. *Soviet Journal of Experimental and Theoretical Physics*, 3, 952.

Gerson, F. (1966) Notiz über das ESR: Spektrum des Phenalenyl-Radikals. *Helvetic Chimica Acta.*, 49(5), 1463–1467.

Gerson, F. and Huber, W. (2003) *Electron Spin Resonance Spectroscopy of Organic Radicals*. Wiley-VCH, Weinheim, Germany.

Goldman, S. A., Bruno, G. V., Polnaszek, C. F., and Freed, J. H. (1972) An ESR study of anisotropic rotational reorientation and slow tumbling in liquid and frozen media. *Journal of Chemical Physics*, 56(2), 716–735.

Guedes, C. L. B., Di Mauro, E., Antunes, V., and Mangrich, A. S. (2003) Photochemical weathering study of Brazilian petroleum by EPR spectroscopy. *Marine Chemistry*, 84(1), 105–112.

Guedes, C. L. B., Di Mauro, E., Campos, A., *et al.* (2006) EPR and fluorescence spectroscopy in the photodegradation study of Arabian and Colombian crude oils. *International Journal of Photoenergy*, 1, 1–6.

Guedes, C. L. B., Di Mauro, E., Mangrich, A. S. *et al.* (2001) Study of the photodegradation of oil by electronic paramagnetic resonance, in: *Série Ciência-Técnica-Petróleo, Seção Química, CD-R* 3 145–154. Available from http://www.uel.br/grupo-pesquisa/meioambiente/fotopetro/arquivos/artigos/0011.pdf.

Hicks, R. G. (2007) What's new in stable radical chemistry? *Organic & Biomolecular Chemistry*, 5(9), 1321–1338.

Hwang, J. S., Mason, R. P., Hwang, L. P., and Freed, J. H. (1975) Electron spin resonance studies of anisotropic rotational reorientation and slow tumbling in liquid and frozen media: III: Perdeuterated 2,2,6,6-tetramethyl-4-piperidone N-oxide and an analysis of fluctuating torques. *Journal of Physical Chemistry*, 79(5), 489–511.

Ikeya, M. (1993) *News Applications of Electron Spin Resonance*, World Scientific, Singapore.

Ikeya, M. and Furusawa, M. (1989) A portable spectrometer for esr spectrometry, dosimetry and dating. *International Journal of Radiation Applications and Instrumentation. Part A. Applied Radiation and Isotope*, 40(10–12), 845–850.

Improta, R. and Barone V. (2004) Interplay of electronic, environmental, and vibrational effects in determining the hyperfine coupling constants of organic free radicals. *Chemical Reviews*, 104(3), 1231–1253.

Janzen, E. G. (1969) Substituent effects on electron spin resonance spectra and stability of free radicals. *Accounts of Chemical Research*, 2(9), 279–288.

Larter, S. R. (1984) Application of analytical pyrolysis techniques to kerogen characterisation and fossil fuel exploration/exploitation, in: *Analytical Pyrolysis: Methods and Applications*, Butterworths, London, 212–275.

Lewis, I. C. and Singer, L. S. (1969) Carbonization of aromatic hydrocarbons. *Preprints of Papers: American Chemical Society, Division of Fuel Chemistry*, 13(4), 86–100.

Maltar-Strmečki, N. and Rakvin, B. (2012) Investigation of the nitrogen hyperfine coupling of the second stable radical in γ-irradiated L-alanine crystals by 2D-HYSCORE spectroscopy. *Journal of Magnetic Resonance*, 222, 81–87.

Montanari, L., Clericuzio, M., Del Piero, G., and Scott, R. (1998) Asphaltene radicals and their interaction with molecular oxygen: An EPR probe of their molecular characteristics and tendency to aggregate. *Applied Magnetic Resonance*, 14(1), 81–100.

Munzarová, M. L. (2004) DFT calculations of EPR hyperfine coupling tensors, in: Kaupp, M., Bühl, M., and Malkin, V. G. (eds), *Calculation of NMR and EPR Parameters: Theory and Applications*, Wiley-VCH Verlag GmbH and Co. KGaA, Weinheim, Germany, 461–482.

Orton, J. W. (1968) *Electron Paramagnetic Resonance*, IIiffe Books Ltd, London.

Owenius, R., Terry, G. E., Williams, M. J., *et al.* (2004) Frequency dependence of electron spin relaxation of nitroxyl radicals in fluid solution. *Journal Physical Chemistry B*, 108(27), 9475–9481.

Pelet, R., Behar, F., and Monin, J. C. (1986) Resins and asphaltenes in the generation and migration of petroleum. *Organic Geochemistry*, 10(1–3), 481–498.

Philp, R. P. and Gilbert, T. D. (1985) Source rock and asphaltene biomarker characterization by pyrolysis-gas chromatographymass spectrometry-multiple ion detection. *Geochimica et Cosmochimica Acta*, 49(6), 1421–1432.

Piccinato, M. T., Costa, M. F., Ota, A. T., *et al.* (2015) ESR and calculations on electronic structure of phenalenyl and phenalenyl derivative radicals. *Magnetic Resonance in Chemistry*, 53(2), 99–102.

Piccinato, M. T., Guedes, C. L. B., and Di Mauro, E. (2009) EPR characterization of organic free radicals in marine diesel. *Applied Magnetic Resonance*, 35(3), 379–388.

Poole, C. P. (1967) *Electron Spin Resonance: A Comprehensive Treatise on Experimental Techniques*, John Wiley & Sons, Inc., New York.

Rabold, G. P., Bar-Eli, K. H., Reid, E., and Weiss, K. (1965) Photochemically generated free radicals: I: The perinaphthenone system. *Journal of Chemical Physics*, 42(7), 2438–2447.

Reid, D. H. (1958) Stable π-electron systems and new aromatic structures. *Tetrahedron*, 3(3), 339–352.

Requejo, A.G., Gray, N.R., Freund, H., *et al.* (1992) Maturation of petroleum source rocks: 1. Changes in kerogen structure and composition associated with hydrocarbon generation. *Energy Fuels*, 6(2), 203–214.

Scott, R. and Montanari, L. (1998) Molecular structure and intermolecular interaction of asphaltenes by FI-IR, NMR, EPR, in: Mullins, O. C. and Sheu, E. Y. (eds), *Structures and Dynamics of Asphaltenes*, Plenum Press, New York, 79–113.

Senglet, N., Faure, D., Des Courières, T., *et al.* (1990) E.S.R. characterization of phenalenyl radicals in various fuel samples. *Fuel*, 69(2), 203–206.

Sogo, P. B., Nakazaki, M., and Calvin, M. (1957) Free radical from perinaphthene. *Journal of Chemical Physics*, 26(5), 1343–1345.

Tissot, B. P. and Welte, D. H. (1984) *Petroleum Formation and Occurrence*, Springer, New York.

Uebersfeld, J., Etienne A., and Combrisson, J. (1954) Paramagnetic resonance: A new property of coal-like materials. *Nature*, 174, 614.

Uesugi, A. and Ikeya, M. (2001) Electron spin resonance measurement of organic radicals in petroleum source rock containing transition metal ions. *Japanese Journal of Applied Physics: Part 1: Regular Papers Short Notes & Review Papers*, 40(4A), 2251–2254.

Wain, A. J., Drouin, L., and Compton, R. G. (2006) Voltammetric reduction of perinaphthenone in aqueous and non-aqueous media: An electrochemical ESR investigation. *Journal of Electroanalytical Chemistry*, 589(1), 128–138.

Yamada, Y. and Toyoda, S. (1973) An electron spin resonance study of the carbonization of acenaphthylene. *Bulletin of the Chemical Society of Japan*, 46(11), 3571–3573.

Yen, T. F., Erdman, J. G., and Saraceno, A. J. (1962) Investigation of the nature of free radicals in petroleum asphaltenes and related substances by electron spin resonance. *Analytical Chemistry*, 34(6), 694–700.

Zaitev, V., Rosokha, S. V., Head-Gordon, M., and Kochi, J. K. (2006) Steric modulations in the reversible dimerizations of phenalenyl radicals via unusually weak carbon-centered π- and σ-bods. *Journal of Organic Chemistry*, 71(2), 520–526.

Zheng, S., Lan, J., Khan, S. I., and Rubin, Y. (2003) Synthesis, characterization, and coordination chemistry of the 2-azaphenalenyl radical. *Journal of American Chemical Society*, 125(19), 5786–5791.

4

High-Field, Pulsed, and Double Resonance Studies of Crude Oils and their Derivatives

Marat Gafurov[1], M. Volodin[1,2], T. Biktagirov[1], G. Mamin[1] and S. B. Orlinskii[1]*

[1] *Kazan Federal University, Kremlevskaya, 18, Kazan, 420008, Russia*
[2] *Sakhalin Energy Investment Company, Ltd., Dzerzhinskogo, 35, Yuzhno-Sakhalinsk, 693020, Russia*

4.1 Introduction

A typical petroleum fluid can be considered as a petroleum disperse system (PDS): a hybrid of a solution and a colloidal dispersion (of crystallizing waxes, self-associating asphaltenes, etc.) (Syunyaev, 1980). Understanding the complex behavior of PDS is a challenge. Nevertheless, as stressed by Evdokimov, Eliseev, and Eliseev (2001, 2004), relatively simple experiments on only one of the PDS components can shed light on details of the structural features and transformations in such systems.

As one of the constituents of PDS, a paramagnetic phase can be the subject of interest: one gram of PDS contains 10^{16}–10^{21} paramagnetic centers (PCs) (Yen and Chilingarian, 1994, 2000). The majority of PC is concentrated in the high-molecular PDS components, such as asphaltenes, resins, and polycyclic aromatic hydrocarbons. The content of the high-molecular PDS components could reach the values of 45 wt% in native oils and up to 73 wt% in natural asphalts and bitumen. Assuming that asphaltenes and resins have a molecular weight of about 1000 Da (Yen and Chilingarian, 1994), they could contain up to one unpaired electron per molecule. Obviously, such a high concentration of PC should affect not only the paramagnetic properties of substance but (at least partially) also the other ones (the electrical qualities of PDS, for example). The analysis of the behavior of the intrinsic PC in PDS could complement the data obtained by other established analytical tools.

Figure 4.1 gives a brief look into the nature of some PCs in condensed matter. The existence of intrinsic PC in PDS is caused mainly by the presence of *d*-metals (first of all V, Ni, Fe) and stable "free" radicals (FR) in PDS. It is usually

*Corresponding author: volodinmikhail@yandex.ru

Analytical Characterization Methods for Crude Oil and Related Products, First Edition.
Edited by Ashutosh K. Shukla.

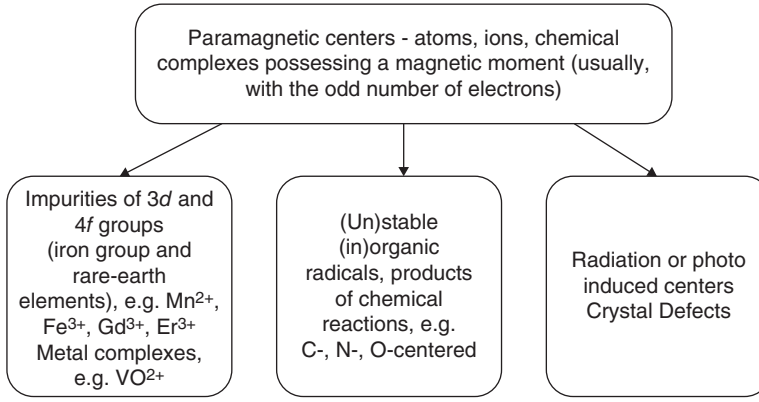

Figure 4.1 Types of paramagnetic centers.

assumed that FR in PDS are mainly concentrated in asphaltenes and arise due to the delocalized π-electrons of the aromatic rings and stable organic radicals of the side chains (Yen and Chilingarian, 1994, 2000). Here we have to note that the exact location and structure of FR in PDS are still undefined and the researchers are conventionally referred to the PC detected in coals (Yen and Chilingarian, 2000).

One of the most powerful methods to detect PCs, identify them, derive their concentrations, establish the structure of the paramagnetic complexes, etc. is the group of techniques of electron paramagnetic resonance (EPR) also named electron spin resonance (ESR). Figure 4.2 presents different modern

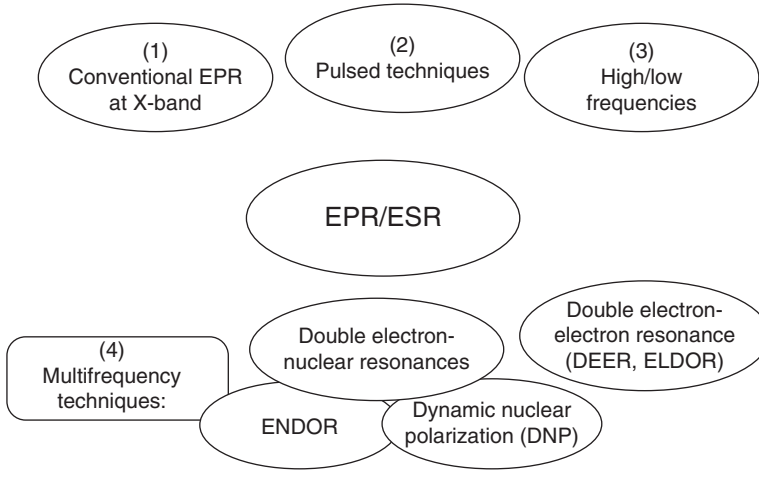

Figure 4.2 The variety of the modern commercially realized EPR techniques.
Source: Stoll and Schweiger (2006). Reproduced with permission of Elsevier.

commercially realized EPR techniques for material analysis that are also widely applied in biochemical/biomedical research (Qin and Warncke, 2015a, 2015b; Burlaka *et al.*, 2016). The reader will be acquainted with the most of them on particular examples in this manuscript. Surprisingly, the abilities of the modern EPR techniques are practically not known in oil-related research (at least so far as we can judge based on the analysis of the open sources). The overwhelming majority of EPR studies are still based on the application of routines of the conventional EPR at X-band with the microwave frequency of approximately 9 GHz (Piccinato, Guedes, and Di Mauro, 2012; Trukhan *et al.*, 2014; Wang *et al.*, 2016; Dolomatov *et al.*, 2016) that were established between the 1950s and 1970s (see Yen and Chilingarian, 1994; Garifyanov and Kozyrev, 1956; Gutowsky *et al.*, 1958; O'Reilly, 1958).

The last few years have seen an increased interest in studying unfractionated PDS by pulsed and high-frequency EPR (Ramachandran *et al.*, 2015; Tayeb Ben *et al.*, 2015; Mamin *et al.*, 2016; Gracheva *et al.*, 2016). One of the aims of this chapter is to show some applications of the "unconventional" EPR techniques and to encourage oil-related specialists to use different EPR approaches. This family of techniques does not face the problem of extraction and dilution of samples (in contrast to optical analysis, for example) and gives us the opportunity to probe the native structure and dynamical properties of PDS. Besides the higher sensitivity and spectral resolution, the advantages of the high-field EPR approaches for the identification of different paramagnetic complexes and their characterization in native oil containing formations are discussed here. For instance, in case of even slight anisotropy of magnetic interaction tensors (such as g and hyperfine tensors), high-field EPR approaches can provide the information about their orientation dependencies and thereby about the spatial structure of the paramagnetic complexes in disordered systems.

This work represents our particular vision based on our experience gathered so far, and does not pretend to be complete. This chapter presents only those experiments and data that were obtained at the Institute of Physics of Kazan Federal University in collaboration with other departments of Kazan Federal University and A. E. Arbuzov Institute of Organic and Physical Chemistry of Russian Academy of Sciences, Kazan, Russia.

4.2 EPR: Basic Principles and Magnetic Interactions

EPR is an effect of the resonant absorption of electromagnetic radiation by unpaired electrons placed in a constant magnetic field. Absorption starts when the frequency of an electromagnetic field coincides with the frequency of an electron's magnetic moment precession. Figure 4.3 demonstrates the reconstruction of the original experimental setup with which the EPR phenomenon was discovered by Evgeny K. Zavoisky in Kazan State University in 1944 (Zavoisky, 1945).

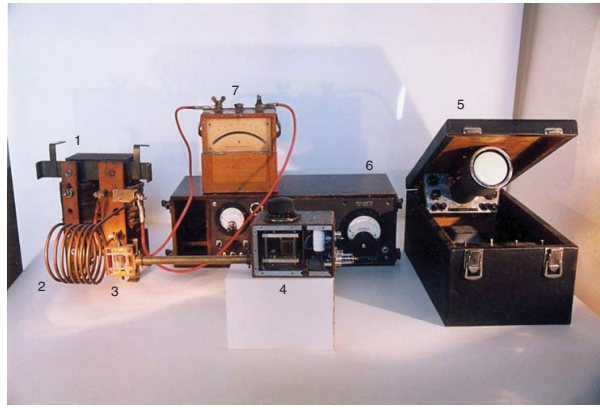

Figure 4.3 Reconstruction of the first EPR machine of E. K. Zavoisky operating at 10 MHz on which the first EPR spectrum in the world was observed in 1944. Courtesy of Igor Silkin, the keeper of E. K. Zavoisky Museum at Kazan Federal University. (1) Transformer. (2) Solenoid supplied by transformer and producing a low-frequency magnetic field that substituted constant magnetic field in this setup. (3) Ampoule with sample inserted into resonator–radio frequency coil, oriented perpendicular to solenoid axis. (4) Autodyne generator working at 10 MHz and signal preamplifier. (5) Oscilloscope. (6) A rheostat for adjusting the current through the transformer. (7) Ammeter used to control the magnetic field inside the solenoid, which is proportional to the alternating current value at the transformer's secondary coil.

Table 4.1 EPR microwave frequency bands with the corresponding wavelengths, energies, and typical magnetic fields for $g = 2$.

Band	Typical frequency, GHz	Wavelength, mm	Energy, cm^{-1}	Magnetic field at $g = 2$, T
L-band	1	300	0.03	0.03
S-band	3	100	0.1	0.11
X-band	9	33	0.3	0.32
Q-band	35	8, 5	1.2	1.25
W-band	95	3	3.2	3.4
G- (or J-) band	263	1	9.5	10.2

Today, the X-band machines (operating at the microwave frequency of ν = 9–10 GHz) are exploited routinely, though apparatus for other frequencies are available (see Table 4.1). Bruker Corporation holds the greatest global share of the production of EPR spectrometers (Bruker, 2016). However, for routine analysis and specific applications a lot of the producers can be found on the market: Adani, Freiberg Instruments (Magnettech), Yaviar, etc. (Adanisystems, 2016; Magnettech, 2016, Yaviar, 2016). The data presented in this manuscript have been obtained using Bruker ELEXSYS 680 (W-band, $\nu = 94$ GHz), Bruker ESP-300 and LABRADOR (both the X-band) EPR spectrometers. Figure 4.4

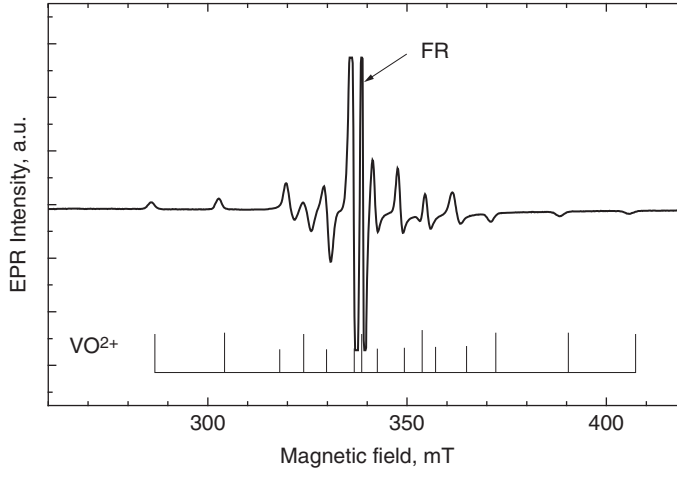

Figure 4.4 Typical EPR spectrum of crude oil sample at X-band at near room temperature.

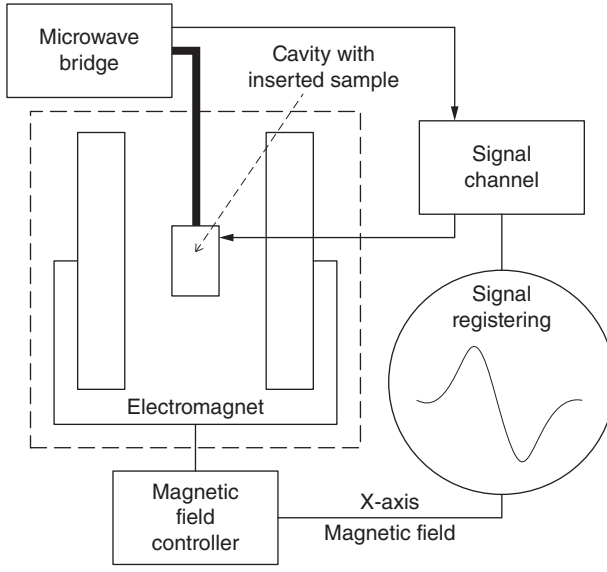

Figure 4.5 The simplified scheme of the conventional EPR spectrometer.

presents typical conventional EPR spectra of crude oil at room temperature (RT). As already mentioned, it is due to FR mainly localized within the polyaromatic condensed nuclei of the asphaltene molecules and VO^{2+} complexes and is discussed in detail below. Usually, the position/lineshape/intensity of the FR and VO^{2+} and the intensity ratio between the FR and vanadyl signals, which serve as the fingerprint of the hydrocarbon origin, are analyzed.

The core elements of the construction of the conventional EPR spectrometers are still the same as for Zavoisky's machine (see Figure 4.5). Typically, the PDS samples are placed in the quartz or glass tubes and then into the EPR cavity (see Figure 4.6). The simple microwave cavity is a metal box with a rectangular or cylindrical shape which resonates with microwaves. Cavity has the geometrical size of about the corresponding wavelength (see Table 4.1). The cavity is an analogue of LC circuit in nuclear magnetic resonance (NMR) and serves to store the microwave energy and to separate the electrical and magnetic components of electromagnetic field because the magnetic one causes the EPR transitions while the electrical component can cause an undesirable sample heating (Eaton *et al.*, 2010). As is shown in Figure 4.6, high-field machines require much less sample volume (of about 500 nL for W-band) that can be an advantage when the limited in amount species should be examined by different analytical methods, after different treatments, etc.

EPR often uses a technique known as phase sensitive detection to enhance the sensitivity of the spectrometer. In this approach the magnetic field

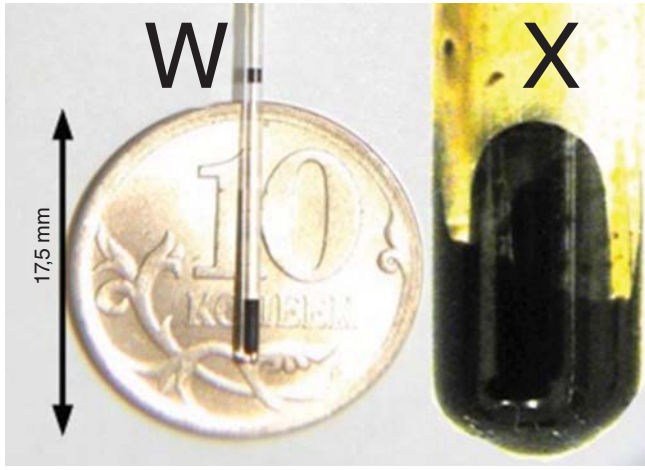

Figure 4.6 Commonly used EPR tubes for PDS samples in the W-band and X-band EPR spectrometers.

strength is modulated by sinusoidal signal with the amplitude of 0.1–1 mT and modulation frequency of about 10–100 kHz. It leads (as a rule) to the record of the first derivative curve of the EPR absorption signal, as shown in Figure 4.4, for example. Therefore, the concentration of the PC can be derived after the double integration of the recorded spectrum. The advantages are that it encodes the EPR signals to make it distinguishable from sources of noise or interference and provides the elimination of baseline instabilities due to the drift in DC electronics (Eaton *et al.*, 2010). In the pulsed mode (see Section 4.3), one can obtain a spectrum that is very often named field-swept electron spin echo (FS-ESE), which is usually close to the absorption spectrum. In some cases (for low-viscous crude oils, for example) low temperatures ($T < 250$ K) are necessary to slow down the electronic relaxation times to be able to obtain spin-echo or FS-ESE with the perceptible signal-to-noise ratio.

Both conventional and FS-ESE EPR spectra are sensitive to a number of interactions between the unpaired spin and the environment:

- the Zeeman interaction between the unpaired spin and the external magnetic field;
- the spin orbit coupling;
- the electron spin–nuclear spin interactions;
- the interaction with other unpaired electrons (spin–spin interaction).

The largest interaction in most cases (especially at W-band frequencies, see Table 4.1) and the one which EPR is based on is the Zeeman effect (see Figure 4.7). The essential aspects of EPR may be illustrated by considering the

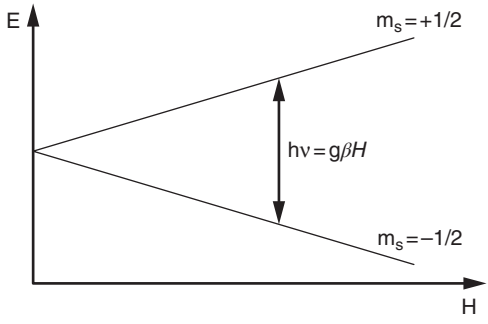

Figure 4.7 The Zeeman effect. An increasing magnetic field is applied in the presence of a fixed microwave frequency. When the resonance condition is reached (position of the arrow), an absorption occurs between the lower energy level (spin magnetic quantum number $m_s = -1/2$) and the upper energy level ($m_s = +1/2$). The energy difference is quantized and is equivalent to the term $g\beta H$.

hypothetical case of a single isolated electron. This electron is characterized by the quantum number $S = 1/2$ and possesses a magnetic moment

$$\overline{\mu}_s = g\beta\overline{S}, \tag{4.1}$$

where $g = 2.0023$ is the electron g-factor (that is sensitive to the spin–orbit interaction, chemical neighborhood of the unpaired electron and, consequently, to structure properties of sample material), $\beta = 9.274 \cdot 10^{-24}$ J·T^{-1}, the electronic Bohr magneton, and $\overline{S}$, the dimensionless electron spin vector. In a magnetic field, there are two energy states for this electron, as illustrated in Figure 4.7. Typical g-factors for PC in PDS are in the range of 1.96 (for VO^{2+}) up to 2.008 (sulfur-containing radicals), which implies the application of magnetic fields B of 0.35 T for X-band and of 3.5 T for W-band to match resonance condition. It implicates a use of superconducting magnets for high microwave frequencies.

Another interaction (commonly applicable to hydrocarbon systems) is the spin–nuclear one. As a nucleus could also have a magnetic moment, the interaction of the unpaired electron with the nucleus splits the electron energy levels, generating a structure called a hyperfine (hf) structure in the EPR spectrum. Each "m_s level" splits into a closely spaced group of $(2I + 1)$ levels, where I is the nuclear spin quantum number.

Only transitions are allowed with $\Delta m_S = \pm 1$ and $\Delta m_I = 0$. Each one of these transitions gives rise to a resonance line in the EPR spectrum. The spacing between the observed lines is the hf coupling constant (A). An analysis of hf splitting of EPR spectra among others again allows us to investigate the structure of the electron's neighborhood. Atoms in the vanadyl porphyrins ($^{51}V^{4+}$, $3d^1$, electronic spin $S = 1/2$, nuclear spin $I = 7/2$) are arranged practically in a plane defining thus the anisotropic g-factor and hf A tensor of axial symmetry (see Figure 4.8). The powder EPR spectrum of the vanadyl ions consists of the 16 "lines" representing the 2×8 hf patterns (the projection of I is allowed to take eight values: $\pm 7/2$; $\pm 5/2$; $\pm 3/2$; $\pm 1/2$) for the parallel and the perpendicular complex orientations (see Figure 4.4 and Figure 4.9).

Petroleum porphyrins in PDS exist in homologous manifolds of several structural classes that contain different types of substitutions and binding moieties. These determine the range of EPR parameters (especially $A_{\perp}$ and $A_{||}$) not only for different PDS samples but even within each of them.

4.3 EPR Pulse Sequences

Pulse methods are able to significantly increase and supplement information obtained from conventional EPR spectra (Schweiger and Jeschke, 2001). While stationary methods use continuous microwave irradiation and reveal splitting of energy levels of paramagnetic system, pulse techniques provide insights into the dynamics of the system and allows us to measure relaxation times, decode complex EPR spectra of several interacting PC, etc.

The main feature of the pulse EPR spectrometer is the presence of an additional pulse former device consequently connected with the microwave generator. As for most NMR spectrometers, the pulses could be applied using several channels. They can be combined into special sequences with the ability to change pulse duration and delays between them. But because the electronic relaxation times (longitudinal or spin-lattice relaxation time T_{1e} and transverse or spin-spin relaxation time T_{2e}) are of 3–6 orders of magnitude shorter than

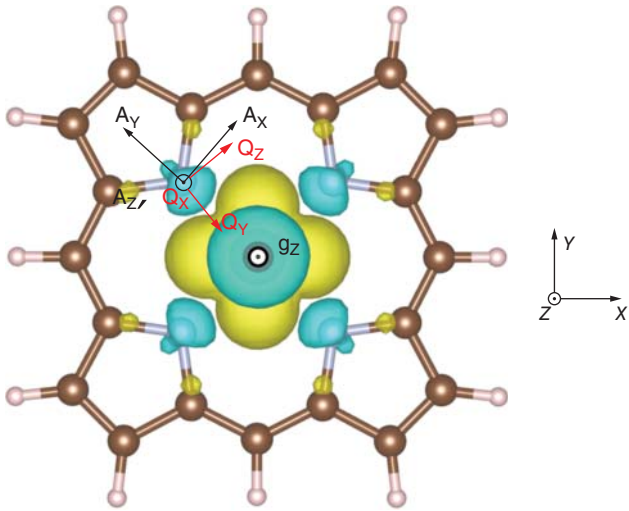

Figure 4.8 Schematic representation of a vanadyl porphyrin molecule backbone. The orientations of nitrogen hf (*A*) and quadrupole coupling (*Q*) tensors derived from DFT calculations are shown for a selected nuclei. Spatial distribution of spin density is visualized as an isosurface. X–Y–Z axes of the molecular frame are shown with the Z axis perpendicular to the porphyrin plane. As shown, the calculated g_z is collinear with the molecular Z axis.

the nuclear ones, the characteristic time parameters are also much shorter. The typical pulse sequences we use in our PDS-related research in the W-band are: (1) $\pi/2{-}\tau{-}\pi$ with the $\pi/2$ pulse duration of 32 ns and the time delay $\tau = 240$ ns to obtain electron spin echo (ESE); (2) T_{2e} is studied by tracking the primary ESE amplitude with the same $\pi/2{-}\pi$ pulse durations while varying τ with the minimal possible step of 4 ns; (3) T_{1e} is extracted from an inversion-recovery studies by applying the $\pi{-}T_{\text{delay}}{-}\ \pi/2{-}\tau{-}\ \pi$ pulse sequence, where π pulse

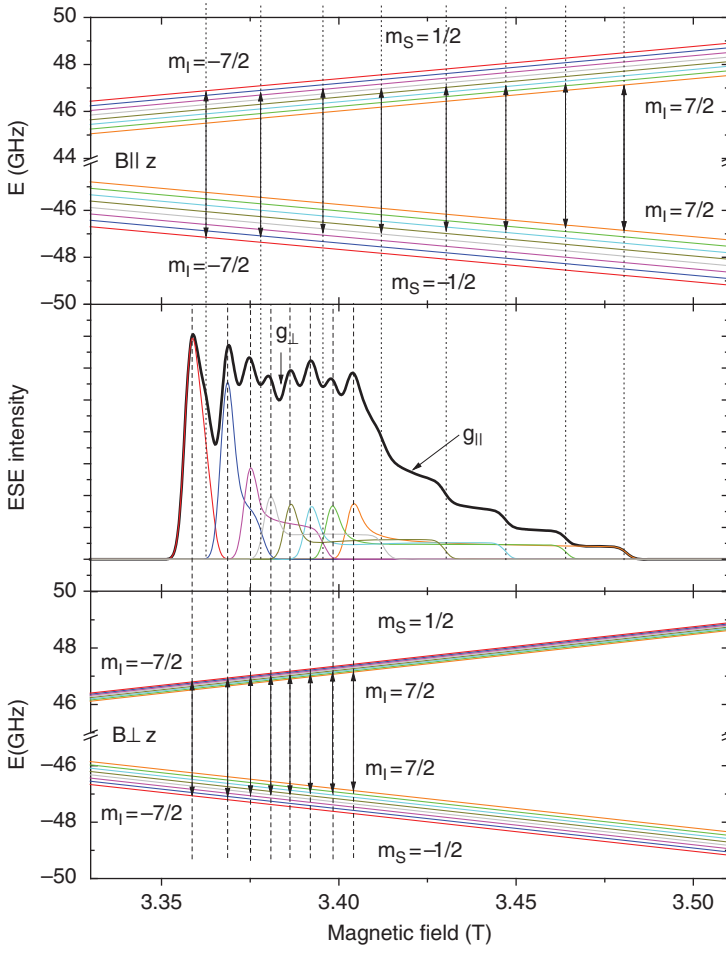

Figure 4.9 The energy levels and the corresponding absorption EPR spectrum for VO^{2+} complex calculated for the microwave frequency $\nu = 94$ GHz, $g_{||} = 1.963$, $g_{\perp} = 1.985$, $A_{||} = 470$ MHz, $A_{\perp} = 150$ MHz. Particular contributions from every EPR transition are color marked. Calculations are done in EasySpin package for Matlab (Stoll and Schweiger, 2006).

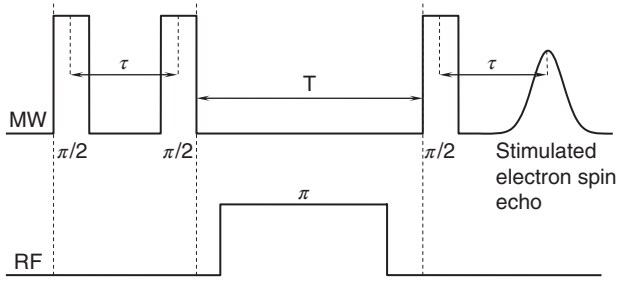

Figure 4.10 Mims pulse sequence at microwave and radio frequencies used to obtain the ENDOR spectra as a function of stimulated electron spin echo amplitude from the frequency of RF pulse.

duration and τ are fixed (64 ns and 240 ns, correspondingly) while T_{delay} is varied.

For electron nuclear double resonance (ENDOR) experiments we used special double (for nuclei and electron) cavities and Mims pulse sequence $\pi/2{-}\tau{-}\pi/2{-}T{-}\pi/2$ with an additional radio frequency (RF) pulse $\pi_{\text{RF}} = 16$ μs inserted between the second and third microwave $\pi/2$ pulses (see Figure 4.10). RF frequency in our setup could be swept in the range of 1–200 MHz.

Some ENDOR basics are briefly described below. One can find more details in the referenced works (Murphy and Farley, 2006; Yavkin *et al.*, 2014).

In the case of a "free" nucleus, RF pulse applied at the Larmor frequency

$$\nu_{Larmor} = |\gamma B_0| \equiv h^{-1}|g_I \beta_I B_0|, \tag{4.2}$$

where γ is a gyromagnetic ratio of the nuclear spin I, h is a Planck constant, g_I is a nuclear g-factor and β_I is a nuclear Bohr magneton, it can change the state of the nuclear spin (the population of the nuclear sublevels). For ^{1}H with $\gamma_{1\text{H}} =$ 42.576 MHz/T that results in $\nu_{Larmor} \approx 144.76$ MHz for $B_0 = 3.4$ T.

In the case of the coupled electron spin S such changing of the nuclear spin can modify the state of the electron spin (can change the population of the energy levels contributing to the EPR spectrum). For the hf coupling constant A and simple electron–nuclear coupling ($S = 1/2$, $I = 1/2$), it can lead to the appearance of the characteristic features in the ENDOR spectrum at the radio frequencies

$$\nu_{ENDOR} = \nu_{Larmor} \pm A/2 \quad \text{or} \tag{4.3}$$

$$\nu_{ENDOR} = A/2 \pm \nu_{Larmor}, \tag{4.4}$$

depending on the ratio between A and ν_{Larmor}.

The ENDOR splitting a_{ENDOR} can help not only to identify a type of nuclei coupled with the electron spins but also to provide spatial relationships between them. For the pure electron–nuclei dipole–dipole interaction in the

point model, the electron–nuclear distance r from the ENDOR splitting can be estimated from

$$a_{ENDOR} \approx g \cdot g_I \cdot (1 - 3\cos^2\theta)/r^3, \tag{4.5}$$

where g is a g-factor of electron spin S, Θ is an angle between directions of the parallel component of g ($g_{||}$) and B_0. As it follows from Equation 4.5, a_{ENDOR} depends on the distance between the electron and nuclear spins and their mutual orientation. In this work we consider ENDOR splitting due to the interaction of vanadyl electron spin and ^{1}H nuclear spins with $S = I = 1/2$ and with ^{14}N nuclear spins with $I = 1$. The values of B_0 at which the ENDOR spectra were measured were defined by the particular values of angle Θ (see Section 4.4).

Additionally, for $I = 1$ an electric nuclear quadrupole coupling exists that can split or shift the ENDOR lines: the nuclear quadrupole interaction is sensitive to the electric field gradient at the site of the nucleus.

4.4 Application Examples

4.4.1 W-Band, Relaxation Studies of VO^{2+} and FR in Asphaltenes Fractions

We have investigated 12 asphaltenes powders that were precipitated from the raw material of different oxidized bitumen and heavy crude oils from the oil refineries and oilfields of the Republic of Tatarstan (Russia) and Kazakhstan by the addition of the petroleum ether (bp 40–70 °C) using a Soxhlet apparatus. Then the filtered asphaltenes were washed out with the benzene, which was then evaporated. The obtained fraction is called A_{init}.

The *A1* and *A2* fractions of asphaltenes were obtained as follows (see Figure 4.11). One gram of A_{init} asphaltenes was first completely dissolved with

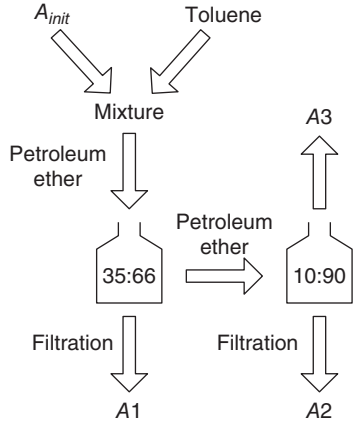

Figure 4.11 The scheme of fractionation of asphaltenes.

28 mL toluene. Petroleum ether (bp 40–70 °C) was then added in the amount of 52 mL. The resulting solution was kept in a dark place for 24 h and then filtered. Precipitated material was washed in a Soxhlet apparatus with toluene until the solvent became colorless, dried, and weighed until there was no change in its mass. The obtained fraction was called *A1*.

Then the petroleum ether was added to the supernatant in the amount of 228 mL and precipitated for 24 h. Using the operations described above, the fresh precipitated material was separated, washed with toluene in a Soxhlet apparatus, and dried. *A2* fraction of asphaltenes was recovered by evaporating the remaining solvent. The investigated samples are listed in Table 4.2.

Figure 4.12 demonstrates a typical FS-ESE detected EPR spectrum at T = 40 K and repetition time of 0.5 μs to intensify the VO^{2+} component of the spectrum. Small difference in the values of g-factors for FR and VO^{2+} allows them to be resolved spectrally and their relaxation times measured separately. The relaxation times were measured at the magnetic fields corresponding to the maximum of ESE signal (marked in Figure 4.12).

The relaxation constants in the T_{1e} processes of the longitudinal relaxation defined under an assumption of its monoexponential character for all the studied samples are presented in Figure 4.13. It can be seen that $T_{1\mathrm{FR}}$ is much longer than $T_{1\mathrm{VO}}$ and, in contrast to the vanadyl complexes, changes significantly from sample to sample and from fraction to fraction. Taking into account that the molecules forming the asphaltenes in both fractions *A1* and *A2* are of comparable size, the difference in the relaxation rates reflects the fact that the FR surrounding in fractions *A1* and *A2* is different while the same fractions' treatment does not change surrounding VO^{2+}. We suppose, therefore, that $T_{1\mathrm{FR}}$ and $T_{1\mathrm{VO}}$ measurements could be used to track the processes of polymerization, chemical or thermal treatments of PDS, etc., in which a role (as yet perhaps undefined, or even multiple roles) for PC is expected. Additional experimental and theoretical efforts are needed to increase our understanding of the main mechanisms defining the longitudinal relaxation in asphaltenes.

Transverse relaxation times of the vanadyl complexes in asphaltenes are also significantly shorter than those for FR, and in all the samples a single

Table 4.2 List of the studied samples.

Sample	Raw Material	Source	Investigated fractions of asphaltenes
# 1	Oxidized bitumen	Oil refinery #1	
# 2	Oxidized bitumen	Oil refinery #2	A_{init}, *A1*, *A2*
# 3	Crude oil	Russian oilfield	
# 4	Crude oil	Kazakhstan oilfield	

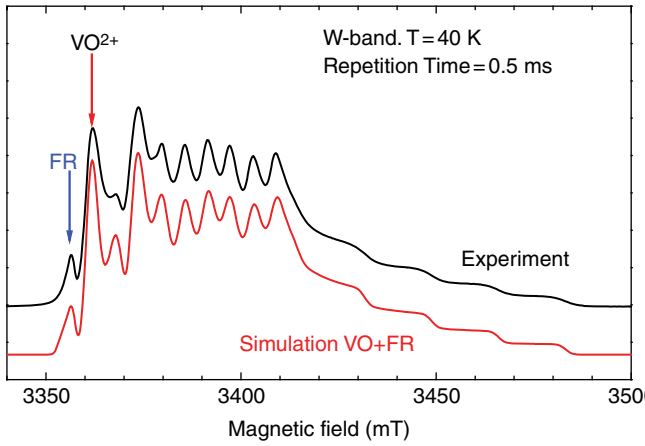

Figure 4.12 Typical W-band EPR spectrum of asphaltene fraction *A1* for sample #3 in pulsed mode at $T = 40$ K and repetition time of 0.5 μs along with its simulation as a sum of VO^{2+} powder spectra with $g_{||} = 1.964$, $g_{\perp} = 1.984$, $A_{||} = 16.8$ mT, $A_{\perp} = 6.0$ mT, and FR single line with $g = 2.0036$. Arrows FR and VO^{2+} mark the values of B_0 at which the electronic relaxation times were measured for "free" radical and vanadyl-porphyrins, correspondingly. Owing to the short repetition time, the amplitude of the FR signal is suppressed. Simulations are performed with the EasySpin package for Matlab (Stoll and Schweiger, 2006).

exponential decay of the transverse magnetization is observed with the time constants T_{2VO} within the range of 80–220 ns.

T_{2FR} magnetization curves look fancy – transverse relaxation character T_{2e} of FR deviates significantly from the exponential decay (see Figure 4.14) and are described nicely for all the investigated samples by the expression

$$I_{echo} = M_{FR} \cdot \exp\left(-\frac{2\tau}{T_{2FR}}\right) \cdot \exp\left(-m \cdot \tau^2\right), \tag{4.6}$$

where M_{FR} is a factor proportional to the concentration of FR, m is a parameter accounting for the spectral diffusion. From the analysis of relaxation times it was shown (Mamin *et al.*, 2016) that the obtained acceleration of T_{2FR} according to Equation 4.6 is caused by the spectral diffusion induced by the presence of the vanadyl porphyrin molecules in the nearest (1–3 nm) surrounding of FR. This finding can explain, for example, the fact of low polarization of FR in dynamic nuclear polarization experiments for some PDS (Alexandrov *et al.*, 2014); though the electronic relaxation times for FR are significantly longer, owing to the strong dipole–dipole FR–VO^{2+} coupling the electronic spin polarization "leaks" through the fast relaxing VO^{2+}. This finding, in our opinion, brings us one step closer to disentangling the structure of asphaltenes and the role of vanadyls in that disentangling.

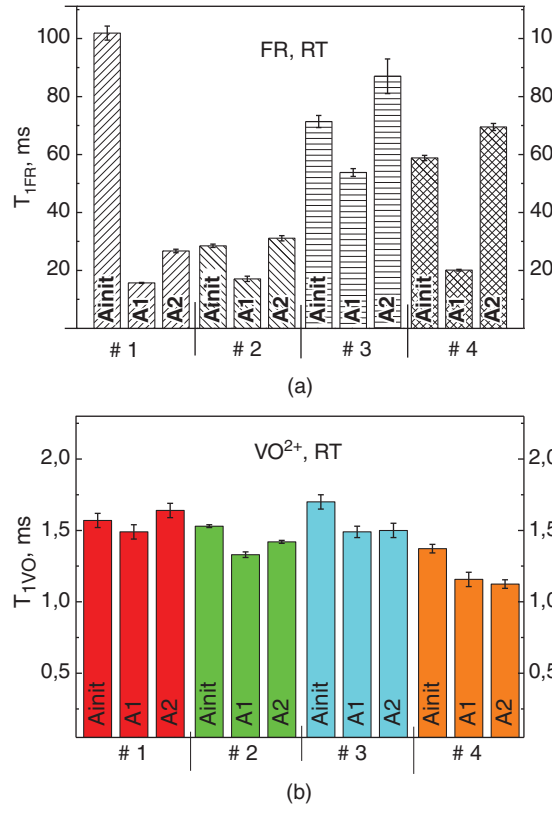

Figure 4.13 FR (a) and VO^{2+} (b) longitudinal relaxation times T_{1e} at RT for all the investigated samples.

Such "acceleration" of T_{2FR} was not reported in the literature and was not obtained by us in the X-band relaxation measurements. We connect this fact with the overlapping of FR and VO^{2+} spectra at lower frequencies (see Figure 4.4 and Section 4.2).

We have shown (Volodin *et al.*, 2013) that relaxation times, as well as intensity ratios between the FR and VO^{2+} signals (which can be determined much more accurately at high fields), can be exploited as additional parameters to characterize the origin of the crude oil and nature of the oil's PC. Indeed, concerning FR in the X-band and the lower magnetic fields, its EPR spectrum in most cases presents a single line with the linewidth of $\Delta H_{pp} = 0.4–0.7$ mT located at g-factor of 2.003 ± 0.001 (Yen, 1994, 2000; Dolomatov *et al.*, 2016). FR lineshape is neither Gaussian nor Lorentzian but a mixture of both. The non-symmetric FR spectrum, obtained in some PDS at high fields (Volodin *et al.*, 2013), could be due to the presence of two or more PCs of different origins with the close values of g-factors and/or due to the small anisotropy of g-factors.

Our experience with different PDS species proves that FR spectra in pulsed mode resemble the powder (anisotropic) spectra, they differ from each other,

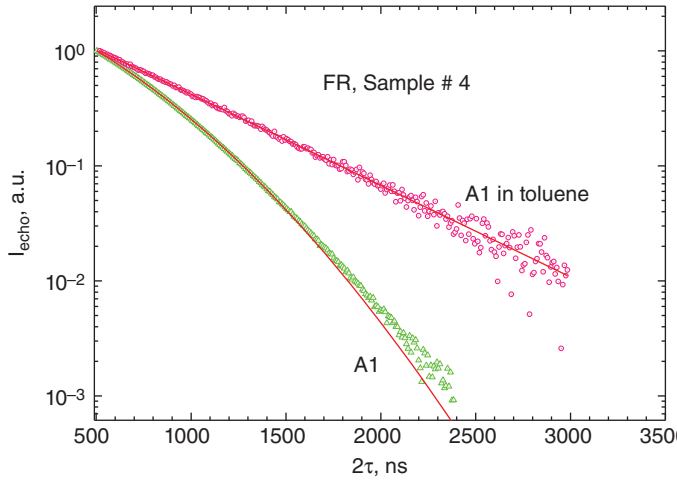

Figure 4.14 Dependencies of the primary ESE amplitude (semilog plot) on the delay τ between the two MW pulses in the pulse sequence of the sample #4 (fraction *A1*) for FR at RT. Symbols indicate the experimental data, solid lines are the results of the fits corresponding to Equation 4.6 with $m = 0$ for the fraction *A1* diluted in toluene (upper curve) and with $m = 3.6 \cdot 10^{-6}$ ns^{-2} for the undiluted fraction *A1* (lower line).

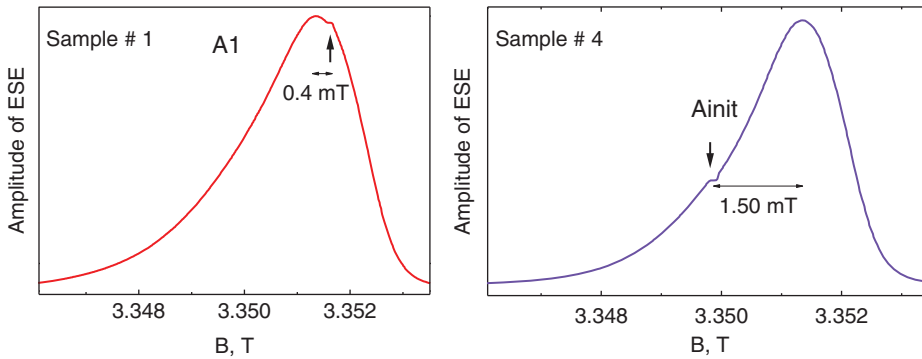

Figure 4.15 Examples of FS-ESE EPR spectra for two fractions from different samples. Splitting between the EPR features (local maxima) are shown.

and very often are split (or additional peaks appear) as Figure 4.15 shows. T_{2e} varies along the FR line. Apparently, the obtained features will be further exploited to unravel the FR nature(s).

4.4.2 ENDOR of VO^{2+} in Crude Oil Samples

There is no exclusive procedure for the isolation of porphyrin complexes from the host material (Yakubova *et al.*, 2016). Presently, one of the most promising and well-established protocols for structural characterization of

metalloporphyrins involves the application of Fourier transform ion cyclotron resonance mass spectrometry (Qian *et al.*, 2008; Zhao *et al.*, 2013, 2014; Putman *et al.*, 2014). Owing to the relatively low concentration of vanadium compounds and the very complex chemical composition of PDS, the successful identification of porphyrins requires chromatographic separation or demetalation.

The ENDOR method can complement mass spectrometry and become a part of a standard analytical toolkit. Since it does not require a special sample preparation procedure, it can be, at the very least, useful for the preliminary characterization of PDS prior to chromatographic separation.

The heavy and light crude oil samples from different oilfields (see Table 4.3) were used as received without any additional sample treatment. Figure 4.16 presents the field-swept pulsed EPR spectra of a heavy oil sample #1 detected at X- and W-bands. Figure 4.17 shows the corresponding ENDOR spectra for

Table 4.3 Samples and their physical properties at RT.

Sample	Description	Origin	Density, kg/m^3/ API gravity	Viscosity, mPa·s
#1	Heavy	Mordovo-Karmalskoye oilfield (Republic of Tatarstan, Russia)	945 / 18.2	1020
#2	(Medium) Light	The West-Siberian petroleum basin (Russia)	871 / 31	38

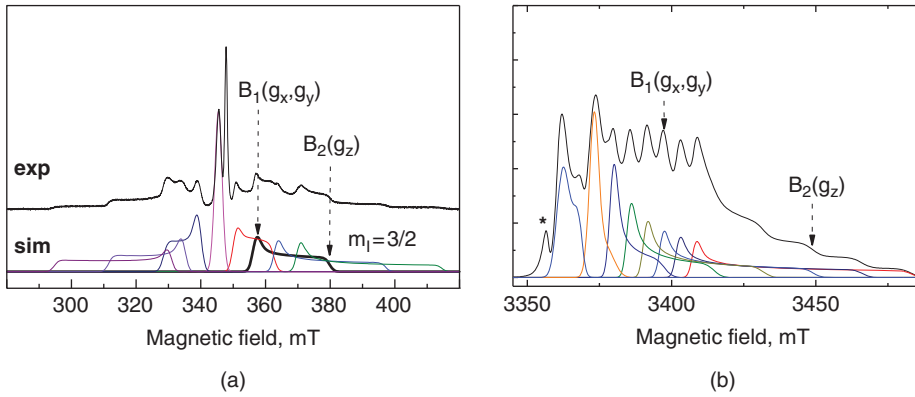

Figure 4.16 (a) X-band and (b) W-band EPR spectra at $T = 50$ K in crude oil sample #1 in pulse mode shown together with separate simulations of the different hf components due to ^{51}V nucleus. Magnetic fields B_1 and B_2 correspond to the g_Z axis parallel and perpendicular to the direction of magnetic field ($m_I = 3/2$). The signal with a *g*-factor of 2.004 related to FR is marked by an asterisk.

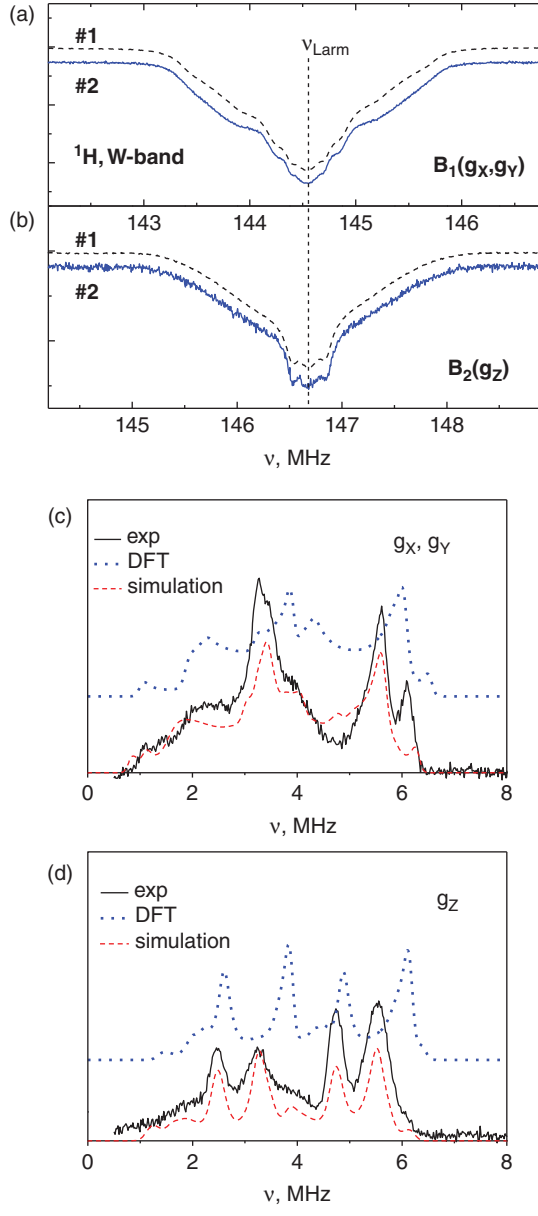

Figure 4.17 (a, b) ^{1}H Mims ENDOR spectra corresponding to different molecular orientations of vanadyl porphyrin detected in the vicinity of proton Larmor frequency at $T = 50$ K for samples #1 and #2. (c, d) ^{14}N ENDOR spectra of vanadyl porphyrins (solid curve) in X-band for crude oil samples #1, simulation (dashed curve) and calculated spectrum with parameters obtained by DFT calculations (dotted curve) at magnetic field B_1, and at magnetic field B_2. Corresponding parameters are listed in Table 4.4.

two particular values of the external magnetic field. In this work we have chosen the values that correspond mainly to the g_Z axis perpendicular (B_1) and parallel (B_2) to the direction of magnetic field for $m_I = 3/2$ transition, for the following reasons: (1) sufficient echo amplitudes to obtain reasonable signal-to-noise ratio for an appropriate amount of time; (2) absence of overlapping with the FR signal. As a result, we report observation of the ENDOR signals near the Larmor frequency of ^{1}H and ^{14}N, as displayed in Figure 4.17.

We have managed to detect for the first time pulsed ^{14}N ENDOR spectra of natural vanadyl porphyrins in the untreated heavy crude oil sample. The measured ^{14}N ENDOR spectra display the presence of both nuclear hf and electric nuclear quadrupole couplings. In order to get some prior information about the values and orientations of the corresponding interaction tensors, we have performed first-principles density functional theory (DFT) calculations (Gracheva *et al.*, 2016) on high-performance computing (HPC) clusters for complex and demanding calculations at Kazan Federal University. The results of these calculations are listed in Table 4.4 and presented in Figure 4.17. The data correspond well with those obtained from the model systems (Gracheva *et al.*, 2016).

It is known that petroleum porphyrins exist in homologous manifolds of several structural classes and can manifest great structural diversity (Gilinskaya, 2008). First of all that means different combinations of side groups. The distribution of the electric field gradient and spin density in a vanadyl porphyrin molecule can be affected by the presence of substituting

Table 4.4 Comparison between spin Hamiltonian parameters of vanadyl porphyrin complex in natural crude oil obtained from the simulation of the experimental EPR and ^{14}N ENDOR spectra and calculated by DFT method ones for VO molecule*.

	Simulation of experimental data	**DFT (VO)**
$g_X\ g_Y\ g_Z$	(1.9845 1.9845 1.9640)	(1.9867 1.9867 1.9710)
^{51}V $A_X\ A_Y\ A_Z$	|156.9 156.9 470.8|	(–157.0 –157.0 –463.9)
^{14}N $A_X\ A_Y\ A_Z$	–6.5 –7.4 –7.8	(–7.6 –7.8 –8.6)
$(\alpha\ \beta\ \gamma)_A$	(90 0 0)	(–3 10 55)
e^2Qq/h	2.2	2.24
η	0.50	0.22
$(\alpha\ \beta\ \gamma)_Q$	(30 90 180)	(40 90 –172)

*Hyperfine couplings tensor components $A_{X,Y,Z}$ and quadrupole coupling constant e^2Qq/h are in MHz. For ^{14}N coupling parameters the values are averaged over the four pyrrole nitrogen nuclei. For VO models, the variance of both hf and quadrupole coupling constants is within 0.1%. The Euler angles ($\alpha\ \beta\ \gamma$, in deg) are presented for a selected ^{14}N nucleus and specify *Z-Y-Z* rotation that transforms the molecular frame with the Z axis being perpendicular to the porphyrin plane to the frames where the hf (A) and quadrupole (Q) tensors for ^{14}N are diagonal. The coupling tensors for other three ^{14}N nuclei are consistent with C_{4v} symmetry of the molecule.

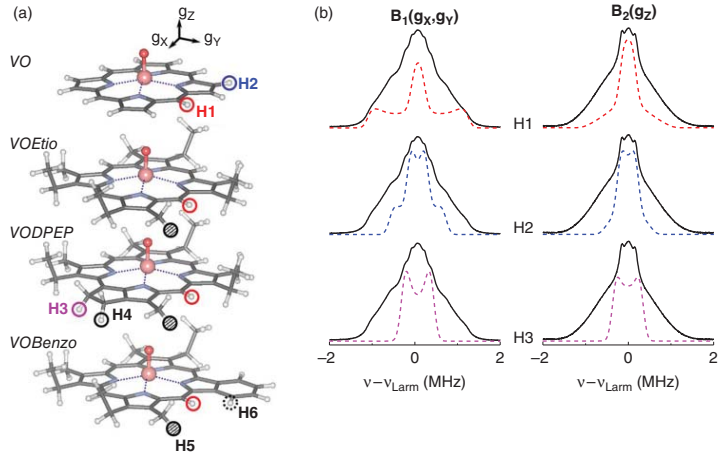

Figure 4.18 (a) Optimized chemical structures of vanadyl porphyrin models (*VO, VOEtio, VODPEP, VOBenzo*). Circles indicate the positions of the representative protons of the porphyrin skeleton (H1 and H2) and those attributed to the possible classes of side groups (H3–H6). The illustrated orientation of the *g*-tensor corresponds to the VO molecule. (b) ENDOR spectra simulated (dashed curve) for the selected protons are presented in comparison with the experimental spectra obtained for sample (solid curve).

side groups via structural perturbations of the porphyrin skeleton, thereby reducing the symmetry of pyrrole nitrogen atoms distribution around the vanadium ion. The consequent distribution of the coupling parameters can potentially increase the broadening of the spectrum, and this is probably why ^{14}N ENDOR cannot be observed in certain (or in most) oil samples. Following the discussion in Gilinskaya (2008), we propose that the possibility to detect ^{14}N ENDOR depends on the relative presence of particular forms of vanadyl porphyrins in the sample. Further experimental studies and calculations are in progress.

From the pattern of ^{1}H splittings in ENDOR spectra it is possible to infer the chemical composition of vanadyl porphyrin molecules in the studied samples (see Figure 4.18). We report observation of the reproducible pattern of hf splitting in the ^{1}H ENDOR spectra of vanadyl. We can attribute the resolved spectroscopic features to the particular positions of the protons in the porphyrin molecule. FR ENDOR studies are on the way and we hope they will shed light on the asphaltene's structure.

4.5 Conclusion

In this chapter we tried to show some capabilities of the pulsed and high-field EPR for the analysis and investigation of PDS. We hope that further research will shed light on more details of PDS dynamics and structure.

Acknowledgments

We are thankful to A. Rodionov, D. Sitdikov, A. Vakhin, A. Galukhin, Yu. Ganeeva, and T. Yusupova (Kazan, Russia) for help with the measurements and sample preparations. The main part of the research was financially supported by the Russian Ministry of Education and Science in the framework of the "5-100" Program for Kazan Federal University.

References

Adanisystems.com (2016) Adani Benchtop Analytical Instruments and Spectroscopy Official Website. Available at: http://lab.adanisystems.com.

Alexandrov, A., Archipov, R., Ivanov, A., *et al.* (2014) The low-field pulsed mode dynamic nuclear polarization in the pentavalent chromium complex and crude oils. *Appl. Magn. Reson.*, 45(10), 1275–1287.

Bruker.com (2016) Bruker Official Website. Available at: http://bruker.com.

Burlaka, A., Gafurov, M., Iskhakova, K., *et al.* (2016) Electron paramagnetic resonance in the experimental oncology: Implementation examples of the conventional approaches. *BioNanoScience*, 6(4), 431–436.

Dolomatov, M. U., Rodionov, A. A., Gafurov, M. R., *et al.* (2016) Concentration of paramagnetic centres at low-temperature thermal destruction of asphaltenes of heavy petroleum distillates. *Magn. Reson. Solids*, 18, Article No. 16101. Available at: http://mrsej.kpfu.ru/contents.html#16101.

Eaton, G., Eaton, S., Barr, D., and Weber, R. (2010) *Quantitative EPR*. Springer-Verlag, Vienna.

Evdokimov, I., Eliseev, N., and Eliseev, D. (2001) Rheological evidence of structural phase transitions in asphaltene-containing petroleum fluids. *J. Petrol. Sci. Eng.*, 30(3–4), 199–211.

Evdokimov, I., Eliseev, N., and Eliseev, D. (2004) Effect of asphaltenes on the thermal properties of emulsions encountered in oil recovery operations. *Fuel*, 83(7–8), 897–903.

Garifyanov, N. and Kozyrev, B. (1956) Paramagnetic resonance in anthracite and other carbon containing materials. *ZheTF*, 30(2), 272–276.

Gilinskaya, L. (2008) EPR spectra of V (IV) complexes and the structure of oil porphyrins. *Journ. Struct. Chem.*, 49, 245–254.

Gracheva, I, Gafurov, M., Mamin, G., *et al.* (2016) ENDOR study of nitrogen hyperfine and quadropole tensors in vanadyl porphyrins of heavy crude oils. *Magn. Reson. Solid*s, 18, Article No. 16102. Available at: http://mrsej.kpfu.ru/contents.html#16102.

Gutowsky, H., Roger Ray, B., Rutledge, R., and Unterberger, R. (1958) Carbonaceous free radicals in crude petroleum. *J. Chem. Phys.*, 28, 744–745.

Magnettech.de (2016) Magnettech Gmbh Official Website. Available at: http://magnettech.de.

Mamin, G., Gafurov, M., Yusupov, R., *et al.* (2016) Toward the asphaltene structure by electron paramagnetic resonance relaxation studies at high fields (3.4 T). *Energy Fuels*, 30 (9), 6942–6946.

Murphy, D. and Farley, R. (2006) Principles and applications of ENDOR spectroscopy for structure determination in solution and disordered matrices. *Chem. Soc. Rev.*, 35, 249–268.

O'Reilly, D. (1958) Paramagnetic resonance of vanadyl etioporphyrin I. *J. Chem. Phys.*, 29(5), 1188–1189.

Piccinato, M., Guedes, C., and Di Mauro, E. (2012) Crude oil by EPR, in: *Crude Oil Emulsions: Composition Stability and Characterization*, Abdel-Raouf, M. (ed.), Rijeka, Croatia: InTech, 147–168.

Putman, J., Rowland, S., Corilo, Y., and McKenna, A. (2014) Chromatographic enrichment and subsequent separation of nickel and vanadyl porphyrins from natural seeps and molecular characterization by positive electrospray ionization FT-ICR mass spectrometry. *Analytical Chemistry*, 86(21), 10708–10715.

Qian, K., Mennito, A., Edwards, K., and Ferrughelli, D. (2008) Observation of vanadyl porphyrins and sulfur-containing vanadyl porphyrins in a petroleum asphaltene by atmospheric pressure photonionization Fourier transform ion cyclotron resonance mass spectrometry. *Rapid Communications in Mass Spectrometry*, 22(14), pp 2153–2160.

Qin, P. and Warncke, K. (2015a) Electron paramagnetic resonance investigations of biological systems by using spin labels, spin probes, and intrinsic metal ions: Part A. *Methods in Enzymology*, 563, 2–684.

Qin, P. and Warncke, K. (2015b) Electron paramagnetic resonance investigations of biological systems by using spin labels, spin probes, and intrinsic metal ions: Part B. *Methods in Enzymology*, 564, 2–613.

Ramachandran, V., van Tol, J., McKenna, A., *et al.* (2015) High field electron paramagnetic resonance characterization of electronic and structural environments for paramagnetic metal ions and organic free radicals in Deepwater Horizon oil spill tar balls. *Anal. Chem.*, 87(4), 2306–2313.

Schweiger, A. and Jeschke, G. (2001) *Principles of Pulse Electron Paramagnetic Resonance*. Oxford University Press, Oxford.

Stoll, S. and Schweiger, A. (2006) EasySpin, a comprehensive software package for spectral simulation and analysis in EPR. *J. Magn. Reson.*, 178, 42–55.

Syunyaev, Z. (1980) Concentration of complex structural units in disperse petroleum systems and methods for regulation of this concentration. *Chemistry and Technology of Fuels and Oils*, 16(7), 484–489.

Tayeb Ben, K., Delpoux, O., Barbier, J., *et al.* (2015) Applications of pulsed electron paramagnetic resonance spectroscopy to the identification of vanadyl complexes in asphaltene molecules: Part 1: Influence of the origin of the feed. *Energy Fuels*, 29(7), 4608–4615.

Trukhan, S., Yudanov, V., Gabrienko, A., *et al.* (2014) In situ electron spin resonance study of molecular dynamics of asphaltenes at elevated temperature and pressure. *Energy Fuels*, 28(10), 6315–6321.

Volodin, M., Mamin, G., Izotov, V., and Orlinskii, S. B. (2013) High-frequency EPR study of crude oils. *J. Phys. Conf. Ser.*, 478, Art. No. 012003.

Wang, W., Ma, Y., Li, S., *et al.* (2016) Effect of temperature on the EPR properties of oil shale pyrolysates. *Energy Fuels*, 30(2), 830–834.

Yakubova, M., Milordova, D., Yakubova, S., *et al.* (2016) Features of the composition of vanadyl porphyrins in the crude extract of asphaltenes of heavy oil with high vanadium content. *Petroleum Science and Technology*, 34(2), 177–183.

Yaviar.ru (2016) Yaviar, Ltd. Official Website. Available at: http://yaviar.ru/produktsiya/spektrometry.

Yavkin, B., Mukhambetov, I., Lamberov, A., and Orlinskii, S. B. (2014) Electron paramagnetic resonance and electron nuclear double resonance study of the paramagnetic complexes of anthraquinone on the surface of γ-Al2O3. *Journal of Physical Chemistry C*, 118(27), 14998–15003.

Yen, T. and Chilingarian, G. (1994) *Asphaltenes and Asphalts: 1: Developments in petroleum science: 40A*, Elsevier, New York.

Yen, T. and Chilingarian, G. (2000) *Asphaltenes and Asphalts: 2: Developments in petroleum science: 40 B*, Elsevier, New York.

Zavoisky, E. (1945) Paramagnetic relaxation of liquid solutions for perpendicular fields. *Journal of Physics (Academy of Sciences of the USSR)*, 9(3), 211–216.

Zhao, X., Liu, Y., Xu, C., *et al.* (2013) Separation and characterization of vanadyl porphyrins in Venezuela Orinoco heavy crude oil. *Energy Fuels*, 27(6), 2874–2882.

Zhao, X., Shi, Q., Gray, M., and Xu, C. (2014) New vanadium compounds in Venezuela heavy crude oil detected by positive-ion electrospray ionization Fourier transform ion cyclotron resonance mass spectrometry. *Scientific Reports*, 4. Art. No 5373.

5

NMR Spectroscopic Analysis in Characterization of Crude Oil and Related Products

Siavash Iravani

Faculty of Pharmacy and Pharmaceutical Sciences, Isfahan University of Medical Sciences, Isfahan, Iran

5.1 Introduction

In general, nuclear magnetic resonance (NMR) spectroscopy is a very important technique in the study of heavy petroleum fractions, and has been suggested as one of the most powerful techniques for laboratory and industrial analysis. This analytical method can be used in the study of the chemical composition of petroleum and in the characterization of petroleum fractions in a short time. Great analysis in only a few minutes per stream can be done in a continuous and online way. Moreover, it has the ability to analyze dark and opaque samples, such as crude samples. Crude oil, shale oil, and sand oil are all sources of petroleum and comprise masses of compounds whose components can be grouped into four essential instructions: (a) saturates (alkanes and cycloparaffins), (b) aromatics (mono-, di-, and polynuclear fragrant hydrocarbons with alkyl side chains), (c) resins (aggregates with a large number of building blocks which includes sulfoxides, amides, thiophenes, pyridines, quinolines, and carbazoles), and (d) asphaltenes (aggregates of prolonged polyaromatics, naphthenic acids, sulfides, polyhydric phenols, fatty acids, and metalloporphyrins) (Rudzinski and Aminabhavi, 2000). In fact, there are some important advantages and disadvantages regarding this analytical technique (Rudzinski and Aminabhavi, 2000; Silva, *et al.*, 2011).

The advantages are a reduction in the time taken for the analysis, and that it is a rapid and non-invasive process. Moreover, by using NMR, it is possible to analyze the chemical nature of individual types of hydrogen and carbon atoms, in various and complex mixtures of petroleum and in the final products obtained by refining processes. In the spectra, the functional groups of aromatics, aliphatics, and olefins are well illustrated; accordingly, it is possible to differentiate a polynuclear aromatic from a mononuclear aromatic and to identify

*Corresponding author: siavashira@gmail.com

Analytical Characterization Methods for Crude Oil and Related Products, First Edition.
Edited by Ashutosh K. Shukla.

the fuel physical properties by the concentration of aromatics and the chain length of aliphatics. On the other side, the high cost, the risk of magnetic disturbances, requiring magnetic shielding, and the overlap of frequency ranges, complex information, and requirement of statistical approach to correlate the spectral data with the characterization of crude oil are some important disadvantages (Silva, *et al.*, 2011).

NMR spectroscopy has already been used in some refinery laboratories to determine the content in paraffinic and aromatic carbon contents of hydrocarbon oils and to determine the aromatic hydrogen and carbon content, as well. Furthermore, the hydrogen content of middle distillate petroleum products by low-resolution pulsed NMR, and the aromatic carbon content of lubricant mineral base oils and middle distillate petroleum fractions by ^{13}C NMR spectroscopy, were determined. Apart from the properties of crude oil, it is possible to analyze the samples using the NMR spectroscopy; however, it is important to notice that the sample density and the viscosity affect the T_1 and T_2 relaxation times (e.g. high density and viscosity samples give spectra with broader signals, and overlaps between different peaks make the NMR assignments difficult).The spin nuclear relaxation parameters are a very important way to obtain information about stereochemistry and molecular dynamics. The nuclear relaxation is related to the structure, flexibility, and molecular mobility that is responsible for the existence of different magnetic fields. Experimentally, the relaxation rate can be determined using the relationship between the relaxation times, T_1 and T_2, and the correlation time for molecular tumbling. The NMR techniques based on the analysis of T_1 (longitudinal or spin-lattice relaxation time) and T_2 (transverse relaxation time) decay curves can be obtained using the low-field ^1H NMR spectroscopy and correlate and supplemented with information taken with the high-field NMR. Analysis of heavy materials (such as asphaltenes) and residuals is also possible (Silva, *et al.*, 2011).

5.2 ^1H NMR and ^{13}C NMR Spectroscopy Analysis Methods

^1H NMR spectroscopy can be applied in the characterization and identification of crude oil fractions, and it is a suitable way to predict the total hydrogen content as well as the distribution of hydrogen among functional groups present in the crude. Furthermore, information about the structural characteristics can be obtained by this method in order to estimate the molecular weight and to analyze the effects in several refining processes. On the other side, suitable information about the molecular carbon skeleton can be obtained by ^{13}C NMR. This NMR technique is important for the structure elucidation and chemical composition of a sample. In addition, it distinguishes the existence of quaternary carbons of many functional groups (C N, C O, C NR, etc.), and produces spectra with well quality (Gunther, 1992). For this reason, ^{13}C NMR has become

one of the most important methods in the analysis of crude oil fractions. When comparing ^{1}H and ^{13}C NMR spectra, it is possible to identify many differences between them. For example, ^{13}C NMR spectra have a much larger chemical shifts scale (more than 220 ppm), which produces less overlapping between peaks. The ^{13}C NMR is less sensitive than ^{1}H NMR, owing to their lower natural abundance (1.1%) and magnetogyric ratio of the ^{13}C nucleus, but in the case of the ^{1}H decoupled ^{13}C NMR spectra, it is much simpler once there is no peak splitting.

5.3 NMR Techniques

Actually, because of the complex mixture of compounds in crude oil, applying suitable and professional techniques to improve the quality of the NMR spectra and to obtain better quantitative information about the sample in analysis are crucial. Therefore, beyond the use of one-dimensional NMR spectroscopy (^{1}H and ^{13}C NMR), it is more suitable to use the "spectral editing" techniques and the two-dimensional NMR experiments. The use of two-dimensional NMR spectroscopy demonstrated great potentialities in structural elucidation and quantification of complex mixtures. The "spectral editing" techniques can be used to improve the analysis of the ^{1}H and ^{13}C NMR spectra, owing to the overlapping of the signals, which makes the identification of some structures difficult. The aim of these "spectral editing" techniques is to participate to the separation of primary (CH_3), secondary (CH_2), tertiary (CH), and quaternary carbons and to a sensitivity improvement. Examples of "spectral editing" techniques are the INEPT (insensitive nuclei enhanced by polarization transfer), DEPT (distortionless enhancement by polarization transfer), GASPE (gated spin echo), PCSE (part-coupled spin echo) and QUAT (quaternary-only carbon spectra). INEPT and DEPT are examples of methods also known as polarization transfer methods. The aim of these methods is to transfer the large excess population (polarization) of the ^{1}H to the insensitive nuclei before its perturbation (in the present case to ^{13}C nuclei).

On the other hand, the two-dimensional NMR spectra rely on the coupling between two nuclei. It is possible to have two-dimensional homonuclear spectra (resulting from the coupling between nuclei of the same type) and the two-dimensional heteronuclear spectra (between nuclei of different types). Two-dimensional correlation spectroscopy (COSY) is an example of a homonuclear spectrum. In this spectrum it is correlated one proton to another proton, depending on the coupling constant value, which leads to identify resonances that are coupled each other (Exarchou, *et al.*, 2001; Lewis *et al.*, 2007; Kontogianni *et al.*, 2009). Moreover, TOCSY (total correlation spectroscopy) is another two-dimensional homonuclear spectrum and is very useful in the analysis of complex mixtures helping in the characterization of the molecule structure. In this case it establishes a correlation between all the

spins in a set of coupled spins in a molecule. Doan *et al.* (1995) has used this technique in the analysis of polyaromatics in crude gas oil mixtures. Heteronuclear correlation (HETCOR) is a two-dimensional heteronuclear spectrum where it is possible to obtain a correlation between coupled heteronuclear spins across a single bond. Furthermore, the diffusion-ordered spectroscopy (DOSY) spectrum is very useful for analyzing the composition of mixtures based on the differences in diffusion coefficients of the individual components. This technique contributes to identify signals from one molecular species, to differentiate these signals from those of another molecular, and with that analyze complex mixtures of petroleum fractions. Additionally, this separation can contribute to differentiate molecules taking into account the size, shape, and even the physical properties of the surrounding environment (Durand, *et al.*, 2008). One does not often find researches where ^{14}N, ^{15}N, ^{33}S, and ^{17}O NMR spectroscopy are used in the analysis of crude oil derivatives. Most of the researches were done via ^{1}H and ^{13}C NMR.

However, the use of different nuclides (such as nitrogen, sulfur, and oxygen) may be a good choice when the concentration of acidic OH and basic N groups are wanted. It will be possible to identify some compounds as ethers, furans, secondary amines, thioethers, and thiophenes (Snape and Fresen, 1986). Ethers are a way to identify oxygen bonds that may have some impact in some processes, such as desulfurization and denitrogenation. In one study, Cookson and Smith (1987) used homonuclear two-dimensional COSY spectra, coupled and decoupled two-dimensional HETCOR spectra, and a two-dimensional relayed coherence transfer (RELAY) NMR method to provide a better analysis of the ^{1}H and ^{13}C NMR spectra, thus making a better structures assignment. In another study, Sarpal *et al.* (1996) used GASPE, PCSE, INEPT, DEPT, QUAT, two-dimensional COSY, and HETCOR to classify the composition of some different base oils into the hydrocarbon types, especially the isoparaffins. Two-dimensional COSY and HETCOR improved the identification and quantification of some branching structures, because these spectra allow clarifying the existing information inside the overlapping signals. The use of DEPT also contributed to solving the signal overlapping, especially in the region 28–40 ppm, as well as contributing to the separation of some carbons of normal paraffins, but did not give any information about the existence of quaternary carbons, which could be due to the size of these structures.

Moreover, Kapur, Findeisen, and Berger (2000) demonstrate that the two-dimensional DOSY NMR spectroscopy is very useful for the interpretation of the ^{1}H and ^{13}C NMR spectra of such complex mixtures as crude oil, which are characterized by great signal overlapping making the identification of some components difficult. In the ^{1}H NMR spectra, the overlapping occurs in the 0.5–2.0 ppm range, owing to the saturated components, whereas in the ^{13}C NMR the overlapping was stronger in the 10–45 ppm range. Using the DOSY

spectra the characteristic overlapping of both ^{1}H and ^{13}C NMR spectra was reduced, allowing a better resolution of the signals and a better structure clarification. It seems that this technique is very helpful in the analysis of heavy petroleum fractions. In another study, Durand *et al.* (2008) reported a DOSY spectrum of a diesel sample and for the first time a ^{1}H DOSY spectrum of asphaltenes. They showed that DOSY NMR technique is very critical to the analysis of complex samples, such as crude oil, which could provide information on the size, molecular weight, aggregation state, and composition of the mixture. The most important advantage of this technique was the potential to provide suitable physical and chemical information all at once when compared to the pulse field gradient spin echo NMR diffusion sequences (PFGSE NMR).

In another study, Behera, Ray, and Singh (2008) used some NMR techniques including the gated-decoupled ^{13}C, DEPT, two-dimensional (^{1}H–^{13}C) HETCOR, and other two-dimensional NMR methods for the better identification of some structures in the very crowded NMR spectra of heavy petroleum fractions. They reported that heteronuclear single quantum coherence (HSQC) and heteronuclear multiple-bond correlation (HMBC) spectra proved to be better able to identify side chain structures of aromatics. They characterized and quantitatively estimated compositions of the high boiling fractions of petroleum feed by NMR analytical methods and especially the complex structure of vacuum gas oil fractions used in Indian refineries. As a result, their work helped in optimizing the product slate of Indian refineries through proper feedstock blending using few hundreds of million metric tons (MMT) of crude oil consisting of blends of light crudes with different heavy crudes and bottom of the barrel due to escalating cost of crudes. Furthermore, Dearing *et al.* (2011) joined together the Raman, IR (infrared), and NMR spectra to give one set of "fused" spectra containing complementary information from Raman and IR (two sources) and one orthogonal source (e.g. NMR) to describe an industrial process. Data fusion enables process modeling and control to be performed using a single data set. This research has applied the concept of data fusion to characterize a series of crude oil fractions. After collection, the respective spectra were scaled and fused together to form one contiguous spectrum (Dearing *et al.*, 2011).

5.4 Application of NMR Analysis in Characterization of Crude Oil and Related Products

NMR has been used in the analysis of heavy petroleum fractions in many researches (Friedel, 1959; Cookson and Smith, 1987; Bansal *et al.*, 1998; Lee and Glavincevski, 1999; Woods *et al.*, 2008; Silva *et al.*, 2011). The main purpose was to help refineries to refine heavy crude oils more efficiently and at low processing costs. NMR analysis is currently being performed

in industrial settings for the monitoring of large-scale reactions. No need for sample preparation and rapid noninvasive remote analysis are the most important advantages of this method, as mentioned above. For instance, in one study, Woods *et al.* (2008) used NMR analysis to characterize the SARA fractions (saturated, aromatics, resins, and asphaltenes) separated from various Canadian crude oils. It was reported from the assignment of different types of proton and carbon atoms in the ^{1}H and ^{13}C NMR spectra of SARA fractions that the aromaticity region (110–150 ppm) increased from saturated to asphaltenes fractions. This was confirmed by the H/C ratio decreasing with the increasing of aromaticity. On the other hand, the saturated fraction was characterized by an aliphatic nature represented with a high H/C ratio.

Moreover, it was reported that the aliphatic chain length increased from saturated < aromatics < resins < asphaltenes. In another study, Cookson and Smith (1987) analyzed the monoaromatic fractions obtained from petroleum, coal, and shale-derived distillate fuels to get new structure information. As a result, all the analyzed diesel fuel had an average of 13–15 carbons atoms per molecule, whereas the kerosene aromatics had a lower value (11–12 carbons atoms). Other similarities between all the seven diesel fractions were observed, such as the same number of side chains per molecule (NS = 3), the same average side chain length (LS ≈ 2.8) (in only six of the samples), and the absence of quaternary carbon branching sites. One of the main differences between the samples was related to the number of ring structures involving aliphatic carbon atoms. The number of rings observed for a specific fraction depends of the original sample; when a fraction is a product of hydrotreatment it has a large quantity of saturated ring structures. Kerosene samples compared with the diesel fractions showed a lower number of saturated rings per molecule and a lower number of carbon atoms per molecule. This phenomenon might be due to the lower number of side chains and to the lower side chain length. From the ^{1}H and ^{13}C NMR spectra, it was possible to determine the average number of specific CH_m groups (—CH_3 and —CH_3) per molecule, as well.

The analysis of proton resonances indicated that normally the intensity near the 2.25 ppm region was due to —CH_3, while for some samples that signal could be 2.1–2.4 ppm. The intensity of these signals generally yields 0.1 or 0.14 —CH_3 groups per molecule, depending on the spectra and on the occurring overlapping. In the ^{1}H NMR spectra, the signal at around 1 ppm was assumed to be due to the —CH_3 groups. In this study, some structures such as methyl, ethyl, propyl, and butyl groups, tetralin, indane, and 1-methylindane ring side chains in the analyzed samples of shale oil diesel were identified (Cookson and Smith, 1987). Moreover, Bansal *et al.* (1998) and Lee and Glavincevski (1999) analyzed the content of aromatics in middle distillate oils and used the NMR spectroscopy method for the determination of the molar content of aromatics. Sergeant *et al.* (1995) used ^{1}H and ^{13}C NMR spectroscopy to analyze different

products from shale deposits in Australia; which made it possible to obtain information about the variety of structural composition of lubricating oils, of maltenes, and of Rundle distillate. From the differences between these products, it is noteworthy that lubricating oils were characterized by the absence of olefinic structures, the Rundle distillate samples by the presence of monoaromatic with some polyaromatic and naphthenic structures, while the maltenes were distinguished by the existence of some olefinic structures and aliphatic chains, which were less substituted.

Andrade, Fernandes, and Miranda (2010) reviewed the determination of conjugated dienes in petroleum products using different chemical and instrumental techniques, including NMR spectroscopy. Actually, there are several methods of quantifying the total conjugated dienes amount in complex hydrocarbon mixtures. But the identification of each conjugated diene has been proved to be a difficult task, although a detailed analysis will enable a good correlation with the gum formation and the catalyst poisoning. They indicated the NMR method as one of the preferred methods for characterizing naphtha or gasoline samples with alcohol and for characterizing conjugated dienes in the samples.

Interestingly, Hirasaki, Lo, and Zhang (2003) analyzed the correlation of relaxation times with viscosity/temperature and Larmor frequency. They reported that relaxation times T_1 and T_2 were equal, in crude oils, at low viscosity and could be correlated with the ratio of viscosity/temperature. However, for high-viscosity crude oils T_1 and T_2 are different. T_1 is a function of the Larmor frequency and T_2 follows the viscosity/temperature correlation. Moreover, they demonstrated that the temperature influenced the viscosity as well as the relaxation time of heavy oils. NMR was used to analyze the existence of water, oil, and gas in the reservoirs of petroleum, taking into account the relationship between diffusivity and relaxation time. From the interpretation of the NMR logs, it was reported that water presented a large relaxation time, the fluids presented different diffusivity, while crude oil presented a huge relaxation time and a large diffusivity distribution. Moreover, Ramos *et al.* (2009) used T_2 of protons in the viscosity prediction of crude oil. The analysis of the expansion of the ^1H raw T_2 relaxation curves of four Brazilian crude oil samples with different viscosities has indicated that there was a decrease in the relaxation decay curve when the oil viscosity increased. Therefore, a shorter T_2 was produced for the sample with high viscosity. Consequently, more viscous oil represents a lower relaxation time and less viscous oil has a larger relaxation time. In crude oil, saturated fractions and resins are responsible for a higher contribution to the T_2 spectra, aromatics are responsible for a lower contribution, while the asphaltene protons are less expressive in the T_2 spectra.

Sarpal *et al.* (1998) used a method to estimate the aromatic content of base oils using ^1H NMR spectroscopy. Owing to the interpretation of the

^{1}H NMR spectra and the use of the two-dimensional HETCOR technique, it was possible to calculate the aromatic carbon content by changing the Brown–Ladner equation, as well as to estimate the bridgehead carbons and the quaternary aromatic carbons content. The need to modify the Brown–Ladner equation was due to the quantity of factors needed to determine the aromatic content, like the elemental H and C content, the average number of hydrogen per-alkyl substituents, the atomic H/C ratio for non-aromatic groups, and the aromatic protons, among others. In another study, Bansal *et al.* (1988) used ^{1}H NMR spectroscopy to estimate the content of total aromatics and their distribution as mono- and polynuclear aromatics. They analyzed the ^{1}H NMR spectra and the two-dimensional HETCOR (^{13}C–^{1}H) NMR spectra of a representative diesel sample and of the aromatic fraction of a diesel sample, respectively. They estimated some structural parameters like the number of substituted aromatic carbons, the average alkyl chain length of aromatic substituents, the number of bridgehead carbons, the number of total aromatics, and the estimation of mono-ring and global di-plus-ring aromatics. Two-dimensional HETCOR spectra were used to improve the analysis and the signals assignment in the ^{1}H NMR spectra, owing to the overlapping. It was concluded that only exist —CH_3 groups between 0.5 and 1.0 ppm and did not exist any overlap; while some —CH_3 (-substitution in aromatic carbons) groups were found between 2.4 and 2.6 ppm. It was possible, as well, to find a relationship between the —CH_2 carbons, 25–40 ppm, and the protons that exist in the 2.4–3.5 ppm region. Moreover, it was reported that some —CH_2, —CH_3 substituents on the aromatics, and also some —CH protons in the range 2.4–3.5 ppm exist. In the ^{13}C NMR spectra, the overlap achieved between 18 and 20 ppm may be due to the methyl substituents of the aromatic carbons. The information given by the ^{13}C NMR spectra was generically similar to that of ^{1}H NMR spectra.

In one study, Yoshida *et al.* (1980) developed a work on some characteristics compounds in the ^{13}C NMR spectra of the ring-type fractions of coal-derived oil aiming to determine the chemical shift ranges of protonated, bridgehead, and substituted carbons of this type of sample and with that determine the equation for structural parameters. Moreover, it was reported that aromatic carbons appear in the order of protonated, bridgehead, and substituted carbons from low to high frequency values. Typically, the chemical shifts of the protonated carbon appear at 115.0–129.2 ppm, the bridgehead carbons at 129.2–132.5 ppm, and the substituted carbons at 132.5–149.2 ppm. However, the existence of the phenolic OH and the amino groups affect the chemical shift of neighboring protonated carbons, shifting them to lower frequency values.

Some of the bridgehead carbons were extended to a field lower than 132.5 ppm and others continued to appear in the range of 129.2–132.5 ppm, depending on whether these carbons were naphthalene and methylated or

just naphthenonaphthalene, respectively. Moreover, the chemical shift of the substituted carbons depends on the type of aliphatic carbons bonded to aromatic rings. In the subsequent ^{13}C NMR spectra analysis it was possible to assign some signals to chemical shifts of model compounds. For example, the signals at 132.5–137.2 ppm were due to substituted aromatic carbons bonded to methyl groups or to cycloparaffinic —CH_2. The signals at 137.2–149.2 ppm corresponded to the resonance of substituted aromatic carbons bonded to some alkyl groups (and do not include methyl or methylene bridges between aromatic rings) and that at 149.2–158 ppm to Ca–OH groups. The coal-derived oil contained a lot of alkyl substituents and naphthenic rings. It was also possible to reach this conclusion through the analysis of some structural parameters such as aromaticity, the ratio of non-bridgehead aromatic carbon to total carbon, and the degree of aromatic ring substitution. In another work, Cookson and Smith (1985) studied a total of nine diesel samples (petroleum and synfuels) with two kerosene samples using the ^{13}C NMR spectroscopy analytical method. They have used the GASPE technique to minimize the overlap of resonances due to C, CH, CH_2, and CH_3 groups that usually occurred in a ^{13}C NMR spectrum of complex mixtures. It was demonstrated that all the diesel samples have an average chain length of 15–16 carbons, while the kerosene examined has about 12 carbons' chain length. However, first it is necessary to estimate the average number of carbons per molecule, which depends on the sample used. The number of carbons per molecule is not always equal to the average n-alkane chain length, and branched, saturated, and cyclic saturated structures may have different average numbers of carbons atoms.

Barbosa *et al.* (2013) used the low-field ^1H NMR technique to predict various properties of petroleum fractions with °API ranging from 21.7 to 32.7. As a result, good correlations between the NMR relaxation data with viscosity, total acid number, refractive index, and API gravity were observed. The important advantages of their approach are its non-destructiveness, speed, and that it does not require any solvents/dilution (Barbosa *et al.*, 2013). In another analytical experiment, Sarpal *et al.* (1997) developed research with some base oils aiming to estimate the content of some structural parameters, like the normal and isoparaffin content, the number of branching sites, and the average alkyl chain length. These base oils, produced from different treatments like hydrocracking and wax isomerization, were hydrofinished solvent-refined oils of high viscosity index, hydrofinished oils of very high viscosity index, and hydrotreated base oils. It was verified that, although there were some similarities between the types of branched structures produced by the hydrocracking and wax isomerization, there were some differences, especially in the obtained quantities. They estimated the percentage of normal and isoparaffin contents.

Fractions of Maya (Mexico) crude oil were analyzed using quantitative liquid-state ^1H and ^{13}C NMR spectroscopy (Morgan *et al.*, 2010). The NMR

information was combined with molecular-mass estimates to calculate average structural parameters. The approach obviously demonstrated structural differences between the fractions and allowed for the inference of detailed information on the chemical structures involved. The sample of crude oil was first fractionated into maltenes and asphaltenes, and the asphaltenes were sub-fractioned into 1-methyl-2-pyrrolidinone (NMP)-soluble (labeled as "MNS") and NMP-insoluble (labeled as "MNI") fractions. The aromatic rings per average molecule value derived were 2–5 for the MM sample, 8–10 for the MA sample, ~5 for the MNS sample, and 11–38 for the MNI sample. Thus, while some differences between maltenes and asphaltenes could be expected from prior general knowledge, some results were unexpected. The MNS fraction turned out to be more aliphatic than the MNI fraction. The MNS sample contained a greater number of smaller aromatic cores, linked by means of biphenyl-like aromatic–aromatic single bonds and aliphatic/naphthenic bridges, and shorter aliphatic side chains. Results for the MNI sample strongly suggested fewer, larger aromatic cores per average molecule, linked by long alkyl side chains and naphthenic structures (Morgan *et al*., 2010). Moreover, Verdier *et al.* (2009) used the ^{13}C NMR data of a broad variety of samples produced from different vacuum gas oils to analyze the molecules with high viscosity indexes. They concluded that oils presenting molecules with long alkyl chains, low aromatic content, ethyl branching, and tertiary carbons presented high viscosity indexes. Interestingly, in other research, the biodegradation of four different crude oil samples (Arabian light, Dubai, Maya, and Shengli) by *Acinetobacter* sp. T4 and by a microbial consortium called SM8 was examined by Sugiura *et al.* (1996). The degree of biodegradation of crude oil components varied according to the crude oil, the saturated fraction being more susceptible to biodegradation than the aromatic fraction in all the crude oil samples. NMR analysis demonstrated that the alkyl side chain of some aromatic molecules was degraded by *Acinetobacter* sp. T4. In contrast, SM8 degraded the polycyclic aromatic compounds in the crude oil samples (Sugiura *et al.*, 1996).

5.5 Asphaltene Characterization using NMR Techniques

Asphaltenes are characterized as complex mixtures containing high quantities of heteroatoms (e.g. nitrogen, oxygen, and sulfur) and metals (e.g. vanadium, nickel, and iron), and condensed aromatic rings, aliphatic chains, and naphthenic rings. They show a dark color and are defined as the fraction from crude oil which is soluble in toluene and insoluble in heptane, and they are the most complicated compounds in crude oil and are very complicated to analyze, owing to their tendency to associate, to the high molecular weight

(approximately 1000 g mol^{-1}) and to the paramagnetism (Calemma *et al.*, 1998; Aske *et al.*, 2002). For instance, the features of molecular structure of seven *n*-C_7 asphaltenes isolated from different feedstocks (i.e. vacuum residue, atmospheric residue, and crude oil) have been investigated by pyrolysis-gas chromatography/mass spectrometry (Py-GC/MS), and their average structural parameters have been estimated using a mathematical optimization method. The results obtained from this research showed that asphaltenes are a complex polydisperse mixture of molecules made up of polyaromatic and hydroaromatic units joined by aliphatic bridges and substituted with aliphatic chains containing up to 25–30 carbon atoms. However, both NMR data and results of structural analysis indicated that the major part of these chains (more than 80%) is formed by short alkyl groups (C_1–C_4) (Calemma *et al.*, 1998). Actually, there is a great deal in the literature regarding asphaltenes (determination and characterization) (Ali, Al-Ghannam, and Al-Rawi, 1990; Ancheyta, *et al.*, 2002; Östlund, *et al.*, 2004; Trejo, Centeno, and Ancheyta, 2004; Trejo *et al.*, 2007; Morgan *et al.*, 2010). For instance, three crude oils were used for the precipitation of asphaltenes using two solvents, n-pentane and n-heptane. Asphaltenes were characterized by VPO molecular weight, liquid state ^1H and ^{13}C NMR, elemental composition, and metal content. As a result, spectra were divided in three and two different regions for ^1H and ^{13}C NMR, respectively, to determine the most important structural parameters of asphaltenes. To avoid errors when determining asphaltene content and characterization, a solvent-to-oil (S/O) ratio of 60:1 was used. This optimal ratio was defined after conducting various experiments with different values of S/O in the range of 5:1 to 100:1. It was reported that the type of solvent influenced the composition of the asphaltenes.

Moreover, aromaticity of asphaltenes was higher when n-heptane was employed (Ancheyta *et al.*, 2002). Furthermore, in another work, Aske *et al.* (2002) studied the aggregation of asphaltenes by pressure depletion both in a live crude oil and model systems of asphaltenes in toluene/pentane solvents. Because of their complex nature, a specific molecular structure or a specific family compound of asphaltenes has not been found, but there are different ideas relative to their composition (Mansoori, 2017). Calemma *et al.* (1995) compared the content of asphaltenes present in the heavy crude oils of seven different sources and reported structural characterization of asphaltenes using NMR and other spectroscopic techniques. By using NMR techniques (^{13}C GASPE), some CH groups in the aliphatic chains, some condensed alicyclic structures (especially in the more aliphatic asphaltene molecules), and the aliphatic CH_3/CH ratio were identified. Moreover, it was possible to characterize the maturity of asphaltenes which is related to their ability to aggregate through aromatic interactions. With the analysis of some molecular parameters from the NMR spectra (e.g. the aromatic carbon fraction, an

average number of carbons per alkyl side chain and the percentage of aromatic rings substitution), it was possible to draw some conclusions.

Almost all the analyzed asphaltenes presented comparable average aromatic condensations and average numbers of polycondensed aromatic rings in the range of 5–7. It was also possible to observe that asphaltenes presented different behaviors with the increase in the carbon content. Consequently, when the carbon content of the asphaltene samples increases, the aromaticity and the average aromatic core size increase, the average length of alkyl side chains decrease, and the heteroatom content and the average molecular weights decrease, as well. Asphaltenes with smaller molecular weight presented more aromatic carbons, less heteroatoms, slightly sulfur, and smaller aliphatic side chains. Furthermore, in another study, Sheremata *et al.* (2004) reported a quantitative molecular representation of Athabasca asphaltenes where ^{1}H and ^{13}C NMR spectroscopy was used to provide data from elemental analysis.

They demonstrated that the combination of ^{1}H and ^{13}C NMR spectroscopy was very helpful in the analysis of asphaltene chemistry, and to better understand the molecular structure of these compounds. Douda, Alvarez, and Bolaños (2008) analyzed some asphaltene mixtures by comparing the asphaltene fractions obtained after pyrolysis (at different temperatures) with the original ones, by using solution-state ^{1}H and ^{13}C NMR spectroscopy. The large bands of aromatic and saturated regions in the ^{1}H and ^{13}C NMR spectra were thought to be due to the high values of different structures of asphaltene compounds. It was concluded that pyrolysis processes at high temperatures were responsible for a higher formation of asphaltenes. Temperature contributed to the asphaltenes' modification, and is very important in the prevention of some problems during crude oil refining, like the deposition of asphaltenes in cooking, cracking, and distillation. In another study, Durand *et al.* (2008) reported ^{1}H DOSY NMR spectrum of asphaltenes. They demonstrated that asphaltenes have more aliphatic than aromatic structures. Moreover, the diffusion coefficient of asphaltenes and toluene using the modified Stokes-Einstein equation was calculated and then compared with the sample concentration.

The intention was to analyze the intermolecular interactions between solvent and solute and their dependence on the solute concentration and to analyze the behavior of the diffusion coefficients, while increasing the sample concentration, which can give some information about the nature of the mixture's constituents. From the signals in the spectrum it was concluded that terminal CH_3 of long alkyl chains was represented by signals at 0.9 ppm, while at 1–2 ppm some CH_2 groups were found, and peaks at 2.1–3 ppm corresponded to CH, CH_2, and CH_3 were found in polycyclic aromatic hydrocarbons. In other research, Östlund *et al.* (2004) studied the characteristics of fractionated asphaltenes with respect to solubility, aromaticity, heteroatom content, and diffusion behavior. Asphaltenes have been fractionated by liquid/liquid extraction, yielding four subfractions. It was demonstrated that asphaltenes from

the four subfractions showed variations in their tendency to flocculate as well as distinct differences in aromaticity. Moreover, NMR self-diffusion studies demonstrated that the average diffusion coefficients differed for asphaltenes from the various subfractions. It was reported that a variation in average size and stability between asphaltenes depended on what subfraction they were owned by. The subfraction which consisted of asphaltenes with the largest average size and the highest aromaticity was also found to contain asphaltenes which had the strongest tendency to flocculate (Östlund *et al.*, 2004).

5.6 Conclusions

In conclusion, the NMR spectroscopy analytical approach is considered one of the essential techniques which helped researches to receive answers and information about the conjugated dienes composition quickly. Moreover, commercial and operational issues are important in NMR spectroscopy. The commercial blessings include the optimization in the feed of refining tactics to adjust the production taking into account the needs of the marketplace, to advantage the attractive charge of some crude, and in saving money by way of the usage of entire systems of acquisition evaluation in a short time. The operational blessings include that it increases the value of a product's yield, maximizes the recovery of misplaced capacity, reduces instability, and enhances the performance of downstream units. Further, the relaxation times are vital in the comprehension of the molecular structure; as an instance, whilst evaluating two molecules, if the relaxation time decreases, it could be due to the existence of intramolecular hydrogen bonds which lower the mobility. NMR spectroscopy may be used in petro-physical characterization, as it does not wreck the original pore structure. Now, the tremendous mission regarding this analytical technique is to use the online NMR once it is able to offer specific evaluation in actual time and control the properties of the crude from the feed to the very last product. Evidently, enhancements in NMR analysis have been made with the use of a few techniques including GASPE, PCSE, INEPT, DEPT, QUAT, two-dimensional COSY and HETCOR, and many others. It must be observed that the use of data fusion with more than one analytical measurement (as an example Raman, IR, together with NMR spectra) reduces the mistakes associated with inferential property models for industrial process monitoring, and consequently makes an allowance for appropriate and elevated manage of industrial processes as well as laboratory ones.

References

Ali, L. H., Al-Ghannam, K. A., and Al-Rawi, J. (1990) Chemical structure of asphaltenes in heavy crude oils investigated by n.m.r. *Fuel*, 69, 519–521.

Ancheyta, J., Centeno, G., Trejo, F., *et al.* (2002) Extraction and characterization of asphaltenes from different crude oils and solvents. *Energy Fuels*, 16, 1121–1127.

Andrade, D.F., Fernandes, D. R., and Miranda, J.-L. (2010) Methods for the determination of conjugated dienes in petroleum products: A review. *Fuel*, 89, 1796–1805.

Aske, N., Kallevik, H., Johnsen, E. E., and Sjöblom, J. (2002) Asphaltene aggregation from crude oils and model systems studied by high-pressure NIR spectroscopy., *Energy & Fuels*, 16, 1287–1295.

Bansal, V., Kapur, G. S., Sarpal, A. S., *et al.* (1988) Estimation of total aromatics and their distribution as mono and global di-plus aromatics in diesel-range products by NMR spectroscopy. *Energy Fuels*, 12(6), 1223–1227.

Bansal, V., Kapur, G. S., Sarpal, A. S., *et al.* (1998) Estimation of total aromatics and their distribution as mono and global di-plus aromatics in diesel-range products by NMR spectroscopy. *Energy Fuels*, 12, 1223–1227.

Barbosa, L. L., Kock, F. V. C., Silva, R. C., *et al.* (2013) Application of low-field NMR for the determination of physical properties of petroleum fractions. *Energy Fuels*, 27, 673–679.

Behera, B., Ray, S. S., and Singh, I. (2008) Structural characterization of FCC feeds from Indian refineries by NMR spectroscopy. *Fuel*, 87, 2322–2333.

Calemma, V., Iwanski, P., Nali, M., *et al.* (1995) Structural characterization of asphaltenes of different origins. *Energy Fuel*, 9, 225–230.

Calemma, V., Rausa, R., D'Anton, P., and Montanari, L. (1998) Characterization of asphaltenes molecular structure. *Energy Fuels*, 12, 422–428.

Cookson, D. J. and Smith, B.-E. (1985) Determination of structural characteristics of saturates from diesel and kerosene fuels by carbon-13 nuclear magnetic resonance spectrometry. *Anal Chem.*, 57, 864–871.

Cookson, D. J. and Smith, B.-E. (1987) One- and two-dimensional NMR methods for elucidating structural characteristics of aromatic fractions from petroleum and synthetic fuels. *Energy Fuel*, 1, 111–20.

Dearing, T. I., Thompson, W. J., Rechsteiner, C. E., and Marquardt, B. (2011) Characterization of crude oil products using data fusion of process Raman, infrared, and nuclear magnetic resonance (NMR) spectra. *Applied Spectroscopy*, 65, 181–186.

Doan, B.-T., Gillet, B., Blondel, B., and Beloeil, J.-C. (1995) Analysis of polyaromatics in crude gas oil mixtures: A new strategy using 1H 2D n.m.r. *Fuel*, 74, 1806–1811.

Douda, J., Alvarez, R., and Bolaños, J.-N. (2008) Characterization of Maya asphaltene and maltene by means of pyrolysis application. *Energy Fuel*, 22, 2619–2628.

Durand, E., Clemancey, M., Quoineaud, A.-A., *et al.* (2008) 1H diffusion-ordered spectroscopy (DOSY) nuclear magnetic resonance (NMR) as a powerful tool for the analysis of hydrocarbon mixtures and asphaltenes. *Energy Fuel*, 22, 2604–2610.

Exarchou, V., Troganis, A., Gerothanassis, I. P., *et al.* (2001) Identification and quantification of caffeic and rosmarinic acid in complex plant extracts by the use of variable-temperature two-dimensional nuclear magnetic resonance spectroscopy. *J Agric Food Chem.*, 49, 2–8.

Friedel, R.-A. (1959) Absorption spectra and magnetic resonance spectra of asphaltene. *J Chem Phys.*, 31, 280–281.

Gunther, H. (1992) *NMR Spectroscopy: Basic Principles, Concepts, and Applications in Chemistry*, 2nd edn. Wiley-VCH Verlag GmbH, Weinheim, Germany.

Hirasaki, G. J., Lo, S.-W., and Zhang, Y. (2003) NMR properties of petroleum reservoir fluids. *Magnetic Resonance Imaging*, 21, 269–277.

Kapur, G. S., Findeisen, M., and Berger, S. (2000) Analysis of hydrocarbon mixtures by diffusion-ordered NMR spectroscopy. *Fuel*, 79, 1347–1351.

Kontogianni, V. G., Exarchou, V., Troganis, A., and Gerothanassis, I.-P. (2009) Rapid and novel discrimination and quantification of oleanolic and ursolic acids in complex plant extracts using two-dimensional nuclear magnetic resonance spectroscopy: Comparison with HPLC methods. *Anal Chim Acta.*, 635, 188–195.

Lee, S. W. and Glavincevski, B. (1999) NMR method for determination of aromatics in middle distillate oils. *Fuel Processing Technology*, 60, 81–86.

Lewis, I. A., Schommer, S. C., Hodis, B., *et al.* (2007) Method for determining molar concentrations of metabolites in complex solutions from two-dimensional 1H–13C NMR spectra. *Anal Chem.*, 79, 9385–9390.

Mansoori, G. A. (2017) *Nanoscale structures of asphaltene molecule, asphaltene steric-colloid and asphaltene micelles and vesicles*. Available from: http://mansoori.people.uic.edu/Asphaltene.Molecule_html.

Morgan, T. J., Alvarez-Rodriguez, P., George, A., *et al.* (2010) Characterization of Maya crude oil maltenes and asphaltenes in terms of structural parameters calculated from nuclear magnetic resonance (NMR) spectroscopy and laser desorption–mass spectroscopy (LD–MS). *Energy Fuels*, 24, 3977–3989.

Östlund, J.-A., Wattana, P., Nydén, M., and Fogler, H. S. (2004) Characterization of fractionated asphaltenes by UV–VIS and NMR self-diffusion spectroscopy. *Journal of Colloid and Interface Science*, 271, 372–380.

Ramos, P. F. O., Toledo, I. B., Nogueira, C. M., *et al.* (2009) Low field 1H NMR relaxometry and multivariate data analysis in crude oil viscosity prediction. *Chemometrics and Intelligent Laboratory Systems*, 99, 121–126.

Rudzinski, W. E. and Aminabhavi, T.-M. (2000) A review on extraction and identification of crude oil and related products using supercritical fluid technology. *Energy Fuels*, 14, 464–475.

Sarpal, A. S., Kapur, G. S., Bansal, V., *et al.* (1998) Direct estimation of aromatic carbon (Ca) content of base oils by 1H-NMR spectroscopy. *PetSci Technol.*, 16, 851–868.

Sarpal, A. S., Kapur, G. S., Chopra, A., *et al.*, (1996) Hydrocarbon characterization of hydrocracked base stocks by one- and two-dimensional n.m.r. spectroscopy. *Fuel*, 75, 483–490.

Sarpal, A. S., Kapur, G. S., Mukherjee, S., and Jain, S.-K. (1997) Characterization by 13C n.m.r. spectroscopy of base oils produced by different processes. *Fuel*, 76, 931–937.

Sergeant, G. D., Stubington, J. F., Barrett, D., *et al.* (1995) A comparative study of products derived from Rundle and Stuart shale oils and petroleum lubricating oil base stocks (based on n.m.r., molecular weight and elemental analysis). *Fuel*, 74, 51–56.

Sheremata, J. M., Gray, M. R., Dettman, H. D., and McCaffrey, W. (2004) Quantitative molecular representation and sequential optimization of Athabasca asphaltenes. *Energy Fuel*, 18, 1377–1384.

Silva, S. L., Silva, A. M. S., Ribeiro, J. C., *et al.* (2011) Chromatographic and spectroscopic analysis of heavy crude oil mixtures with emphasis in nuclear magnetic resonance spectroscopy: A review. *Analytica Chimica Acta.*, 707, 18–37.

Snape, C. E. and Fresen, Z. (1986) Application of NMR to fossil fuels: An assessment of recent advances. *Anal Chem.*, 324, 781–785.

Sugiura, K., Ishihara, M., Shimauchi, T., and Harayama, S. (1996) Physicochemical properties and biodegradability of crude oil. *Environ Sci Technol.*, 31, 45–51.

Trejo, F., Ancheyta, J., Morgan, T. J., *et al.* (2007) Characterization of asphaltenes from hydrotreated products by SEC, LDMS, MALDI, NMR, and XRD. *Energy Fuels*, 21, 2121–2128.

Trejo, F., Centeno, G., and Ancheyta, J. (2004) Precipitation, fractionation and characterization of asphaltenes from heavy and light crude oils. *Fuel*, 83, 2169–2175.

Verdier, S., Coutinho, J. A. P., Silva, A. M. S., *et al.* (2009) A critical approach to viscosity index. *Fuel*, 88, 2199–2206.

Woods, J., Kung, J., Kingston, D., *et al.* (2008) Canadian crudes: A comparative study of SARA fractions from a modified HPLC separation technique. *Oil Gas SciTechnol.*, 63, 151–123.

Yoshida, T., Maekawa, Y., Uchino, H., and Yokoyama, S. (1980) Derivation of structural parameters for coal-derived oil by carbon-13 nuclear magnetic resonance spectrometry. *Anal Chem.*, 52, 817–820.

6

NMR Spectroscopy in Bitumen Characterization

Catarina Varanda[1,2], *Inês Portugal*[1], *Jorge Ribeiro*[3], *Carlos M. Silva*[1] *and Artur M. S. Silva*[2]*

[1] *Department of Chemistry, CICECO, Aveiro Institute of Materials, University of Aveiro, Aveiro 3810-193, Portugal*
[2] *Department of Chemistry, QOPNA, University of Aveiro, Aveiro 3810-193, Portugal*
[3] *Galp Energia, Rua Belchior Robles, Refinaria de Matosinhos, Leça da Palmeira 4450-802*

6.1 Introduction

Owing to its binding properties and hydrophobic nature, bitumen is commonly used for the construction of pavements and waterproof systems (Baldino *et al.*, 2013; Masson, 2008). Bitumens differ in their physical properties according to the nature of their crude oil sources, subsequent production processes and severity of the operating conditions. Relevant physical properties of bitumen are consistency (i.e. hardness or softness) and ductility within a certain temperature range, generally dictated by the local climatic conditions. These properties are intrinsically related to the methods used to characterize bitumen, such as the standard tests to evaluate the penetration depth and ductility at 25 °C, the "ring and ball" softening point, and the Fraass breaking point temperature (Jeglic *et al.*, 2003). Nonetheless, these are essentially empirical methods and yield a limited amount of information concerning bitumen chemistry and its behaviour for different ranges of temperature (Filippelli *et al.*, 2012).

Bitumen properties are naturally related to its composition. However, the precise identification of the molecular composition and structure of bitumen is rather difficult and so its characterization is often accomplished by fractionation techniques (Jones, 1992; Masson, 2008). For instance, the SARA method is based on the separation of bitumen components into four generic groups depending on their polarity and solubility, namely: saturates (S), aromatics (A), resins (R) and asphaltenes (A) (Kharrat *et al.*, 2007; Lesueur, 2009; Masson,

*Corresponding author: artur.silva@ua.pt

Analytical Characterization Methods for Crude Oil and Related Products, First Edition.
Edited by Ashutosh K. Shukla.

2008). Interestingly, bitumens are frequently specified in terms of the relative contents of their SARA fractions (Polacco *et al.*, 2015).

The structure of bitumen is controversial but the colloidal model, proposed by Rosinger (1914) although generally attributed to Nellensteyn (1924), still prevails especially to explain the interactions between modifiers and bitumen fractions (Lesueur, 2009; Pfeiffer and Saal, 1940). According to this model, bitumens are classified into three distinct types depending on their rheological properties, specifically: "Sol" (viscous) bitumens, which possess a colloidal structure constituted by non-interacting micelles and behave as Newtonian fluids; "Gel" (elastic) bitumens, which are characterized by a three-dimensional colloidal structure and high resilience; and, "Sol-Gel" (viscoelastic) bitumens, which exhibit an intermediate behaviour with elastic effects in the initial stages of deformation and a colloidal structure characterized by the presence of super-micelles (Bonemazzi and Giavarini, 1999; Giavarini *et al.*, 2000). Despite some flaws, the colloidal model is preferred over newer homogeneous models such as the dispersed polar fluid (DPF) approach that considers bitumen as a mixture of neutral and amphoteric molecules, with acid and basic functions interacting with each other to establish viscoelasticity within the neutral fraction (Christensen and Anderson, 1992; Le Guern *et al.*, 2010; Masson, 2008; Petersen *et al.*, 1994). In fact, the colloidal model is generally more appropriate to explain a wide range of experimental data (e.g. rheological measurements, ageing kinetics, and thermal properties) and the effects of polymer modification on bitumens (Lesueur, 2009).

According to the colloidal model, bitumen is considered an emulsion of asphaltene micelles peptized by resins in an oily medium constituted by saturates and aromatics, i.e. maltenes (Borrego *et al.*, 1996; Cheung and Cebon, 1997; Masson, 2008; Pfeiffer and Saal, 1940). Commonly, saturates are constituted by *n*-alkanes and iso-alkanes; aromatics, also called naphthene aromatics, are slightly aliphatic with lightly condensed aromatic rings; resins, also named polar aromatics, are constituted by fused aromatic rings with a simpler aromatic structure than that of asphaltenes; and, asphaltenes possess a complex structure formed by multiple fused aromatic rings (Lesueur, 2009; Masson, 2008). In addition, bitumen contains heteroatoms, such as sulfur, oxygen and nitrogen, normally embedded in the molecular structure of the aromatic rings (Masson and Gagne, 2008; Jones, 1992). Overall, the presence of these polar heteroatoms increases the hydrogen-bonding interactions and reactivity, thus influencing the chemical and physical properties of bitumen (Jones, 1992).

Owing to the high chemical complexity of bitumen, individual analysis of all structural components is almost impossible and thus some researchers have suggested it should be characterized by average molecular parameters. Nuclear magnetic resonance (NMR) spectroscopy is one of the most suitable methods for this purpose (Michon *et al.*, 1999a), especially because the NMR spectra of complex mixtures containing non-interacting or weakly interacting

components is approximately the sum of the individual spectra of the pure compounds (Molina *et al.*, 2010). Both ^{1}H and ^{13}C NMR spectra provide data about the relative content of protons and carbons in certain molecular environments (Woods *et al.*, 2008). For instance, Michon *et al.* (1997b,1999a) used quantitative ^{13}C NMR data together with molecular weight measurements to estimate average structural parameters of bitumen such as, for example, the number of alkyl substituents, naphthenic and aromatic rings per molecule (see further details in Section 6.2). Their aim was to define a "fingerprint" (Michon *et al.*, 1997b) particularly for the aromatic part of the spectra, in order to disclose the aromatization mechanisms behind bitumen oxidation (Michon *et al.*, 1999a). Molina *et al.*, (2010) developed a very fast and inexpensive method for petroleum residue analysis based on correlations between the area of ^{1}H NMR signals with the SARA fractions and some physicochemical properties (e.g. density and the contents of S, N and wax). ^{1}H and ^{13}C NMR analysis have been frequently used to investigate the chemical transformations base bitumens undergo during ageing/oxidation processes (Herrington *et al.*, 1994; Siddiqui, 2009, 2010; Siddiqui and Ali, 1999) and also to study the influence of bitumen modifiers, such as polyphosphoric acid (PPA) (Ali and Siddiqui, 2001; Gentile *et al.*, 2012; Rossi *et al.*, 2015). For example, the existence of macro-aggregates in PPA-modified bitumen was related to different ^{1}H NMR spin–spin relaxation times (Gentile *et al.*, 2012). Furthermore, the structure of phosphorus-containing compounds eventually present in PPA modified bitumen can be studied by ^{31}P NMR (Miknis and Thomas, 2008).

In addition to ^{1}H, ^{13}C and ^{31}P NMR spectroscopy, both NMR imaging and solid-state NMR can be used for bitumen analysis. The former is a valuable technique to measure interfacial surface properties in bitumen (Miknis *et al.*, 2005) and, moreover, it allows online non-invasive characterization of chemical and physical processes (Miknis *et al.*, 1998). The later, solid-state NMR, is a technique usually recommended to evaluate the fraction of amorphous and crystalline phases in bitumen (Michon *et al.*, 1999b).

6.2 ^{1}H and ^{13}C NMR Spectroscopy

The first experiments using ^{1}H NMR to investigate average structural parameters of petroleum were performed in the late 1950s (Williams, 1958). For example, a "branchiness index" was defined as the ratio of the signals due to methyl and methylene groups, and found to correlate linearly with the carbon content of naphthenic rings in the saturate fractions of gas oils from different crude sources. However, evaluation of the average parameters of the aromatic and olefinic fractions required additional data from elemental analyses and molecular weight measurements, to estimate the C/H weight ratio of the alkyl groups (Williams, 1958). The method was used for the structural characterization of asphalts (Ramsey *et al.*, 1967) and pitch materials (Smith *et al.*, 1976).

Table 6.1 ^{1}H NMR chemical shifts (δ, ppm) and corresponding hydrogen types. *Source:* (Molina *et al.*, 2010). Reproduced with permission of Elsevier.

δ (ppm)	Hydrogen type
0.5–1.0	γ-CH_3, some naphthenic CH and CH_2
1.0–1.7	β-CH_2, and some β-CH
1.7–1.9	Most CH, CH_2 in β-positions
1.9–2.1	α-CH_3 in olefins
2.1–2.4	α-CH_3 of aromatic compounds
2.4–3.5	α-CH, CH_2 of aromatic compounds
3.5–4.5	Bridging CH_2
4.5–6.0	Olefins
6.0–7.2	Mono-aromatics
7.2–8.3	Di-aromatics and some tri- and tetra-aromatics
8.3–8.9	Some tri- and tetra-aromatics
8.9–9.3	Some tetra-aromatics

Similarly, ^{13}C NMR was used to assess the structural parameters of petroleum fractions (Dickinson, 1980; Silva *et al.*, 2011) and coal-derived oil (Yoshida *et al.*, 1980).

In general, NMR spectroscopy provides qualitative and quantitative information about the hydrogen and carbon types and/or functional groups of the sample without its fractionation (Ali and Siddiqui, 2001). NMR analysis is based on the division of the aromatic and/or aliphatic regions of the spectra into smaller sections (chemical shift ranges) assigned to different chemical functionalities, as shown in Tables 6.1 and 6.2. Since the resonance signal is directly proportional to the number of nuclei with the associated chemical shift (Molina *et al.*, 2010), the relative peak areas of the NMR spectra provide quantitative data about the concentration of the respective functional groups. It is important to note that current ^{1}H NMR spectra can be used for quantitative determination, but quantitative ^{13}C NMR spectra analysis requires a specific technique, owing to high relaxation delays and long acquisition times (Giraudeau and Baguet, 2006).

Examples of ^{1}H and ^{13}C NMR spectra of bitumen are presented in Figures 6.1 and 6.2, respectively. It should be noted in advance that the spectra present some peak broadening and overlapping typical of complex mixtures, which may make its interpretation difficult. However, in the ^{1}H NMR spectrum (Figure 6.1) the two sharp peaks with a chemical shift between 0.5 and 1.5 ppm indicate the presence of γ-CH_3, β-CH_2 and some naphthenic CH and CH_2 hydrogens; the broad signal between 2 and 3 ppm indicates the presence of α-CH, α-CH_2

Table 6.2 ^{13}C NMR chemical shifts (δ, ppm) and identification of the corresponding types of carbon atoms. *Source:* Michon *et al.* (1997a). Reproduced with permission of American Chemical Society.

	δ (ppm)	Assignment	
Aliphatic carbons	10.0–55.0	C_{ali}	Aliphatic carbon atoms
	10.0–18.6	CH_3	Terminal or branched methyl groups in aliphatic chain (except for the case of two terminal methyl groups or the case of methyl groups branched in the α- or β-position in an alkyl chain from a ring)
	18.6–23.0	$CH_{3\alpha}$	Methyl groups branched to an aromatic or naphthenic ring
			The case where two methyl groups are terminal The case of methyl groups branched in an α- or β-position on an alkyl chain from a ring
	23.0–32.5	CH_2	Methylene groups of alkyl chains (except the case when they are branched in an α or β-position from an aromatic ring or in an α-position from a naphthenic ring)
			Methylene groups of naphthenic rings
	32.5–34.6	CH	Methine (or methylylidene) groups in aliphatic chains
	34.6–42.7	$CH_{2\alpha}$	The case of methylene groups branched in α or β position from an aromatic ring or in α position from a naphthenic ring
	42.7–55.0	CH_α	Methine groups of naphthenic rings
Aromatic carbons	115.0–145.0	C_{aro}	Aromatic carbon atoms
	115.0–129.3	CH_{aro}	Aromatic protonated carbon atoms
	129.3–137.1	C_{qp}	Aromatic bridgehead quaternary carbon atoms
	137.1–145.0	C_{qs}	Aromatic substituted quaternary carbon atoms

and α-CH_3 relative to aromatic compounds; and finally the small peak near 7 ppm corresponds to monoaromatic hydrogen types (see Table 6.1). Regarding the ^{13}C NMR spectrum of bitumen (Figure 6.2), two regions are identified and clearly assigned to aliphatic carbons (several small peaks in the range 10–55 ppm) and aromatic carbons (115–145 ppm), as detailed in Table 6.2. However, it is important to notice that these ranges are not consensual in the structural characterization of oils, coals or derived fractions (Avella and Fierro, 2010).

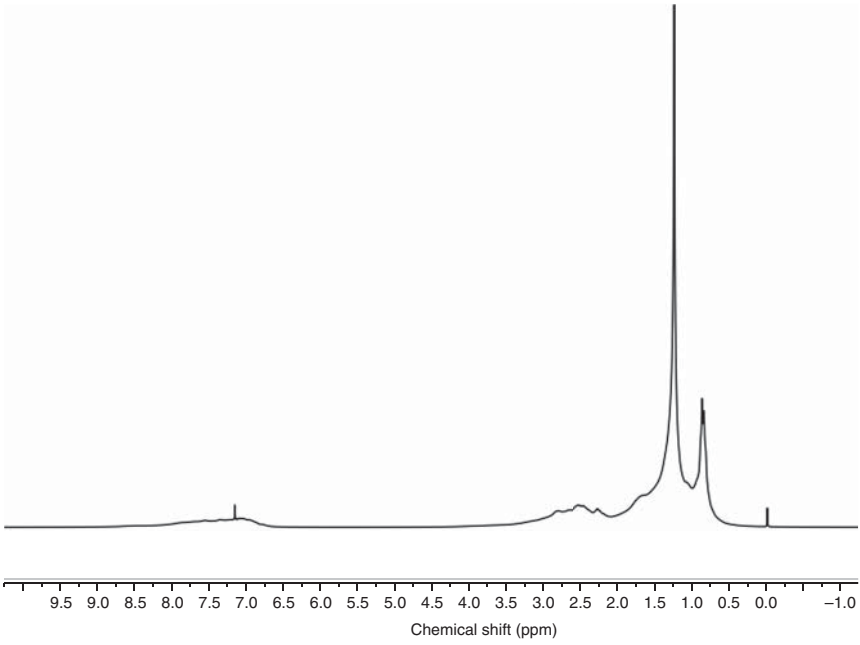

Figure 6.1 Characteristic ^{1}H NMR spectrum of bitumen.

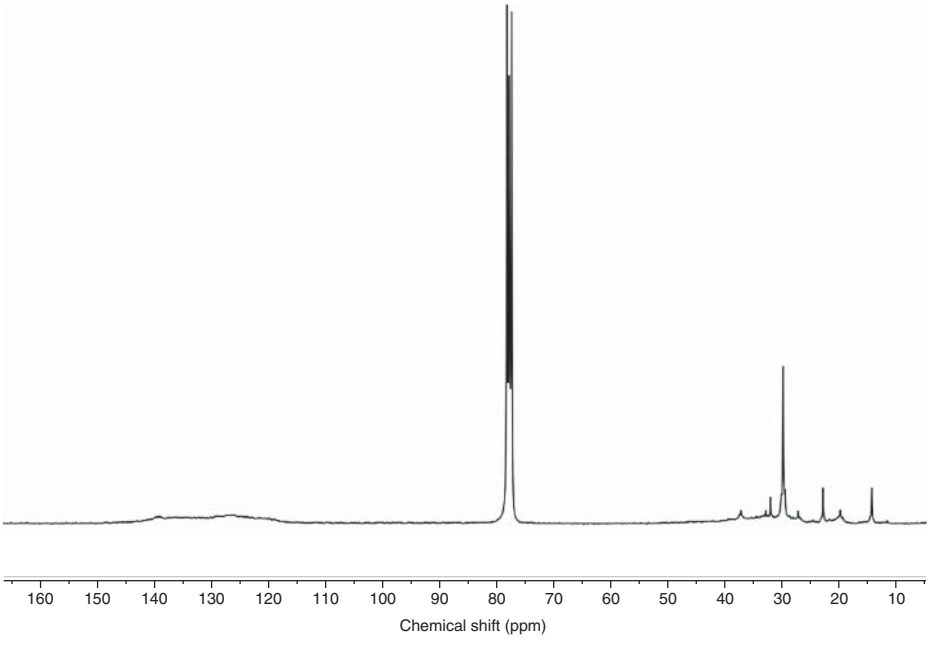

Figure 6.2 Typical ^{13}C NMR spectrum of bitumen.

Table 6.3 Structural average molecular parameters. *Source:* Michon *et al.* (1997b). Reproduced with permission of Elsevier.

Parameter	Description
$C_t = C_{ali} + C_{aro}$	Total number of carbon atoms
$C_s\ (\%) = 100 \times (C_{ali}/C_t)$	Percentage of saturated carbon atoms
$C_a\ (\%) = 100 \times (C_{aro}/C_t)$	Percentage of aromatic carbons atoms
$f_a = C_{aro}/C_t$	Aromaticity
$R_a = 0.25 \times (C_{aro} - 1)$	Number of aromatic rings
$R_s = C_{qs}$	Number of alkyl substituents
$n = C_{ali}/C_{qs}$	Number of carbon atoms per alkyl substituents
$f = (12\ C_{ali})\ /\ [3\ (CH_3 + CH_{3\alpha}) + 2\ (CH_2 + CH_{2\alpha}) + (CH + CH_\alpha)]$	Carbon/hydrogen weight ratio of alkyl substituents
$R = n \times (1 - 6/f) + 0.5$	Number of naphthenic rings per alkyl substituent
$R_n = r \times C_{qs}$	Number of naphthenic rings
$C_{anb} = CH_{aro} + C_{qs}$	Number of non-bridge aromatic ring carbon atoms
$C_{anb}\ (\%) = 100 \times (C_{anb}/C_t)$	Percentage of aromatic carbons atoms
$S\ (\%) = 100 \times (C_{qs}/C_t)$	Percentage of substituted aromatic carbon atoms

Both ^{1}H and ^{13}CNMR data have been used to calculate bitumen average molecular parameters (Michon *et al.*, 1997b; Smith *et al.*, 1976). Typical ^{13}C NMR-based parameters defined by Michon *et al.* (1997b) are summarized in Table 6.3. For example, the use of a proper internal standard (e.g. dioxane) allows the quantification of aliphatic (C_{ali}), aromatic (C_{aro}) and aromatic substituted quaternary (C_{qs}) carbon atoms based on the peak areas corresponding to their chemical shifts (Table 6.2). Afterwards, one can calculate bitumen aromaticity (f_a), and the number of aromatic (R_a) and naphthenic (R_n) rings per average molecule, using the equations presented in Table 6.3. Furthermore, distortionless enhancement by polarization transfer (DEPT) ^{13}C NMR enables the discrimination between methyl (CH_3), methylene (CH_2), methine (CH) and quaternary carbons and the analysis of hydrocarbon branching (Michon *et al.*, 1997b). The method provides data to calculate additional average structural parameters, such as the carbon/hydrogen weight ratio of alkyl substituents and the average number of naphthenic rings per alkyl substituents, as described in Table 6.3. In summary, these parameters have been used to characterize unaged and aged bitumens, and are the basis of the mechanisms proposed by Michon *et al.* (1999a) to explain the aromatization that occurs during bitumen ageing.

Avella and Fierro (2010) proposed a distinct approach for the structural characterization of heavy fractions of petroleum, based on ^{1}H and ^{13}C NMR spectroscopy and elemental analysis. The authors proposed unified integration intervals of chemical shifts in the NMR spectra, statistically optimized (based on data retrieved form the scientific literature) and corrected to account for partial overlapping of some signals assigned to different proton/carbon moieties within the same integration interval, and developed correlations to calculate average structural parameters of oil, coal and their fractions. Recently, Cardoso *et al.*, (2016) compared the Avella and Fierro (2010) approach with the earlier methods of Siddiqui and Ali (1999) and Hasan *et al.* (1983), for the structural characterization of fresh (unfractionated) bitumen by NMR. They reported several advantages of the former method for bitumen analysis, namely: (1) it provides a more detailed structural characterization because it considers a larger number of intervals in the spectrum (37 in ^{1}H NMR, and 39 in ^{13}C NMR) assigned to a greater number of distinct structural fragments; (2) it allows the quantification of different types of carbons in the aliphatic and aromatic fractions, including the determination of the quaternary carbons content and the discrimination of those bonded to a heteroatom; (3) it incorporates a useful factor to convert the integrals between NMR spectra (^{1}H NMR or ^{13}C NMR) of the same sample; and (4) it permits the estimation of an average empirical formula, molecular mass and degree of unsaturation.

NMR can be combined with different chemometric methods in order to generate quantitative structure–activity relationship (QSAR) models to predict physicochemical properties of bitumen. For instance, Molina *et al.* (2007, 2010) and Molina *et al.* (2014) used chemometrics and NMR data to accurately predict the boiling point, specific gravity, density and colloidal instability indices of crude oils and fractions thereof. Similarly, chemometric analysis was used to correlate the SARA fractions with NMR data for vacuum residues, based on partial least square (PLS) and multiple linear regression (MLR) methods (Molina *et al.*, 2010). The PLS approach requires pre-processing NMR data by the so-called binning procedure (i.e. the frequency of the peaks within a given chemical shift interval are replaced by a representative value, usually the area under the spectrum for each segment) and related to a specific property of the samples being analysed. Figure 6.3 illustrates the bin partition applied to the ^{1}H NMR spectrum of a crude oil, which is also adopted for NMR analysis of petroleum residues, bitumen and their derivatives (Cardoso *et al.*, 2016). The correlations between measured and predicted SARA fractions of a crude oil are plotted in Figure 6.4, illustrating the reliability of the procedure which is faster and cheaper than the conventional methods.

Similarly, ^{13}C NMR spectra can be sectioned into bins within specific chemical shift intervals. For example, Michon *et al.* (1997a) used quantitative structure properties relationship (QSPR) models, more specifically neural networks (NN) analysis, to correlate the rheological parameters of bitumens

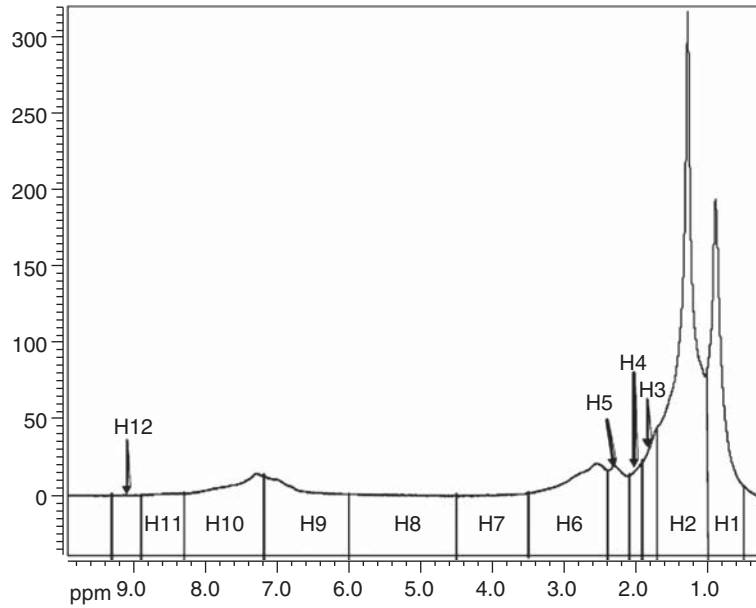

Figure 6.3 ^{1}H NMR spectrum of a crude oil and spectral partition. *Source:* Molina *et al.*, (2007). Reproduced with permission of American Chemical Society.

with the average molecular parameters characterizing their hydrocarbon skeleton.

Low field NMR relaxometry, also known as time-domain nuclear magnetic resonance (TD-NMR), is a rapid and inexpensive method to characterize the molecular dynamics of polymeric materials. It has been used for the characterization of oil and gas reservoirs in Texas and in the North Sea (Kantzas, 2009). The method is based on the measurement of amplitudes and relaxation times of ^{1}H NMR signals, thus providing information about the content and relative mobility of hydrogen-bearing molecules in the sample, respectively. Typically, both longitudinal (T_1) and transverse (T_2) relaxation times are measured (Kantzas, 2009), where the former is associated with short-range motions and the latter is mainly determined by the mobility of polymer chains as a whole (Kovalakova *et al.*, 2013).

The spin–spin relaxation time (T_2) of ^{1}H nuclei can be used to determine the softening point of bituminous materials and hence evaluate their colloidal morphology (Filippelli *et al.*, 2012; Rossi *et al.*, 2015). In fact, the distribution of the T_2 relaxation times of bitumen at different ageing stages and temperatures, when combined with microscale scanning electron microscopy analysis, enlightens the nature of the interactions between the additives and the colloidal network (Rossi *et al.*, 2015). This is illustrated in Figure 6.5

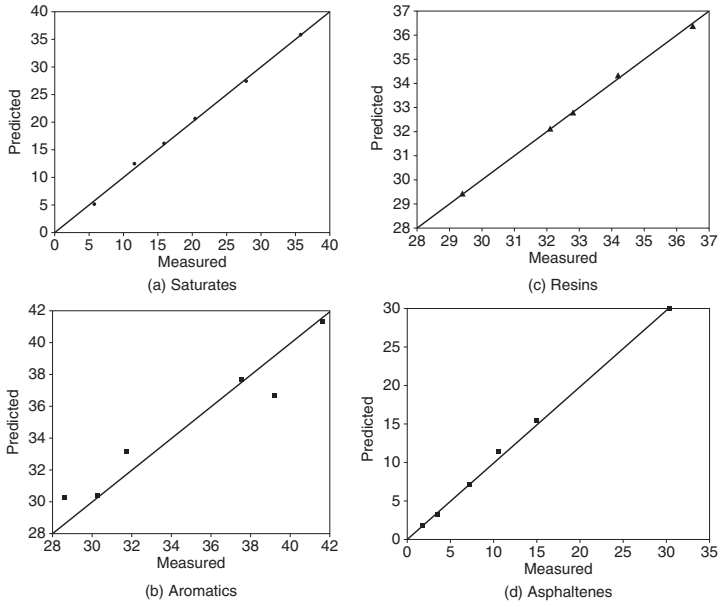

Figure 6.4 Correlation between the SARA fractions of vacuum residues from Colombian crude oils measured and predicted by ^{1}H NMR analysis. *Source:* Molina *et al.* (2010). Reproduced with permission of Elsevier.

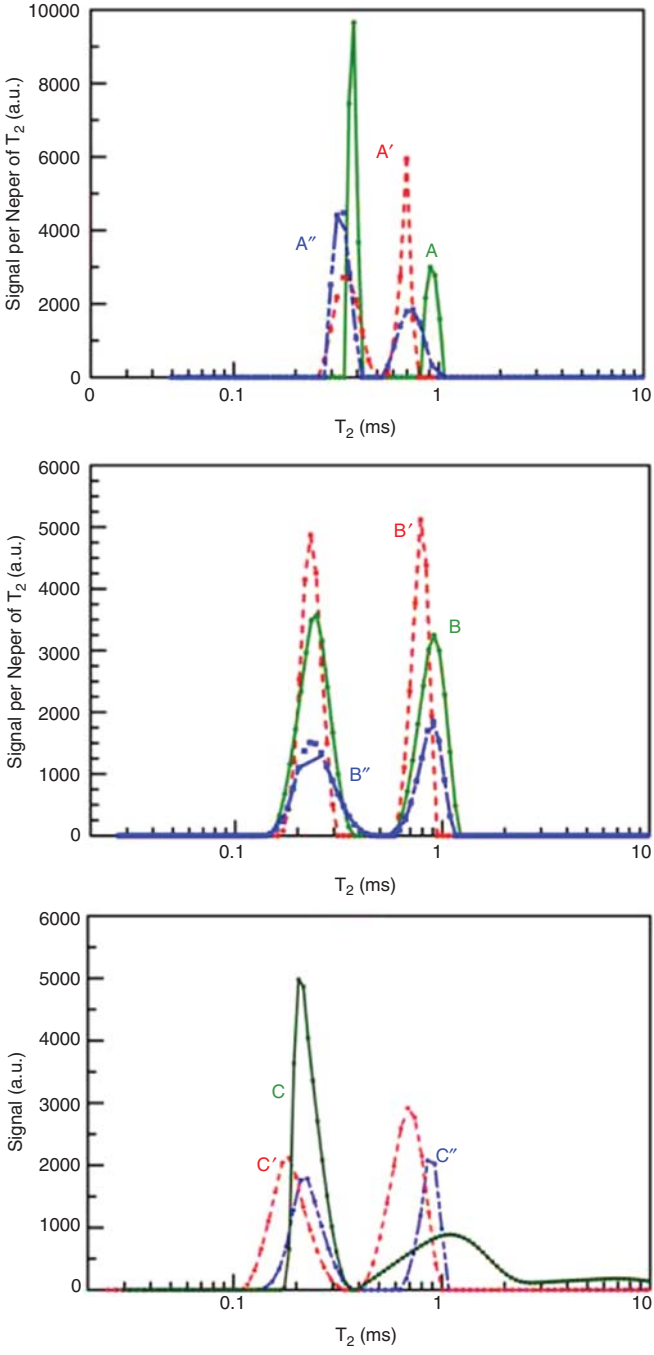

Figure 6.5 Distribution of transverse (T_2) relaxation times for bitumen (A), bitumen modified with SBS (B) and bitumen modified with SBS and PPA (C) analysed at 30 °C after different ageing steps, namely: no ageing (A, B, C), RTFOT ageing (A′, B′, C′) and PAV ageing (A″, B″, C″). *Source:* Rossi *et al.*, (2015). Reproduced with permission of Elsevier.

for a base bitumen from Kazakhstan, unmodified, modified with a linear styrene-butadiene-styrene (SBS) polymer (4 wt%), and modified sequentially with SBS (4 wt%) and PPA (0.2 wt%). In all cases, bitumens were aged by two different methods to simulate short-term and long-term ageing, namely the rolling thin film oven test (RTFOT) and the pressure ageing vessel (PAV) test, respectively. In Figure 6.5, the peaks at smaller T_2 times (around 0.3 ms) were assigned to the more rigid supramolecular aggregates of asphaltenes, while the peaks at higher T_2 times (between 0.6 and 1.0 ms) were attributed to the more mobile maltene fraction (Rossi *et al.*, 2015). In general, the positions of the two peaks shift towards shorter relaxation times, indicating a gradual increase of bitumen rigidity and viscosity upon ageing. The stabilizing effect of SBS (anti-ageing agent) is clearly revealed by the smaller change in peak positions for SBS modified bitumen. The influence of PPA is not so obvious (probably because of its low content), yet the slight shift towards shorter times was related to smaller sizes of the micellar aggregates in PPA/SBS-modified bitumen (Rossi *et al.*, 2015).

6.3 Phosphorus-31 NMR Spectroscopy

The interaction of PPA with bitumen and model compounds of bitumen has been studied by ^{31}P NMR spectroscopy to elucidate the mechanisms behind PPA modification. For example, Miknis and Thomas (2008) used ^{31}P NMR to analyse the structure of phosphorus-containing compounds eventually formed by the reaction of PPA (105% grade) with bitumen. In opposition to the earlier hypothesis of Orange *et al.* (2004), they concluded that organic phosphate esters are not formed and they suggested that phosphorus is initially (i.e. immediately after mixing PPA with bitumen) present as phosphoric acid (H_3PO_4) and also in end and middle groups of polyphosphate chains. However, as the reaction proceeds the resonance signals of phosphorus in end groups disappear progressively, indicating that instead of incorporating the organic molecules of bitumen PPA hydrolyses back to H_3PO_4, owing to the presence of residual water in bitumen (Miknis and Thomas, 2008). Varanda *et al.* (2016) arrived at the same conclusions in their study of PPA modified bitumen blends (see Figures 6.6 and 6.7). In fact, the ^{31}P resonance peaks assigned to phosphorus in polyphosphate chains (−13 ppm and −26 ppm, respectively for end and middle groups) are clearly visible in the spectrum of PPA (Figure 6.6) and absent from the spectra of PPA modified bitumen blends (Figure 6.7). The broad signal observed for the blends, approximately at 1 ppm, indicates that PPA was completely hydrolysed back to H_3PO_4, as previously reported by Miknis and Thomas (2008).

Although mainly used to study the interactions between PPA and bitumen, ^{31}P NMR can be useful to study the influence of other additives on PPA

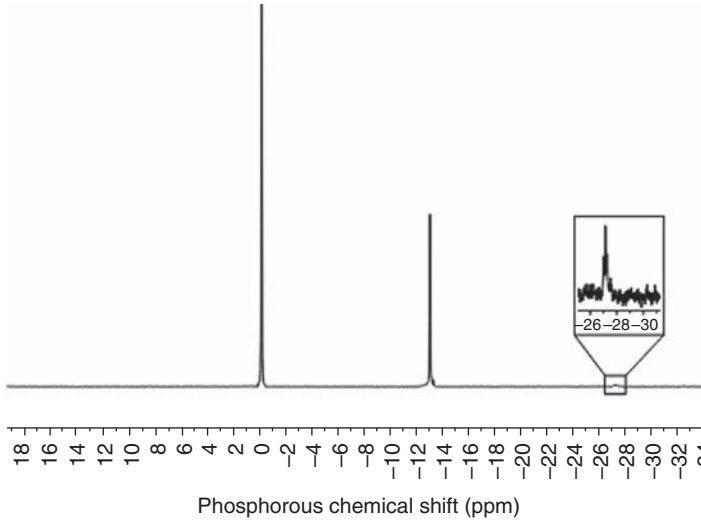

Figure 6.6 ^{31}P NMR spectrum of commercial PPA (105% grade): the resonance peak at 0 ppm is attributed to phosphorus in H_3PO_4, a smaller peak at −13 ppm is assigned to phosphorus in end groups of PPA chains and a much smaller peak around −26 ppm is ascribed to phosphorus in middle groups of PPA chains. *Source:* Varanda *et al.* (2016).

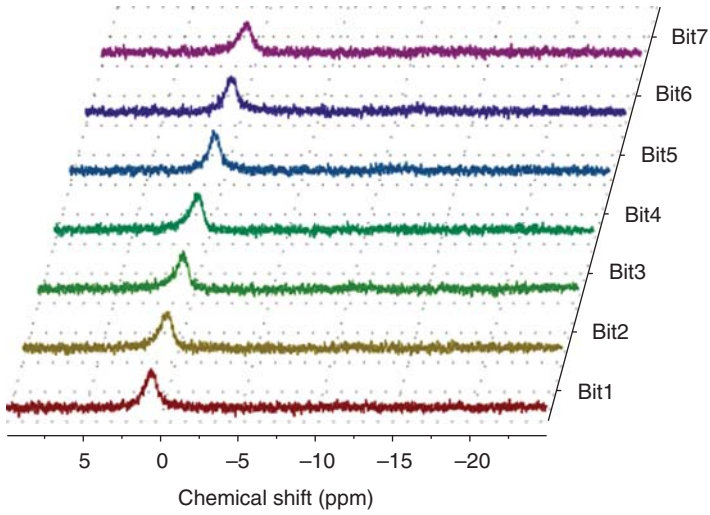

Figure 6.7 ^{31}P NMR spectra of PPA modified bitumen blends (Bit1 to Bit7). The resonance peak around 1 ppm corresponds to phosphorus in H_3PO_4. The peaks attributed to phosphorus in polyphosphate chains (see Figure 6.6) are clearly absent. *Source:* Varanda *et al.* (2016).

modified bitumen. For instance, Miknis and Schuster (2009) analysed the effect of hydrated lime (an antistrip agent) added to bitumen samples before or after PPA modification. In both cases, the ^{31}P NMR spectra revealed the presence of calcium phosphate salts in bitumen, formed by acid-base reactions between PPA and hydrated lime. The same phenomenon was observed with real samples from a paving road mix (Schuster *et al.*, 2011). Interestingly, no reactions were observed between PPA and limestone fines commonly used as fillers (Miknis and Schuster, 2009). These findings are very important since any improvement of bitumen-binding properties obtained by PPA modification may be lost if hydrated lime is used as an additive.

6.4 NMR Imaging and Solid-State NMR

6.4.1 Solid-State NMR

Solid-state NMR techniques are generally used to determine the mass fractions of amorphous and crystalline phases in polymers, and thus the crystallinity. The technique has been applied to evaluate the crystallinity of asphalts which was found to correlate with the fracture temperature, i.e. a low temperature cracking parameter (Michon *et al.*, 1999b).

The solid-state ^{13}CNMR spectra for asphalts from different geographic sources (see Figure 6.8) present well-defined resonance peaks assigned to long-chain *n*-alkanes terminal methyl groups (at ca. 14 ppm) and internal methylene carbons (in the region of 30–32 ppm), and broad resonance in the range of 15–27 ppm due to branched alkane methyl groups, and others (Michon *et al.*, 1999b). The narrow peak at ca. 32 ppm and the broader peak at ca. 30 ppm have been assigned to internal methylene carbons in crystalline and amorphous phases, respectively (Netzel, 1998). Since the crystalline peak is associated to long-chain *n*-alkanes, it reveals the content of macrocrystalline wax in asphalts, whereas microcrystalline waxes (branched alkanes) of an asphalt are not easily observed by ^{13}C NMR because of their resonances at different chemical shift positions (Michon *et al.*, 1999b).

Detailed analysis of solid-state ^{13}C NMR spectra by peak deconvolution and integration provides additional information about composition and average structural parameters of asphalts, such as aromaticity, aliphatic and methylene carbon fractions, crystallinity. (Jennings *et al.*, 1993; Michon *et al.*, 1999b).

Solid-state ^{31}P NMR measurements can also be used to determine the fate of PPA in real pavements such as those built-in Mn Road, a sophisticated pavement test track owned and operated by the Minnesota Department of Transportation (http://www.dot.state.mn.us/mnroad/). The data collected confirmed that most PPA reacted with hydrated lime to form calcium phosphates (Schuster *et al.*, 2011).

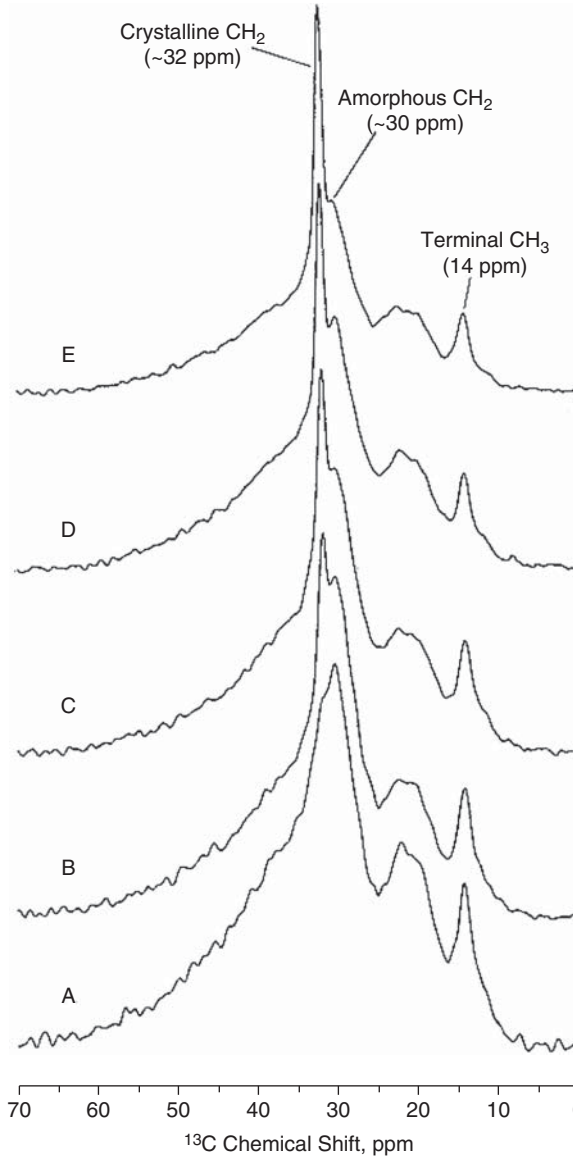

Figure 6.8 ^{13}C cross polarization magic-angle spinning (CPMAS) NMR spectra of asphalts from different sources, at −45 °C: (A) Venezuela, (B) Middle East, (C) Italy, (D) Africa and (E) North Africa. *Source:* Michon *et al.* (1999b). Reproduced with permission of American Chemical Society.

6.4.2 NMR Imaging

NMR imaging is a powerful non-invasive technique widely used in medicine. It may be used to follow chemical and physical transformations of the inner regions of untreated samples, over time. Owing to the opaque nature of

bitumen, magnetic resonance imaging (MRI) provides information not obtainable by other methods (Miknis *et al.*, 1998).

MRI combines the basic principles of NMR with spatial encoding to provide a visualization of the distribution of specific fluids in a sample (Miknis and Netzel, 1996). Water is the preferred fluid for MRI, mainly because of the high sensitivity of the hydrogen nucleus in NMR and the favourable relaxation times. Accordingly, ^{1}H NMR imaging may be used to obtain information about bitumen susceptibility to water and moisture damage mechanisms (Miknis and Netzel, 1996).

MRI measurements use spin echo (SE) imaging techniques for non-viscous materials because the associated relaxation times are generally long, thus more favourable for SE imaging (Miknis and Netzel, 1996). For viscous and elastomeric materials, such as bitumens, the relaxation times of protons are generally too short for SE imaging and thus three-dimensional techniques are used instead (Miknis and Netzel, 1996). NMR imaging has been used to study asphaltenes precipitation (Miknis *et al.*, 1998), the effects of heating on rubber incorporated in bitumen (Miknis and Michon, 1998) and to measure the surface tension of water drops on bitumen (Miknis *et al.*, 2005). Figure 6.9 illustrates this example, presenting the NMR images of a water droplet falling on different bitumen samples over a period of one week (Miknis *et al.*, 2005).

In a study on natural and styrene-butadiene crumb rubbers dissolved in asphalt it was possible to demonstrate that MRI can be used to assess different interactions between crumb rubbers and asphalt, such as swelling by asphalt molecules, possible dissolution of rubber components in asphalt and devolatilization and crosslinking in rubber when heated at high mix temperatures (170 °C) (Miknis and Michon, 1998).

6.5 Conclusion

NMR spectroscopy has gained increasing relevance in the area of structural and molecular characterization of complex compounds such as bitumen. Several examples have been presented for ^{1}H, ^{13}C and ^{31}P NMR, and also for NMR imaging and solid-state NMR (^{13}C and ^{31}P).

NMR spectroscopy has been used to obtain detailed chemical information about the proton and carbon chemistry of neat bitumen and modified bitumens, in addition to their structure and rheological behaviour. Overall, NMR techniques are powerful and accessible tools useful for investigating fundamental aspects of bitumen chemistry and to improve the quality of bitumens and derivatives thereof. Moreover, it is also a valuable source of data for chemometric analysis and model development to predict physical and/or chemical properties of bitumen.

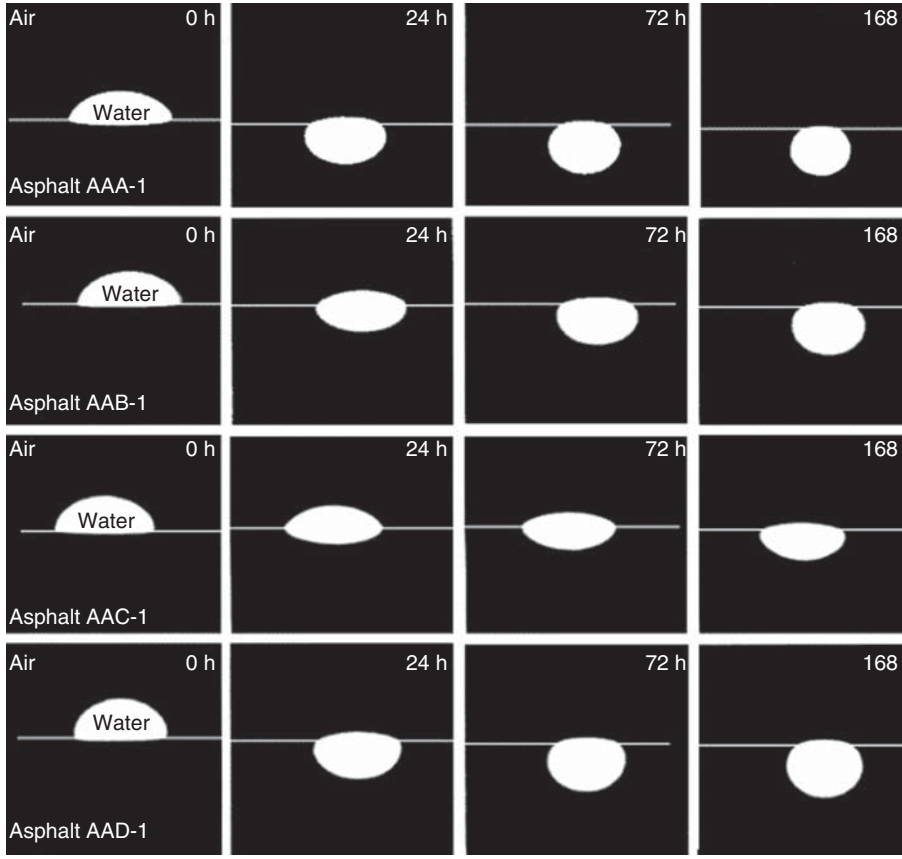

Figure 6.9 NMR images of water drops falling into four asphalts (AAA, AAB, AAC and AAD) from the Strategic Highway Research Program (SHRP) over a period of one week *Source:* Miknis *et al.* (2005). Reproduced with permission of Elsevier.

References

Ali, M. F. and Siddiqui, M. N. (2001) Changes in asphalt chemistry and durability during oxidation and polymer modification. *Petroleum Science and Technology*, 19, 1229–1249.

Avella, E. and Fierro, R. (2010) Intervalos de integración unificados para la caracterización estructural de petróleos, carbones o sus fracciones por RMN 1H y RMN 13C. *Revista Colombiana de Química*, 39, 87–109.

Baldino, N., Gabriele, D., Lupi, F. R., *et al.* (2013) Rheological effects on bitumen of polyphosphoric acid (PPA) addition. *Construction and Building Materials*, 40, 397–404.

Bonemazzi, F. and Giavarini, C. (1999) Shifting the bitumen structure from sol to gel. *Journal of Petroleum Science and Engineering*, 22, 17–24.

Borrego, A. G., Blanco, C. G., Prado, J. G., *et al.* (1996) 96/04879 1H NMR and FTIR spectroscopy studies of bitumen and shale oil from selected Spanish oil shales. *Fuel and Energy Abstracts*, 37, 344.

Cardozo, F. B., Moreno, E. A. and Trujillo, C. A. (2016) Structural characterization of unfractionated asphalts by 1H NMR and 13C NMR. *Energy & Fuels*, 30, 2729–2740.

Cheung, C. Y. and Cebon, D. (1997) Deformation mechanisms of pure bitumen. *Journal of Materials in Civil Engineering*, 9, 117–129.

Christensen, D. W. and Anderson, D. A. (1992) *Chemical-Physical Property Relationships for Asphalt Cements and the Dispersed Polar Fluid*, American Chemical Society, Washington DC.

Dickinson, E. M. (1980) Structural comparison of petroleum fractions using proton and 13C n.m.r. spectroscopy. *Fuel*, 59, 290–294.

Filippelli, L., Gentile, L., Rossi, C. O., *et al.* (2012) Structural change of bitumen in the recycling process by using rheology and NMR. *Industrial & Engineering Chemistry Research*, 51, 16346–16353.

Gentile, L., Filippelli, L., Rossi, C. O., *et al.* (2012) Rheological and 1H-NMR spin-spin relaxation time for the evaluation of the effects of PPA addition on bitumen. *Molecular Crystals and Liquid Crystals*, 558, 54–63.

Giavarini, C., Mastrofini, D., Scarsella, M., *et al.* (2000) Macrostructure and rheological properties of chemically modified residues and bitumens. *Energy & Fuels*, 14, 495–502.

Giraudeau, P. and Baguet, E. (2006) Improvement of the inverse-gated-decoupling sequence for a faster quantitative analysis of various samples by 13C NMR spectroscopy. *Journal of Magnetic Resonance*, 180, 110–117.

Hasan, M. U., Ali, M. F. and Bukhari, A. (1983) Structural characterization of Saudi Arabian heavy crude oil by n.m.r. spectroscopy. *Fuel*, 62, 518–523.

Herrington, P. R., Patrick, J. E. and Ball, G. F. A. (1994) Oxidation of roading asphalts. *Industrial & Engineering Chemistry Research*, 33, 2801–2809.

Jeglic, P., Apih, T., Lahajnar, G., *et al.* (2003) NMR-melting-curve study of bitumen of different types and origin. *Applied Magnetic Resonance*, 24, 13–23.

Jennings, P. W., Pribanic, J. A., Desando, M. A., *et al.* (1993) *Binder Characterization and Evaluation by Nuclear Magnetic Resonance Spectroscopy*, SHRP report A-335, National Research Council, Washington DC.

Jones, D. R. (1992) Technical Memorandum #4: *Understanding How the Origin and Composition of Paving-Grade Asphalt Cements Affect Their Performance*. SHRP Asphalt Research Program Center for Transportation Research, University of Texas, Austin, TX.

Kantzas, A. (2009) Advances in magnetic resonance relaxometry for heavy oil and bitumen characterization. *Journal of Canadian Petroleum Technology*, 48, 15–23.

Kharrat, A. M., Zacharia, J., Cherian, V. J., *et al.* (2007) Issues with comparing SARA methodologies. *Energy & Fuels*, 21, 3618–3621.

Kovalakova, M., Fricova, O., Hronsky, V., *et al.* (2013) Characterisation of crumb rubber modifier using solid-state nuclear magnetic resonance spectroscopy. *Road Materials and Pavement Design*, 14, 946–958.

Le Guern, M., Chailleux, E., Farcas, F., *et al.* (2010) Physico-chemical analysis of five hard bitumens: Identification of chemical species and molecular organization before and after artificial aging. *Fuel*, 89, 3330–3339.

Lesueur, D. (2009) The colloidal structure of bitumen: Consequences on the rheology and on the mechanisms of bitumen modification. *Advances in Colloid and Interface Science*, 145, 42–82.

Masson, J. F. (2008) Brief review of the chemistry of polyphosphoric acid (PPA) and bitumen. *Energy & Fuels*, 22, 2637–2640.

Masson, J. F. and Gagne, M. (2008) Ionic pairs in polyphosphoric acid (PPA)-modified bitumen: Insights from model compounds. *Energy & Fuels*, 22, 3390–3394.

Michon, L., Hanquet, B., Diawara, B., *et al.* (1997a) Asphalt study by neuronal networks: Correlation between chemical and rheological properties. *Energy & Fuels*, 11, 1188–1193.

Michon, L., Martin, D., Planche, J.-P., *et al.* (1997b) Estimation of average structural parameters of bitumens by 13C nuclear magnetic resonance spectroscopy. *Fuel*, 76, 9–15.

Michon, L., Netzel, D. A., Hanquet, B., *et al.* (1999a) Carbon-13 molecular structure parameters of RTFOT aged asphalts: Three proposed mechanisms for aromatization. *Petroleum Science and Technology*, 17, 369–381.

Michon, L. C., Netzel, D. A., Turner, T. F., *et al.* (1999b) A C-13 NMR and DSC study of the amorphous and crystalline phases in asphalts. *Energy & Fuels*, 13, 602–610.

Miknis, F. P. and Michon, L. C. (1998) Some applications of nuclear magnetic resonance imaging to crumb rubber modified asphalts. *Fuel*, 77, 393–397.

Miknis, F. P. and Netzel, D. A. (1996) Use of nuclear magnetic resonance imaging to study asphalt. Preprints of Papers, American Chemical Society, Division of Fuel Chemistry, Medium: X; Size: pp. 1327–1331.

Miknis, F. P., Pauli, A. T., Beemer, A., *et al.* (2005) Use of NMR imaging to measure interfacial properties of asphalts. *Fuel*, 84, 1041–1051.

Miknis, F. P., Pauli, A. T., Michon, L. C., *et al.* (1998) NMR imaging studies of asphaltene precipitation in asphalts. *Fuel*, 77, 399–405.

Miknis, F. P. and Schuster, W. C. (2009) NMR study of hydrated lime and limestone in polyphosphoric acid modified bitumen. *Road Materials and Pavement Design*, 10, 815–831.

Miknis, F. P. and Thomas, K. P. (2008) NMR analysis of polyphosphoric acid-modified bitumens. *Road Materials and Pavement Design*, 9, 59–72.

Molina, D., Angulo, R., Dueñez, F. Z., *et al.* (2014) Partial least squares (PLS) and multiple linear correlations between Heithaus stability parameters (Po) and the colloidal instability indices (CII) with the 1H nuclear magnetic resonance (NMR) spectra of Colombian crude oils. *Energy & Fuels*, 28, 1802–1810.

Molina, D., Uribe, U. N. and Murgich, J. (2007) Partial least-squares (PLS) correlation between refined product yields and physicochemical properties with the 1H nuclear magnetic resonance (NMR) spectra of Colombian crude oils. *Energy & Fuels*, 21, 1674–1680.

Molina, D., Uribe, U. N. and Murgich, J. (2010) Correlations between SARA fractions and physicochemical properties with 1H NMR spectra of vacuum residues from Colombian crude oils. *Fuel*, 89, 185–192.

Nellensteyn, F. J. (1924) The constitution of asphalt. *Journal of the Institution of Petroleum Technologists*, 10, 311–323.

Netzel, D. (1998) Low temperature studies of amorphous, interfacial, and crystalline phases in asphalts using solid-state 13C nuclear magnetic resonance. *Transportation Research Record: Journal of the Transportation Research Board*, 1638, 23–30.

Orange, G., Depuis, D., Martin, J. V., *et al.* (2004) *Chemical Modification of Bitumen through PPA: Properties-microstructure relationship*. Third Euroasphalt and Eurobitume Congress, Vienna, 12th–14th May 2004.

Petersen, J., Robertson, R., Branthaver, J., *et al.* (1994) *Binder Characterization and Evaluation: Volume 1*. SHRP report A-367, National Research Council, Washington DC.

Pfeiffer, J. P. and Saal, R. N. J. (1940) Asphaltic bitumen as colloid system. *Journal of Physical Chemistry*, 44, 139–149.

Polacco, G., Filippi, S., Merusi, F. and Stastna, G. (2015) A review of the fundamentals of polymer-modified asphalts: Asphalt/polymer interactions and principles of compatibility. *Advances in Colloid and Interface Science*, 224, 72–112.

Ramsey, J. W., McDonald, F. R. and Petersen, J. C. (1967) Structural study of asphalts by nuclear magnetic resonance. *I&EC Product Research and Development*, 6, 231–236.

Rosinger, A. (1914) Beiträge zur Kolloidchemie des Asphalts. *Kolloid-Zeitschrift*, 15, 177–179.

Rossi, C. O., Spadafora, A., Teltayev, B., *et al.* (2015) Polymer modified bitumen: Rheological properties and structural characterization. *Colloids and Surfaces A: Physicochemical and Engineering Aspects*, 480, 390–397.

Schuster, W. C., Wolf, J. M. and Miknis, F. P. (2011) Phosphorous-31 NMR studies of Mn Road Test Track Cells. *Road Materials and Pavement Design*, 12, 931–944.

Siddiqui, M. N. (2009) NMR finger printing of chemical changes in asphalt fractions on oxidation. *Petroleum Science and Technology*, 27, 2033–2045.

Siddiqui, M. N. (2010) NMR Fingerprinting of chemical changes in asphalt fractions on oxidation. *Petroleum Science and Technology*, 28, 401–411.

Siddiqui, M. N. and Ali, M. F. (1999) Investigation of chemical transformations by NMR and GPC during the laboratory aging of Arabian asphalt. *Fuel*, 78, 1407–1416.

Silva, S. L., Silva, A. M. S., Ribeiro, J. C., *et al.* (2011) Chromatographic and spectroscopic analysis of heavy crude oil mixtures with emphasis in nuclear magnetic resonance spectroscopy: A review. *Analytica Chimica Acta*, 707, 18–37.

Smith, W. E., Napier, B. and Horne, O. J. (1976) Characterization of petroleum pitches used for coke production. In: *Petroleum Derived Carbons*. American Chemical Society, Washington, DC, 63–76.

Varanda, C., Portugal, I., Ribeiro, J., *et al.* (2016) Influence of polyphosphoric acid on the consistency and composition of formulated bitumen: standard characterization and NMR insights. *Journal of Analytical Methods in Chemistry*, 16.

Williams, R. B. (1958) Characterization of hydrocarbons in petroleum by nuclear magnetic resonance spectrometry. In: Symposium on composition of petroleum oils, determination and evaluation. *ASTM Spec Techn Publ.*, 224, 168–194.

Woods, J., Kung, J., Kingston, D., *et al.* (2008) Canadian crudes: A comparative study of SARA fractions from a modified HPLC separation technique. *Oil & Gas Science and Technology: Revue D Ifp Energies Nouvelles*, 63, 151–163.

Yoshida, T., Maekawa, Y., Uchino, H., *et al.* (1980) Derivation of structural parameters for coal-derived oil by carbon-13 nuclear magnetic resonance spectrometry. *Analytical Chemistry*, 52, 817–820.

7

Applications of Low Field Magnetic Resonance in Viscous Crude Oil/Water Property Determination

Jonathan L. Bryan[1, 2] *and Apostolos Kantzas*[1, 2]

[1] *Department of Chemical and Petroleum Engineering, Schulich School of Engineering, University of Calgary, Calgary, Alberta, Canada*
[2] *PERM Inc., 3956 29 St NE, Calgary, Alberta, Canada T1Y 6B6*

7.1 Introduction

Nuclear magnetic resonance (NMR) is a measurement of the response of atomic nuclei to the presence of external magnetic fields. The premise behind NMR is that many elements contain a net magnetic moment and an angular momentum, or nuclear spin (Coates, Xiao, and Prammer, 1999; Dunn, Bergman, and LaTorraca, 2002). When these elements are placed inside a static magnetic field, the external field produces a torque that tends to align the elements in the direction of this field. If the magnetic moment of the element acted just like a tiny bar magnet, the nuclei would simply align in the direction of the external magnetic field. However, nuclei also have momentum, so this causes them to behave like a gyroscope, precessing around the direction of the external field lines (Dunn, Bergman, and LaTorraca, 2002). This precession action is important to NMR because different elements will each rotate at their own frequencies. Designers of NMR equipment can set their receivers to pick up signals at a given frequency corresponding to a desired element, and thus measure the NMR signals from just these components.

The nucleus of hydrogen contains only one proton and no neutrons, and thus hydrogen has a fairly strong magnetic moment and will precess at a much higher frequency than other elements (Coates, Xiao, and Prammer, 1999). NMR tools can therefore be tuned to pick up the response of protons in magnetic fields. Protons are also abundant in both water and hydrocarbons, so hydrogen NMR tools can be used to measure and interpret the response from reservoir fluids (oil and water). NMR measurements are non-destructive, they can be run on fairly small samples if needed, and most importantly can be run on fluids in porous media. In this state, the NMR signal comes only from the

Analytical Characterization Methods for Crude Oil and Related Products, First Edition.
Edited by Ashutosh K. Shukla.

pore fluids and not from the rock material. This means that NMR data are not sensitive to the type of rock system studied (e.g. sandstone vs. carbonate), which is beneficial when running tests in complex and heterogeneous rock types.

On a further practical note, if NMR tools need only to be tuned to measure the signal from hydrogen, these tools can be operated at very low frequencies (1–2 MHz). This is known as "low field NMR," in contrast to the high field units used in NMR spectroscopy or in medical MRI systems. The low frequency of these tools allows them to be used easily in laboratory settings or even in oilfield operations, as logging tools to measure the signal of pore fluids at reservoir conditions.

The application of low field NMR for reservoir petrophysics dates back to the 1950s and 1960s (Brown and Gamson, 1960). In these early applications, the goal was to measure the total fluid present and to gain an understanding of the viscosity of the fluid based on the fluid NMR relaxation times. It was during the 1990s, however, when pulsed NMR logging tools were introduced to the oil industry, that this technology gained widespread exposure and acceptance. A key part of the increased usage of NMR was the discovery that water in porous media relaxed much more quickly than bulk fluids, so NMR could now be used not only to evaluate the pore fluids but also the pore size distributions of various rock types (Dunn, Bergman, and LaTorraca, 2002). The focus moved away from reservoir fluid characterization and on to evaluation of bound vs. mobile fluids (Kleinberg and Vinegar, 1996; Straley *et al*., 1997; Chang *et al*., 1997; Cannon and Cao, 1998) and rock permeability (LaTorraca, Dunn, and Brown, 1993; Kenyon, 1997; Coates, Xiao, and Prammer, 1999).

The increase in low field NMR usage in petrophysics during the 1990s also corresponded with the time oil producers were also focusing more heavily on production of heavy oil and bitumen. Technological advances like horizontal wells and progressive cavity pumps were opening up new viscous oil deposits for recovery, and as a result the evaluation and characterization of heavy oil and bitumen systems also gained widespread significance. Early NMR models developed for conventional oil (Kleinberg and Vinegar, 1996; Straley *et al*., 1997) were extended to heavy oil systems (LaTorraca *et al.*, 1999; Mirotchnik *et al*., 1999; Galford and Marschall, 2000; Bryan *et al*., 2002a, 2003, 2005a). These NMR viscosity correlations have since been applied to *in situ* viscosity predictions in log and core (Bryan *et al*., 2005b, 2007; Burcaw, Kleinberg, and Bryan, 2008; Chen and Bryan, 2013).

This chapter focuses on interpretation of low field NMR relaxation distributions in heavy oil and bitumen systems. The basics of obtaining NMR relaxation distributions are provided as a basis for understanding how to interpret the relaxation distributions. Much more detailed explanations of NMR signal acquisition can be found in other literature sources (Coates, Xiao, and Prammer, 1999; Dunn, Bergman, and LaTorraca, 2002). This chapter studies the NMR response in mixtures of oil and water and diluted oils with solvents, with the goal of measuring fluid content (saturations) and fluid properties in heavy oil systems.

7.2 Background for NMR Measurements

As discussed previously, an NMR measurement begins with protons aligned and precessing about the external magnetic field lines: the longitudinal axis. At this time, a second magnetic field is applied to tip the protons 90° onto the transverse axis. In a traditional NMR measurement (known as a T_2 measurement) the signal is recorded on this transverse axis. Initially, all protons are tipped onto this axis and the signal is at its maximum value, as shown in Figure 7.1. Protons still have angular momentum so they continue to precess around the transverse axis. As they rotate around, several things may happen: (1) protons may lose phase coherence so the apparent signal on the transverse plane may disappear or (2) protons may give off energy and return to their equilibrium position aligned with the longitudinal plane. The loss of phase coherence is known as "free induction decay" (Dunn, Bergman, and LaTorraca, 2002) and does not represent a true loss of energy in the system. For this reason, NMR tools are run using pulse sequence processes that realign protons on the transverse plane so the true loss in energy can be measured. Details of this pulse sequencing are provided in other sources (Coates, Xiao, and Prammer, 1999; Dunn, Bergman, and LaTorraca, 2002).

With acquisition pulse sequencing used to obtain the true loss of signal on the transverse plane, what is measured is the decaying signal on this plane as protons give off energy and return to their equilibrium direction, precessing about the longitudinal plane. Figure 7.1 is an example of a measured decay curve.

The actual loss in signal as measured in Figure 7.1 is known as T_2 relaxation, or spin–spin relaxation (Bloembergen, Purcell, and Pound, 1948). In order to

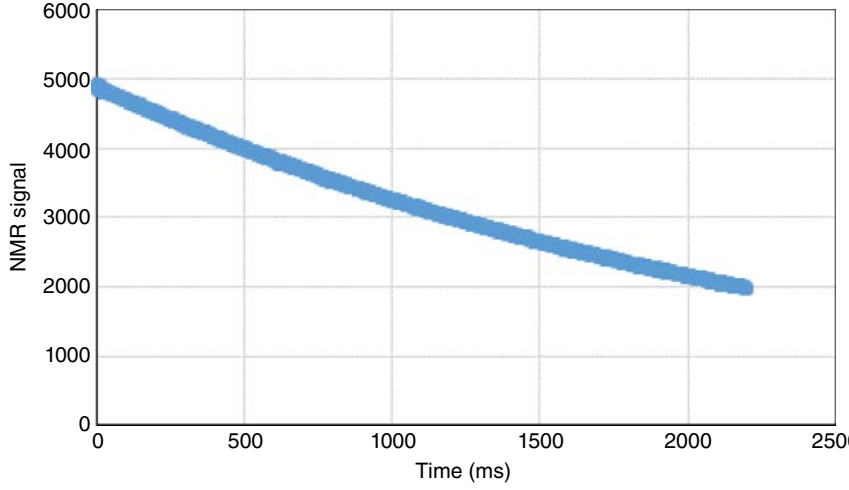

Figure 7.1 Measured NMR T_2 decay curve.

tip the protons initially onto the transverse plane, energy is provided to the nucleus. This energy is ideally lost by protons colliding with one another or into the walls of the porous medium enclosing these protons. As energy is lost the protons will stop precessing about the transverse plane and this is exhibited as an exponential loss in signal in the transverse plane.

An exponential trend line could be fitted to the decaying signal from Figure 7.1 and the representative relaxation time can be found for this single fluid. For more complex fluids like hydrocarbons, which contain a range of different compounds, or even for simple fluids which lose energy to the wells of porous media surrounding the fluid, each fluid component or pore size will relax at its own rate. The overall measured decay curve is therefore the combination of all of these terms. The decay is fitted to a multi-exponential function with a wide range of relaxation time constants using non-negative least squares (NNLS), and the output is a set of amplitudes corresponding to these various T_2 time constants. Figure 7.2 is an example of an output relaxation distribution. In this case, the relaxation data are fitted to a set of 51 pre-defined T_2 values ranging from 0.1 to 10,000 ms, and the NNLS procedures minimize the errors between the measured and reconstructed decay curve. All analysis of fluid properties and pore size distributions of the porous media containing these fluids are performed based on these relaxation distributions.

NMR relaxation distributions provide a measure of amplitude peaks at various T_2 relaxation times. The total amplitude of the entire relaxation distribution is the initial amplitude (time = 0) in Figure 7.1. The relaxation distribution may be split into multiple peaks. The summation of amplitude

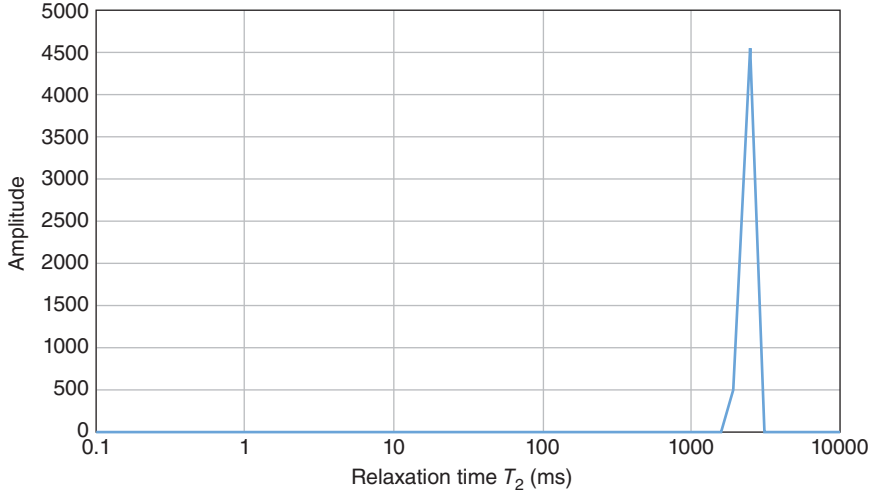

Figure 7.2 NMR T_2 relaxation distribution processed from measured decay curve.

within each peak is a measure of fluid volume in this range of T_2 values. The mean relaxation time for the peak is given by (Straley *et al.*, 1997):

$$T_{2gm} = exp\left[\sum \frac{ln(T_{2i})A_i}{A_{sum}}\right] \tag{7.1}$$

where:

T_{2gm} = geometric mean T_2 value (ms)
$T_{2i} = T_2$ values for which there is amplitude in that peak
A_i = individual amplitude values corresponding to each T_{2i} point in the peak
A_{sum} = cumulative (total) amplitude of the peak.

The calculation of T_{2gm} (Equation 7.1) allows for relaxation distributions to be understood in terms of the cumulative amplitude in each peak, and the mean T_2 value for that peak. With this as the output information from an NMR measurement, rock and fluid properties can be understood by interpreting the meaning of amplitudes and relaxation times.

7.2.1 Interpretation of NMR Relaxation Rates

The total NMR relaxation rate ($1/T_2$) is the sum of several terms (Coates, Xiao, and Prammer, 1999):

$$\frac{1}{T_2} = \frac{1}{T_{2B}} + \frac{1}{T_{2S}} + \frac{1}{T_{2D}} \tag{7.2}$$

Where:

$1/T_{2B}$ = bulk relaxation rate
$1/T_{2S}$ = surface relaxation rate
$1/T_{2D}$ = enhanced apparent relaxation of protons in the presence of external field gradient.

The term $1/T_{2D}$ is apparent relaxation, or loss of signal in the transverse plane, due to the presence of magnetic field gradients. Some NMR acquisitions can use this as a tool to acquire information about the fluids being tested (Freedman, 2001), but in low field NMR applications any gradient effects will be internal to the system (e.g. heterogeneities caused by minerals in the rocks). Therefore, the effect of T_{2D} can be neglected or taken as a background constant, and the total NMR relaxation is the sum of the bulk and surface relaxation terms.

Bulk relaxation ($1/T_{2B}$) is the rate that protons will lose energy by interacting with other protons. This is the NMR relaxation rate of bulk fluids, where relaxation is controlled by Brownian motion. The NMR bulk relaxation rate is given by the following expression (Straley *et al.*, 1997; Coates, Xiao, and Prammer, 1999):

$$\frac{1}{T_{2B}} \propto \mu \tag{7.3}$$

where μ = liquid kinematic viscosity (mPa s).

Eyring's theory of viscosity (Bird, Stewart, and Lightfoot, 2002) states that liquid molecules exist in a cage-like structure. The free space between molecules is not large enough for the molecules to move freely by one another. This means that, for any one molecule to move, other surrounding molecules must first give way and move into vacant lattice sites to create a space for the first molecule to move into. This phenomenon leads to the measured value of a liquid viscosity: viscous liquids contain molecules that cannot easily move and create space for flow, so higher shear stresses must be applied to move these liquids. As temperature increases, molecules become spaced further apart and as a result as a given molecule moves (flow) it is easier for other molecules to make space for this molecule to enter, and lower shear is required to move the liquid.

At the molecular level, NMR bulk relaxation occurs when protons are able to transfer energy to neighboring proton spins. If liquid molecules are viscous and cannot easily move past one another, this leads to a fast transference of energy compared to a lower viscosity liquid. For this reason, as liquid viscosity increases, this leads to a faster mean NMR relaxation time for that fluid, as shown in Figure 7.3. This figure shows the relaxation of various oils, each consisting of multiple components. For this reason, each oil signal is a range of T_2 values. The low viscosity oil (< 10 mPa s) has a mean relaxation time that is in the order of hundreds of ms, compared to the high viscosity bitumen that has a mean T_2 value of under 1 ms.

For bulk liquids measured in low field NMR, the total NMR relaxation rate ($1/T_2$) is just the bulk relaxation. Thus, the mean T_2 value will be inversely proportional to viscosity: higher viscosity liquids will exhibit shorter mean T_2 values. This is shown in Figure 7.4, which plots the correlation between

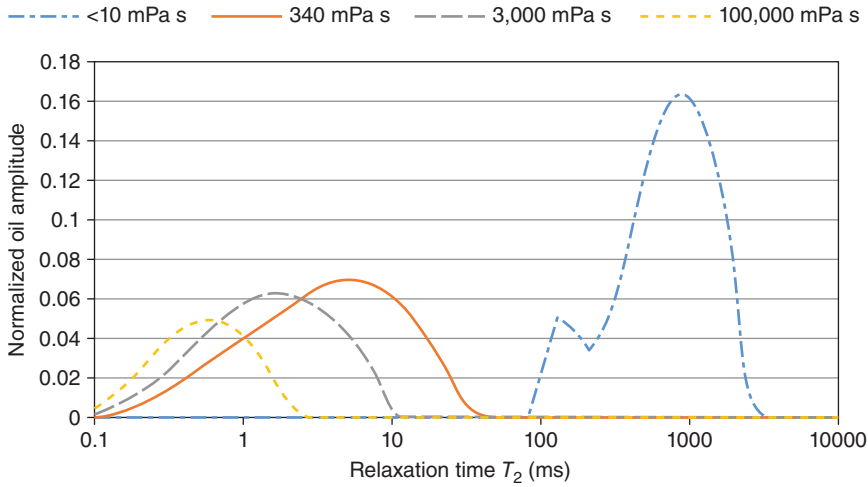

Figure 7.3 NMR bulk relaxation of fluids of variable viscosity.

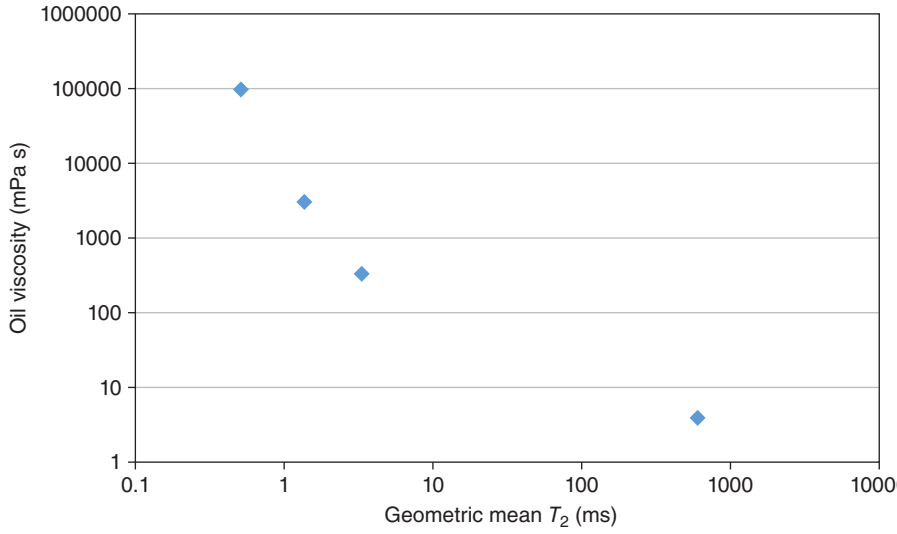

Figure 7.4 NMR bulk relaxation: relationship between viscosity and T_{2gm}.

mean relaxation time and viscosity for the oil samples shown in Figure 7.3. As expected, there is a clear and monotonic relationship between viscosity and T_{2gm} for these bulk oils.

When protons are given energy in an NMR acquisition measurement and are tipped onto the transverse plane, they need to give off this energy in order to return to their equilibrium state. This energy can be lost to other protons ($1/T_{2B}$) or alternatively protons can lose energy to the walls of the solid that contains the fluid being studied. Surface relaxation ($1/T_{2S}$) in Equation 7.2 is this NMR relaxation that occurs from protons giving off energy to the walls of the solid. In a bulk liquid system (i.e. liquid in a sample vial) the wall effect is insignificant so relaxation is dominated by bulk relaxation. However, when the liquid is present in a porous medium, protons within each pore are constrained from moving freely into other pores, and as a result they will most easily collide into the walls of rock pores and lose energy to the walls instead of to other protons in the liquid. NMR surface relaxation is given by the following expression (Kenyon, 1997):

$$\frac{1}{T_{2S}} = \rho_s \frac{S}{V} \tag{7.4}$$

where:

ρ_s = surface relaxivity of rock (i.e. the amount of energy lost to the rock in each collision)

S/V = surface-to-volume ratio of the pore within which the energized proton resides.

Taking the simplifying assumption that pores are like cylinders, the surface-to-volume ratio can be shown to be the inverse of the pore radius. For low viscosity fluids in porous media, bulk relaxation is much slower than surface relaxation, so the total relaxation rate ($1/T_2$) is essentially just from surface relaxation effects. In this instance, the range of T_2 values measured is essentially proportional to a pore size distribution, where small values of T_2 are small pores.

Figure 7.5 shows the measured NMR relaxation distributions for water found in rocks of varying permeability. All samples exhibit a range of T_2 values, since rocks consist of a range of pore sizes. The mean T_2 value of each system can be thought of as corresponding to characteristic pore sizes. The highest permeability sample (660 mD) has the largest T_2 values, or the largest pore sizes. Likewise, the lowest permeability rock (12 mD) has the smallest mean T_2 values, or the smallest pore sizes.

NMR permeability models relate measured permeability to porosity and to some measure of the mean pore size of the rock (Hawkins and Scopec, 1998; Coates, Xiao, and Prammer, 1999). An example of NMR permeability compared to measured brine permeability in sandstone cores is provided in Figure 7.6. When pores are well connected and randomly distributed in porous media, there is a good relationship between porosity, pore size, and permeability, and NMR can be used to predict permeability of rocks.

For low viscosity fluids like water, NMR relaxation in porous media is controlled by surface relaxation. As fluid viscosity increases, the bulk relaxation term will become more significant and correspondingly the total measured relaxation will be the contribution of both bulk and surface terms.

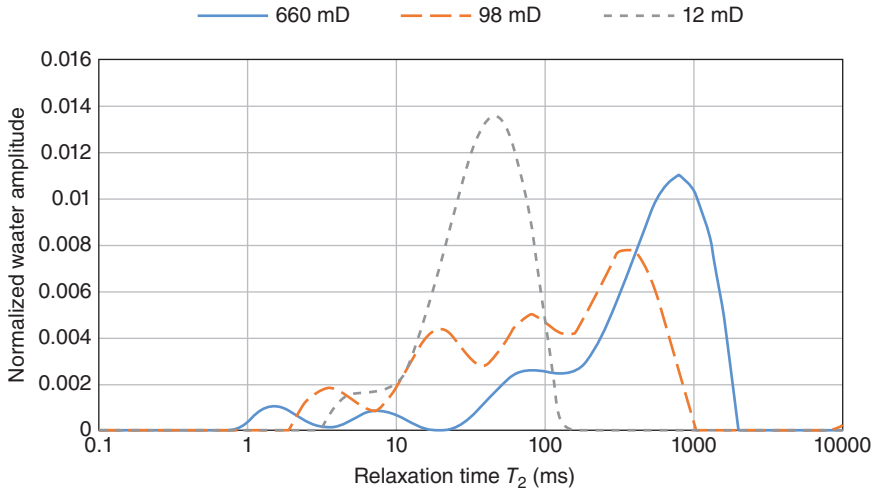

Figure 7.5 NMR surface relaxation of water in various pore sizes.

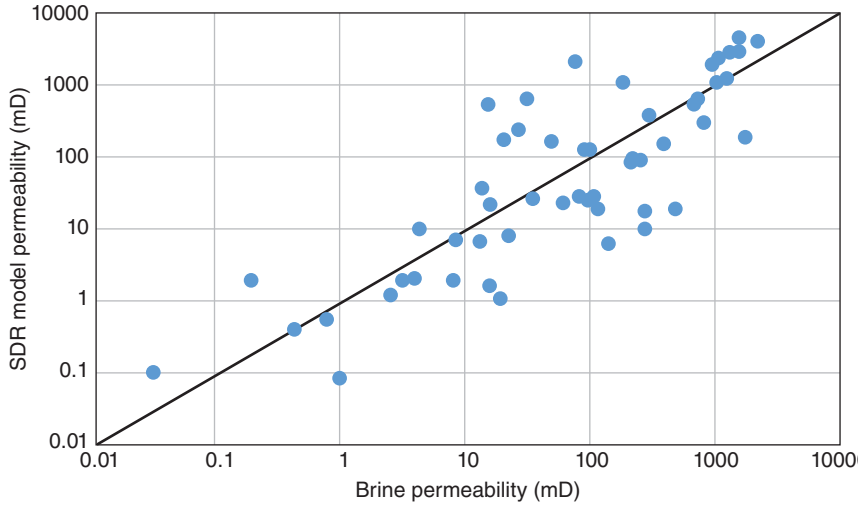

Figure 7.6 NMR surface relaxation: relationship between permeability and T_{2gm}.

7.2.2 Interpretation of NMR Amplitudes

NMR relaxation distributions have two outputs: the mean relaxation time for each peak and the cumulative amplitude in all of the peaks. The total amplitude represents the protons that are present in the entire sample, while the amplitude within a given peak is the protons that are present in this viscosity of fluid, or in this pore size of rock. Figure 7.7 represents the relationship

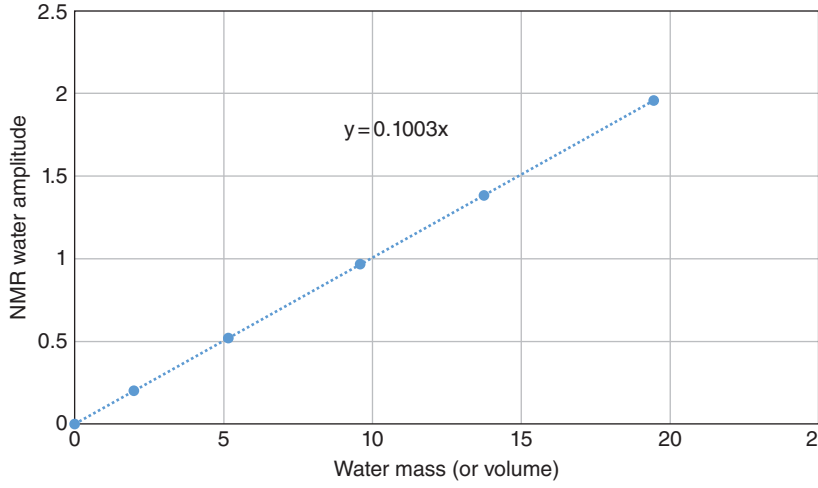

Figure 7.7 Relationship between NMR signal and fluid mass or volume.

between total amplitude and mass (or volume) of water measured over several sample masses. There is a linear relationship between the amount of water and the amount of NMR signal measured. The amplitude in this figure is the initial amplitude of the decay curve (Figure 7.1) at time = 0, or the cumulative amplitude measured in each relaxation distribution that is generated from the measured decay. Since the magnitude of the signal is caused by the number of protons that are flipped onto the transverse plane, a linear correlation between signal amplitude and fluid mass or volume is expected. If the amount of water doubles, the number of measured protons will also double and thus the signal amplitude will double as well. The slope of the line in Figure 7.7 is called the "amplitude index" of water, or the measured water amplitude per unit mass of water (Mirotchnik *et al.*, 1999):

$$Amplitude\ Index\,(AI) = \frac{NMR\ amplitude}{unit\ mass\ of\ liquid} \tag{7.5}$$

Each NMR system will have its own value of amplitude index (AI) for water, and this should be run as part of the initial calibration of the instrument. The absolute value of AI is equipment dependent and cannot be used from calibration measurements unless they are conducted in the specific instrument under use.

When quantifying the signal from other fluids (e.g. hydrocarbon), it is often useful to consider the number of protons in the fluid compared to the baseline response of water. This is called the "hydrogen index" of the fluid (Brown and Gamson, 1960; Dunn, Bergman, and LaTorraca, 2002):

$$Hydrogen\ index\,(HI) = \frac{Amount\ of\ hydrogen\ in\ unit\ volume\ of\ sample}{Amount\ of\ hydrogen\ in\ unit\ volume\ of\ water} \tag{7.6}$$

Different oils (e.g. saturated hydrocarbons vs. aromatic hydrocarbons) will contain different amounts of hydrogen per unit volume, and accordingly their HI values may be greater or less than one. Laboratory measurements are often easier to make on the basis of mass instead of volume, so rather than calculate the HI of various oils it is often to measure the oil AI by making NMR measurements of known masses of oil and calculating AI from Equation 7.5.

If the oil AI is known, its value can be normalized to the value of water, similar to what is shown in Equation 7.6. This is called the "relative hydrogen index" of the fluid (Mirotchnik *et al.*, 1999; Bryan *et al.*, 2003):

$$Relative\ hydrogen\ index\,(RHI) = \frac{AI\ of\ oil}{AI\ of\ water} \tag{7.7}$$

The main difference between the RHI from Equation 7.7 and the HI from Equation 7.6 is that RHI can be based on either mass or volume units, while HI is all normalized to volume. Furthermore, the RHI in Equation 7.7 is based on

the measured oil amplitude and not necessarily the actual amount of hydrogen present in the oil. This is an important distinction in heavy oil and bitumen, where the same oil will have a different *RHI* at ambient vs. elevated temperatures. The physical oil is unchanged, but the amount of signal measured by NMR may be affected by the properties of the oil. Thus, while *HI* is a constant for each oil, the measured NMR *RHI* may change for the same oil as a function of temperature or NMR acquisition parameters. Also, the values of *RHI* should be independent of the piece of equipment used.

Table 7.1 shows the calculation of oil *RHI* for a sample of low viscosity conventional oil. In this table, oil *RHI* as calculated by the ratio of oil and water *AI* values is greater than one. The reason for this is that the *RHI* in Equation 7.7 is based on the amplitude per unit mass of fluid. Oil and water have different densities, so the fluid amplitude per unit volume can also be calculated. On the basis of volume, the oil *RHI* is close to one, so the actual high of conventional oil is essentially unity. This is shown further in Figure 7.8, which plots the volume-based mixture *AI* normalized to the volume-based *AI* of water. With oil content changing from 0 to 100%, the total mixture has a volume-based *RHI* (i.e. *HI*) of one. In conventional oil systems NMR estimates of porosity are based on the total amount of measured signal and, since the volume-based *RHI* is one, porosity predictions are independent of the oil and water saturations present in the system.

Since NMR is measuring the signal of hydrogen (protons) in the presence of a magnetic field, if what is measured is an oilfield brine, it is only the H_2O portion of the brine that is giving an NMR signal. Most reservoir brines are of relatively low salinity, so the volume occupied by salt ions in the water is not significant enough to make a measurable change in the water's *AI* value. Under very high salinity conditions (e.g. seawater or some Middle East reservoirs), the salt content is so high that the NMR *AI* of brine is less than the *AI* of water. However, this is only when the salt content is in the range of 80,000 ppm or higher (Dunn, Bergman, and LaTorraca, 2002; Chung and Kantzas, 2007).

Table 7.1 Calculation of conventional oil amplitude signal (*RHI*).

*AI*_water (amplitude/gram)	0.113
*AI*_oil (amplitude/gram)	0.134
Oil *RHI*	1.177
Water density (g/cm^3)	0.997
Oil density (g/cm^3)	0.840
Water amplitude/cm^3	0.113
Oil amplitude/cm^3	0.112
Oil *RHI*_volume basis	0.992

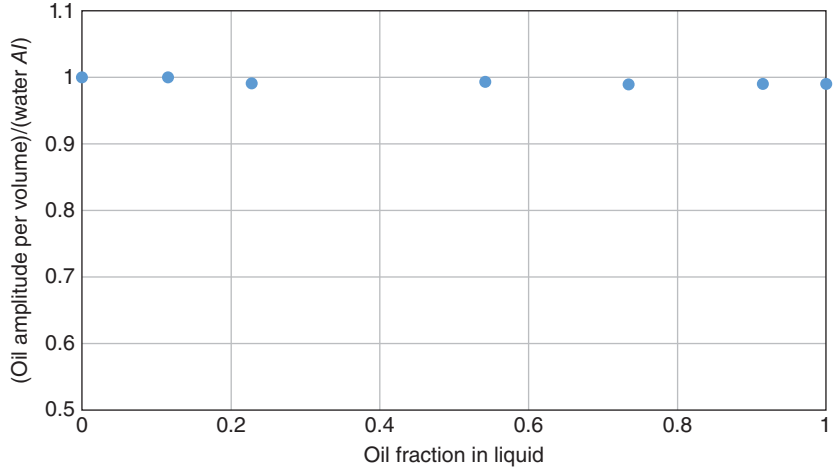

Figure 7.8 Conventional oil systems: change of *RHI* with variable oil content in liquid.

For hydrocarbons, viscous heavy oil and bitumen relax so quickly through bulk relaxation that some of the actual signal is not measured by NMR. The oil *AI* that is measured is only the portion of the oil that can be measured using the acquisition parameters of the low field NMR system.

Table 7.2 is a calculation of oil *RHI* for one such sample of heavy oil. In contrast to the conventional oil, which had an *RHI* value of greater than one, this heavy oil has an *RHI* of only 0.659 when conventional T_2 measurements are taken (known as the CPMG pulse sequence (Coates, Xiao, and Prammer, 1999). The density of the oil is actually higher than that of water, so when converted to a volume basis the oil *RHI* is higher instead of lower. Even on this volume basis, however, this viscous oil has an *RHI* that is much less than one.

This character of heavy oil and bitumen is important because it both affects the ability to measure how much oil and water are present in a given system and

Table 7.2 Calculation of viscous heavy oil amplitude signal (*RHI*).

*AI*_water (amplitude/gram)	0.113
*AI*_oil (amplitude/gram)	0.074
Oil *RHI*	0.659
Water density (g/cm^3)	1.008
Oil density (g/cm^3)	1.011
Water amplitude/cm^3	0.114
Oil amplitude/cm^3	0.075
Oil *RHI*_volume basis	0.661

provides a means for identifying when a system contains heavy oil and bitumen. In logging tool applications, the total amplitude of oil and water is summed and divided by the *AI* of water, all on a volume basis. The fact that the oil *RHI* is low means that if this is not accounted for the total predicted porosity from NMR will be less than the porosity estimated from other means such as density logs. This low signal amplitude in the presence of heavy oil is one of the key indicators of a viscous oil-bearing zone in logging tool outputs (Galford and Marschall, 2000). However, this characteristic of heavy oil and bitumen can also be used to estimate the viscosity of this fluid, as is discussed later.

7.3 Fluid Content in Oil/Water Systems

Heavy oil and bitumen production systems are difficult to monitor. The production from these reservoirs is generally through steam injection, so the produced fluids are at high temperatures and oil and water are produced often in an emulsified state. Test separators work poorly in these systems because of the similar oil and water densities, and the fact that as oil cools it becomes viscous makes a proper separation of water and monitoring of accurate production water cuts difficult to obtain. As a result, production water cuts are often made using online metering tools that measure water cuts using a range of technologies such as infrared optical detection, microwave adsorption, and electrical resistance or capacitance (Wright *et al.*, 2004). These various methods will be highly sensitive to conditions such as changing salinity of the aqueous phase (e.g. through production of connate brine mixed with fresh steam condensate), whether fluids are free or emulsified and which emulsions are present, and changes in density with temperature. These metering tools can be tuned to measure the water cut in production streams, but with any changes in the process conditions these calibrations will fall apart and the results of the online meters will be suspect.

The benefit of using low field NMR as a water cut metering tool is that, for bulk liquids, NMR relaxation is through bulk processes only and is proportional to the fluid viscosity. As a result, NMR relaxation distributions show separate oil and water peaks on the basis of the different viscosity of the liquids, and are not affected by parameters such as changing water salinity or emulsion type.

Figure 7.9 shows the relaxation distributions of three mixtures of oil and water: a heavy oil (2000 mPa s), a bitumen (70,000 mPa s), and a conventional oil mixed with water. As expected, the oil peak shifts to shorter T_2 values with increasing viscosity.

What is significant in this figure is that the low viscosity water in the sample always relaxes slowly, in the order of 1000 ms. On this basis, Figure 7.9 shows a dashed line indicating the cutoff between oil and water. The water amplitude can be summed and divided by the known water *AI* value to obtain the water

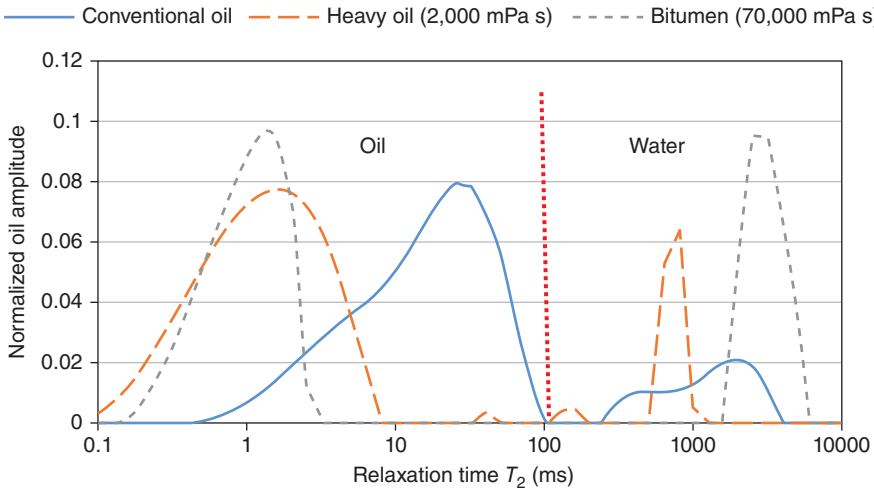

Figure 7.9 Separation of fluid NMR signals in mixtures of oil and water.

mass in the sample (Equation 7.5). Water cut is then given by the following expression:

$$Water\ cut = \frac{\left(A_w / AI_w\right)}{mass_{sample}} \tag{7.8}$$

where:

$Water\ cut$ = water mass fraction in the sample
A_w = cumulative water amplitude in the measured NMR relaxation distribution
AI_w = water amplitude index (i.e. NMR amplitude per gram of water)
$mass_{sample}$ = total mass of oil and water in the tested sample.

Figure 7.10 shows the results of testing of water content made on a suite of production bitumen/water samples from a thermal operation in northern Alberta. NMR relaxation distributions were obtained on all of these samples and oil and water amplitudes were separated using the approach shown in Figure 7.9. Water amplitudes were converted to mass and water cut using Equation 7.8. The NMR results of water cut are compared against the measured water cuts as determined by Dean–Stark extraction (ASTM D95-05). Dean–Stark is also a measure of water mass fraction in a given sample, so both the NMR and Dean–Stark outputs are in the same units. Figure 7.10 shows that, for the entire range of water cuts, NMR predictions are able to track the measured Dean–Stark values. Note that these are also produced emulsion samples, so oil and water are sometimes free phases and are sometimes mixed together. The NMR water cut method works because of the viscosity contrast

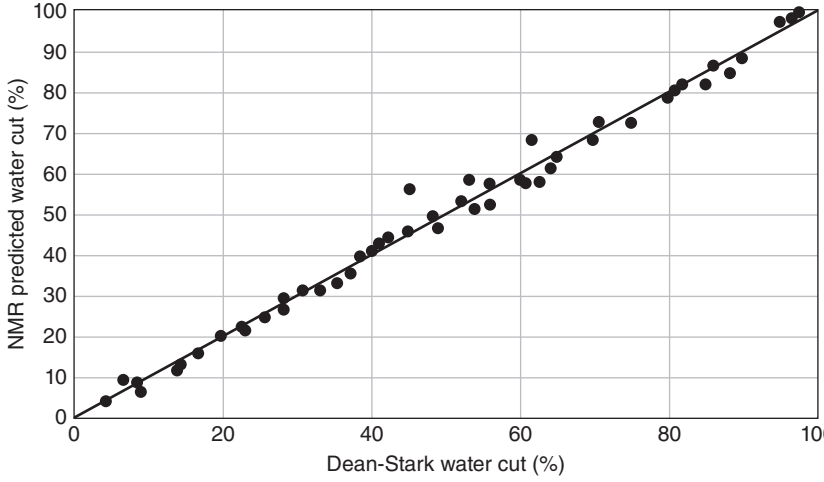

Figure 7.10 NMR vs. Dean–Stark predictions of water cut in laboratory oil-water samples. *Source*: Wright *et al.* (2004). Reproduced with permission of the *Journal of Canadian Petroleum Technology*.

between oil and water, which allows for a clear cutoff in the peaks of these two fluids in the NMR relaxation distribution.

With NMR proven to match measured Dean–Stark water cuts on ambient temperature samples, the next step is to consider how this same technology can be applied as a wellhead or well pad-level tool, as an online meter of producing water cuts. Most heavy oil and bitumen are produced from thermal operations (steam injection) so produced fluids will be at elevated temperatures. Both oil and water viscosity becomes lower with increasing temperature, and as a result the cutoff point between oil and water needs to shift compared to ambient temperature relaxation distributions. Figure 7.11 shows the relaxation distributions of two heavy oil/water samples with similar water content, but one measurement is at 25 °C, while the other is at 165 °C. At ambient temperature the oil is viscous so (a) it has a short T_{2gm} value and (b) some of the signal relaxes too quickly to be measured. The oil shows up as a low amplitude peak at around 1 ms. All other signal is water, including an emulsified water peak at around 100 ms. At 165 °C for a similar amount of oil and water, the oil now consists of a broad peak, with a signal ranging from 1 to 200 ms. The total amplitude of the oil is also much larger, since at elevated temperature the entire signal from the lower viscosity heated bitumen can be measured. At 165 °C, water is also less viscous so its peak is also shifted to longer T_2 values as well: 3–4 seconds compared to 1–2 seconds for the ambient temperature sample.

Figure 7.12 shows two elevated temperature samples: one with a water cut of 0.52 and one with a water cut of 0.85. The oil and water peaks are shifted at high temperatures, as previously shown. What is significant from this figure is

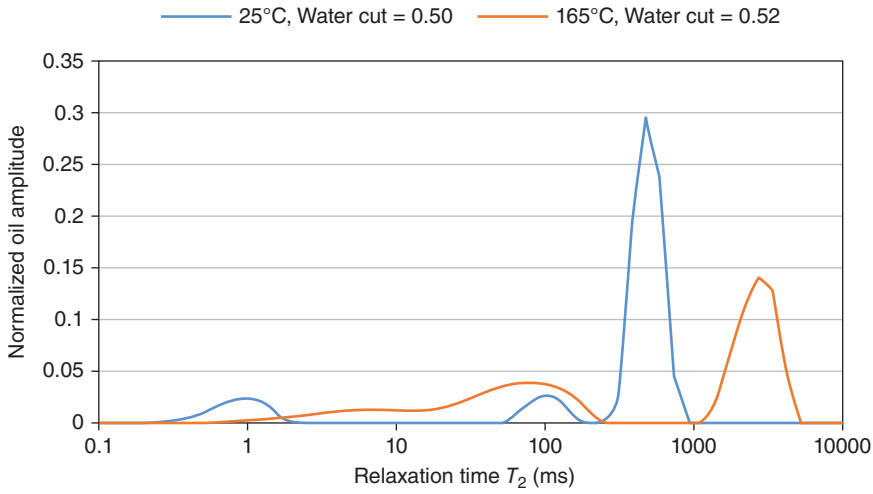

Figure 7.11 NMR relaxation distributions for water cut predictions at ambient and elevated temperatures.

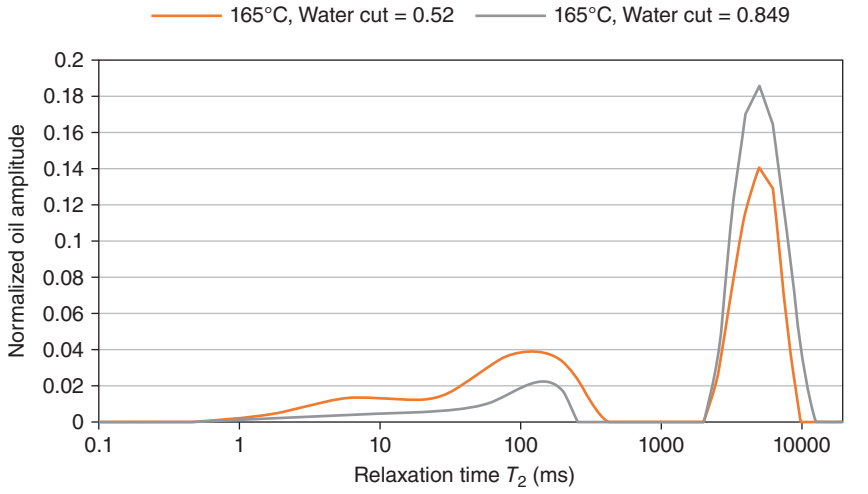

Figure 7.12 NMR relaxation distributions of low and high water cut samples at elevated temperatures.

that for these samples the changing water cut can be measured not only in the water peak amplitudes but also in the oil amplitudes. Some ambient temperature oil/water mixtures contain oil that is so viscous that the oil is difficult to measure accurately and oil amplitude will not always change consistently with mass. When temperatures are high and the entire signal from the oil can be measured, the oil and water amplitudes both change proportionally with mass.

NMR meters have now been pilot tested in the field as thermal water cut metering tools constantly since 2010, and earlier prototypes were tested for shorter periods of time from 2001 to 2003. Field-based measurements of NMR relaxation distributions in elevated temperature produced fluid from a thermal operation and indicate that total amplitude remains relatively constant with changing oil and water cuts. This is an indication that oil *RHI* is approximately one at high temperatures. The oil/water cutoff points are shifted compared to ambient temperatures, but even at 150–200 °C there is still a distinct viscosity contrast between oil and water, so clear cutoffs can still be distinguished. Figure 7.13 plots the results of NMR meter water cuts vs. centrifuge measurements acquired from wellhead samples from a thermal operating well. There is more scatter than what was measured in the NMR vs. Dean–Stark test in Figure 7.10, but this is because the NMR measurements are made for the actual production stream while the centrifuge tests require samples to be collected and spun. There is still a good correlation between both data sets, proving that the online NMR tool works, and in fact the results from this tool will likely be more reliable than the discrete sample data points collected at the wellhead.

Figure 7.14 plots the results of NMR water cut trends measured for several wells in a single pad of producers from cyclic steam stimulation in a northern Alberta bitumen property. Changes in temperature indicate when wells were switched and flowed through the NMR meter. The meter tracks changing water cuts from high and low oil producers, and results appear to be very stable over time for the same well.

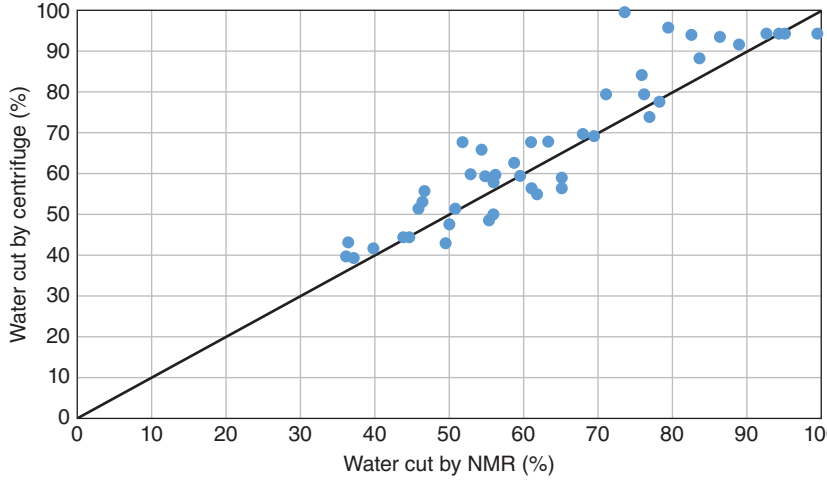

Figure 7.13 Thermal production wellhead samples: water cuts by centrifuge and NMR. *Source*: Allsopp *et al.* (2001). Reproduced with permission of the *Journal of Canadian Petroleum Technology*.

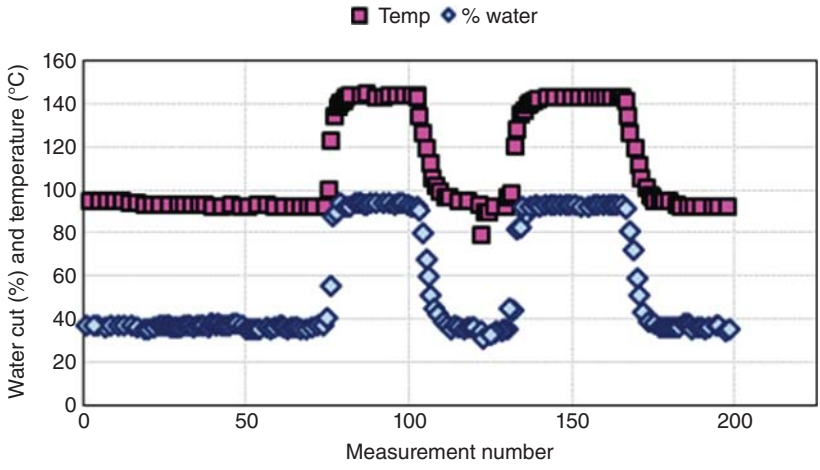

Figure 7.14 Production water cuts from thermal operating wells in northern Alberta. *Source*: Allsopp *et al.* (2001). Reproduced with permission of the *Journal of Canadian Petroleum Technology*.

The challenge to NMR metering of producing thermal operations is that an NMR T_2 measurement requires fluid to be stationary. Current NMR meters are therefore placed in slipstreams that extend off the main flow line for each producing pad. In between measurements the production fluid is flowed both through the main line and through the NMR slipstream line, to ensure that the NMR system contains a representative fluid. The NMR system is then shut in and the T_2 measurement is taken, while flow from the well continues just through the main production flow line (Allsopp *et al*., 2001; Wright *et al*., 2004). This "trap and capture" approach means that NMR water cuts are being measured only at discrete times, but since NMR measurements are fast (under three minutes long) it is possible to measure water cuts and flush out lines in preparation for a new measurement all in under 5 minutes. With many samples taken through time, the output in Figure 7.14 represents a pseudo-continuous measurement of production water cut.

The other operational factor that must be considered when making measurements of production water cuts in high temperature and pressure samples is that steel pipes cannot be placed through the magnets of the NMR. As a result, early iterations of the NMR water cut meter used thermoplastic materials that would go through the magnet and hold the fluids, and connect to steel piping outside of the instrument (Allsopp *et al*., 2001). Even with proper design of thermoplastic pipes, it becomes challenging to meet the strength and operating conditions of the surrounding steel, so as not to de-rate the pressure limits of the entire system. Current NMR operations use a specialized titanium pipe with an internal receiver coil (Krioutchkov, Kantzas, and Wang, 2016) that allows for

relaxation distributions to be acquired at elevated temperatures and pressures without losing the pressure rating of existing thermal operations.

7.4 Oil Viscosity from NMR

The key to measuring oil and water cuts using NMR is that the fluids have different viscosities and this leads to distinctly different NMR relaxation times. In these systems, the total NMR relaxation is controlled by the bulk relaxation rate, which is supposed to be inversely proportional to fluid viscosity (Equation 7.3). Figure 7.15 shows the relationship between oil viscosity and mean relaxation (T_{2gm}) for bulk oil samples taken from various heavy oil and bitumen fields from Alberta and Saskatchewan. The first observation that can be made from this figure is that, as expected, viscosity and T_{2gm} are related for these bulk liquids. The early NMR viscosity correlations (Kleinberg and Vinegar, 1996; Straley *et al.*, 1997) relate viscosity inversely to the T_{2gm} of the oil peak. Temperature is also sometimes included in NMR viscosity correlations (Kleinberg and Vinegar, 1996; LaTorraca *et al.*, 1999), but the fact that all the data in Figure 7.15 follow the same trend line means that the effect of temperature is already captured within the changing viscosity and T_{2gm} terms. There is no need for temperature to be an additional input parameter to NMR viscosity models.

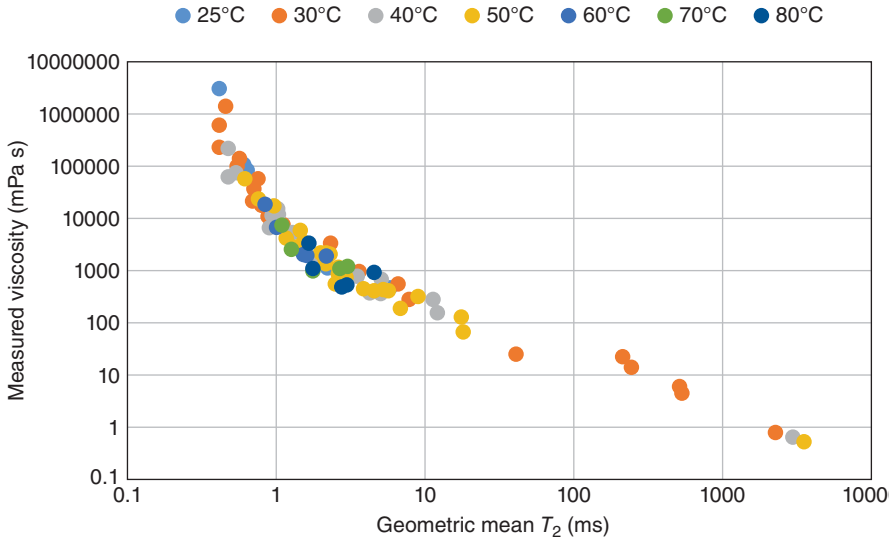

Figure 7.15 Relationship between NMR mean relaxation time and oil viscosity for multiple temperature samples. *Source*: Bryan *et al.* (2005a). Reproduced with permission of SPE Reservoir Evaluation and Engineering.

Conventional models that relate viscosity inversely to T_{2gm} work well for low viscosity oils, where this linear relationship is evident in Figure 7.15. When oil viscosity increases above 1000 mPa s, the linear relationship between these terms starts to deviate. In fact, as oil viscosity continues to increase, the change in T_{2gm} becomes smaller even for order of magnitude increases in viscosity. The reason for this is that, for high viscosity bitumen, the oil is now relaxing so quickly that it is at the limit of what can be measured using the low field NMR acquisition parameters. Recall that NMR relaxation distributions output data in the range of T_2 values from 0.1 to 10,000 ms, and the actual rate of data capture during the decay will generally be between 0.1 to 1 ms. For highly viscous oils that are under 1 ms as their mean T_2 value, the oil is relaxing so quickly that it simply cannot be measured accurately by the CPMG sequence in the low field NMR systems. For this reason, the relationship between viscosity and T_{2gm} becomes non-linear in this range of viscosities.

The significance of bulk relaxation is that it represents a fluid property (viscosity), as explained by the closeness of protons and their ability to give off energy to one another. Thus, NMR measurements do not require the fluids to be flowing like in a conventional viscosity measurement.

Figure 7.16 plots the correlation between viscosity and NMR oil *RHI* for these same samples, measured over the same temperature range. As previously discussed, *RHI* for low viscosity oils (under 1000 mPa s) is approximately equal to one. As oil viscosity increases above 1000 mPa s, *RHI* drops more significantly

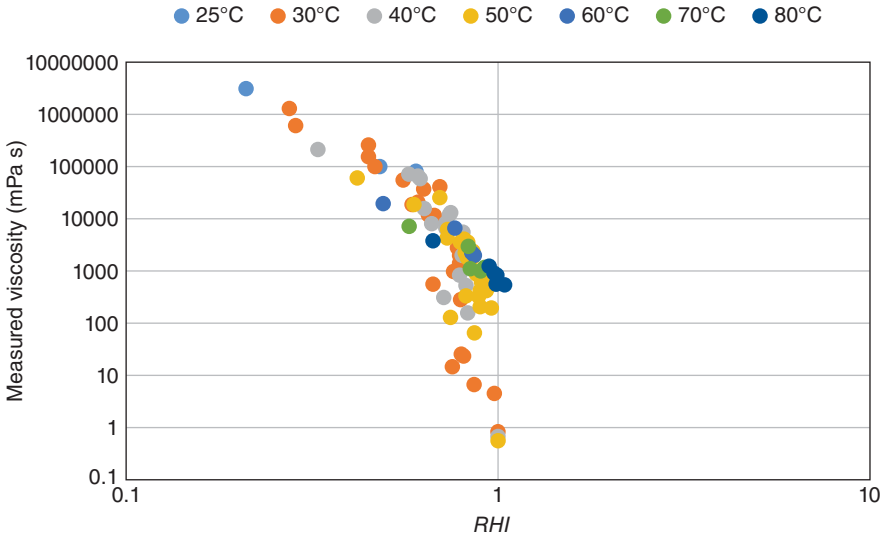

Figure 7.16 Relationship between NMR normalized *AI* and oil viscosity for multiple temperature samples. *Source*: Bryan *et al.* (2005a). Reproduced with permission of SPE Reservoir Evaluation and Engineering.

and for bitumen with viscosity of over 100,000 mPa s, *RHI* is less than 0.5. It was previously discussed that *RHI* is not the same as the true high of a given sample: *RHI* is the measured oil amplitude per gram, normalized to the water *AI* value. Viscous oils are relaxing so quickly that a portion of the signal is too fast to be measured, and NMR is only capturing the signal from some of the oil. The reducing *RHI* values from Figure 7.16 are due to this phenomenon. This can be shown by measuring the NMR signal of oil at various NMR acquisition parameters: when data are captured at larger intervals, even more of the signal is lost and the correlation between *RHI* and viscosity may be even a function of the NMR parameters used to capture the decaying signal on the transverse plane.

Another example of how *RHI* is related to viscous oil simply relaxing too quickly to be measured is the relaxation distributions in Figure 7.17. These are measurements taken on the same oil sample (i.e. the amount of hydrogen physically present per unit mass or volume of the oil is constant). As the sample is heated from 30 to 60 °C, its viscosity drops. Not only does the mean T_2 of the oil shift to longer times but also the oil peak grows in amplitude as well for this constant oil mass. This is equivalent to the oil *RHI* increasing with temperature, as the lower viscosity oil relaxes more slowly and more of the oil signal can be measured. This means that, for heavy oil and bitumen, *RHI* and T_{2gm} are not two independent parameters that correlate with viscosity but rather the *RHI* is affected by the actual relaxation rate of the oil. Figure 7.18 plots the correlation between *RHI* and T_{2gm} for this tested oil over 30–60 °C. There is a non-linear correlation between these two variables, so while both can be used to estimate viscosity it is important to understand that the reason *RHI* correlates with viscosity is because of this portion of the oil relaxing too fast to be measured.

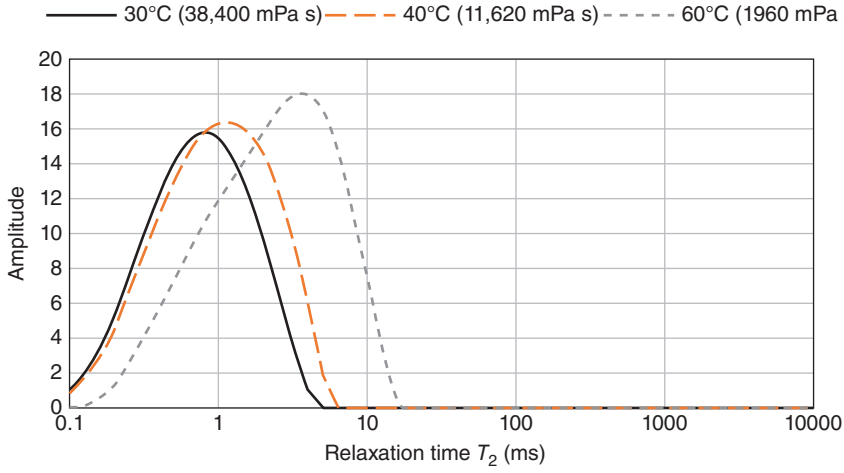

Figure 7.17 Single oil sample at multiple temperatures: change in oil relaxation time with viscosity.

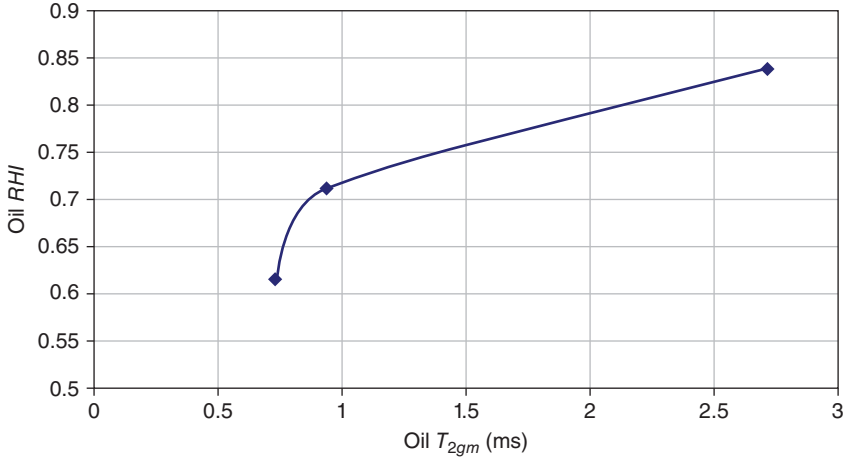

Figure 7.18 Single oil sample at multiple temperatures: relationship between *RHI* and oil T_{2gm}.

Bryan *et al.* (2003, 2005a) proposed the following form of an NMR viscosity model, which uses both *RHI* and T_{2gm} terms to measure viscosity.

$$\mu = \frac{\alpha}{(RHI)^{\beta} T_{2gm}} \tag{7.9}$$

where α and β are empirical fitting parameters.

It is important to emphasize that *RHI* and T_{2gm} are not independent of one another, as shown in Figure 7.18. The reason for using both terms in the NMR viscosity correlation is that it utilizes the measured relationship between viscosity and these parameters for different viscosity ranges. When oil viscosity is relatively low, *RHI* is close to one, so this term becomes a constant. However, viscosity and T_{2gm} are inversely proportional, as shown in Figure 7.15. Conversely, when oil viscosity is high the oil becomes difficult to measure so T_{2gm} changes only to a small degree with large changes in viscosity. However, when this happens there is a strong correlation with decreasing *RHI* so while the T_{2gm} term becomes more like a constant, the *RHI* term is the main factor used in the viscosity prediction. As such, a correlation of the form of Equation 7.9 presents a single form that can be used to predict both high and low oil viscosities.

For this range of samples (1 to 3,000,000 mPa s) the values for α and β were determined empirically through a minimization of errors in the viscosity prediction. The following tuned model was used to generate the predictions in Figure 7.19:

$$\mu = \frac{2166}{(RHI)^{3.80} T_{2gm}} \tag{7.10}$$

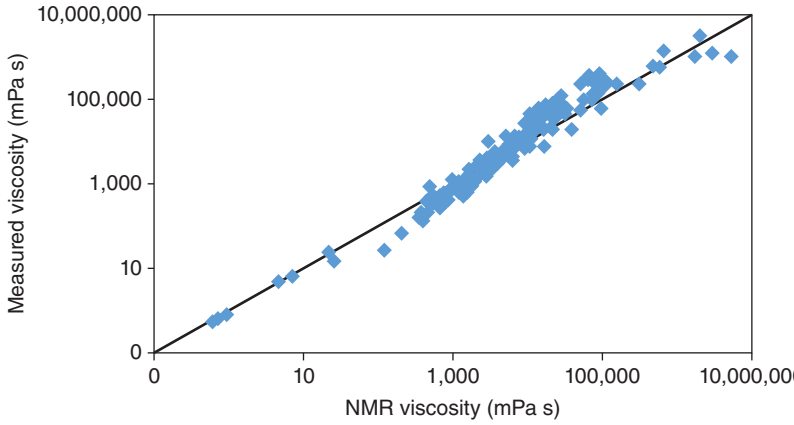

Figure 7.19 General NMR correlation viscosity predictions.

Note that this correlation was developed using an NMR instrument with a magnet frequency of 1.2 MHz and an echo spacing (i.e. interval used to measure decaying signal) of 0.3 ms. If data are acquired under other conditions the values of α and β may change so if the model from Equation 7.10 is to be used to predict oil viscosity it is important to use the same acquisition parameters. Alternatively, data can be collected on a different machine and the same form of model can be generated for each machine, but with tuned α and β for that instrument.

While it is useful to have a single model to predict a wide range of oil viscosities from NMR, the data in Figure 7.19 are plotted on a log scale, so the NMR predictions are only of order-of-magnitude accuracy. This is sufficient for a first-pass approach, but often in reservoir characterization the goal is to understand viscosity variations with depth in a formation (Bryan *et al*., 2007), which may be smaller than order of magnitude in their differences. When improved prediction accuracy is required, it is necessary to extract oil samples (e.g. from core) and develop a tuned viscosity correlation for the specific formation or field being tested. Figure 7.20 shows the general NMR viscosity correlation predictions for a set of oils from a single field, and the improvements in viscosity profiling that can be achieved by tuning the parameters α and β in Equation 7.9. Clearly with tuning the predictive ability of the NMR viscosity correlation is improved significantly.

If tuning can improve the predictions made by the general viscosity correlation (Equation 7.10) then one possibility is that α and β could be found for different ranges of oil viscosity, and used to improve the overall predictions made by the general model.

Table 7.3 shows the tuned values of α and β made for different oils of variable viscosity. For each oil, viscosity and NMR were measured over multiple

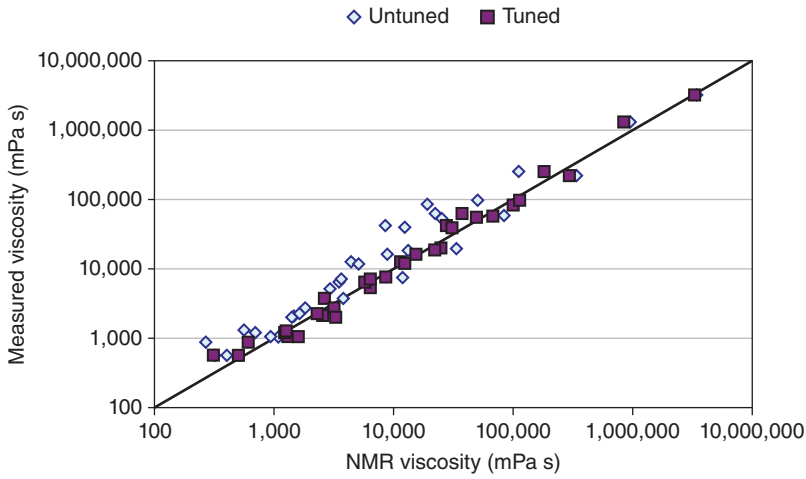

Figure 7.20 Improvements in NMR viscosity from tuning to specific oils. *Source*: Bryan *et al.* (2005a). Reproduced with permission of SPE Reservoir Evaluation and Engineering.

Table 7.3 Tuning of NMR viscosity coefficients for different oil samples with temperature. *Source*: From Bryan *et al*. (2005a). Reproduced with permission of SPE Reservoir Evaluation and Engineering.

Oil sample	30 °C viscosity (mPa s)	α	β
1	1,311,950	703	4.84
2 (Peace River, AB)	246,460	2022	4.47
3	55,260	1411	5.37
4 (Cold Lake, AB)	41,620	1198	7.68
5	11,630	2613	4.73

temperatures (30–80 °C) and these data were used to obtain the tuned values of α and β. No monotonic trend is observed between these parameters and the baseline (30 °C) oil viscosity.

This table shows that the NMR viscosity correlation parameters α and β cannot be simply determined *a priori*. Rather, the fact that there is no monotonic trend in the parameters with oil viscosity means that tuning for individual oils is required, and this behavior needs to be measured and calibrated for individual oils. NMR can be tuned empirically to measure changes in a given oil, or fluid from a single field, as they change with temperature. If the goal is determination of viscosity from a new field, for example, or through

measurements of *in situ* core log viscosity, the accuracy of the NMR model will be only the order-of-magnitude values given by the general model in Figure 7.19, unless samples of oil are taken to empirically tune the correlation.

7.4.1 Viscosity Predictions in High Viscosity Bitumen

As discussed previously, the basis for including both *RHI* and T_{2gm} in the NMR viscosity model is that they have significance for high and low viscosity regions. When measuring highly viscous bitumen (i.e. greater than 100,000 mPa s) Figure 7.21 shows that the relationship between viscosity and T_{2gm} may be completely lost. Viscosity changes two orders of magnitude, with a corresponding change in bulk oil T_{2gm} of only 0.1–0.2 ms. Any viscosity prediction made using the relaxation times in this range would be extremely inaccurate.

In contrast, for high viscosity bitumen there is a strong correlation between *RHI* and viscosity, as shown in Figure 7.22. If the reservoir that is being tested has such high viscosity oil, it is preferable to predict viscosity just using the *RHI* of the oil because incorporating the T_{2gm} will lead to more scatter in the viscosity predictions. This is the approach used in several works (Galford and Marschall, 2000; Chen and Bryan, 2013).

The relationship between *RHI* and viscosity is not as strong as the T_{2gm} viscosity correlation that exists at lower viscosity values. This is because the correlation built in Figure 7.22 contains data for multiple zones in the formation (i.e. different oils) and multiple temperatures tested for each oil. As temperature increases or as a given oil is physically less viscous, the oil

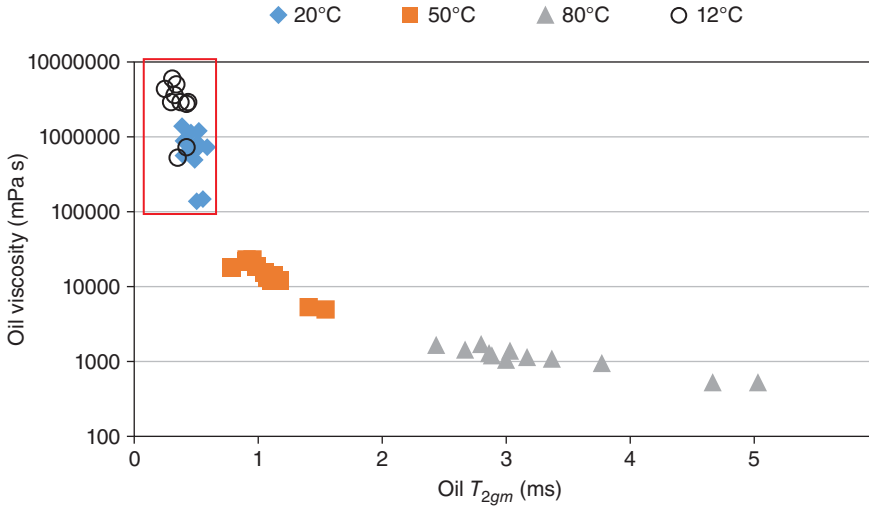

Figure 7.21 Loss of viscosity: T_{2gm} relationship for high viscosity oils. *Source*: Chen and Bryan (2013). Reproduced with permission of SPE Proceedings.

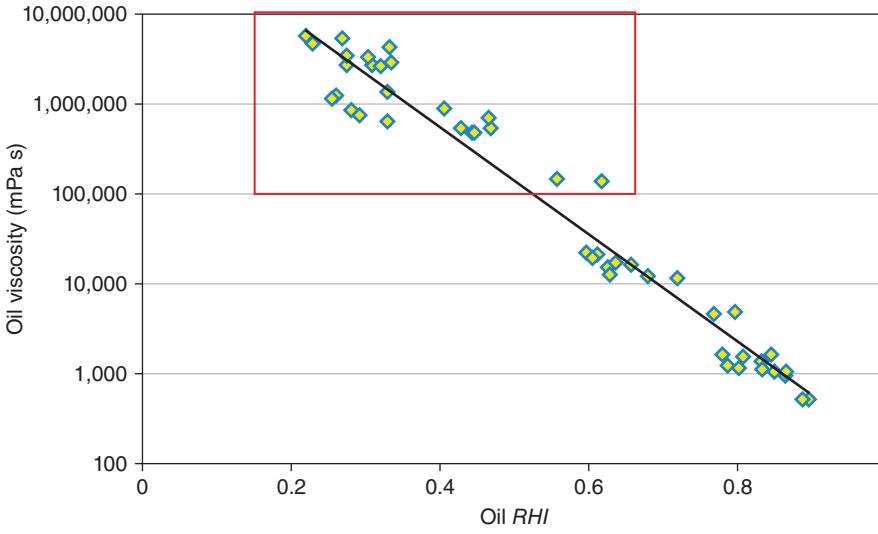

Figure 7.22 Correlation between viscosity and oil *RHI* for high viscosity oils. *Source*: Chen and Bryan (2013). Reproduced with permission of SPE Proceedings.

will exhibit a longer T_{2gm} value, so as long as the oil is not relaxing too fast to be measured this correlation will be strongly evident. When measuring *RHI* from oils at multiple temperatures, this is complicated by the fact that as temperature increases the NMR amplitude strength of water decreases, owing to the Curie effect (Mirotchnik *et al*., 1999; Dunn, Bergman, and LaTorraca, 2002). While the *AI* of water decreases with temperature, the *AI* of oil is increasing since more of the oil can now be measured. The *RHI* in Figure 7.22 is this increasing oil *AI*, normalized to a decreasing water *AI* at high temperatures. Figure 7.23 shows how the overall relationship plotted in Figure 7.22 is actually the general trend through all the different temperatures. In fact, for any given temperature the relationship between viscosity and *RHI* may be different from the overall trend line.

If sufficient oil samples have been acquired to predict viscosity variations in a bitumen system, the improved *RHI* vs. viscosity correlation from Figure 7.23 will yield the most accurate predictions of viscosity. If only a few samples were collected, however, and these samples were tested at multiple temperatures in order to have more data points in the overall model, then even the general *RHI* vs. viscosity correlation can be used to predict viscosity vs. depth or location in a given property. The general model will be valid to measure viscosity changes within the reservoir (i.e. zones of higher or lower viscosity) but tuning for multiple oils at the reservoir temperature will be required to improve the model's accuracy.

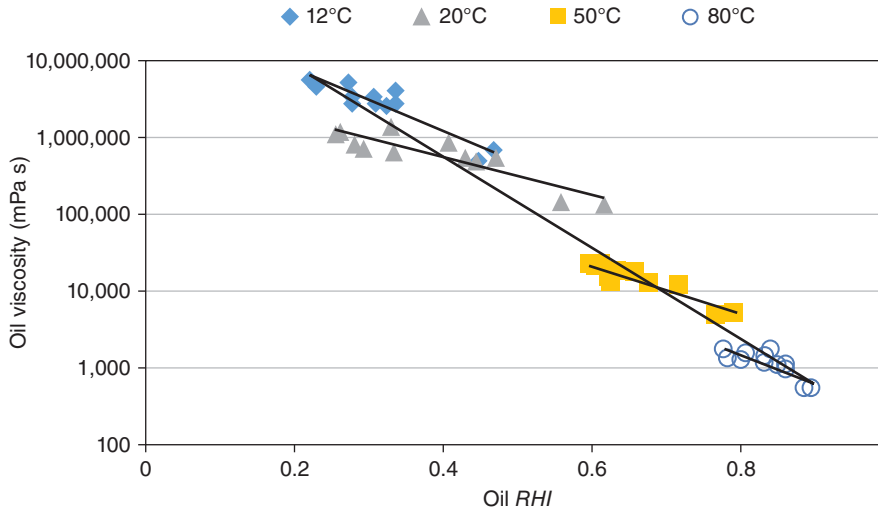

Figure 7.23 Correlation between viscosity and oil *RHI* for high viscosity oils: individual relationships at each temperature vs. total *RHI*-viscosity trend. *Source*: Chen and Bryan (2013). Reproduced with permission of SPE Proceedings.

7.4.2 Viscosity Predictions in Oilfield Emulsions

When oil and water are flowing together, either from flow through valves and tubing or even flow in porous media, the shear induced by the flow can cause the fluids to mix into oil-in-water and water-in-oil emulsions. When oil is continuous in water, the continuous phase (water) has low viscosity, so it is relatively easy for oil droplets to coalesce and for the phases to separate. In the case of a water-in-oil emulsion, however, the continuous oil phase is viscous and this makes it difficult for water droplets to coalesce. For this reason, most oilfield emulsions in heavy oil and bitumen systems are water-in-oil emulsions (Kokal, 2002).

The viscosity of an emulsion is strongly related to the viscosity of the continuous phase: a water-in-oil emulsion will be more viscous than an oil-in-water emulsion since low viscosity water is the continuous phase in the latter case. However, aside from the continuous phase viscosity, the overall emulsion viscosity is also strongly affected by the presence of the emulsion droplets of the second fluid. When the continuous fluid contains emulsion droplets of a second immiscible liquid, the flow stream lines become distorted and the rate of energy dissipation increases, owing to increased hydrodynamic interactions between the molecules (Pal *et al.*, 1992). This leads to an increase in the overall viscosity of the emulsion. When water is emulsified into heavy oil, even though water itself is much less viscous than the oil, the water droplets act as barriers to flow of the oil molecules and the emulsion becomes more viscous than the oil phase

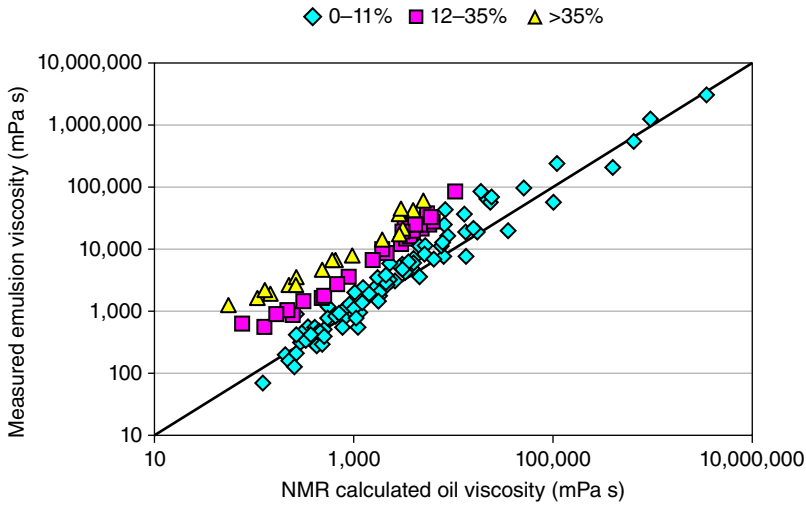

Figure 7.24 Prediction of viscosity of water-in-oil emulsions using the NMR oil viscosity correlation. *Source*: Bryan *et al*. (2002a). Reproduced with permission of the Society of Core Analysts.

alone. This is shown in Figure 7.24, which compares measured emulsion viscosity to the viscosity predicted using the general NMR viscosity correlation (Equation 7.10). It was previously shown that this correlation was able to generate order-of-magnitude accuracy prediction of oil viscosity, but when the oil phase contains emulsified water, the measured viscosity appears to be larger than the viscosity of the oil phase alone.

The viscosity of samples with emulsion water cuts of under 12% by mass appear to be predicted with order-of-magnitude accuracy using the NMR bulk oil correlation. For samples with higher emulsion water content the effect of the emulsified water is clearly evident: while the NMR model focuses on prediction of the oil-phase viscosity the overall emulsion is more viscous, and in fact the offset between measured viscosity and the NMR correlation becomes more significant for higher water cuts.

Water droplets emulsified in oil still have a very different viscosity than the oil phase, so NMR can be easily used to evaluate the water content in a mixture of oil and water. This was the basis for the NMR water cut meter application. The approach taken is therefore to measure the NMR response of the emulsion, and then predict oil phase viscosity using Equation 7.10 and emulsion water cut by cutting the oil and water signals and applying the water AI value to the water amplitudes. The following empirical correlation can then be used to predict the heavy oil emulsion viscosity (Bryan *et al*., 2002a):

$$\mu = \left[\frac{2166}{(RHI)^{3.80} T_{2gm}}\right]\left[\frac{1}{(1-x_w)^{4.46}}\right] \tag{7.11}$$

where x_w is the NMR water cut (mass water/total mass of sample).

The emulsion viscosity correlation in Equation 7.11 basically follows the emulsion viscosity form proposed by Pal *et al*. (1992):

$$\mu_{emulsion} = \mu_{continuous}\left[\frac{1}{(1-x_w)^{\gamma}}\right] \tag{7.12}$$

where γ is an empirical fitting constant for the emulsion system being tested. The value of 4.46 in Equation 7.11 was found by correlating the NMR oil viscosity and the NMR water content (x_w) to the measured water-in-oil emulsion viscosity. Figure 7.25 shows that when the water content is accounted for in the viscosity model the predicted viscosities now line up much more closely to the measured value.

It should be noted that the emulsion droplet size distribution may also play a role in the viscosity of the emulsion: smaller droplets tend to lead to higher viscosity systems because larger droplets may deform and flow more easily under shear conditions (Pal, 1996). Water droplets emulsified into heavy oil may relax faster than the bulk T_2 value of low viscosity water, since there may be some surface relaxation effects on the water droplets. However, the surface relaxivity of water and oil (Equation 7.4) is unknown, and will not necessarily be a constant for different oils. Therefore, it is not trivial to quantitatively evaluate emulsion droplet size distributions from the NMR T_2 values of water in oil. Accounting for the emulsion water fraction alone and not its droplet size distribution (Equation 7.11) already leads to a reasonable prediction of emulsion viscosity. This means that water droplets are relatively small and are acting as stable barriers to flow, compared to the response of large deformable water droplets. This makes sense since if emulsion viscosities are measured these are likely stable

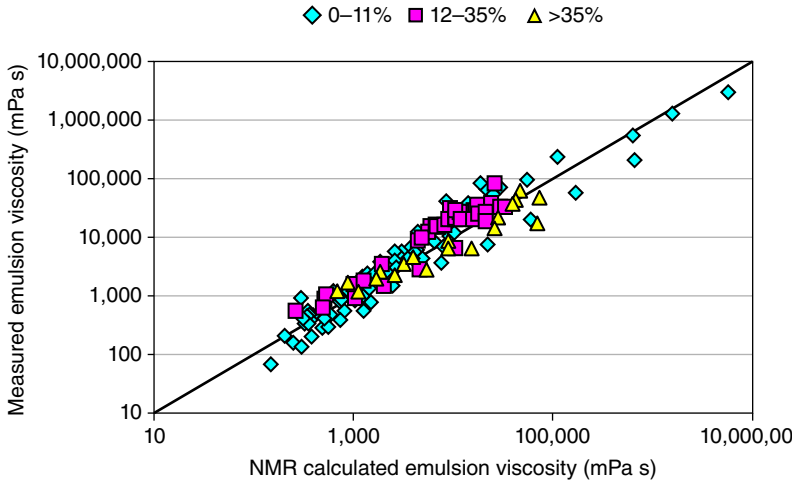

Figure 7.25 Prediction of viscosity of water-in-oil emulsions using the NMR oil viscosity correlation corrected for NMR water content. *Source*: Bryan *et al*. (2002a). Reproduced with permission of the Society of Core Analysts.

emulsions, so droplet sizes are small and this is what prevented the water from separating out of the oil. Therefore, accounting for the water fraction should already be sufficient for order-of-magnitude accuracy emulsion viscosity predictions; the impact of accounting for droplet size distribution will be in the fine-tuning of the model in a single oil system.

7.5 Fluid Saturations and Viscosity in Porous Media

In the previous section, viscosity predictions of oil (both tuned and general) were made on bulk oil systems, where NMR relaxation was clearly through bulk processes and was therefore controlled by the oil viscosity. Bulk liquid correlations can be useful in conditions where only a small amount of oil can be extracted from core. The true value of an NMR viscosity prediction, however, is if these measurements can be made on *in situ* fluids within the reservoir. In this application, NMR could either be used as a core analysis or log analysis tool to profile the viscosity of oil as a function of depth and location within the reservoir. For primary production or non-thermal injection processes this allows for the identification of optimal well placement locations. Even in thermal operations where oil will be heated to steam conditions in order to drain, viscosity variations will lead to potential variations in steam chamber growth in different parts of the reservoir (Gates, Adams, and Larter, 2008). NMR viscosity predictions need to be made for *in situ* oil in order to output this information.

The location of fluids within porous media can be understood by interpreting the NMR response of rock containing oil and water at various saturation states. Figure 7.26 shows the NMR relaxation distributions of a sandstone core sample under two saturation states: fully saturated with water and flooded with heavy oil to connate water saturation. For low viscosity water in porous media, bulk relaxation is much slower than surface relaxation, so, as discussed previously, the NMR relaxation distribution is analogous to a pore size distribution where short T_2 values are small pores. The sandstone core used for this study is permeable and contains mainly large pores.

When flooded with heavy oil, the water signal is considerably reduced in the longer T_2 values (i.e. the larger pores). This shows that water has been displaced out of these pores and the non-wetting oil phase now resides in the large pores. The NMR of the core at this oil-flooded state has a fast-relaxing peak that is under 10 ms: this is the signal of viscous oil. Even though oil is physically located in the largest pores of the rock, the oil is viscous, so energy is lost quickly between protons in the liquid and bulk relaxation effects dominate the overall relaxation of the oil. This fast-relaxing peak cannot be due to the signal from water, since the water-saturated relaxation distribution already confirms that there are no small pores that would lead to water signals under 10 ms. Therefore, the fast-relaxing peak is only the signal from viscous heavy oil in the core.

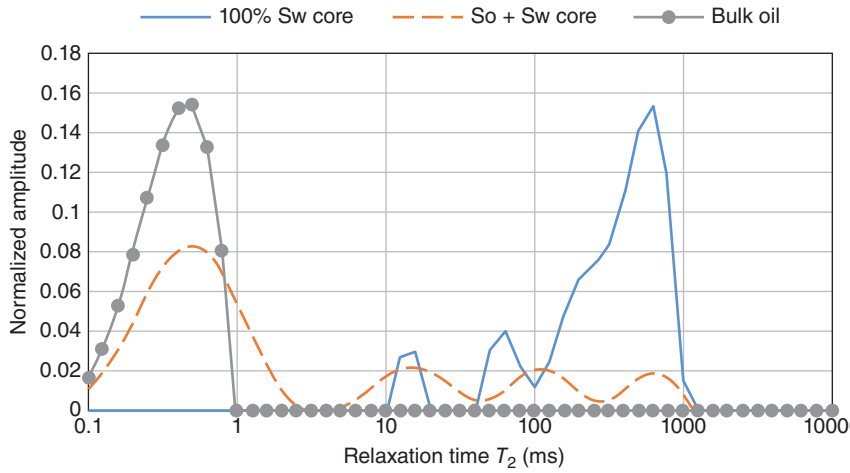

Figure 7.26 Heavy oil in porous media: location of oil and connate water. *Source*: Bryan *et al*. (2005b). Reproduced with permission of the Society of Core Analysts.

Figure 7.26 also shows the normalized signal of the bulk oil used to flood this core. The bulk oil peak occurs at similar T_2 values as the oil within the sandstone core. This effect is significant because it means that when fluid is viscous bulk relaxation dominates over surface relaxation effects, and the NMR T_{2gm} of the oil in porous media will be similar to the T_{2gm} value of the bulk oil. This conclusion means that it is possible to build a tuned NMR viscosity correlation using bulk oils and then use this model to predict viscosity of oil within porous media.

7.5.1 Prediction of Saturations and Viscosity from T_2 relaxation distributions

The NMR viscosity correlation (Equation 7.9) relates viscosity to both the oil T_{2gm} and the *RHI*. Alternatively, in the example of highly viscous bitumen (Figure 7.21 and Figure 7.22) the oil T_{2gm} did not change much with viscosity and the viscosity prediction was based solely on the *RHI* empirical correlation. In either case, NMR parameters *RHI* and T_{2gm} need to be determined for *in situ* relaxation distributions in order to use these models.

The conclusion reached from the test in the consolidated sandstone core (Figure 7.26) is that the fast-relaxing peak in the relaxation distribution of the oil/water system is the signal from viscous heavy oil. Unconsolidated oil sand samples may contain clay and fast-relaxing water that relaxes at similar T_2 values as the oil (Manalo, Bryan, and Kantzas, 2002; Manalo *et al*., 2003). An example of this fast-relaxing water is provided in Figure 7.27, which shows the NMR relaxation distributions of water as a bulk liquid, in sand, and in various

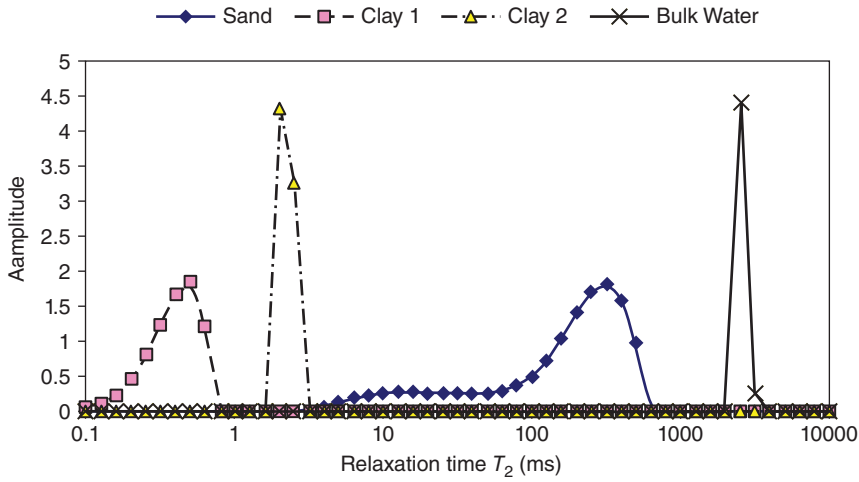

Figure 7.27 Representative relaxation distributions of water in unconsolidated sand and clay. *Source*: Bryan *et al*. (2006). Reproduced with permission of SPE Reservoir Evaluation and Engineering.

clays. As the pore sizes get smaller, bulk relaxation becomes negligible and surface relaxation leads to shorter water T_2 peaks. For water bound to clay, the NMR T_2 values are generally under 10 ms (Manalo, Bryan, and Kantzas, 2002; Manalo *et al*., 2003).

When heavy oil or bitumen is present in the oil sand, the viscosity of the hydrocarbon means that its bulk relaxation effects dominate, the oil signal should always be found within the first peak of the NMR oil sand relaxation distribution. Figure 7.28 compares the location of the first peak in the NMR oil sand relaxation distribution to the NMR peak of bulk oil, and demonstrates that the bulk vs. *in situ* oil response is essentially the same, as was also shown in Figure 7.26. Therefore, even if there is some clay-bound water present also in the first peak of the NMR oil sand relaxation distribution, certainly the entire measurable oil signal is in the first peak and similar bulk vs. *in situ* oil T_{2gm} values are expected.

Figure 7.29 presents the correlation between bulk and *in situ* measured heavy oil T_{2gm} values for a suite of heavy oil samples from a cold heavy oilfield in northern Alberta. There is some scatter in the values, most likely owing to uncertainties caused by the presence of clay-bound water in the first peak of the relaxation distributions. Overall, however, there appears to be a strong correlation between bulk and *in situ* oil T_{2gm} values. This means that the first peak of the oil sand relaxation distributions can be used to estimate the bulk oil T_{2gm}, and this is one of the required terms in the NMR viscosity correlation.

The oil *RHI* is the second term that is required for predicting viscosity of *in situ* oils. When bulk oils are tested *RHI* is measured directly: the oil amplitude is measured through NMR, and the mass of oil is measured directly to get

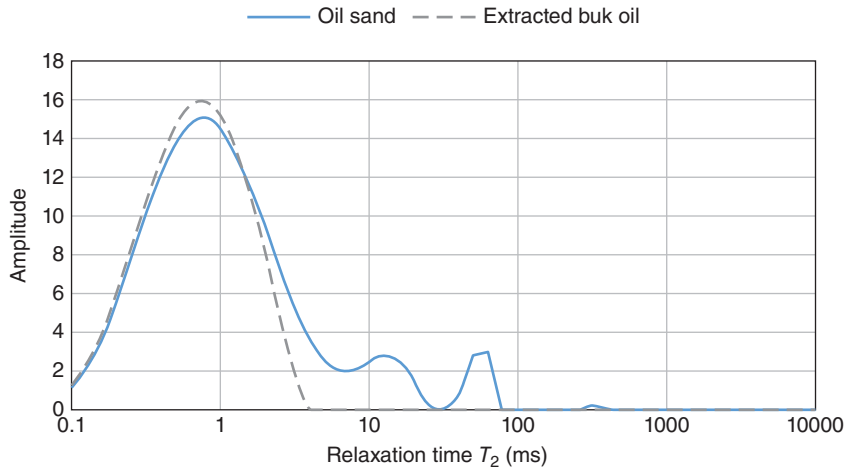

Figure 7.28 Comparison of bulk heavy oil relaxation distribution to relaxation distribution of oil and water in oil sand.

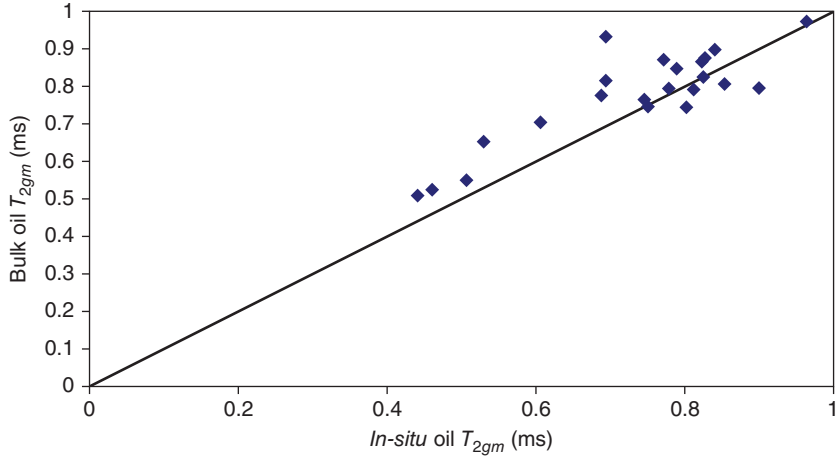

Figure 7.29 Comparison between bulk and *in situ* oil mean relaxation times. *Source*: Bryan *et al*. (2006). Reproduced with permission of SPE Reservoir Evaluation and Engineering.

the oil *AI* and *RHI*. For oil in porous media, the amplitude of the first peak may be measured and assumed to be the contribution from oil, but even with this assumption the oil mass is not known, so *RHI* can no longer be measured directly. Instead, the fact that *RHI* and T_{2gm} are related can be used to generate a correlation between these terms. One such correlation was previously shown for a single oil measured over multiple temperatures (Figure 7.18), and another correlation is shown in Figure 7.30, using the same bulk oil samples from Figure 7.29. When oil viscosity is higher, the measurable oil T_{2gm} is lower

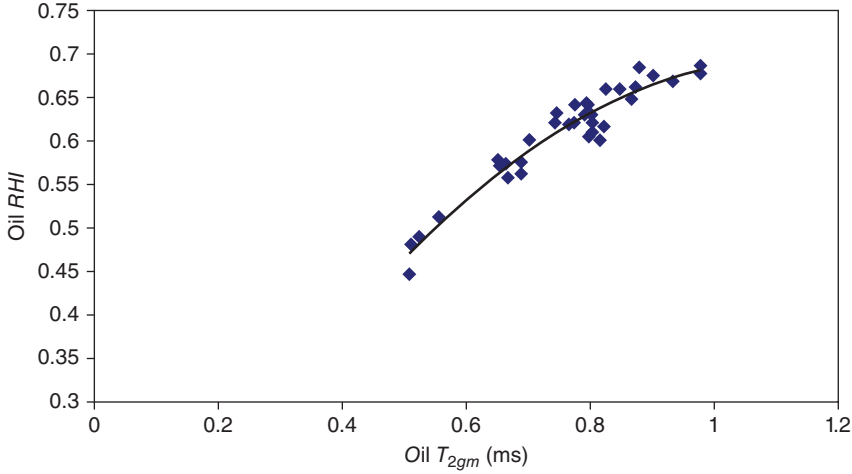

Figure 7.30 Prediction of *in situ* oil *RHI* from oil T_{2gm}. *Source*: Bryan *et al*. (2006). Reproduced with permission of SPE Reservoir Evaluation and Engineering.

and also a portion of the oil relaxes too quickly to be measured, so accordingly *RHI* is low as well. If *RHI* is predicted based on the bulk oil T_{2gm} values, then the viscosity correlation (Equation 9) is really just a non-linear function of the oil T_{2gm}. The *in situ* oil T_{2gm} is calculated on the basis of the first peak of the oil sand relaxation distribution, the oil *RHI* is obtained from the *RHI*-T_{2gm} correlation in Figure 7.30, and both terms are used in Equation 7.9 to predict the *in situ* viscosity of the oil.

Figure 7.31 shows an example output using this non-linear T_{2gm}-based approach to predict viscosity on samples of core from a heavy oil non-thermal production well. Samples of oil were extracted from the core and used to build a tuned NMR viscosity model for this reservoir, following the form of Equation 7.9. The oil sand relaxation distributions were then measured, and the first peaks of these relaxation distributions were used to calculate the *in situ* oil T_{2gm} and *RHI* values. Figure 7.31 then shows that the predictions made in the core show the same variation in viscosity with depth was what was measured for the extracted bulk oils. This approach could be applied to full core logging of a well (i.e. NMR relaxation distributions measured along the entire length of the cored zone to get a proper high resolution viscosity profile) or even in logging tool relaxation distributions measured for the oil at reservoir temperature and pressure.

The approach taken in Figure 7.30 and Figure 7.31 was to determine *in situ* oil T_{2gm} directly, and then to predict the other required viscosity term (*RHI*) based on the non-linear correlation between *RHI* and T_{2gm}. This methodology requires oil viscosity to be in the range where there is an observable relationship

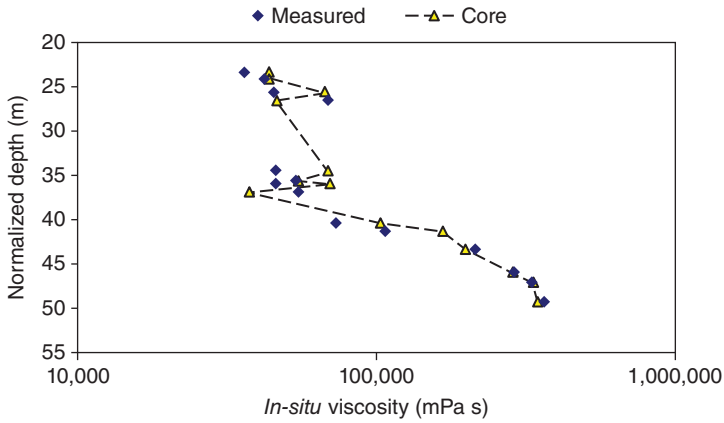

Figure 7.31 Prediction of *in situ* oil viscosity on core samples using non-linear T_{2gm}-based approach. *Source*: Bryan *et al*. (2006). Reproduced with permission of SPE Reservoir Evaluation and Engineering.

between viscosity, *RHI* and T_{2gm}. In the case of high viscosity bitumen where the oil relaxes so quickly that the T_{2gm}–viscosity relationship is poor, another means is required to predict *RHI*. The other piece of information available in log or core analysis is a measure of the total porosity, based on the density of the medium. The total pore space needs to be filled with liquid (oil and water). If the rock is water-saturated, the water *AI* is calibrated and NMR can be used to measure the porosity of the rock (Straley *et al*., 1997; Coates, Xiao, and Prammer, 1999). However, when the porous medium contains viscous oil, only a portion of the actual oil signal is measured and the rest relaxes too quickly to be measured in the NMR decay curve. The result is that, without knowing *a priori* how to calibrate the oil signal, the total porosity predicted by the NMR (amplitude divided by water *AI*) will be lower than the true porosity of the system. Heavy oil and bitumen zones can be seen in NMR logs and core measurements as regions where NMR porosity is lower than the density porosity of the system (Galford and Marschall, 2000; Chen and Bryan, 2013).

Figure 7.32 shows the output from an NMR log relaxation distribution, and illustrates this phenomenon of porosity underestimation. The first peak in the NMR signal is the contribution from viscous bitumen (and perhaps some fast-relaxing clay-bound water). Any signal beyond the first peak has to come only from connate water present in the formation. The bottom half of Figure 7.32 shows the splitting of total volume into matrix and pore fluid components. The porosity fraction is filled with oil and water. The key assumption made in this analysis approach is that, in the bitumen-bearing sand, the contribution from clay-bound water is small. Therefore, the amplitude in the first peak can be entirely taken to be the amplitude of bitumen, and water saturation

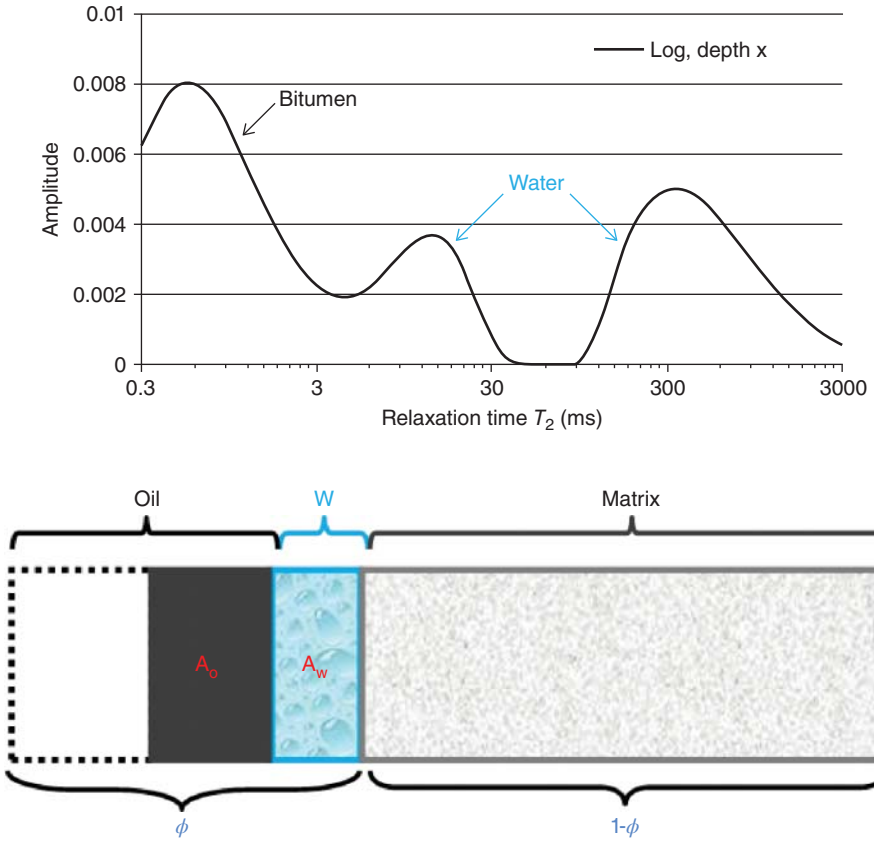

Figure 7.32 Interpretation of *in situ* oil *RHI* from combined NMR/density log data. *Source*: Chen and Bryan (2013). Reproduced with permission of SPE Proceedings.

corresponds to the water NMR signal after the first peak. This approach is valid in relatively clean oil sand zones (Kantzas *et al*., 2005; Bryan *et al*., 2006).

In logging tool applications, the water amplitude measured is normalized to the signal of 100% porosity filled with water. As a result, the output from NMR logs is porosity units of water (i.e. water amplitude/amplitude for porosity = 1). NMR water saturation is given by the following expression:

$$S_w = \frac{A_w}{\phi} \tag{7.13}$$

where:

S_w = water saturation (fraction)
A_w = NMR water amplitude (i.e. signal after the first peak) expressed as porosity units
ϕ = total porosity of this zone, as measured independently by the system bulk density.

Since water relaxes in a range that can be properly captured by low field NMR, all the water signal has been measured and the water saturation calculated from Equation 7.13 should match with other independent measurements. If that is true, then the remaining NMR amplitude (i.e. the signal in the first peak of the relaxation distribution) is the amplitude from viscous bitumen. If all the oil signal had been measured (i.e. if oil had an $RHI = 1$), the summation of oil and water amplitudes should equal the total porosity of the system. Instead, because part of the oil relaxed too quickly to be measured, the porosity output from the NMR oil portion of the relaxation distribution is less than the actual oil-occupied pore space. *RHI* is then calculated from the following expression:

$$RHI = \frac{A_o}{\phi(1 - S_w)} \tag{7.14}$$

where

A_o = measured oil amplitude expressed as porosity units
$\phi(1 - S_w)$ = oil-saturated portion of the pore space.

Equation 7.14 shows that the oil *RHI* is the measured oil signal, normalized to the NMR signal that should have been measured if viscosity were low (i.e. if $RHI = 1$). Using this approach, *RHI* can be calculated for each measured point in the oil-bearing zone, and viscosity can be either predicted using a correlation of the form of Equation 7.9 or using a viscosity vs. *RHI* correlation like that shown in Figure 7.23.

By following this approach, NMR can give a combined output of both oil and water saturation in the system and also the viscosity of oil. Figure 7.33 shows an example of both water content (i.e. fluid saturation) and *in situ* oil viscosity that was made on core samples from a heavy oil system in northern Alberta. If oil and water signals can be separated in NMR relaxation distributions, the water amplitude can be used to get water saturation vs. depth in the system. Likewise, the oil *RHI* values can be used to predict oil viscosity variations within the formation.

Figure 7.34 shows a similar approach for the combined output of both fluid saturation and *in situ* viscosity, but now from an NMR logging tool run in a bitumen formation. Track 3 in this figure is porosity outputs from the density log, NMR, and from discrete measurements taken on core plugs within the zone. The core and density porosity values track one another closely, indicating that the density log is a reliable output of the total porosity in this zone. The NMR log underestimates porosity in this region, which is an indication that this is a bitumen-bearing zone. The green region in Track 3 is the porosity under-call from the NMR log.

Track 4 in Figure 7.34 is water saturation predictions made using Equation 7.13 and splitting the relaxation distributions at the local minimum indicating the end of the first peak of the NMR relaxation distribution. The core data points are Dean–Stark water saturation measurements, which track the NMR log output values well with depth. This provides confidence

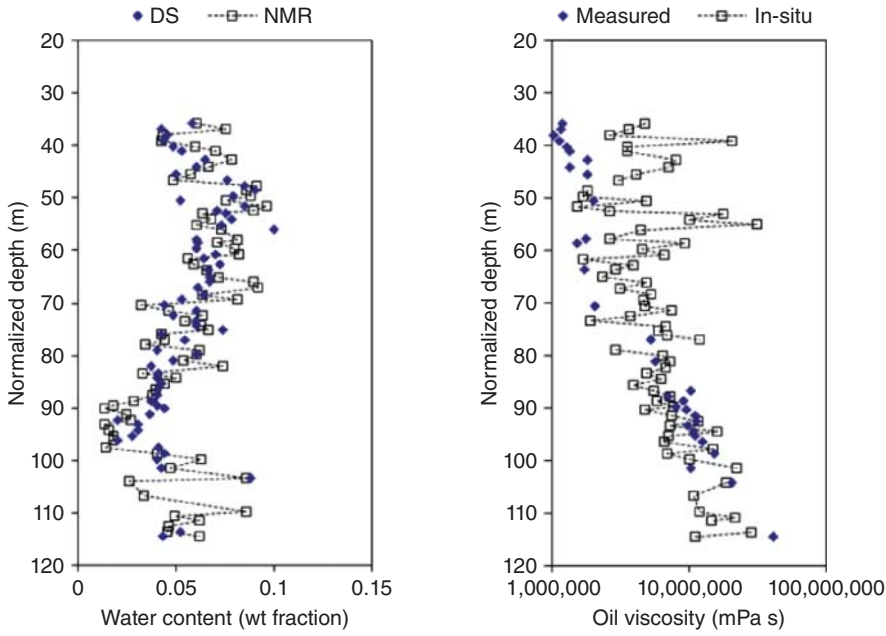

Figure 7.33 Example of NMR predictions of fluid content and *in situ* oil viscosity in oil sand core.

that the proposed amplitude peak splitting approach is correct: the signal from water is the NMR response after the first peak in the relaxation distributions.

Track 5 in Figure 7.34 is the oil *RHI* as calculated from Equation 7.14. This bitumen formation did not exhibit any variation in the oil T_{2gm} because viscosity was so high that relaxation was at the limit of what could be measured by the low field NMR tool. Instead, viscosity was predicted using an *RHI* equation similar to what is shown in Figure 7.23, and Track 6 of Figure 7.34 is the predicted bitumen viscosity profile in the well. Also shown in this track are the values of viscosity measured for extracted bulk oil from the core samples. NMR tracks the measured viscosity profile quite well, so through combining the NMR density log outputs, predictions could be made for both saturation and oil viscosity within this zone.

7.5.2 Prediction of Saturations from T_1–T_2 Relaxation Distributions

The method described for determining oil and water saturations from log or core assumes that a cutoff point can be assigned to separate oil and water signals from the NMR relaxation distributions. Specifically, the amplitude within the first peak is mainly the contribution from oil, while water saturations are calculated from the signals after the first peak. Certain deconvolutions may

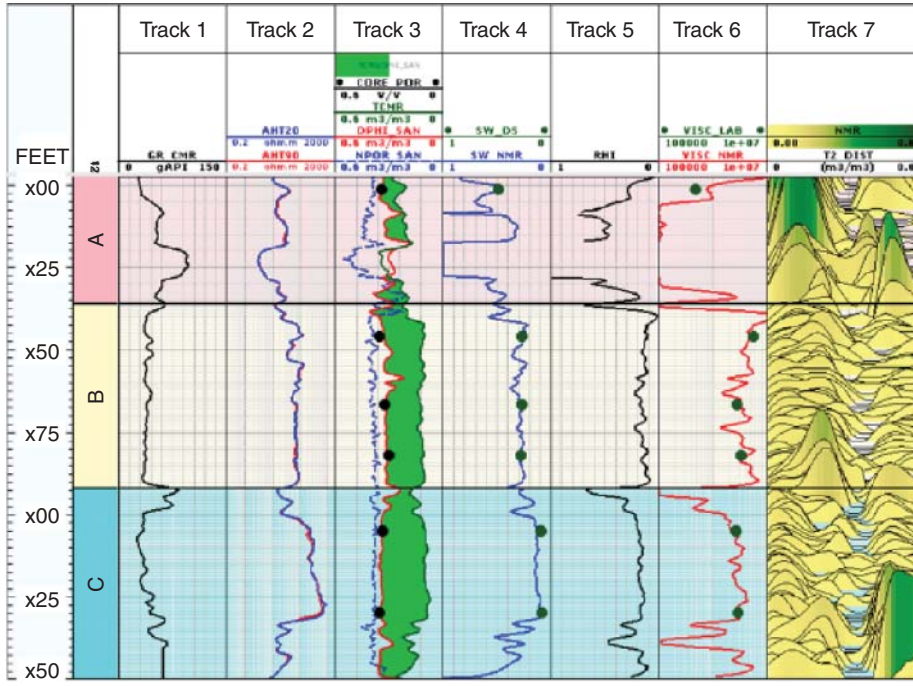

Figure 7.34 Oil sand log prediction of in-situ bitumen viscosity using *RHI*-based model. *Source*: Chen and Bryan (2013). Reproduced with permission of SPE Proceedings.

be applied to further refine this cutoff point (Kantzas *et al*., 2005; Bryan *et al*., 2006; Kryuchkov *et al*., 2003), but overall the analysis is similar in all of these approaches.

In many cases this approach works well: in the two case studies shown in Figure 7.33 and Figure 7.34 it is possible to track saturations vs. depth in both wells. Many good-quality oil sand relaxation distributions are similar to what are shown in Figure 7.28, and so the first peak of the distribution can be essentially taken to be the contribution from oil, and connate water is the signal after the first peak in the oil sand distribution. Water in clays can relax in the same T_2 range as heavy oil (Figure 7.27), but when the clay-bound water fraction is small, overall saturations and viscosity predictions can be made by just assuming that this water is insignificant and all the signal in the first peak is from oil. An important distinction, however, is that, while the oil signal will be entirely within the first peak of the oil sand distribution, the signal from the first peak is not necessarily all oil. When the clay-bound water fraction is large, there can be significant water saturation in this peak as well. In this case, the approach of splitting oil and water as signal before and after the first peak may

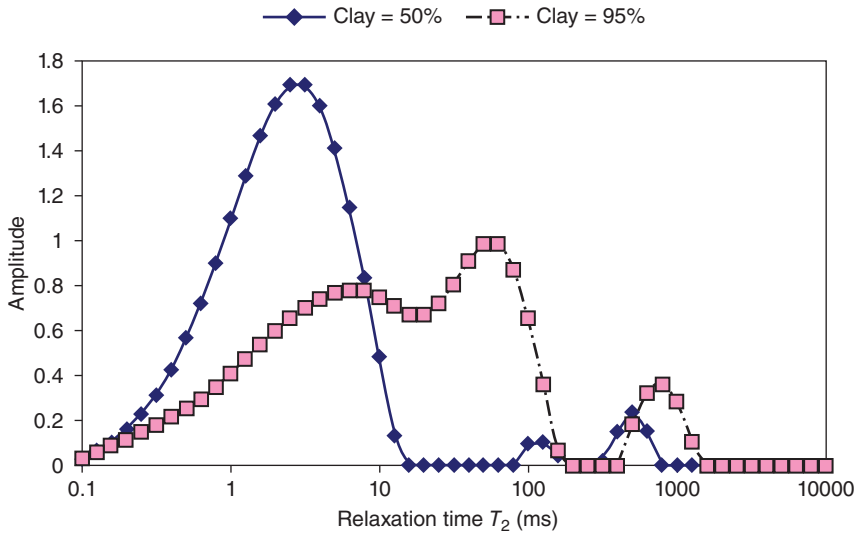

Figure 7.35 Synthetic oil sand with 4.5 wt% bitumen and clays between 50 and 90% of total solids mass. *Source*: From Bryan *et al.* (2006). Reproduced with permission of SPE Reservoir Evaluation and Engineering.

no longer be valid and the subsequent NMR saturation and viscosity predictions will be wrong.

Figure 7.35 shows the NMR relaxation distributions for two sets of synthetic oil sand samples, both containing 4.5 wt% bitumen (oil saturation = 0.30). In one sample the solids consists of 50% clay by mass, while the other sample solids are 95% by mass. Therefore, the connate water in both samples will be largely bound to the clay. In the case of the sample with only 50% clay, there is still a clear first peak that relaxes in the order of 1–2 ms on average. Note that the water after the first peak is small, even though this oil sand contains 70% water saturation. This means that there is considerable amplitude of water within the first peak. There is still a good contribution of oil in this peak, but by assuming that all the amplitude in the first peak is oil, this would lead to significant underestimation of the actual water saturation in this sample. The sample with solid consisting of 95% clay has an even higher degree of overlap between oil and bound water peaks. Here the clay was only loosely packed so water appears to relax more slowly and there may in fact be a better separation between oil and water, but even in this sample it is inaccurate to assume that all the signal up to the first local minimum is from oil, and there is no water overlapping with the oil amplitude in the first peak of the relaxation distribution.

Figure 7.36 shows results of two more synthetic oil sand samples, both with the solids containing 50% clay by mass. One sample is the low oil content (30% saturation) from Figure 7.35. The other sample has a much higher oil content, and an overall higher porosity. For the same amount of clay in the

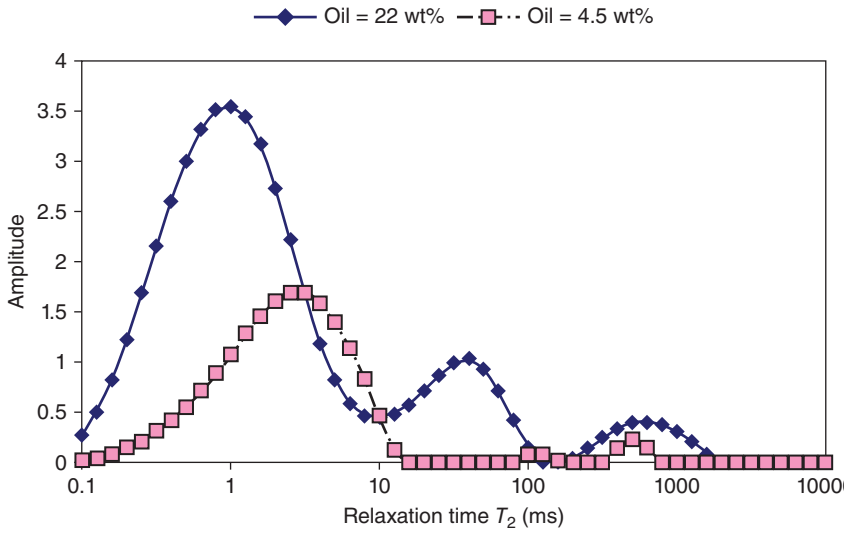

Figure 7.36 Synthetic oil sand with solid containing 50% clay, but oil content varied between 4.5 and 22 wt%. *Source*: From Bryan *et al*. (2006). Reproduced with permission of SPE Reservoir Evaluation and Engineering.

sample, but less water bound to clay and a larger signal from oil, the first peak is clearly related again mainly to the signal from oil. This sample can likely be used to calculate viscosity and saturations, but when the clay-bound water signal is high and the oil signal is small, a T_2-based approach alone may not be sufficient to properly discriminate between oil and clay-bound water amplitudes.

Jones *et al*. (2014) made NMR measurements of actual oil sand samples containing variable oil and water contents, as determined by Dean–Stark analysis. Samples 1 and 2 in Figure 7.37 have variable oil content for the same amount of water. Sample 3 contains a much higher water content for a similar amount of oil as in Sample 2. Finally, Sample 4 contains the similar oil content as in Samples 2 and 3, but even lower water content. While all samples contain the same bitumen (i.e. oil with a given *RHI* and T_{2gm} value), the varying amount of oil and water in the samples leads to overlap in the oil and bound water peaks, and it is not clear how to separate these signals accurately on the basis of the T_2 relaxation distribution alone.

Instead, what is proposed is to measure the T_1–T_2 two-dimensional (2D) array that is shown in Figure 7.38. T_2 relaxation has already been discussed throughout this chapter: this is the loss of signal on the transverse plane. T_1 relaxation measures the signal on the longitudinal plane. At time = 0 the signal is zero since all protons have been tipped onto the transverse plane, and as the signal decays on the transverse plane, the protons return on their equilibrium direction and signal grows on the longitudinal plane. For fluids like bulk

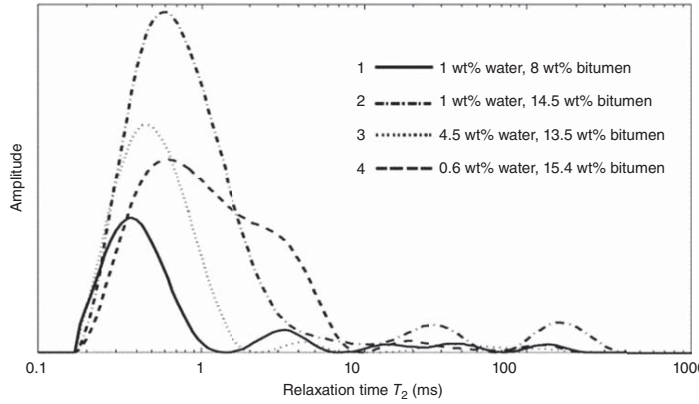

Figure 7.37 Example oil sand samples containing variable measured oil and water contents. *Source*: Jones *et al*. (2014). Reproduced with permission of SPE Proceedings.

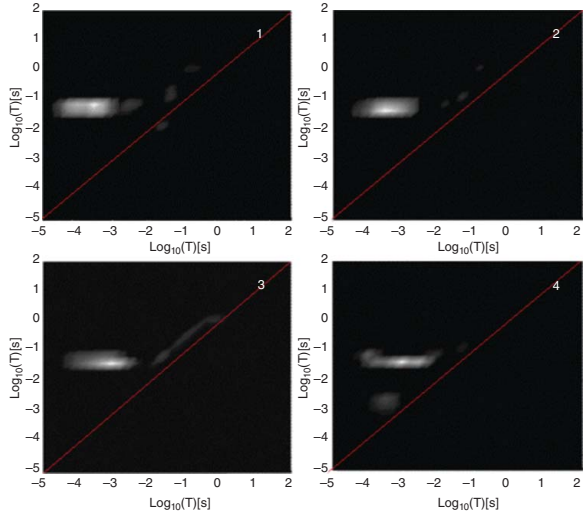

Figure 7.38 T_1–T_2 two-dimensional NMR array for separating overlapping bitumen and clay-bound water signals in oil sands. *Source*: Jones *et al*. (2014). Reproduced with permission of SPE Proceedings.

water or water in porous media, T_1 and T_2 should mirror one another since the only way for the signal to be lost on the transverse plane is for the protons to give off energy and return to their equilibrium position. For viscous heavy oil and bitumen, however, molecules are complex and sometimes interwoven, and some of the signal on the transverse plane is lost because of signal de-phasing rather than the true loss of energy on the transverse plane (Dunn, Bergman, and LaTorraca, 2002). The result of this is that, while the signal appears to have decayed on the transverse plane (i.e. short T_2 value), the protons have not yet fully returned to their equilibrium direction, so the T_1 representative time is much longer than the T_2 value. This loss of coherence on the transverse plane explains why viscous oil, which contains a fixed amount of hydrogen per unit mass, appears to have a variable *RHI* with temperature. When the oil is highly viscous, the apparent relaxation rate is too fast to be measured (i.e. some of the oil is relaxing faster than what should have corresponded to the oil viscosity from the correlation in Equation 7.10). This is an apparent very fast T_2 value that does not represent true relaxation of the oil but just a loss of signal in the transverse plane. The true relaxation of the oil is understood in its T_1 value, which is when the protons return to their actual equilibrium direction.

The red diagonal lines through the 2D relaxation distributions in Figure 7.38 represent the line where $T_1 = T_2$ (i.e. relaxation on the transverse plane is due to a true loss of energy). When data are skewed from the line (i.e. where $T_1 > T_2$), this is loss of signal coherence on the transverse plane, which is the signal from the viscous oil. In this manner, the 2D relaxation distributions can be used to evaluate the amplitude of water (close to the $T_1 = T_2$ line) and bitumen (off from the line, with $T_2 \ll T_1$). This approach allows for oil and water amplitudes to be determined, and fluid saturations measured, even in the absence of a clear split between oil and water in the T_2 relaxation distributions alone. 2D measurements are much slower than simple T_2 measurements, so each sample takes significantly longer to measure. For this reason, T_2 measurements are generally preferred. However, for cases when saturation needs to be measured in samples with significant oil and bound water overlap in the T_2 relaxation distributions, the 2D approach has the potential to discriminate between these different fluids.

7.6 NMR in Oil-Solvent Systems

The major challenge to the production of heavy oil and bitumen is its high viscosity. Heat is a very effective way to reduce viscosity of oil, so most production of heavy oil and bitumen is through thermal methods, specifically steam injection into the reservoir. If the reservoir exhibits sensitivity to fresh water, if it is too deep for steam, or if it has poor containment, all of these can make steam processes difficult to implement. In these reservoirs, another major way of reducing viscosity is through the use of solvents to dilute the oil. Solvents

may be injected as a vapor phase into heavy oil (Das and Butler, 1998; Ivory *et al*., 2010) or solvents may be added as a liquid to oil, usually in combination with steam (Nasr *et al*., 2003; Stark, 2013).

In produced mixtures of solvent and heavy oil or bitumen, certain parameters are of particular interest: (1) the fraction of solvent and oil in the produced mixture in order to do proper material balance closure and (2) viscosity of the solvent-diluted oil. The value of a tool like NMR is that is has already been shown to be capable of measuring viscosity is liquid systems. Moreover, since the NMR measures decay and relates this to viscosity, the system does not need to be flowing, or it can be at a non-equilibrium state and the NMR predictions can still be valid. The interpretation of relaxation distributions in liquid and vapor phase solvent systems is different, so these will be treated separately in the following sections.

7.6.1 Predictions of Solvent Content in Oil–Liquid Solvent Systems

Figure 7.39 shows NMR relaxation distributions of a bitumen sample, a bulk paraffinic solvent (heptane) and the final mixture of solvent-diluted oil. These are all liquids so the T_2 distributions are related to the viscosity of each liquid. The bitumen is a viscous oil with a fast-relaxing peak under 10 ms, and with a T_{2gm} of 1–2 ms. Heptane is a low viscosity fluid: like water, it relaxes in the order of 2000–3000 ms, and has a narrow peak since it is a single component, compared with the multi-component bitumen. When bitumen and heptane are mixed together, both fluids still have hydrogen so both still give off an NMR signal. However, the oil is now less viscous, so it relaxes more slowly and also

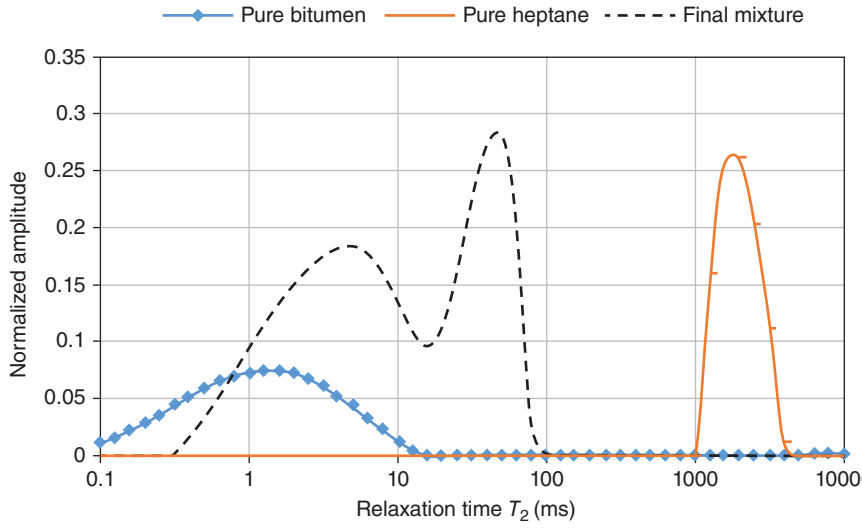

Figure 7.39 NMR relaxation distributions of bitumen, liquid solvent, and oil/solvent mixture. *Source*: Bryan *et al*. (2002b). Reproduced with permission of SPE Proceedings.

has more amplitude. Likewise, the solvent is now mixed with the oil so its peak is shifted to shorter T_2 values, reflecting the fact that the overall mixture is more viscous than the solvent alone.

Although the final oil/solvent mixture in Figure 7.39 still consists of two peaks, the overall mixture could be represented by a single T_{2gm} value that is the average T_2 of the entire mixture relaxation distribution. Figure 7.40 shows the T_{2gm} of bitumen/heptane mixtures with varying solvent content. Three oils are tested, ranging from heavy oil (6000 mPa s) to viscous bitumen (670,000 mPa s). Each oil is mixed with various concentrations of solvent, and the final mixture viscosities were measured. NMR was also measured, and Figure 7.40 shows a strong and monotonic relationship between viscosity and T_{2gm}. Viscosity and T_{2gm} are inversely related until viscosities are above 1000 mPa s, at which point the correlation deviates from linearity and changes in viscosity have smaller associated change in T_{2gm}. The nature of the relationship shown in Figure 7.40 is exactly what was previously observed for bulk oils of variable viscosity. This means that mixing oil with solvent results in just a lower viscosity oil, and NMR is measuring slower transference of energy between protons similarly to what was measured in solvent-free oils. The trend of solution *RHI* and viscosity in Figure 7.41 is also the same as what was observed for different bulk oils.

It should be noted that, for the *RHI* correlation with viscosity, for very low viscosity mixtures (i.e. high solvent content) the solution *RHI* can actually be greater than one. Both of these figures demonstrate that the solution can be

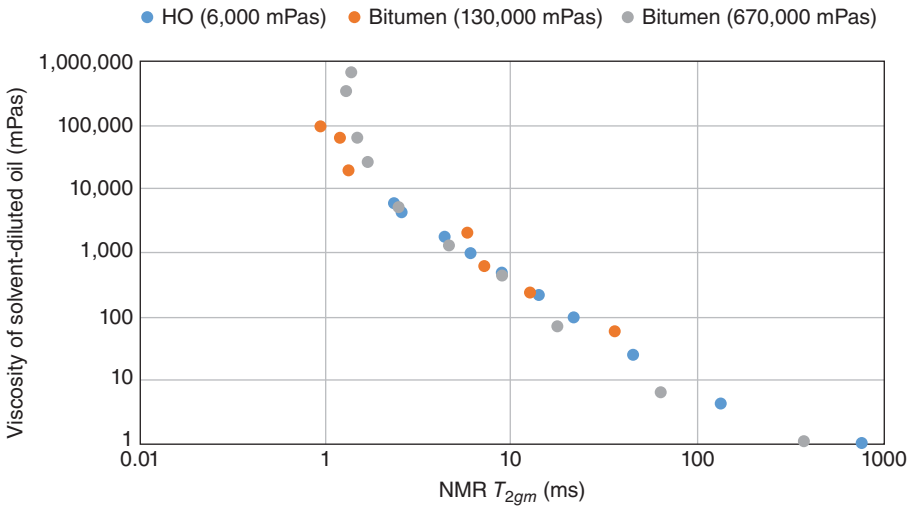

Figure 7.40 Correlation between diluted oil viscosity and mixture mean relaxation time for solutions of oil and paraffinic solvent (heptane). *Source*: From Wen, Bryan, and Kantzas (2005). Reproduced with permission of the Journal of Canadian Petroleum Technology.

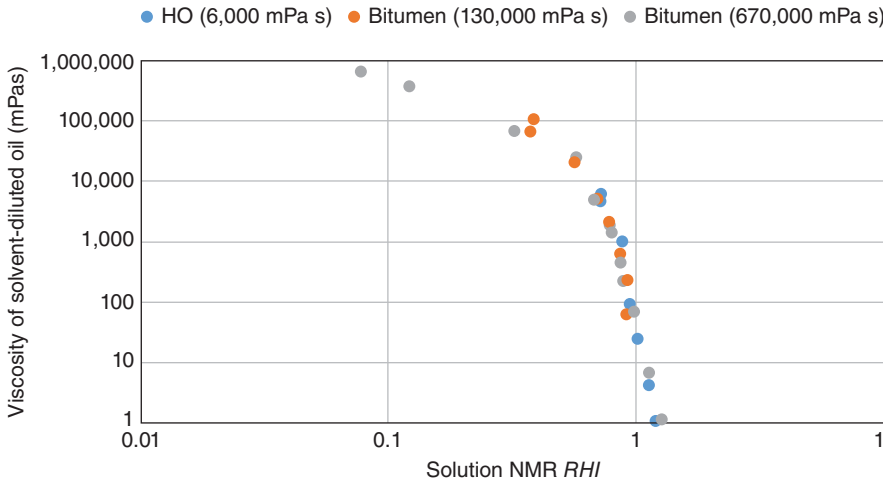

Figure 7.41 Correlation between diluted oil viscosity and mixture *RHI* for solutions of oil and paraffinic solvent (heptane). *Source*: From Wen, Bryan, and Kantzas (2005). Reproduced with permission of the Journal of Canadian Petroleum Technology.

represented by its mean T_{2gm} and *RHI* values, and that dissolving solvent into heavy oil or bitumen is just the same as having a lower viscosity oil.

While solvent solution into oil yields a lower viscosity mixture, it is important to note that not all solvents are equal in terms of their ability to affect the properties of oil. Figure 7.42 shows the results of the same bitumen (130,000 mPa s) but mixed with two solvents: octane (C_8H_{18}) and pentane (C_5H_{12}). Figure 7.42 plots the bitumen mass fraction against the pseudo-NMR viscosity term, which is the inverse of $RHI \cdot T_{2gm}$. This term has a similar form of the NMR viscosity correlation (Equation 7.9) and serves to demonstrate that, for the same mass fraction of oil, pentane results in a lower mixture viscosity than octane. This can be explained using mixing rules for diluted oil viscosity (Shu, 1984), which state that the viscosity of a mixture is a weighted combination of oil and solvent phase viscosities. For the same oil mixed at the same fraction with both solvents, pentane has a lower viscosity than octane and the result is a lower mixture viscosity.

Bitumen (130,000 mPa s) was mixed with various paraffinic solvents: pentane, hexane, heptane, and naphtha (a light solvent consisting of a range of components, from butane to heptane). Known oil/solvent mixtures were prepared and the mixture viscosity and NMR were measured for each solvent.

Table 7.4 lists the tuned values of α and β for the NMR viscosity correlation (Equation 7.9). Similarly to what was shown in Figure 7.42, different solvents lead to different mixtures viscosities, so the NMR tuned viscosity coefficients are also different for each system. There is no apparent correlation between

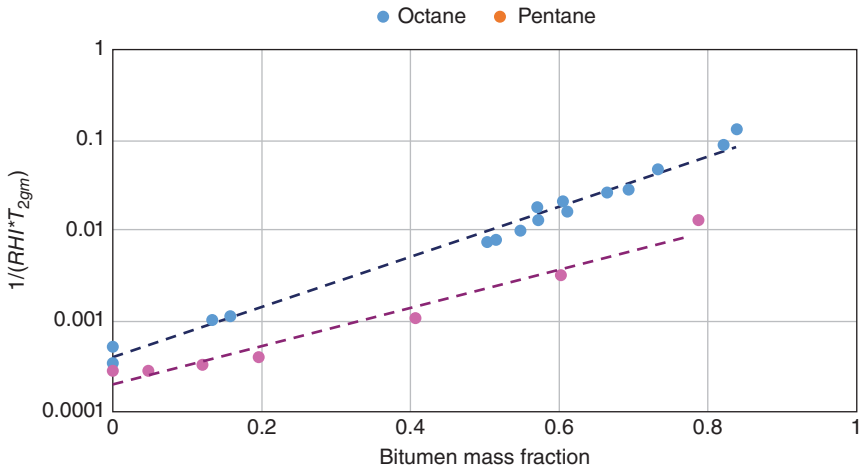

Figure 7.42 NMR pseudo-viscosity correlation vs. bitumen content for different paraffinic solvents. *Source*: From Salama and Kantzas (2005). Reproduced with permission of SPE Proceedings.

Table 7.4 NMR viscosity model parameters for bitumen (130,000 mPa s) and various paraffinic solvents. *Source*: From Wen, Bryan, and Kantzas (2005). Reproduced with permission of the Journal of Canadian Petroleum Technology.

Solvent	α	β
Pentane	2805	4.90
Hexane	2216	5.19
Heptane	4349	3.77
Naphtha	1694	5.29

solvent carbon number and the values of α and β. If solvents are simply diluting oil by unlocking large molecules in the oil, viscosity mixing rules predict that the lowest viscosity should be with pentane, and the highest viscosity should likely be heptane. The fact that there is no apparent correlation between NMR coefficients and the solvent used means that liquid solvents are also leading to compositional changes within the oil.

A sample of heavy oil was mixed with heptane (paraffinic) or toluene (aromatic) and mixture viscosities and NMR relaxation distributions were measured. Figure 7.43 plots the mixture viscosity against the geometric mean relaxation time of each mixture. Both toluene and heptane solution in oil

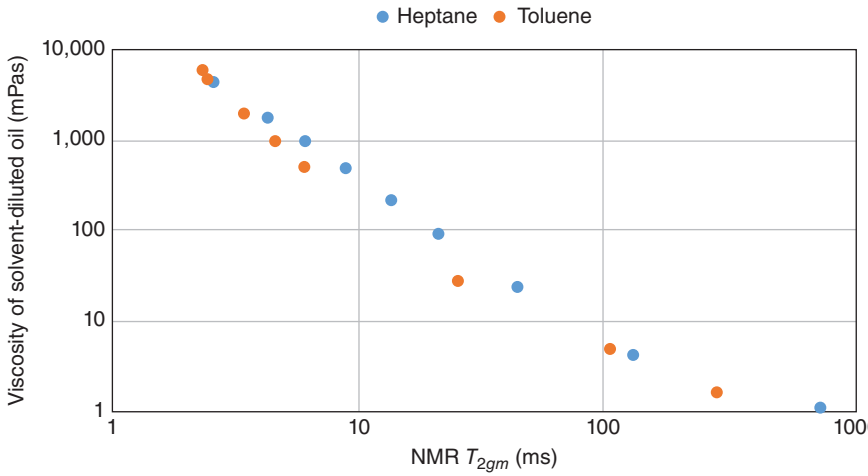

Figure 7.43 Correlation between diluted oil viscosity and mixture mean relaxation time for solutions of oil and paraffinic or aromatic solvent.

reduce the viscosity of the oil, and the relationship between NMR T_{2gm} and viscosity is similar for both solvents. When comparing viscosity vs. *RHI* for the paraffinic and aromatic solvents (Figure 7.44) a different trend appears. In this figure, *RHI* is shown in a linear scale to illustrate differences between the two solvents for low viscosity (high solvent content) mixtures. With the aromatic solvent, oil *RHI* increases as the solution is mixed with oil, which is

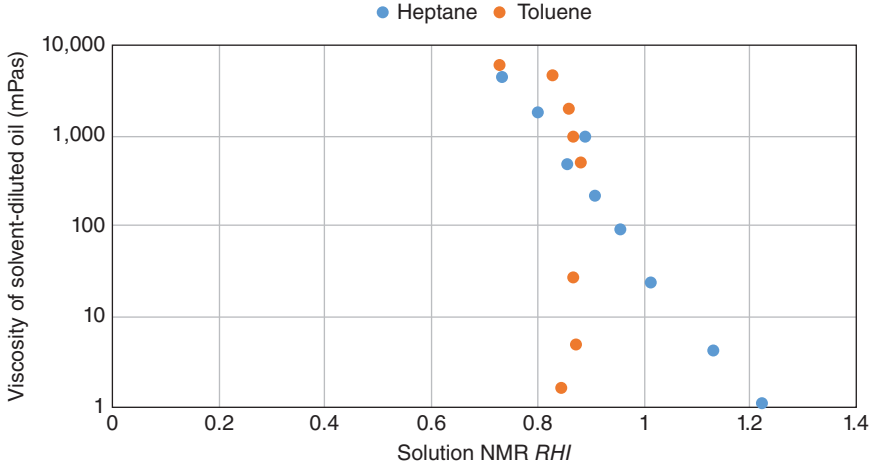

Figure 7.44 Correlation between diluted oil viscosity and mixture *RHI* for solutions of oil and paraffinic or aromatic solvent).

the contribution of adding solvent to the mixture and also measuring more of the signal from the now slower relaxing oil. Eventually, however, *RHI* appears to level out while for the paraffinic solvent, the *RHI* continues to increase with increasing solvent and in fact becomes larger than one, as also observed in Figure 7.41. In both cases the solvent has dramatically reduced the viscosity of the oil, and the entire signal from the oil can be measured, but the changing *RHI* in the case of the paraffinic solvent is an indication that something has been altered compositionally within the oil.

Figure 7.45 shows this effect more clearly, by plotting solution *RHI* vs. bitumen mass fraction for bitumen mixed with either toluene or various paraffinic solvents. In the range of 0–15% solvent by mass, or up to around 50 mol% solvent in the oil, all the solvents behave the same way: *RHI* increases with decreasing solvent content. In this range of solvent contents the impact of the solvent is to reduce the viscosity of the oil, most likely through the unlocking of complex hydrocarbon chains. Subsequently, for an aromatic solvent (toluene), viscosity is already low (i.e. the entire relaxation signal of the oil is being measured), and *RHI* changes as a linear mixing rule of the oil and solvent components.

A key difference in the case of paraffinic solvents present in high mole fractions is that asphaltenes can start to drop out of the oil (Wen, Bryan, and Kantzas, 2005). Precipitated asphaltenes are solids and relax too quickly to be measured by low field NMR, so what is measured is the asphaltene-free fraction of the oil, mixed with solvent. Thus, the oil *RHI* is an upgraded fraction of the oil, which does not include many of the complex rings and

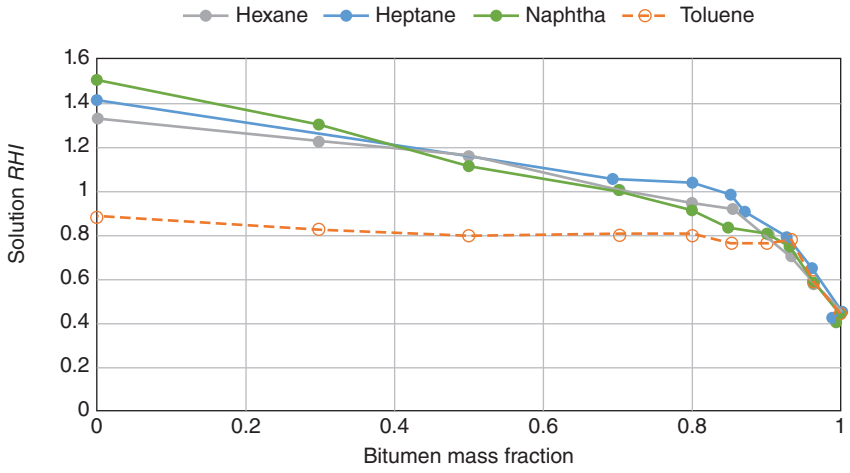

Figure 7.45 NMR *RHI* for paraffinic vs. aromatic solvents, showing potential asphaltene dropout in oil/solvent mixtures. *Source*: From Wen, Bryan, and Kantzas (2005). Reproduced with permission of the Journal of Canadian Petroleum Technology.

heavy molecules associated with asphaltenes. Since precipitated asphaltenes are not measured in low field NMR, the actual oil mass giving a signal is only the asphaltene-free portion of the oil. While the mass of oil is lower, the signal from the upgraded oil is also more significant and, as a result, the shape of the oil-solvent mixing rule changes.

More work is needed to quantify changes in NMR relaxation distributions in the presence of liquid solvents with the effect of asphaltenes dropping out of the oil. However, it is clear that the correlations between *RHI* and bitumen content are distinctly different for paraffinic vs. aromatic solvents, and this can potentially be used to understand the upgrading potential of the oil. This upgrading can have a dramatic impact on mass transfer in porous media, and also on the value of the produced oil, so this is an area that still needs more study.

7.6.2 Predictions of Non-Equilibrium Viscosity in Oil–Vapor Solvent Systems

The goal of vapor phase solvent injection is either to assist in pressurizing reservoirs that have void space from previous primary production (Ivory *et al*., 2010) or to allow for gravity drainage of solvent-diluted oil (Das and Butler, 1998; Nenniger and Dunn, 2008). The goal of solvent injection is the same as in liquid solvent systems: the dilution of oil and reduction in its viscosity. A key difference is that, in the case of solvent vapor, solubility is a function of pressure so oil will only hold a certain amount of solvent at any given mixing pressure and the final saturated live oil viscosity is a function of how much solvent is dissolved into the oil. The diluted oil is then mobilized either under the influence of gravity or by pressure depletion. Since the reduced oil viscosity is caused by solvent solution, it is imperative that solvents are released only slowly from the oil, so viscosity will stay low during pressure depletion cycles. This non-equilibrium is compressible and contains varying solvent content with pressure and with time, so conventional viscosity measurements (e.g. capillary viscometer testing) are highly inaccurate in these systems. NMR viscosity modeling is based on the closeness of protons and how quickly energy is lost from tipping protons onto the transverse plane, so this method does not require flow and will not be affected by the compressible nature of this fluid.

Figure 7.46 shows the relationship between viscosity and oil T_{2gm} for a heavy oil sample that is either measured dead (no solution gas) with temperature, or at a single temperature but saturated with different solvents. As expected, as the dead oil is heated, molecules move further apart and this leads to lower viscosity and longer NMR relaxation times. What is significant is that when solvent is dissolved into the oil this has the same effect as increasing temperature. Solvent swells the oil and pushes its molecules apart, so viscosity reduction from solvent vapor has the same mechanism as heating of the oil. In Figure 7.46 both CO_2 and propane (C_3H_8) have the same effect on oil viscosity, since both solvents follow the same trend line as the temperature–viscosity curve.

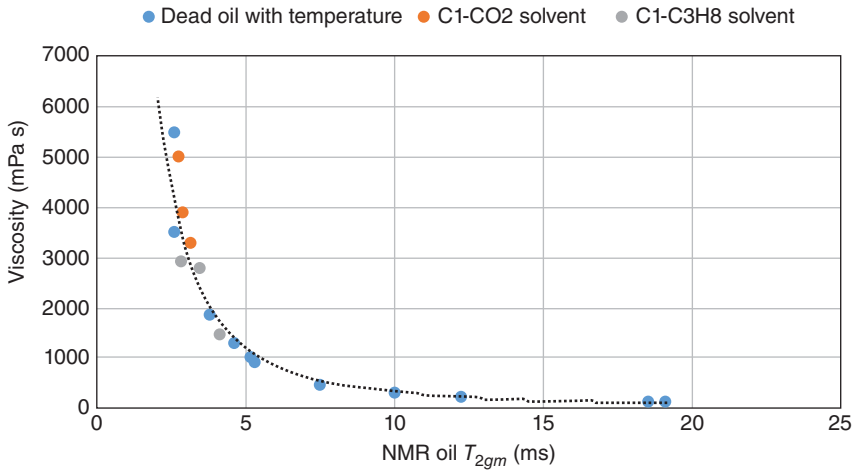

Figure 7.46 Correlation between oil viscosity and mean relaxation time for gas-free oil with temperature or live oil saturated with vapor phase solvent.

For any given oil and solvent system, an NMR calibration of viscosity and T_{2gm} can be built using the form of Figure 7.46. During pressure depletion, a sample of live oil is placed into the low field NMR unit and pressure is withdrawn at a constant rate from the system. The oil phase will swell with the drop in pressure, and eventually gas (solvent) will leave the solution. When this happens, the remaining oil phase will become more viscous again and the NMR T_{2gm} values can be used to track how viscosity changes over time. An example of this output is shown in Figure 7.47, which plots NMR predicted viscosity with pressure during slow (pseudo-equilibrium) and fast (non-equilibrium) depletion of a heavy oil saturated with methane. The saturation (bubble point) pressure is shown as the dotted vertical line in this figure. Saturation pressure is the pressure at which the live oil was mixed, since this system was prepared by saturating oil with methane at this fixed pressure.

The test begins with live oil (i.e. oil that has been saturated with methane at $P = P_{sat}$) at pressures above the saturation pressures. Pressure is either withdrawn in small increments every day or dropped at a fixed rate to understand the non-equilibrium response of this system. In the pseudo-equilibrium system gas starts to evolve out of the oil at the bubble point, and accordingly oil viscosity rises as pressure drops and more gas evolves. This is the classic behavior expected in a solvent-vapor system. As pressure drops below the bubble point, microscopic gas bubbles that are released from the oil take time to grow and coalesce into a free gas phase. During the pseudo-equilibrium process, the system pressure is only dropped slightly every day, so sufficient time is provided for the free gas phase to separate from the oil. The time for gas to be released is a function of the oil viscosity: slower growth and release of gas is observed

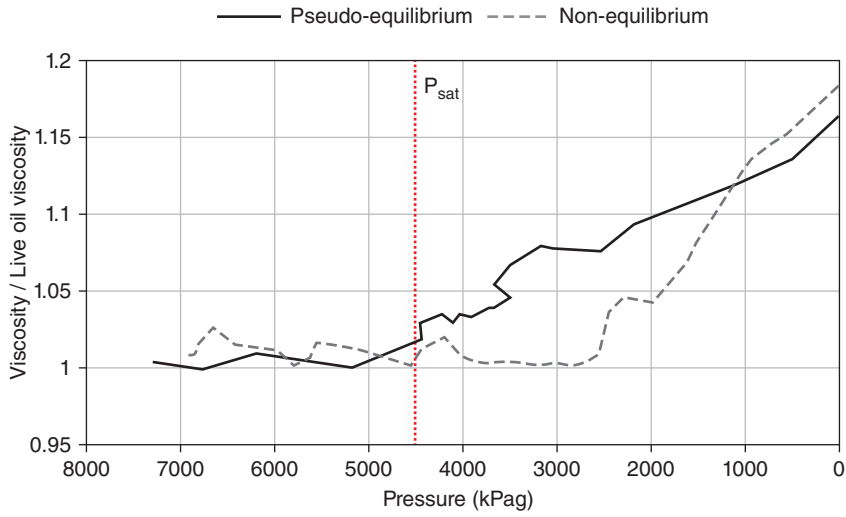

Figure 7.47 NMR predicted viscosity of live oil during equilibrium vs. non-equilibrium pressure depletion of a methane-live oil system. *Source*: Goodarzi *et al*. (2007). Reproduced with permission of SPE Journal.

in more viscous oil systems. Thus, when pressure is dropped quickly, the gas bubbles do not have time to grow and coalesce, and the system behaves like a live oil until pressure has dropped significantly below the bubble point. This shows that the effect of the vapor phase solvent is to not only reduce oil viscosity but also maintain this low value during high rate pressure depletion, so what is produced in high drawdown primary production operations is low viscosity live oil.

The value of NMR as a tool for testing in these systems is that it can yield viscosity data for the oil/solvent system even in a non-equilibrium state. Furthermore, it has been previously shown that viscosity correlations can also be applied to fluids in porous media, so NMR can be used to evaluate the changing oil viscosity with pressure and time within porous media. This could be in the form of laboratory-scale core testing, or even through observation wells in the field.

7.7 Summary of NMR and Fluid Property Measurements

The key to understanding NMR T_2 relaxation distributions is whether the fluid that is measured is relaxing through bulk or surface processes. For low viscosity fluids like water in porous media, surface relaxation dominates and NMR relaxation distributions can be used to understand the pore size distribution of the

system, and where water is located in a system that contains both oil and water saturation. For viscous heavy oil and bitumen, relaxation is dominated by bulk processes, which are related to the viscosity of the system. Specifically, higher viscosity fluids exhibit faster relaxation times and lower NMR signal amplitude compared to lower viscosity fluids. Heavy oil and bitumen are so viscous, in fact, that their relaxation rate in NMR is independent of whether these fluids exist as bulk liquids or liquids in porous media. This allows for NMR characterization of fluid content and *in situ* oil viscosity in reservoir characterization.

- In bulk liquid systems, NMR can be used to evaluate the water cut of a given production stream.
- NMR can also provide a measure of the oil viscosity or the viscosity of a water-in-oil emulsion.
- When the oil and water are present in porous media, so long as the signals from oil and water can be separated, the output from NMR is a profile of water saturations and *in situ* oil viscosity within the oil-bearing zone.
- In the presence of solvents, NMR is used to evaluate the viscosity of the oil/solvent mixture.
- Calibrated NMR results can be used to understand the oil content in a given oil/solvent stream, the viscosity of this solution, and provide an indication of upgrading or de-asphalting that may occur at high solvent contents.
- In the case of vapor phase solvents, NMR relaxation distributions prove that the viscosity reduction mechanism is the same as heating of dead oil, and can be used to evaluate non-equilibrium solvent release rates in different systems.
- The basis for measurements in all of the tested systems is the fact that NMR provides a means for understanding fluid viscosity in terms of how close protons are and how quickly they can give off energy.
- NMR may require calibration to improve its accuracy compared to general model results, but overall this is a powerful tool that can be used to characterize fluid fractions and oil viscosity in heavy oil and bitumen systems.

Acknowledgments

The authors wish to acknowledge the contributions of many past and present researchers whose work has contributed to this. Past researchers at the University of Calgary or PERM Inc Laboratory include Kevin Allsopp, Phebe Chung, Nina Goodarzi, David Lastockin, An Mai, Florence Manalo, Konstantin Mirotchnik, Dalia Salama, Wendy Wen, and Ian Wright. Special thanks to Jessica Butron and Sergey Kryuchkov, who have provided assistance and guidance in the preparation of this manuscript. Past and present financial support for our work in NMR development has come from the Natural Sciences and Engineering Research Council of Canada (NSERC), Alberta Innovates and

the Canada Research Chair programs, and from multiple industrial partners: Shell/Albian Sands, Nexen, Devon Canada, Suncor, CNRL, Athabasca Oil Corp, Laricina Energy Ltd, Brion Energy, and Husky Energy.

References

Allsopp, K., Wright, I., Lastockin, D., *et al.* (2001). Determination of oil and water compositions of oil/water emulsions using low field NMR relaxometry. *Journal of Canadian Petroleum Technology*, 40(7), 58–61.

ASTM D95-05 (2010) Standard test method for water in petroleum products and bituminous materials by distillation. *Manual of Petroleum Measurement Standards (MSPS)*, Chapter 10.5.

Bird, R., Stewart, W., and Lightfoot, E. (2002) *Transport Phenomena*, 2nd edn. John Wiley & Sons, Inc., New York.

Bloembergen, N., Purcell, E. M. and Pound, R. V. (1948) Relaxation effects in nuclear magnetic resonance absorption. *Physical Review*, 73(7), April, pp. 679–715.

Brown, R. and Gamson, B. (1960) Nuclear magnetism logging. *AIME Petroleum Transactions*, 219.

Bryan, J., Kantzas, A. and Bellehumeur, C. (2002a) Using low field NMR to predict viscosities of crude oils and crude oil emulsions. SCA Paper 2002-039, 2002 *International Symposium of the Society of Core Analysts*, Monterey, California USA, September 22–25.

Bryan, J., Kantzas, A. and Bellehumeur, C. (2005a) Oil viscosity predictions from low field NMR measurements. SPE Paper 89070, *SPE Res. Eval. & Eng.*, 8(1), 44–52.

Bryan, J., Kantzas, A., Badry, R., *et al.* (2007) In situ viscosity of heavy oil: Core and log calibrations. *J. Can. Pet. Tech.*, 46(11), 47–55, November.

Bryan, J., Kantzas, A. and Moon, D. (2005b) In-situ viscosity of oil sands using low field NMR. *J. Can. Pet. Tech.*, 44(9), 23–30.

Bryan, J., Mai, A., Hum, F., and Kantzas, A. (2006) Oil- and water-content measurements in bitumen ore and froth samples using low field NMR. *SPE Res. Eval. & Engg.*, 654–663, December.

Bryan, J. L., Manalo, F. P., Wen, Y., and Kantzas, A. (2002b) Advances in heavy oil–water property measurements using low field nuclear magnetic resonance. SPE Paper 78970, *SPE/CIM/CHOA Resource 2 Reserves 2 Results Conference and Exhibition*, Calgary, AB Canada, November 4–7.

Bryan, J. L., Mirotchnik, K. and Kantzas, A. (2003) Viscosity determination of heavy oil and bitumen using NMR relaxometry. *J. Can. Pet. Tech.*, 42(7), 29–34.

Burcaw, L., Kleinberg, R., and Bryan, J. (2008) Improved methods for estimating the viscosity of heavy oils from magnetic resonance data. *SPWLA 49th Annual Logging Symposium*, Edinburgh, Scotland, May 25–28.

Cannon, D. and Cao, C. (1998) Quantitative NMR interpretation. SPE Paper 49010, *1998 SPE Annual Technical Conference and Exhibition*, New Orleans, LA USA, September 27–30.

Chang, D., Vinegar, H., Morriss, C., and Straley, C. (1997) Effective porosity, producible fluid, and permeability in carbonates from NMR logging. *The Log Analyst*, 38(2), March–April, 60–72.

Chen, J. and Bryan, J. (2013) In situ bitumen viscosity and saturation estimation from core log integration for Canadian Oil Sands. SPE Paper 165517, *SPE Heavy Oil Conference*, Calgary, AB Canada, June 11–13.

Chung, P.M. and Kantzas, A. (2007) Study of hydrated clay reactions to various cations using low field NMR. PS 2007-107, Petroleum Society's 8th Canadian International Petroleum Conference, Calgary, AB Canada, June 12–14.

Coates, R. G., Xiao, L., and Prammer, M .G. (1999) *NMR Logging Principles & Applications*, Halliburton Energy Services, Houston.

Das, S. K. and Butler, R. M. (1998) Mechanism of the vapour extraction process for heavy oil and bitumen. *Journal of Petroleum Science and Engineering*, 21, 43–59.

Dunn, K.-J, Bergman, D. J., and LaTorraca, G. A. (2002) *Nuclear Magnetic Resonance Petrophysical and Logging Applications: Handbook of Geophysical Exploration: Vol. 32*, Elsevier Science Ltd, Oxford.

Freedman, R., Lo, S., Flaum, M., *et al.* (2001) A new NMR method of fluid characterization in reservoir rocks: Experimental confirmation and simulation results. *SPE Journal*, December, 452–464.

Galford, J. and Marschall, D. (2000) Combining NMR and conventional logs to determine fluid volumes and oil viscosity in heavy-oil reservoirs. SPE Paper 63257, *2000 SPE Annual Technical Conference and Exhibition*, Dallas, TX USA, October 1–4.

Gates, I. D., Adams, J. M and Larter, S. (2008) The impact of oil viscosity heterogeneity on the production characteristics of tar sand and heavy oil reservoirs: Part II: Intelligent, geotailored recovery processes in compositionally graded reservoirs. *Journal of Canadian Petroleum Technology*, 47(9), 40–49.

Goodarzi, N., Bryan, J., Mai, A., and Kantzas, A. (2007) Heavy oil fluid testing with conventional and novel techniques. SPE Paper 97803, *SPE Journal*, 305–315, September.

Hawkins, J. and Skopec, R. (1998) Nuclear magnetic resonance versus air/brine capillary pressure correlations: How good are our assumptions in the empirical determination of permeability. SCA 9824, 1998 International Symposium of the Society of Core Analysts, The Hague, September 14–16.

Ivory, J., Chang, J., Coates, R., and Forscner, K. (2010) Investigation of cyclic solvent injection process for heavy oil recovery. *Journal of Canadian Petroleum Technology*, 49(9), 22–33.

Jones, M., Taylor, S., and Huang, Z. (2014) Two-dimensional magnetic resonance study of synthetic oil sands. SPE Paper 170006, *SPE Heavy Oil Conference*, Calgary, AB Canada, Jun 10–12.

Kantzas, A., Bryan, J., Mai, A., and Hum, F. (2005) Low field NMR applications in oil sands mining and extraction. SCA paper 2005-23, International Symposium of the Society of Core Analysts, Toronto, OT Canada, August 21–25.

Kenyon, W. (1997) Petrophysical principles of applications of NMR logging. *The Log Analyst*, 38(2), March–April, 21–43.

Kleinberg, R. and Vinegar, H. (1996) NMR properties of reservoir fluids. *The Log Analyst*, 37(6), November–December.

Kokal, S. (2002) Crude oil emulsions: A state-of-the-art review. SPE Paper 77497, *2002 SPE Annual Technical Conference and Exhibition*, San Antonio, TX, USA, September 29–October 2.

Krioutchkov, S., Kantzas, A., and Wang, Z. V. (2016) Multiphase metering device for oilfield applications. US Patent # US 2016/0047762 A1, February 28.

Kryuchkov, S., Mirotchnik, K., Obidi, V., and Baishev, A. (2003) New approach for determination of bitumen and water contents in tar sands. PS 2003–134, Petroleum Society's Canadian International Petroleum Conference, Calgary, AB Canada, Jun 10–12.

LaTorraca, G., Dunn, K.-J., and Brown, R. (1993) Predicting permeability from nuclear magnetic resonance and electrical properties measurements. SCA 9312, 1993 International Symposium of the Society of Core Analysts, Houston, TX, USA, August 9–11.

LaTorraca, G., Stonard, S., Webber, P., *et al.* (1999) Heavy oil viscosity determination using NMR logs. SPWLA 40th Annual Logging Symposium, May 30–June 3.

Manalo, F. P., Bryan, J. L., and Kantzas, A. (2002) Addressing the clay/heavy oil interaction when interpreting low field nuclear magnetic resonance logs. SPE Paper 78971, *SPE/PS-CIM/CHOA. International Thermal Operations and Heavy Oil Symposium and International Horizontal Well Technology Conference,* Calgary, AB Canada, November 4–7.

Manalo, F. P., Ding, M., Bryan, J., and Kantzas, A. (2003) Separating the signals from clay bound water and heavy oil in NMR spectra of unconsolidated samples. SPE Paper 84480, *SPE Annual Technical Conference and Exhibition*, Denver, CO, USA, October 5–8.

Mirotchnik, K., Allsopp, K., Kantzas, A., *et al.* (1999) Low field NMR-tool for bitumen sands characterization: A new approach. SPE Paper 56764, *SPE Annual Technical Conference and Exhibition*, Houston, TX, USA, October 3–6.

Nasr, T. N., Beaulieu, G., Golbeck, H., and Heck, G. (2003) Novel expanding solvent-SAGD process "ES-SAGD". *Journal of Canadian Petroleum Technology*, 42(1), Jan.

Nenniger, J. E. and Dunn, S. G. (2008) How fast is solvent based gravity drainage? PS-2008-139, Canadian International Petroleum Conference, Calgary, AB Canada, June 17–19.

Pal, R. (1996) Effect of droplet size on the rheology of emulsions. *AIChE Journal*, 42(11), November.

Pal, R., Yan, Y., and Masliyah, J. (1992) Rheology of emulsions, in: Schramm, L. (ed.) *Emulsions Fundamentals and Applications in the Petroleum Industry*, American Chemical Society, Washington.

Salama, D. and Kantzas, A. (2005) Experimental observations of miscible displacement of heavy oils with hydrocarbon solvents. SPE Paper 97854, *SPE International Thermal Operations and Heavy Oil Symposium*, Calgary, AB Canada, Nov 1–3.

Shu, W. R. (1984) A viscosity correlation for mixtures of heavy oil, bitumen and petroleum fractions. SPE Paper 11280, *Society of Petroleum Engineers Journal*, June, 277–282.

Stark, S. D. (2013) Cold lake commercialization of the liquid addition to steam for enhancing recovery (LASER) process. SPE Paper 16795, International Petroleum Technology Conference, Beijing, China, Mar 26–28.

Straley, C., Rossini, D., Vinegar, H., *et al.* (1997) Core analysis by low field NMR. *The Log Analyst*, 38(2), March–April.

Wen, Y., Bryan, J., and Kantzas, A. (2005) Evaluation of bitumen-solvent properties using low field NMR. *J. Can. Pet. Tech.*, 44(4), 22–28.

Wright, I., Lastockin, D., Allsopp, K., *et al.* (2004). Low field NMR water cut metering. *Journal of Canadian Petroleum Technology*, 43(5), 17–21.

8

Application of Near-Infrared Spectroscopy to the Characterization of Petroleum

*Patricia Araujo Pantoja[1], Juan López-Gejo[2], Claudio Augusto Oller do Nascimento[3] and Galo Antonio Carrillo Le Roux[3]**

[1] *Universidad de Ingeniería y Tecnología (UTEC), Jr. Medrano Silva 165, Barranco, Lima, Peru*
[2] *SICPA SA, Av de Florissant 41, 1008 Prilly, Switzerland*
[3] *Departamento de Engenharia Química, Escola Politécnica da Universidade de São Paulo Av. Prof. Luciano Gualberto, trav. 3, 380, 05508-020 São Paulo, Brasil*

8.1 Introduction

Petroleum is a complex mixture of thousands of hydrocarbon compounds and it is produced from an oil well in the form of reservoir fluid (Riazi, 2005; Acevedo *et al.*, 2007; López-Gejo *et al.*, 2008). The study of the molecular structure of crude oil has been very important in the field of petro-chemistry during the last few decades, because its physicochemical properties are closely related to its composition and chemical structure (Speight, 2007; Zhang *et al.*, 2009; Melendez *et al.*, 2012). Parameters such as API gravity, viscosity, and chemical composition characterize the crude oil and its derivatives.

A variety of spectroscopic techniques (Kvalheim *et al.*, 1985; Gautam, Jin, and Hansen, 1998; Mohamed and Zaky, 2005; Hongfu *et al.*, 2006; Mullins *et al.*, 2007; Pantoja *et al.*, 2011) has been used over the last few decades for the analysis, characterization and classification of crude oil in drilling fields, for the analysis of petroleum products and for the detection of oil spills (Fingas and Brown, 1997; Basta, 2010). In this group of techniques, infrared (IR) is probably the spectroscopic technique most extensively applied in the industry because it has a low cost, good signal-to-noise ratio, rapid response potential for online applications, non-destructive and non-invasive instrumentation, and simple or nearly no specific sample preparation (Buchanan, 2007). In consequence, IR has been extensively used in the characterization and classification of different crude oils (medium and heavy), gasoline, and associated products that have

*Corresponding author: galoroux@usp.br

Analytical Characterization Methods for Crude Oil and Related Products, First Edition.
Edited by Ashutosh K. Shukla.

been carried out with this technique that is based on the characteristic vibrational modes of the functional groups present in the sample (Xing *et al.*, 2006; Chung, 2007; Cramer *et al.*, 2009; Morris *et al.*, 2009; Balabin and Smirnov, 2011; Ferreiro-Gonzalez *et al.*, 2015).

Environmental protection agencies are working together with government on the developments of novel IR spectroscopy techniques for the characterization of petroleum products and its production process. Goals are diverse, from inspection purposes to guarantee quality avoiding potential adulteration, to reduce pollution by producing more environmentally friendly fuels. IR spectroscopy has also been applied in environmental studies for the detection and identification of oil spills (qualitative analysis) and the determination of petroleum, oil, and hydrocarbon concentrations in wastewater and soils (quantitative) (Pereira *et al.*, 2006; Balabin *et al.*, 2011a; Khanmohammadi, Garmarudi, and De la Guardia, 2012).

8.2 Sample Handling and Preparation

Sampling, preparation, transportation, and storage are the main sources of error in the analysis of a complex sample such as crude oil. Although near-infrared (NIR) technology has become recognized as a rapid, accurate, precise, and pollution-free method of analysis, a specific sampling procedure is essential to prevent any degradation of the petroleum or the loss of the more volatile components, such as methane. Betancourt *et al.* (2006) designed facilities and strategies for the safekeeping of crude oil samples, and developed the "chain of custody" concept: samples are reconditioned in high-pressure bottles at conditions equal to reservoir pressure and temperature, with agitation, for five days. This procedure showed particular sensitive to methane content. Evidently, adequate transportation and storage procedures are always required, but any error in the estimation of parameters may lead to expensive miscalculations.

Falla *et al.* (2006) used sealed glass bottles stored below 5 °C, for crude oil samples obtained at industrial conditions in order to reduce the loss of light components and the effects of the natural degradation processes.

William (2008) summarized about 30 factors affecting the accuracy and precision of NIR analysis in a table, that were classified into three main columns: sampling (stand out type of sampler, location of sampler, material to be sampled, size of sample, flow characteristics, sample transfer method, blending, storage, frequency of sampling, variability of population, sample selection), samples (stand up type of material, composition, physical texture, blending, identification/documentation), and sample preparation (stand up type/model of instrument, type of test: intermittent, in-/online, sample cell type, sample cell size, particle size, bulk density, composition, physical nature, stratification, cell cleanup, grinder type).

In many cases, improvements in the statistics of the success of an NIR calibration lie in developments in one or more of the factors involved in the sample itself, its preparation, and its presentation to the instrument.

8.3 Near-Infrared Spectroscopy

NIR spectroscopy is a fast and simple analytical technique typically used to identify chemical components based on specific functional groups. The NIR region of the electromagnetic spectrum includes wavelengths in the range of 12000–4000 cm^{-1} (833–2500 nm) (Paso, Kallevik, and Sjöblom, 2009; Pantoja, 2010). Even though NIR spectra are often broad and highly overlapping, they contain some important vibrational information. The most prominent bands are found in the region of 5665–5900 cm^{-1}, which corresponds to the first overtones of C–H stretching vibrations, whose fundamental frequency is in the 3000–2800 cm^{-1} region in the mid-infrared. Furthermore, the weak second overtone of the C–H stretch and C–H combination bands appears at 8700–8150 cm^{-1} and in the region from 7350 to 6950 cm^{-1}, respectively. Aromatic functionalities absorb at 8750 cm^{-1} (C–H stretch, second overtone), 6915 cm^{-1}, 7050 cm^{-1} (C–H combinations), 5950 cm^{-1} (C–H stretch, first overtone), and 4650–4550 cm^{-1} (C–H, C=C combinations) (Hannisdal, Hemmingsen, and Sjöblom, 2005; López-Gejo *et al.*, 2008; Abbas *et al.*, 2012). Figure 8.1 shows some typical NIR spectra of several different Brazilian crude oils in three regions.

Before the 1940s, many spectroscopists considered this region confused with many weak and overlapping peaks of numerous overtone and combination bands, and, besides, baselines were hard to define. Modern NIR technology relies heavily on the personal computer (PC). In the 1980s, the first PCs were introduced with designs adequate for compatibility. The PC soon became the driving force behind NIR instrumentation (Hindle, 2008). The microprocessor helps to control and acquire data from the apparatus, and facilitates calibration and data analysis (Kubelka and Munk, 1931). In 1990, Mullins and Parisi published two important studies. Mullins (1990) began the question of the relative magnitudes of light absorption and scattering by asphaltene particles in crude oils in the NIR spectral range. He compared the effect of dilution with carbon tetrachloride on crude oil spectra and similar measurements on crude oils with an immiscible wax phase. Separation of crude oils into asphaltenes and maltenes allows the measurement of the absorption of individual crude oil components. The comparison of the original and composite spectra clearly shows that absorption dominates scattering in the NIR region. The functional forms expected for absorption and scattering are examined and found to be consistent with the experimental data. Contrasting the spectra of crude oils with those of the added spectra of the crude oil components, asphaltenes and

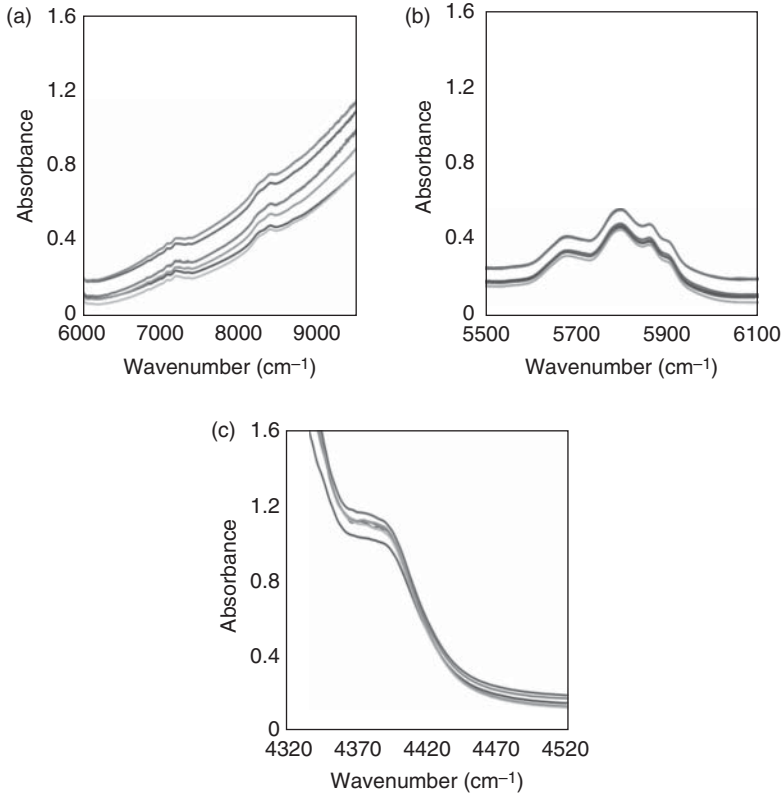

Figure 8.1 NIR spectra of some Brazilian crude oil samples in three regions: (a) second overtone of the C–H stretch and C–H combination bands appear; (b) the first overtones of C–H stretching vibrations; and (c) C–H stretch, first overtone and C–H, C=C combinations.

maltenes, again illustrates the dominance of absorption over scattering by asphaltic crude oils. Parisi, Nogueiras, and Prieto (1990) demonstrated the success of NIR using optical fiber in combination with multivariate calibration to determine fuel quality parameters in gasoline and diesel samples. They correlated NIR spectra using optical fiber with octane number – research octane number (RON) and motor octane number (MON) – and paraffin, olefin, naphthene and aromatics (PONA) content analysis of gasolines, and cetane number in diesel fuels. The difficulties and possible solutions due to bubble formation in the online measurement flow cell were explored. They recommend adopting appropriate sampling techniques and careful data pretreatment in order to avoid erroneous results.

Many applications appeared that demonstrate the success of NIR for the prediction of physical and chemical properties of crude oil and petroleum

products. In this century, Hidajat and Chong (2000) correlated NIR spectra with the true boiling point (TBP) and API density of crude oils. Fourteen partial least square (PLS) models were calibrated by a training set of 110 samples. MSC (multiplicative scatter correction) was used as the pretreatment technique and cross validation was used as the validation method. Chung and Ku (2000) correlated NIR spectra with API density of atmospheric residue (AR). They compared NIR, IR, and Raman spectroscopy for heavy petroleum products. NIR region provided better spectral reproducibility with higher signal-to-noise ratio in comparison to Raman and IR spectroscopies. PLS regression was utilized to develop calibration models. NIR spectra of AR samples were broad, and baselines were variable, owing to the strong absorption in the visible range. However, the necessary information was successfully extracted and correlated to the reference API gravity with PLS regression. API gravities in the prediction set were accurately predicted with standard error of prediction (SEP) and showed approximately three times better repeatability compared to the ASTM reference method. Lima and Leite (2004) predicted some properties used to characterize and classify asphalt cement grade. Principal components regression (PCR) and partial least squares regression (PLSR) were employed to develop linear models to predict penetration value, absolute viscosity at 60 °C, kinematic viscosity at 135 °C, and the flash point of asphalt cements. The best results were achieved employing PLSR as a multivariate calibration method and both normalization and first derivative as spectra pretreatment. The RMSEP (root mean squared error of prediction) values obtained for the properties investigated were in the acceptable limits of their reference methods; other statistical parameters, such as correlation coefficient R^2, were also acceptable for the calibration following the chemometric parameters mentioned above.

Falla and coworkers (2006) proposed a methodology for the estimation of the SimDis (simulated distillation) properties of crude oil based on NIR. First, the spectral reproducibility was analyzed under the effect of temperature (between 25 and 30 °C) and of the data pretreatment method. The spectra analyzed correspond to the hydrocarbon NIR overtone absorption range (5600–6000 cm^{-1}). To evaluate spectral reproducibility, six spectra of a sample were collected, at different time intervals. The relative standard deviation with respect to the mean spectrum of the set chosen for the test is presented in Figure 8.2. The values obtained, corresponding to the hydrocarbon NIR overtone absorption range (5600–6000 cm^{-1}), varied between 0.78 and 3.5%. The figure shows that the set of spectra used is well distributed, since potential variations from external (environmental conditions) and internal (scattering, etc.) effects do not significantly affect the spectral representation of the crude oil samples. Afterwards, the NIR spectral data were correlated with SimDis curves (weight percent vaporized at a given temperature) and the salt content of the petroleum by neural network techniques. SimDis curves of crude oil

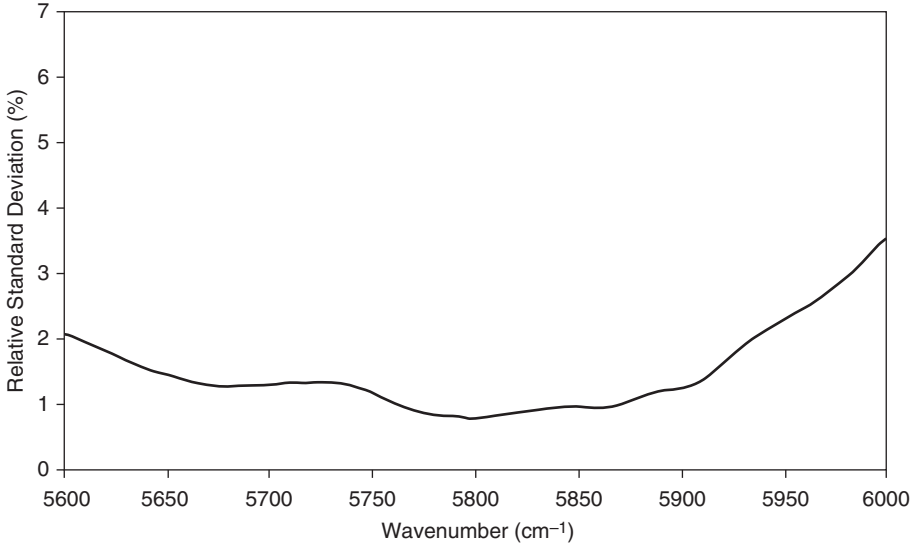

Figure 8.2 Relative standard deviation for reproducibility analysis. *Source:* Falla *et al.* (2006). Reproduced with permission of Elsevier.

were successfully predicted from NIR petroleum spectra via a neural network model without any sample conditioning. Two error parameters were calculated (root mean square error of prediction, or RMSEP, and R^2 statistic) in order to evaluate the modeling quality.

Özdemir (2008) demonstrated the application of genetic algorithm-based multivariate calibration to NIR spectroscopic determination of several diesel full parameters. Genetic algorithms are one useful tool for solving wavelength selection problems and may improve the predictive ability of conventional multivariate calibration methods. The parameters studied were cetane number, boiling and freezing points, total aromatic content, viscosity, and API density. Multivariate calibration models were generated using the genetic inverse least squares (GILS) method and used to predict the diesel fuel parameters based on their NIR spectra. For each property, a different data set was used and in all cases the number of samples was around 250. Overall, percent standard error of prediction (%SEP) values ranged between 2.48 and 4.84% for boiling point, total aromatics, viscosity, and density. However, %SEP results for cetane number and freezing point were 11.00 and 14.86%, respectively. They concluded that the NIR spectroscopy can be used for the simultaneous determination of the chemical and physical properties of diesel fuels. On the other hand, the genetic algorithm used in the GILS method is

capable of selecting and extracting the relevant information to build successful calibration models that have a high predictive ability for independent test samples.

8.3.1 Near-Infrared in Refineries

The crude oil unit, as part of the atmospheric and vacuum distillation plant, is the first processing unit in a refinery. Owing to its position (with products becoming either final products or feedstock for the other processing units), it is very important to make use of powerful instruments to accurately study it (Radulescu, 2007). In the last decade the combination of techniques based on NIR spectra and simulation software was suggested in order to improve the characterization of the crude oil. Predictive models for the main physicochemical properties (SimDis distillation and API density) were established using chemometrics. For real-time optimization (RTO) a reference model must be frequently adjusted to fresh operation data. The adaptation of the model is necessary in order to ensure that it represents the system even if there are changes in its constitutive parameters. This feature also guarantees that the mathematical optimization problem to be solved in order to obtain the set points of a new operating mode for the process does represent an optimal solution, or at least is close to it. A steady-state model was implemented using Aspen HYSYS simulation software. The objective was to evaluate the effect on the accuracy of the predictions obtained from the process simulator when the NIR characterization is used as an input.

The methodology is promising, because the simulation permits not only to compare the predictions but also to obtain the reconciliation of the measured variables. The real-time characterization of the crude oil feed will allow the optimization problem to reach realistic solutions. Both the characterization techniques were applied to petroleum samples available for a very long interval of operation (a year) and their results were introduced into the detailed model that was adjusted to the operating data available for this same time range.

Khanmohammadi, Garmarudi, and De la Guardia (2012) published a review on the application of infrared spectroscopy in the petroleum industry. They focused on the methods proposed for the determination of a wide range of characteristics in petroleum-based products. They considered that the application of NIR spectroscopy petroleum seemed to focus on environmental aspects and process analytical technology together with efforts to increase the sensitivity of measurements and the capability of the technique for multiparametric analysis.

In summary, process improvements, product characterization, and safety enhancements are still demanded by the oil and gas industry, and NIR

spectroscopy is one tool that can successfully fulfill those demands (Radulescu, 2007; Xu *et al.*, 2013; Onajake, Abrakasa, and Osuji, 2015; Milanez *et al.*, 2016; Paulo, Barros, and Barbeira, 2016). Considering the improvements in instrumentation technologies and computer science, the ability to use NIR has increased. Several papers were presented to demonstrate the wide range of applications in the petroleum industry for which NIR spectroscopy is a useful tool.

8.4 Chemometrics

The main task of the computer in NIR spectroscopy, aside from driving the instrument or collecting data, is to interpret the spectra using a variety of multivariate mathematical techniques. These techniques are used to produce a mathematical calibration model. NIR spectroscopy technology involves the multidisciplinary approaches of the analytical chemist, statistician, and computer programmer. "Chemometrics" is a term applied to the generic discipline containing computers and mathematics to derive meaningful chemical information from samples of varying complexity (Workman, 2008; Bampi, Scheer, and Catilhos, 2013; Gredilla *et al.*, 2016).

8.4.1 Pretreatment

In routine NIR analysis, the spectra should be pretreated to enhance informative signals of the interested components and reduce uninformative signals as much as possible (Pantoja, 2006). Smoothing, MSC, mean centering, and Savitzky–Golay derivation are commonly applied to pretreat the spectra before modeling in order to remove the scattering effect created by diffuse reflectance and to decrease baseline shift, overlapping peak, and other detrimental effects on the signal-to-noise ratio (Boysworth and Booksh, 2008; He *et al.*, 2015; Tong *et al.*, 2015).

8.4.1.1 Smoothing

Smoothing method was developed to reduce spectral noise without losing important chemical information. Figure 8.3 shows the effect of smoothing in three different first-derivative spectra. The dark-gray lines are the original unsmoothed spectra. The three superimposed light-gray lines are the result of smoothing with the Savitzky–Golay method with 35 points. The noise is greatly reduced and the peak itself is changed, making it easier to estimate its position, height, and width directly, by graphical or visual estimation.

8.4.1.2 Multiplicative Scatter Correction

MSC was developed to reduce the effect of scattered light on diffuse reflection and transmission NIR spectra. This method has also shown utility as a means

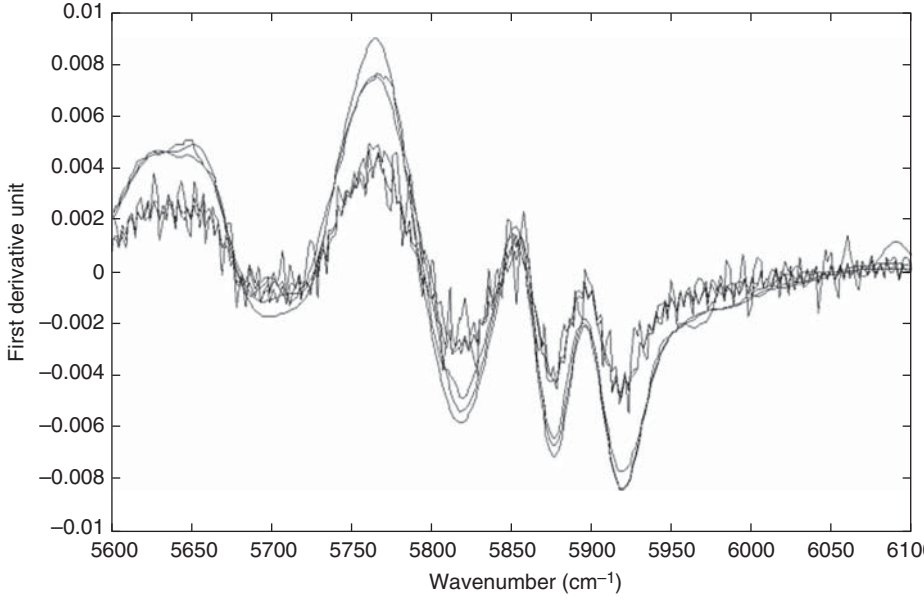

Figure 8.3 Effect of smoothing (Savitzky–Golay method) to three different first-derivative spectra.

of removing varying background spectra with non-scattering origins. Consequently, MSC sometimes appears as multiplicative signal correction.

However, a more advanced version of MSC that assumes a unique scattering model for different regions of the spectra also exists. In this method, each spectral value is modeled as a linear function of the average spectrum of the total set. Better calibration results can be obtained by using MSC, because it simplifies the calibration model by improving the linearity of the system. It can be analyzed by looking at plots of individual spectral values versus the average spectrum. Different regression lines are due to scatter effects, and deviations from the regression lines represent chemical information (López-Gejo *et al.*, 2008).

8.4.1.3 Mean Centering

Mean centering is applied by subtracting the mean spectrum of the data set from every spectrum in the data set. The practical consequence of mean centering data is often a more simple and interpretable regression model.

Although the spectra do not appear to be visually interpretable, none of the variance within the data set is altered. The major effect of mean centering is removing the broad sloping background from the data collection.

8.4.1.4 Derivation

The derivation technique is usually used in spectroscopy and permits spectral discrimination, in which the first and second derivations exhibit significant enhancement to the calibration model. Small differences between similar spectra are often revealed, with the additional effect of improving the resolution of overlapping bands (Falla *et al.*, 2006; López-Gejo *et al.*, 2008; Boysworth and Booksh, 2008).

Oliveira *et al.* (2014) applied first-order Savitzky–Golay derivative preprocessing in NIR spectra of biodiesel blends. They described two applications of a variant of the multivariate curve resolution alternating least squares method with a correlation constraint.

Figure 8.4 shows the NIR spectra for 50 crude oil samples before and after first derivative. First-derivative well-defined peaks were observed. They still look quite similar, as the subtle differences in relative peak height are masked by peak magnitude.

The data pretreatment improved the discrimination of the spectral information. The absence of preprocessing could cause critical problems for the effectiveness of the calibration models.

8.4.2 Calibration Model

The goal of calibration is to relate the observed spectra, in a predictive manner, to a property of interest. A model to correlate the spectral information

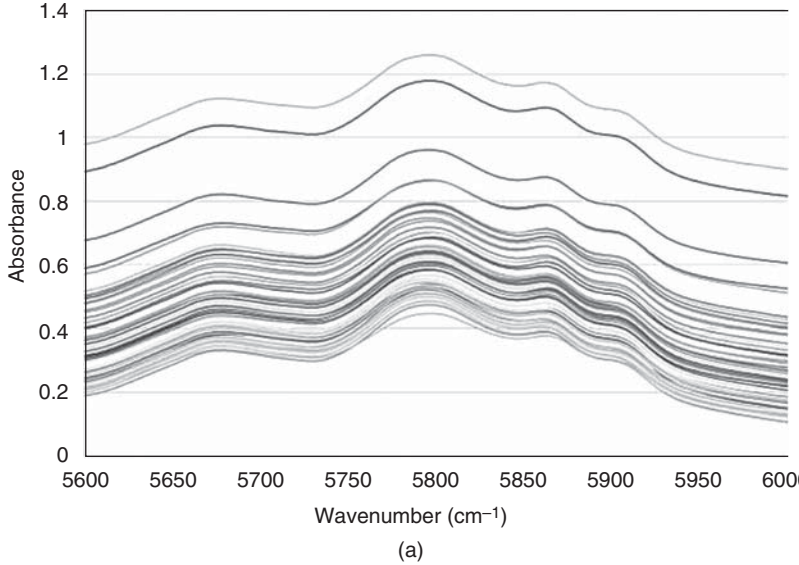

Figure 8.4 (a) NIR spectra of 50 crude oil samples. (b) First-derivative NIR spectra of 50 crude oil samples.

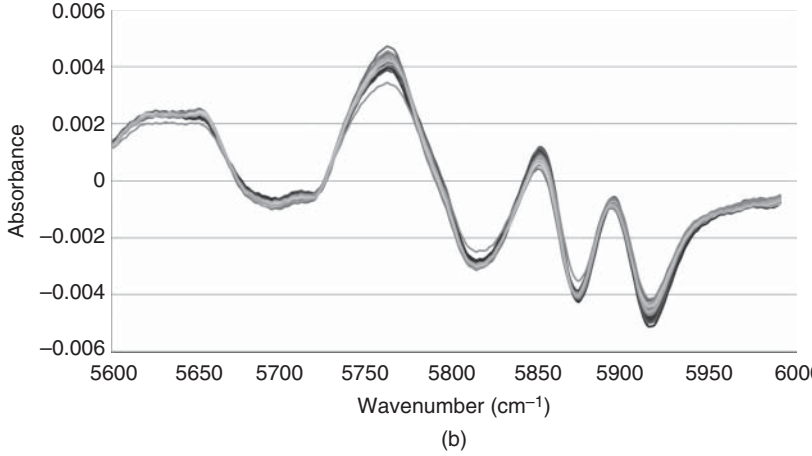

Figure 8.4 (*Continued*)

appropriately pretreated with physicochemical properties of crude oils is calibrated. With calibration it is possible to predict relevant physicochemical properties of an unknown crude oil that compare accurately with reference information on these properties. This is the main objective of the construction of calibration models.

In order to obtain a robust model, the quality of the calibration set (crude oil samples) is crucial because the samples must represent the range of variability of the calibration set and also be representative of the samples that will be analyzed. The main calibration methods are described in the following sections (López-Gejo *et al.*, 2008).

8.4.2.1 Principal Component Analysis (PCA)

PCA is a way of identifying arrangements in data, and expressing the data in such a way as to enhance their similarities and differences. With this method you have found relevant information in the data, and you compress the data in "principal components" (PCs), "factors," or "latent variables," reducing the number of dimensions, without losing much information while avoiding multicollinearity. The PCs are linear combinations of the original variables. Figure 8.5 shows a decomposition process in PCs. The first PC represented the direction of maximum variation through the data. The second PC lies along a direction orthogonal to the first PC. The new variables (PCs) are uncorrelated with each other (orthogonal).

The coefficients of the linear combinations are called "loadings" and represent the relationships among variables (contribution of each variable to the

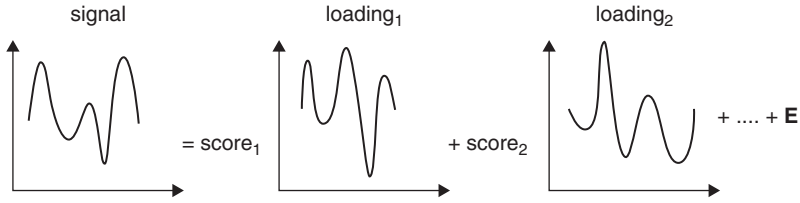

Figure 8.5 Schematic representation of the decomposition process in the PCA method.

total variance or information). The coordinates of spectra in the new system are called "scores" and represent the relationships among samples.

8.4.2.2 Partial Least Squares Regression

PLS regression, which is the most common method for quantitative analysis, involves projecting the real data into a new coordinate system defined by factors. The set of variables in the new coordinate system is then used for calibration. PLS utilizes both an analytical response (data matrix) as well as concentration information (a concentration matrix) to build a model. Therefore, a model built using PLS regression simultaneously describes the variation in both analytical responses and concentrations (Chung, 2007).

It uses the information contained in the dependent variables (Y) for the decomposition of the original data set. In this manner, PLS leads to PCs that not only capture the spectral information but also simultaneously maximize the correlation between the spectral information X and Y. The NIPALS (non-linear iterative partial least squares) algorithm is commonly used for PLS calculations because it provides orthogonal PCs. The advantage of applying PLS is the possibility of obtaining calibration models that are simpler than those obtained via PCR. The graphic interpretation of models is helpful because much of the relevant information in Y that is related to spectral information is modeled by the first PCs.

Figure 8.6 shows the correlations between the measurement versus predicted values of (a) API degrees and (b) viscosity (cP), for 48 Brazilian crude oil samples and five crude oil samples for validation by PLS regression. Differences were observed between these two linear methods: the main difference was the build of each calibration model: the API model required five latent variables and the viscosity model required seven latent variables. There are several ways of evaluating the performance of a calibration model. Therefore, no single estimate of optimal model complexity of model performance should be considered an exact value. Each estimate should have error bounds assigned. However, the proper manner to assign the error bounds is not known.

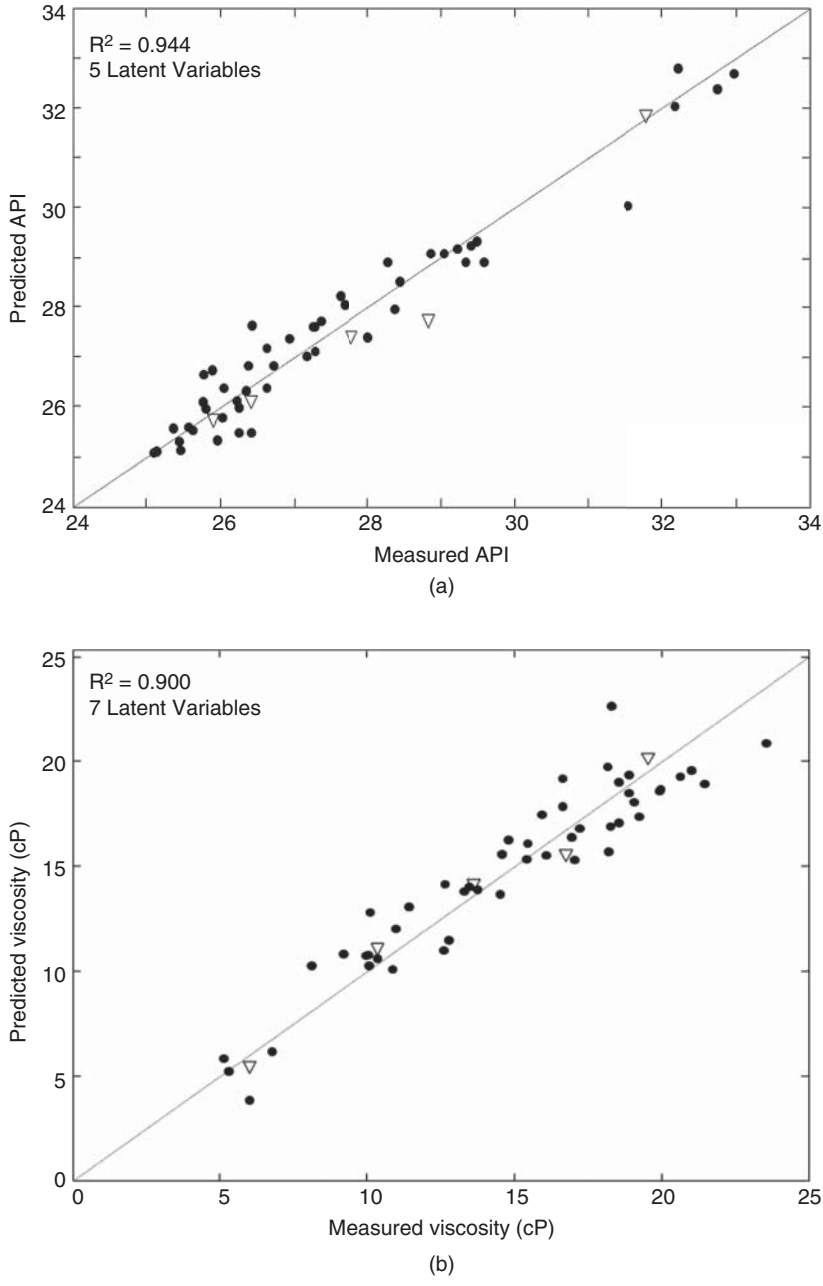

Figure 8.6 Relationship between the measured values and the predicted ones for (a) API degrees and (b) viscosity (cP). (●) Calibration samples. (Δ) Validation samples.

8.4.2.3 Artificial Neural Networks

Artificial neural networks (ANNs) have attracted great interest as predictive models. They are powerful tools for the correlation of data in non-linear systems because they possess the ability to "learn" how to correlate data without actually modeling the physical/chemical laws that govern the system (Balabin *et al.*, 2011b; Balabin and Smirnov, 2011; Meng, Jia, and Wang, 2014; Elfghi, 2016).

Feed forward neural networks, using sigmoid transfer functions, have been commended as universal non-linear approximators, and their application in the field of chemical and petroleum engineering has grown quickly (Zendehboudi *et al.*, 2014).

Recently the use of ANNs has been reported in the literature with advantages in some cases over PLS models, owing to its non-linearity. Balabin and co-workers (2010) compared multivariate techniques using NIR data of gasoline. They compared the performance of nine different multivariate calibration methods: linear discriminant analysis (LDA), quadratic discriminant analysis (QDA), regularized discriminant analysis (RDA), soft independent modeling of class analogy (SIMCA), partial least squares (PLS) classification, K-nearest neighbor (KNN), support vector machines (SVMs), probabilistic neural network (PNN), and artificial neural network multilayer perceptron (ANN-MLP), for grouping gasoline. KNN, SVM, and PNN techniques for arrangement were found to be among the most effective ones. ANN-MLP approach based on PCA, which was believed to be efficient, has shown much worse results.

8.4.3 Validation

Validation is the procedure by which the predictive quality of the calibration model is assessed. Its objective is to evaluate the performance with respect to its complexity. This is done by applying the model to predict the properties of samples that were not used in the development of the model (external validation) to confirm the proper selection of model parameters, and estimate the method error. Validation also has an important role to avoid fitting the model to perfection on a given set of training samples at the expense of reducing its ability to predict new samples, as the consequence of a model overfit (Gredilla *et al.*, 2016; Martens and Naes, 1989).

The quality of the predictions is translated into a prediction error index that is used in order to determine the optimal complexity of the model. Estimating too few or too many constants in the calibration model will both give higher prediction errors. This error contains two parts that are related to the calibration process. With increasing complexity of the calibration model, one part of the predictions error decreases (systematic interferences from other chemical constituents and from optical phenomena in the spectra data), but at the same time another part of prediction error increases (random errors in the

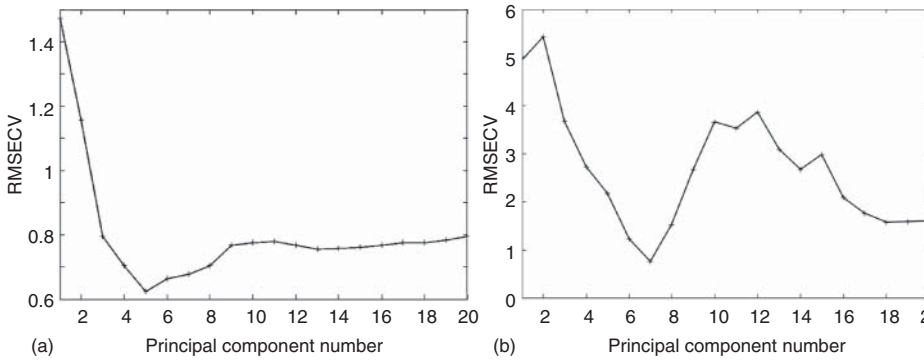

Figure 8.7 Validation curves for NIR models developed using PLS for API degree (a) and viscosity (b) of crude oil samples.

calibration data). The more elaborated the calibration model is, the higher is the probability of drawing noise from the spectral and chemical calibration data into the calibration coefficient (overfitting). An optimal prediction is obtained by balancing the two types of errors. This balancing depends on the nature of the interference problem and the precision of the calibration data (Martens and Naes, 1984; Martens and Dardenne, 1998).

One of the most used validation indexes is the leave-one-out cross-validation statistic, in which the subgroups used for calibration correspond to all the data with one sample excluded at a time. Prediction error is evaluated for the excluded sample. A very popular prediction error index is the RMSECV (root mean squared error of cross-validation) because its units are the same as those of the properties modeled (Hidajat and Chong, 2000; Siesler *et al.*, 2002). Figure 8.7 shows the validation curves corresponding to the NIR models for viscosity and API degree of crude oil samples (scatter plots are shown in Figure 8.6) as a function of the number of PCs. These curves justify the selection of five PCs to construct the optimal API degree model and seven for viscosity model.

8.4.4 Other Methods

The use of the full spectral region from NIR spectroscopic analysis does not always lead to a good multivariate calibration model, as many of the wavelengths do not contain useful information. Owing to the complexity of the spectra, some of the wavelengths or regions may, in fact, disturb the model building step. Genetic algorithms (Paso, Kallevik, and Sjöblom, 2009; Yun *et al.*, 2014, 2015) are one of the useful tools for solving wavelength selection problems and may improve the predictive ability of conventional multivariate calibration methods.

8.5 Commercial NIR Equipment and Industrial Applications

Based on the outstanding advances had in the field of NIR spectroscopy during the last decades, today NIR spectroscopy is an everyday tool used by the oil and gas industry. Thus, NIR equipment can be found along the entire supply chain, from wells to refineries and even tank stations, while applications goes from characterization of crude oil and related products to process control and optimization as well as inspection activities with quality control purposes.

As mentioned before, NIR does not require any specific sample preparation, requires short acquisition time, and allows performing an online measurement in a non-intrusive way. This is critical for the oil and gas industry since the product, as crude oil or white fuel, remains almost its entire lifetime in pipelines. To perform an NIR online measurement there are two possibilities. Either an immersion probe or a flow cell is used. Immersion probes are most widely used for Fourier transform near infrared (FT-NIR) measurements in process control and can work in a transmission mode or a reflection depending on the transmittance of the sample. For crude oil, reflectance will be typically used, while, for white fuels, transmission can be the most appropriate. Besides immersion probes, flow cells are widely used. In this case, the sample flows directly through the cell where the spectrum is measured and measurement is done exclusively in transmission mode. Typically, a flow cell probe allows one to acquire the spectra of a fluid flowing in a pipeline at a high pressure, while the immersion probe is designed to measure at pressures close to atmospheric.

Several manufactures offer online NIR equipment and have developed applications. A summary of the main instruments in the market is presented in Table 8.1 (information obtained from manufacturers brochures and manuals).

A large number of properties are measured with NIR spectroscopy these days at refineries with the final goal of ensuring quality or optimizing the production process. Those properties go from RON (research octane number), MON (motor octane number), cetane index, % aromatics, % olefins, % benzene and % oxygenates, to RVP [kPa] (Reid vapor pressure), D10%, D50%, D90%, Pour Point, Cloud Point, and Cold Filter Plugging Point or E170, to name a few.

8.5.1 Industrial Applications

NIR has been used in the oil and gas industry since the late 1970s and early 1980s. Nevertheless, the recent development of chemometric techniques together with the increase of computing power has significantly increased the possibilities of this technology and new applications have been developed.

Table 8.1 Summary of the main instruments in the market in online NIR.

Model	Manufacture	Spectral Range (nm)	Repeatability	Accuracy	Sample Temp (°C)	Sample Pressure (bar)
OMA 300	Applied Analytical	400–1100 nm	±0.5%	±0.004 AU	−20 to 150	100 bar (imm. probe), 206 bar (Flow cell)
ANALECT® PCM™ Series	Applied Instrument Technologies	833–8333 nm			−20 to 50	
HP260X	ABB	714–2630 nm	±0.001 cm^{-1}		10 to 30	
XDS Process Analytics™	FOSS NIR Systems Inc.	800–2200 nm		<0.08 nm	0 to 35	
PetroScan™	Light Technology Industries, Inc.	1200–2400 nm	0.01 nm		Up to 150	Up to 69 bar
412 XNIR	Guided Wave Process Analytical Systems	1000–2100 nm		±0.20 nm	0 to 40	
Beacon 3000 Process NIR Analyzer	Modcon Systems LTD		<0.01 nm	<0.15 nm	−40 to 70	Up to 40 bars
Luminar 3010	Brimrose	1100–2300 nm	±0.01 nm	±0.5 nm		
Series 5000	Teledyne	340–5000 nm	±1%	±2%	0 to 50	
NIRS XDS Process Analyzer	Metrohm	850–2200 nm	<0.004 nm	<0.08 nm	0 to 35	

8.5.1.1 Pipeline Product Analysis and Identification

NIR has been used successfully to monitor the input and output streams of crude oil distillation units, naphtha crackers, reformers, and other downstream processes, such as paraxylene.

8.5.1.2 Crude Distillation Optimization

During this process, the crude oil is distilled, yielding the different raw products such as light naphtha, heavy naphtha, and diesel. Real-time knowledge of crude properties is critical to ensure that full value is extracted from the crude in the refining activity. The most successful approach has been the prediction of the physicochemical properties of crude oils by correlating the data obtained by a rapid, surrogate method (usually spectroscopic) to the data obtained by the conventional, lengthy crude assays. NIR has proved to be one of the most successful spectroscopic methods to obtain this data.

8.5.1.3 Product Blending

Product blending is considered the final stage in the conversion of crude oil into useful fuels. The blender mixes together several streams from various process units to provide fuel that meets government, international, or customer specifications. NIR spectroscopy is used to measure product qualities in real-time which are fed to an online blending optimizer, ensuring the most economic blending operation to achieve blend targets.

8.5.1.4 Ethanol Fermentation

Ethanol fermentation at the bioethanol industry can be monitored in-line thanks to NIR spectroscopy, which provides real-time measurement data including ethanol, sucrose, fructose, glucose, total acids, yeast%, glycerol, degrees Brix, and pH. The data can be used to control the fermentation processes and to control feeding pipes of syrup and juice.

8.5.1.5 Conjugated Diolefins in Pygas

Pyrolysis gasoline (pygas) is a by-product of high-temperature naphtha cracking during ethylene and propylene production. Pygas can be blended with other hydrocarbons as a gasoline additive, but before that some unwanted conjugated diolefins should be eliminated or reduced to acceptable levels of 2 mg/g (0.2 %). In order to do so, the pygas is treated in a selective hydrogenation unit (SHU). In contrast to the wet-chemical determination, which takes several hours and requires trained chemists, NIR offers a very fast and robust quantitative method for diolefins determination.

8.5.1.6 Regulatory Fuel Screening

To ensure compliance with local or international regulatory standards, fuels can be analyzed with NIR *in situ* at gas stations by inspectors. NIR is particularly suitable for this type of regulatory inspection since no sample preparation

and consumable is required, allowing a very fast and robust analysis. Portable NIR equipment is transported into a car which moves from one location to the other performing analysis of RON, total aromatics, and olefins for gasoline while density, viscosity, cetane index, and distillation points are measured for diesel with the same NIR equipment.

8.6 Conclusions

NIR was depicted as a modern and accessible technology for the characterization of petroleum and related products. An introduction to the multivariate methods mostly used as well as an up-to-date list of the commercial NIR equipment and applications were presented. This information should be useful when deciding what technology to choose for an industrial application. It could also shed some light on the steps necessary for its successful implementation.

References

Abbas, O., Rebufa, C., Dupuy, N., *et al.* (2012) PLS regression on spectroscopic data for the prediction of crude oil quality: API gravity and aliphatic/aromatic ratio. *Fuel*, 98, 5–14.

Acevedo, S., Castro, A., Negrin, J. G., *et al.* (2007) Relations between Asphaltene Structures and Their Physical and Chemical Properties: The Rosary-Type Structure. *Energy Fuels*, 21, 2165–2175.

Balabin, R. M., Lomakina, E. I., and Safieva, R. Z. (2011a) Neural network (ANN) approach to biodiesel analysis: Analysis of biodiesel density, kinematic viscosity, methanol and water contents using near infrared (NIR) spectroscopy. *Fuel*, 90, 2007–2015.

Balabin, R. M., Safieva, R. Z., and Lomakina, E. I. (2010) Gasoline classification using near infrared (NIR) spectroscopy data: Comparison of multivariate techniques. *Anal. Chim. Acta*, 671, 27–35.

Balabin, R. M., Safieva, R. Z., and Lomakina, E. I. (2011b) Near-infrared (NIR) spectroscopy for motor oil classification: From discriminant analysis to support vector machines. *Microchem. J.*, 98, 121–128.

Balabin, R. M. and Smirnov, S. V. (2011) Variable selection in near-infrared spectroscopy: Benchmarking of feature selection methods on biodiesel data. *Anal. Chim. Acta*, 692, 63–72.

Bampi, M., Scheer, A. P., and Catilhos, F. (2013) Application of near infrared spectroscopy to predict the average droplet size and water content in biodiesel emulsions. *Fuel*, 113, 546–552.

Basta, J. S. (2010) Spectroscopic studies on some crude oils from the North Western Desert, *Egypt. Petrol. Scien. & Techn.*, 28, 779–789.

Betancourt, S. S., Bracey, J., Gustavson, G., *et al.* (2006) Chain of custody for samples of live crude oil using visible-near-infrared spectroscopy. *Appl. Spetrosc.*, 60, 1482–1487.

Boysworth, M. K. and Booksh, K. S. (2008) Aspects of multivariate calibration applied to near-infrared spectroscopy. In: Burns, D. A. and Ciurczak, E. W. (eds), *Handbook of Near-Infrared Analysis*, 3rd edn. CRC Press, Boca Raton, FL.

Buchanan, B. (2007) Use of near-IR spectroscopy in the petrochemical industry. In: Burns, D. A. and Ciurczak, E. W. (eds), *Handbook of Near-Infrared Analysis*, 3rd edn. CRC Press, Boca Raton, FL.

Chung, H. (2007) Applications of near-infrared spectroscopy in refineries and important issues to address. *Appl. Spectrosc. Rev.*, 42, 251–285.

Chung, H. and Ku, M.-S. (2000) Comparison of near-infrared, infrared, and Raman spectroscopy for the analysis of heavy petroleum products. *Appl. Spectrosc.*, 54, 239– 245.

Cramer, J. A., Morris, R. E., Hammond, M. H., and Rose-Pehrsson, S. L. (2009) Ultra-low sulfur diesel classification with near-infrared spectroscopy and partial least squares. *Energy & Fuels*, 23, 1132–1133.

Elfghi, F. M. (2016) A hybrid statistical approach for modeling and optimization of RON: A comparative study and combined application of response surface methodology (RSM) and artificial neural network (ANN) based on design of experiment (DOE). *Chem. Eng. Res. Des.*, 113, 264–272.

Falla, F. S., Larini, C., Le Roux, G. A. C., *et al.* (2006) Characterization of crude petroleum by NIR. *J. Petro. Sci. Eng.*, 51, 127–137.

Ferreiro-Gonzalez, M., Ayuso, J., Alvarez, J. A., *et al.* (2015) Gasoline analysis by headspace mass spectrometry and near infrared spectroscopy. *Fuel*, 153, 402–407.

Fingas, M. F. and Brown, C. E. (1997) Review of oil spill remote sensing. *Spill Sci. and Technol. Bull.*, 4, 199–208.

Gautam, K., Jin, X., and Hansen, M. (1998) Review of spectrometric techniques for the characterization of crude oil and petroleum products. *Appl. Spectrosc. Rev.*, 33, 427–443.

Gredilla, A., Fdez-Ortiz de Vallejuelo, S., Elejoste, N., and Alberto de Diego, Madariaga, J. M. (2016) Non-destructive spectroscopy combined with chemometrics as a tool for green chemical analysis of environmental samples: A review. *Trends in Anal. Chem.*, 76, 30–39.

Hannisdal, A., Hemmingsen, P. V., and Sjöblom, J. (2005) Group-type analysis of heavy crude oils using vibrational spectroscopy in combination with multivariate analysis. *Ind. Eng. Chem. Res*, 44, 1349–1357.

He, K., Qian, F., Cheng, H., and Du, W. (2015) A novel adaptive algorithm with near-infrared spectroscopy and its application in online gasoline blending processes. *Chemometr. Intell. Lab*, 140, 117–125.

Hidajat, K. and Chong, S. M. (2000) Quality characterization of crude oils by partial least squares calibration of NIR spectral profiles. *J. Near Infrared Spectrosc.*, 8, 53–59.

Hindle, P. H. (2008) Historical development. In: Burns, D. A. and Ciurczak, E. W. (eds), *Handbook of Near-Infrared Analysis*, 3rd edn. CRC Press, Boca Raton, FL.

Hongfu, Y., Xiaoli, C., Haoran, L., and Yupeng, X. (2006) Determination of multi-properties of residual oils using mid-infrared attenuated total reflection spectroscopy. *Fuel*, 85, 1720–1728.

Khanmohammadi, M., Garmarudi, A. B., de la Guardia, M. (2012) Characterization of petroleum-based products by infrared spectroscopy and chemometrics. *TrAC: Trends Anal. Chem.*, 35, 135–149.

Kubelka, P. and Munk, F. (1931) Ein Beitrag zur Optik der Farbanstriche. *Zeits. Tech. Physik.*, 12, 593–601.

Kvalheim, O. M., Aksnes, D. W., Brekke, T., *et al.* (1985) Crude oil characterization and correlation by principal component analysis of i3C nuclear magnetic resonance spectra. *Anal. Chem.*, 57, 2858–2864.

Lima, F. S. G. and Leite, L. F. M. (2004) Determination of asphalt cement properties by near infrared spectroscopy and chemometrics. *Pet Sci Technol.*, 22, 589–600.

López-Gejo, J., Pantoja, P. A., Falla, F. S., *et al.* (2008) Electronical and vibrational spectroscopy. In: *Petroleum Science Research Progress*, Publisher, Inc., 187–233.

Martens, H. A. and Dardenne, P. (1998) Validation and verification of regression in small data sets. *Chemometr. Intell. Lab*, 44, 99–121.

Martens, H. and Naes, T. (1984) *Multivariate calibration. Trends in Anal. Chem.*, 3, 204–210.

Martens, H. and Naes, T. (1989) *Multivariate Calibration*. John Wiley & Sons, Ltd, New York.

Melendez, L. V., Lache, A., Orrego-Ruiz, J. A., *et al.* (2012) Prediction of the SARA analysis of Colombian crude oils using ATR-FTIR spectroscopy and chemometric methods. *J Pet Sci Eng*, 90–91, 56–60.

Meng, X., Jia, M., and Wang, T. (2014) Neural network prediction of biodiesel kinematic viscosity at 313K. *Fuel*, 121, 133–140.

Milanez, K. D. T. M., Silva, A. C., Paz, J. E. M., *et al.* (2016) Standardization of NIR data to identify adulteration in ethanol fuel. *Microchem. J.*, 124, 121–126.

Mohamed, N. H. and Zaky, M. T. (2005) Characterization and classification of some Egyptian petroleum crude waxes using different techniques. *Pet. Sci. Technol.*, 23, 483–493.

Morris, R. E., Hammond, M. H., Cramer, J. A., *et al.* (2009) Rapid fuel quality surveillance through chemometric modeling of near-infrared spectra. *Energy & Fuels*, 23, 1610–1618.

Mullins, O. C. (1990) Asphaltenes in crude oil: Absorbs and/or scatterers in the near-infrared region? *Anal. Chem.*, 62, 508–514.

Mullins, O. C., Betancourt, S. S., Cribbs, M. E., *et al.* (2007) The colloidal structure of crude oil and the structure of oil reservoirs. *Energy & Fuels*, 21, 2785–2794.

Oliveira, R. R., Lima, K. M. G., Tauler, R. T., and Juan, A. (2014) Application of correlation constrained multivariate curve resolution alternating least-squares

methods for determination of compounds of interest in biodiesel blends using NIR and UV–visible spectroscopic data. *Talanta*, 125, 233–241.

Onajake, M. C., Abrakasa, S., and Osuji, L. C. (2015) Chemometric representation of molecular marker data of some Niger Delta crude oils. *Egypt. J. Pet.*, 24, 139–143.

Özdemir, D. (2008) Near infrared spectroscopic determination of diesel fuel parameters using genetic multivariate calibration. *Pet. Sci. Technol.*, 26, 101–113.

Pantoja, P. A. (2006) *Aplicação da espectroscopia de infravermelho próximo na caracterização da carga de petróleo para o processo de destilação atmosférica*. MSc. Thesis. Universidade de São Paulo – Brasil.

Pantoja, P. A. (2010) *Caracterização de petróleo por técnicas espectroscópicas e sua utilização na avaliação e desenvolvimento de métodos de inferência em processo de refino*. PhD Thesis. Universidade de São Paulo – Brasil.

Pantoja, P. A., Lopez-Gejo, J., Le Roux, G. A. C., *et al.* (2011) Prediction of crude oil properties and chemical composition by means of steady-state and time-resolved fluorescence. *Energy & Fuels*, 25, 3598–3604.

Parisi, A. F., Nogueiras, L., and Prieto, H. (1990) On-line determination of fuel quality parameters using near-infrared spectrometry with fibre optics and multivariate calibration. *Anal. Chim. Acta*, 238, 95–100.

Paso, K., Kallevik, H., and Sjöblom, J. (2009) Measurement of wax appearance temperature using near-infrared (NIR) scattering. *Energy Fuels*, 23, 4988–4994.

Paulo, J. M., Barros, J. E. M., and Barbeira, P. J. S. (2016) A PLS regression model using flame spectroscopy emission for determination of octane numbers in gasoline. *Fuel*, 176, 216–221.

Pereira, R. C. C., Skrobot, V. L., Castro, E. V. R., *et al.* (2006) Determination of gasoline adulteration by principal components analysis-linear discriminant analysis applied to FTIR spectra. *Energy & Fuels*, 20, 1097–1102.

Radulescu, G. (2007) An original approach for the dynamic simulation of a crude oil distillation plant. *Rev. Chim.*, 58, 239–242.

Riazi, M. R. (2005) *Characterization and Properties of Petroleum Fractions*. American Society for Testing and Materials, West Conshohocken, PA.

Siesler, H. W., Ozaki, Y., Kawata, S., and Heise, H. M. (2002) *Near-Infrared Spectroscopy: Principles, Instruments, Applications*. Wiley-VCH, Weinheim, Germany.

Speight, J. G. (2007) *The Chemistry and Technology of Petroleum*, 4th edn. CRC Press, Taylor and Francis Group, Boca Raton, FL.

Tong, P., Du, Y., Zheng, K., *et al.* (2015) Improvement of NIR model by fractional order Savitzky–Golay derivation (FOSGD) coupled with wavelength selection. *Chemometr. Intell. Lab*, 143, 40–48.

Workman, J. J., Jr (2008) NIR spectroscopy calibration basic. In: Burns, D. A. and Ciurczak, E. W. (eds), *Handbook of Near-Infrared Analysis*, 3rd edn. CRC Press, Boca Raton, FL.

Xing, Z. N., Wang, J. X., Ye, Y., and Shen, G. (2006) Rapid quantification of kinematical viscosity in aviation kerosene by near-infrared spectroscopy. *Energy & Fuels*, 20, 2486–2488.

Xu, J., Zhang, H., Zhang, J., *et al.* (2013) The determination of diesel density and refractive index bye near infrared spectroscopy. *Pet Sci Technol.*, 31, 2489–2493.

Yun, Y. H., Cao, D. S., Tan, M. L., *et al.* (2014) A simple idea on applying large regression coefficient to improve the genetic algorithm-PLS for variable selection in multivariate calibration. *Chemometr. Intell. Lab*, 130, 76–83.

Yun, Y. H., Wang, W. T., Deng, B. C., *et al.* (2015) Using variable combination population analysis for variable selection in multivariate calibration. *Anal. Chim. Acta*, 862, 14–23.

Zendehboudi, S., Shafiei, A., Bahadori, A., *et al.* (2014) Asphatene precipitation and deposition in oil reservoirs: Technical aspects, experimental and hybrid neural network predictive tools. *Chem. Eng. Res. Des.*, 92, 857–875.

Zhang, G. Z., Guo, S., Zhao, S., *et al.* (2009) Alkyl side chains connected to aromatic units in Dagang vacuum residue and its supercritical fluid extraction and fractions (SFEFs) *Energy Fuels*, 23, 374–385.

9

Raman and Infrared Spectroscopy of Crude Oil and its Constituents

Johannes Kiefer[1] *and Stella Corsetti*[2]

[1] *Technische Thermodynamik, Universität Bremen, Bremen, Germany*
[2] *College of Life Sciences, University of Dundee, Dundee, United Kingdom*

9.1 Introduction

Over the past decades, vibrational spectroscopic methods in terms of Raman and infrared (IR) spectroscopy have been established as versatile analytical tools in a large variety of fields, including the analysis of crude oil and its constituents. Vibrational methods are capable of detecting virtually all molecular species. The corresponding spectrum is a highly species-specific molecular fingerprint and enables a multitude of chemical information to be extracted.

Crude oils are basically mixtures of thousands of different hydrocarbon species. Besides compounds consisting of carbon and hydrogen, there are nitrogen, oxygen, sulfur, and metals. This complexity makes a detailed compositional analysis difficult or even impossible. In most applications, the chemical analysis is therefore performed in such a way that the amounts of certain groups of species are determined. This means that instead of quantifying individual species, classes of chemicals with similar properties are considered. A common classification is the distinction of the so-called SARA fractions: saturates (S), aromatics (A), resins (R), and asphaltenes (A). The saturates represent the group of aliphatic hydrocarbons, including normal-chain and branched alkanes as well as cycloalkanes (naphthenes). Molecules with CC double and triple bonds are not included. The group of aromatics contains benzene and its derivatives, including compounds with multiple rings. Polar molecules (possibly containing heteroatoms like nitrogen, oxygen, or sulfur) are characteristic of the resin fraction. Finally, there is the class of asphaltenes, which contain larger amounts of heteroatoms as well as organometallic constituents. Asphaltenes are mainly polycyclic aromatic compounds and have a complex structure. These brief SARA definitions already demonstrate that it may be difficult to unambiguously classify a given compound to one

Analytical Characterization Methods for Crude Oil and Related Products, First Edition.
Edited by Ashutosh K. Shukla.

particular class. The main reason is that the saturates and aromatics are defined by their chemical structure, but resins and asphaltenes are defined by their chemical and physicochemical behavior. This needs to be kept in mind when interpreting the results from analytical methods applied to crude oil and its constituents.

9.2 Fundamentals of Raman and Infrared Spectroscopy

The existence of discrete, species-specific vibrations in a molecule is the basis of vibrational spectroscopy. These vibrations are due to the non-static nature of covalent bonds between atoms. A two-body system, in which two masses are connected with each other by a spring, represents a simple model to illustrate the vibrational phenomena at the molecular level (see Figure 9.1). Such a system has a single degree of freedom for vibrations (stretching mode) and the normal frequency ν of the harmonic oscillation between two bodies of masses m_1 and m_2, and the bond strength k (equivalent to the force constant of a spring connecting the bodies) is given by

$$\nu = \frac{1}{2\pi}\sqrt{\frac{k\cdot(m_2 + m_1)}{m_2\cdot m_1}}. \tag{9.1}$$

The constituents of crude oil are usually polyatomic molecules with a complex electron distribution. Such compounds have a multitude of bending (scissoring), rocking, wagging, and twisting vibrations in addition to the normal stretching modes (Figure 9.2). Hence, their vibrational signature yields a unique molecular fingerprint. For spectroscopy, all these modes are expressed as energy differences between the corresponding ro-vibrational states. They can be given in joules or in the more common unit of reciprocal centimeters, cm^{-1} (wavenumber). The wavenumber $\tilde{\nu}$ is the energy E in joules normalized by the product of the Planck constant h and the speed of light in vacuum c.

$$\tilde{\nu} = \frac{E}{hc} \tag{9.2}$$

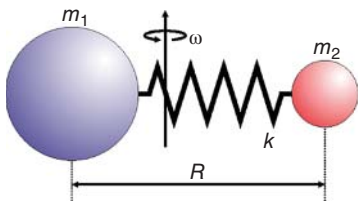

Figure 9.1 Two-body system as a model for molecular vibration and rotation. Masses m_1 and m_2, bond strength (spring constant) k, interatomic distance R, and angular velocity ω.

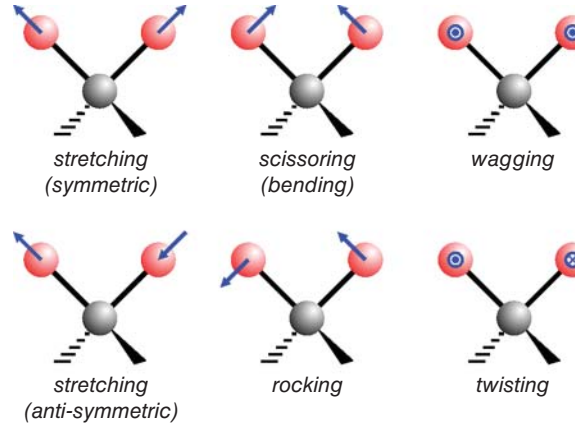

Figure 9.2 Illustration of the different types of vibrational modes in polyatomic molecules.

Its wide use in the field of spectroscopy comes from the fact that it is proportional to energy and at the same time it is the reciprocal value of the wavelength of photons with the same energy. Hence, it is a very useful and sensible unit in all fields of optical spectroscopy. A detailed description of vibrational states and their coupling with molecular rotation can be found in the common physics and spectroscopy texts, see, for example, Banwell and McCash (1994) and Haken and Wolf (1995).

IR and Raman spectroscopy are the most common vibrational spectroscopic techniques. IR spectroscopy is based on the direct absorption of electromagnetic radiation by a molecule, when the energy of the photon to be absorbed matches the energy difference between two molecular ro-vibrational energy levels. On the other hand, Raman spectroscopy takes advantage of the inelastic scattering of light at molecules. The term "inelastic" means that the scattered radiation is frequency shifted with respect to the incident light. In other words, an energy exchange takes place during the light-matter interaction. Both absorption and inelastic scattering are depicted in Figure 9.3. In IR, the molecule reaches the excited state directly by taking up the right portion of energy via absorption of an IR photon. In Raman, a photon exceeding this right portion of energy interacts with the molecule and the emission of a photon with reduced energy compared to the incident one results in the molecule reaching the same excited state as in the IR case. The intermediate state n is often referred to as the "virtual energy state" as it does not represent an energy level that is part of the molecule's natural structure. Consequently, the lifetime is extremely short and the Raman "excitation-emission" process can be considered instantaneous. On a side note, Albert Einstein described the difference between IR and Raman with a vending machine metaphor: "IR: Insert 10 cents in a Coke machine and receive a Coke; Raman: Insert 1 dollar and receive a Coke and 90 cents change."

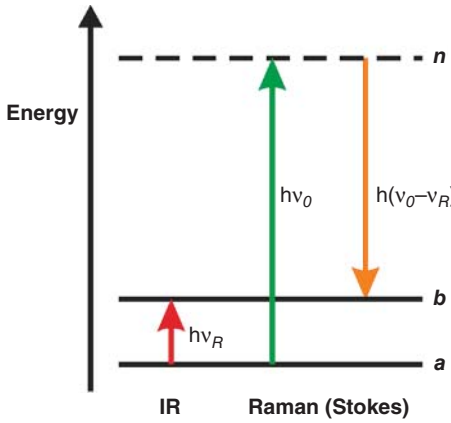

Figure 9.3 Schematic energy level diagram illustrating the direct absorption process of a photon (energy $h\nu_R$) between the ro-vibrational energy states *a* and *b*, and the inelastic scattering of an incident photon (energy $h\nu_0$) yielding the emission of a Raman photon (energy $h(\nu_0\text{-}\nu_R)$).

The vibrational spectrum of a species is a molecular fingerprint, as all functional groups and their geometric arrangement yield an individual structure of energy levels. In crude oil and its constituents, there is a multitude of different chemical compounds each consisting of a multitude of functional groups. As mentioned in Section 9.1, the main constituents are alkanes, naphthenes, aromatics, and asphaltics. The most relevant groups and the wavenumber ranges of their vibrations are summarized in Table 9.1.

Table 9.1 Functional groups and their normal vibrational bands in cm^{-1}.

Functional group	Vibrational bands (cm^{-1})
NH stretching	3300–3500
OH stretching	3200–3600
aromatic CH stretching	3000–3200
aliphatic CH stretching	2700–3000
SH stretching	2500–2600
C≡N stretching	2200–2300
C≡C stretching	2100–2300
C=O stretching	1700–1850
aromatic ring	1500–1600
CH deformation	1400–1600
CN stretching	1000–1300
S=O stretching	1000–1200
CO stretching	950–1300
aromatic ring	700–900
CH rocking	700–800

9.3 Infrared Spectroscopy

Only a brief account of the basics of IR spectroscopy and its implementation is given here. For a detailed description, the reader is referred to the literature, see for example, Haken and Wolf (1995), Schrader (1995), and Griffiths and De Haseth (2007).

As aforesaid, IR spectroscopy utilizes the direct absorption of electromagnetic radiation. For this purpose, the frequency of the electromagnetic wave must be equal to the oscillating frequency of a molecular vibrational mode. For completeness, we note that near-infrared (NIR) spectroscopy, in which vibrational overtone and combination bands are probed, is very similar. As NIR methods find wide applications in the analysis of crude oil as well, Chapter 8 is dedicated to this area; here, we focus on the mid-IR spectral range. The mid-IR spectral range is normally specified as 2.5–50 μm (200–4000 cm^{-1}) and the NIR covers the range 0.75–2.5 μm (4000 to 13,333 cm^{-1}). Consequently, the mid-IR contains the normal vibrations, while overtone and combination bands are predominantly found in the NIR.

A requirement for IR absorption is that a change in the oscillating dipole moment is produced during the vibrational motion of the molecule. Mathematically this means that

$$\left(\frac{\partial \mu}{\partial q}\right) \neq 0, \tag{9.3}$$

where μ is the dipole moment and q is the normal coordinate. When this pre-requisite is fulfilled, the vibrational mode is called "IR-active."

The measured quantity in IR spectroscopy is the intensity I of the light transmitted by a sample of thickness d. The intensity I divided by the incident light intensity I_0 is the transmission T, which is determined as a function of wavelength to yield the IR spectrum. The data are eventually plotted against wavenumber either as transmission, absorption ($=1 - T$), or absorbance ($A = -\log(T)$) spectrum.

The above quantities are connected with each other by the Beer–Lambert relation

$$A = -\log\left(\frac{I}{I_0}\right) = \varepsilon(\lambda) \cdot c \cdot d, \tag{9.4}$$

with the extinction coefficient ε as a function of wavelength λ and the concentration c of absorbing molecules. An IR spectrum comprises all individual contributions (i.e. all the different vibrations from all the molecules in the system under investigation). Hence, extracting quantitative information about the chemical composition is a challenge, because of the spectral complexity. Employing Equation 9.4 for quantification purposes is only possible when the species of interest exhibits an isolated peak that is not sensitive

to molecular interactions. A complicated fluid like crude oil, where many different but structurally similar species are present, calls for more sophisticated approaches to data evaluation. An overview of possibilities for analyzing vibrational spectra is given in Section 9.5.

Nowadays, there are numerous IR instruments commercially available. Most of them utilize an interferometric analysis (Michelson interferometer) when recording the data. The interferogram is then Fourier transformed to obtain the spectrum in the frequency domain (i.e. as function of wavenumber); hence, they are called Fourier transform infrared (FTIR) spectrometers. Most instruments offer a variety of modes to enable the interaction of the radiation with the sample (e.g. transmission, diffuse reflection, and attenuated total reflection). Those concepts are illustrated in Figure 9.4. In *transmission* measurements, the sample is placed in between two transmittive windows, and the transmitted light is recorded as a function of wavelength. The appropriate sample thickness depends on the absorption coefficient and the molecular density of the target species. As crude oil is a rather opaque and highly viscous fluid, data acquisition in transmission mode is usually not the method of choice. The high viscosity makes the fluid rather sticky and hence the cleaning effort is high when a sample is prepared as a thin layer between two flat windows. In addition, the low transmittance of the sample established a need for a very thin layer (e.g. with a thickness of a few microns). Precise spacers that ensure a sample thickness below 25 μm are difficult to use and expensive. Another drawback of the transmission mode is that the window material must be transmittive for the IR radiation. Consequently, conventional borosilicate or fused silica quartz glasses cannot be used. Crystalline materials, such as KBr, CaF_2, and NaCl, are better suited. However, one serious problem arises, as these salt materials may be affected and be irreversibly damaged even by small amounts of water/moisture in the samples. The next option, diffuse reflectance, is better suited for crude

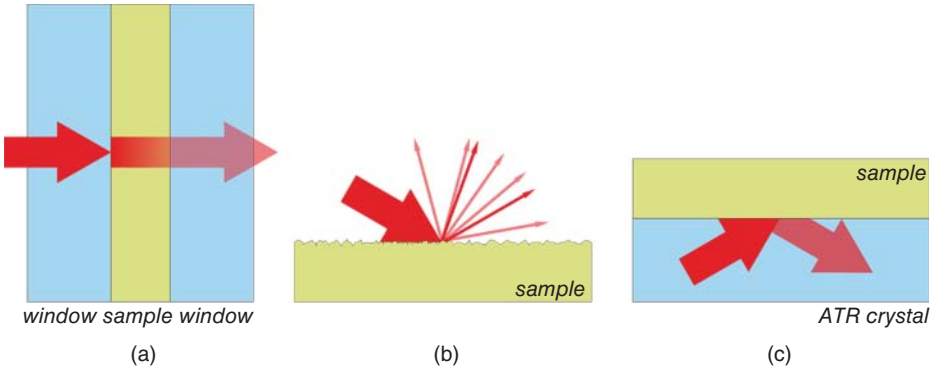

Figure 9.4 Illustrations of the most common IR concepts: (a) transmission, (b) diffuse reflectance, and (c) attenuated total reflection.

oil. In this mode, the sample surface is illuminated by the IR radiation and the scattered/reflected photons are detected at a defined angle. This arrangement allows obtaining spectra of opaque samples. However, a disadvantage is that the spectra acquired through the diffusely scattered radiation have a limited reproducibility and thus a quantitative analysis is challenging.

Many applications of IR spectroscopy to liquids employ attenuated total reflection (ATR) spectroscopy. In such an experiment, the IR radiation is propagating in a transmittive high-refractive-index material (often ZnSe, Ge, or a diamond crystal), the internal reflection element (IRE, with refractive index n_{IRE}). The sample has a lower refractive index, n_{sample}. When the sample is in contact with the IRE surface and the radiation is reflected at an angle α at this surface (total internal reflection), the evanescent field can interact with the sample. The reflected beam is attenuated and carries the spectroscopic information if absorption takes place. Like diffusive reflectance, ATR is suitable for analyzing opaque samples, and sample preparation is minimal.

An advantage of the transmission mode is its well-defined sample thickness, which is given by the geometry of the measurement cell. On the other hand, in ATR experiments, the penetration depth, d_{p}, of the evanescent field is a complicated function of the wavelength (recall that the refractive index is a function of wavelength). This must be taken into account when ATR-IR spectra are interpreted quantitatively (Kiefer *et al.*, 2014). The penetration depth is usually described as

$$d_p = \frac{\lambda}{2\pi \cdot n_{IRE} \cdot \left(\sin^2\alpha - \left(\frac{n_{sample}}{n_{IRE}} \right)^2 \right)^{1/2}}. \tag{9.5}$$

However, we must note that this parameter must not be used as a path length and inserted in the Beer–Lambert relation (see Equation 9.4). The penetration depth is the distance from the surface at which the exponentially decaying electric field reaches a fraction of 1/e with respect to its value at the surface. In the context of quantitative measurements, the effective path length, d_{eff}, is the parameter of interest. It represents the corresponding sample thickness that would lead to the same absorption in a transmission experiment (Averett and Griffiths, 2008). Note that the effective path length is a kind of auxiliary parameter, which cannot be determined in a straightforward manner (Harrick and du Pré, 1966; Averett and Griffiths, 2008; Kiefer *et al.*, 2014).

9.4 Raman Spectroscopy

Like for IR spectroscopy, only a brief account of the basics of Raman spectroscopy and its implementation is given here. For a detailed description, the

reader is referred to the literature, see, for example, Banwell and McCash (1994), Haken and Wolf (1995), and Schrader (1995).

Raman spectroscopy is based on the inelastic scattering of light at molecules. This means that the scattered photons have a different energy than the incident light and thus are frequency shifted. In the case of "Stokes Raman scattering," which is shown in Figure 9.3 and the physical process relevant in most practical applications, the scattered light is shifted toward lower frequency (called a "red-shift"). This means that energy is transferred from the incident light to the molecule and it reaches an excited state via this indirect two-photon process. Recall that in IR spectroscopy the same state was reached directly by absorption. The frequency difference between the incident and scattered light is molecule-specific. The above explanation involving photons is basically from quantum mechanics. However, the existence of the frequency-shifted Raman bands can also be explained using the wave nature of light. In this case, an oscillating Hertz dipole can be considered. It emits waves of the exciting frequency plus side bands that are frequency shifted by the harmonic oscillation frequency of the dipole itself. The wave explanation eventually leads to a simple mathematical expression that needs to be fulfilled in order to observe Raman scattering:

$$\left(\frac{\partial \alpha}{\partial q}\right) \neq 0, \tag{9.6}$$

with the polarizability α and the normal coordinate q. When Equation 9.6 is fulfilled, the molecule or a specific vibrational mode is called "Raman-active."

The signal intensity I_{RS} for a Stokes Raman line is often simplified as linearly dependent on the species' number density c, the intensity of the incident light I_0, the solid angle of the signal collection optics Ω, and the Raman "scattering cross-section," $\partial\sigma/\partial\Omega$. A common empirical relation is given by

$$I_{RS} = k_{\mathrm{exp}} \cdot \Omega \cdot \frac{\partial \sigma}{\partial \Omega} \cdot c \cdot l \cdot I_0, \tag{9.7}$$

where k_{exp} is a constant of the experiment and l is the length of the collection volume. Similar to IR, a Raman spectrum comprises the contributions from all the different vibrations from all the molecules in the system under investigation. Hence, Equation 9.7 can only be used to extract quantitative information from a spectrum, if the target species exhibits an isolated peak that is not sensitive to molecular interactions. Hence, in most practical applications, more sophisticated approaches to data analysis are needed. An overview will be given later.

It should be emphasized that Raman scattering is a non-resonant process. In other words, none of the involved photons matches the energy difference between two molecular states. This means that the wavelength of the light source can basically be chosen arbitrarily, which is a great advantage over many other techniques. However, there are a couple of effects related to Raman

that need to be taken into account. First, the Raman scattering cross-section is a strong function of wavelength (proportional to λ^{-4}). This means that a short wavelength laser (visible or ultraviolet) will give a stronger signal than a near-IR one with the same power. Consequently, it seems best to go for short wavelengths. However, the laser may resonantly excite some species in the measurement volume. These electronically excited molecules can emit fluorescence, which can represent a severe interference. Crude oil usually contains aromatic compounds and they are likely to emit fluorescence, when they are excited in the ultraviolet or visible spectral range. As fluorescence signals can be many orders of magnitude stronger than the non-resonant Raman scattering, the latter may be completely masked. Therefore, the use of a near-IR laser will be the light source of choice in most cases when crude oil and its constituents need to be characterized. For completeness, an overview of techniques to suppress fluorescence interference in Raman spectra can be found in the review of Wei, Chen, and Liu (2015).

The main components for a Raman spectroscopy experiment are a light source and a spectrograph or monochromator equipped with a sensitive detector in order to record the weak signals as a function of wavelength. The light source is normally a laser, but recent developments have made light-emitting diodes suitable alternatives as well (Greer, Petrov, and Yakovlev, 2013; Schmidt and Kiefer, 2013). Its specifications depend on the measurement task. For example, for gas-phase analysis, high optical power (in the order of W) is required as the molecule density is low, whereas for liquids a commercial laser pointer (mW) may be sufficient. For analyzing fluids like crude oil, a laser power in the order of 10–100 mW is usually sufficient. The wavelength should be in the NIR in order to avoid fluorescence interference, as described above. Suitable detectors include intensified charge-coupled device (ICCD) cameras, electron-multiplying CCD (EMCCD) cameras, back-illuminated CCD (BICCD) cameras, and photo-multiplier tubes (PMTs). ICCDs offer higher performances than EMCCD cameras. They can reach very short gating times (order of hundreds of picoseconds) and their high sensitivity allows single-photon detection. However, they are generally more expensive than EMCCD cameras, even though the necessity of a cooling system to cool the EMCCD chip down to temperatures around 170 K adds additional costs to the EMCCD camera. BICCD cameras are used to increase the quantum efficiency with respect to the front-illuminated CCD cameras in which the incident photons fall on the part of the CCD chip containing the circuit mask that covers half of the sensitive detector area. PMTs offer higher sensitivity and higher signal-to-noise ratio than CCD cameras do, but they do not allow recording the entire spectrum simultaneously. The spectrum has to be scanned stepwise with the monochromator.

There are two common experimental arrangements for Raman spectroscopy: the 90° and the backscattering setup. In the 90° setup, the scattered Raman

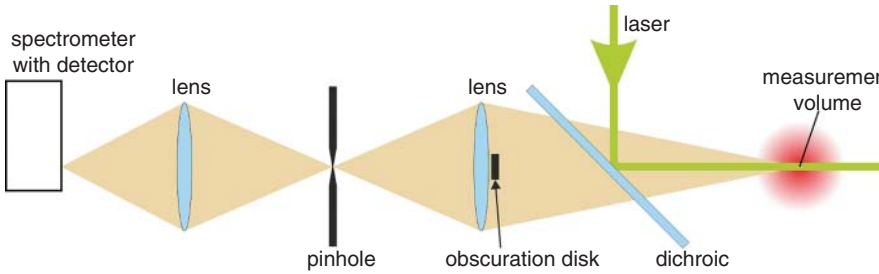

Figure 9.5 Schematic Raman backscattering setup.

signal is collected by a lens in direction perpendicular to the laser beam and delivered to a spectrometer. In the spectrometer, the signal is spectrally dispersed and detected as a function of wavelength. This setup can easily be arranged but a requirement is that the sample transmits the laser beam and the signal. For an application of Raman spectroscopy to crude oil, this poses a challenge and thus the alternative backscattering geometry is more suitable. In Raman backscattering spectroscopy the part of the signal, which is scattered against the laser propagation direction, is collected and analyzed. Figure 9.5 shows a schematic of a Raman backscattering setup. The laser beam is reflected toward the measurement volume by a dichroic mirror that operates also as a Rayleigh filter. It does in fact block more than 99% of the light elastically backscattered from the sample and it is transmissive for the Raman signal wavelengths. Therefore, the backscattered signal can be collected by the collection lens and focused into the spectrometer by the focusing lens. An additional notch filter is usually placed between the two lenses to further reduce the Rayleigh signal before entering the spectrometer. The backscattering geometry allows recording Raman signals from surfaces of condensed phase matter. Another advantage of this setup is its robustness as the laser beam and signal are partly guided by the same optical components. The backscattering principle is often used in Raman microscopy and fiber-coupled Raman probes for process monitoring. As can be seen in Figure 9.5, the collection lens focuses the signal through a pinhole. Together with an obscuration disk, this pinhole ensures that only signal from a defined measurement volume is guided to the spectrometer. They act as a spatial filter. This setup can be modified by placing the collection lens before the dichroic mirror. This arrangement facilitates focusing the laser to a small spot in the measurement volume and collecting the signal confocally with the same lens. This approach is used in confocal Raman microscopy and enables spectroscopy with very high spatial resolution in the order of micrometers and better.

For a comparison, the main features and pros and cons of Raman and IR spectroscopy are summarized in Table 9.2.

Table 9.2 Advantages and disadvantages of IR and Raman spectroscopy.

	Infrared	Raman
Sensitivity	High sensitivity can be obtained With conventional IR spectroscopy a limit of detection (LOD) in the order of 0.1% and better can be obtained. However, strongly absorbing species may virtually completely absorb the wavelength of interest and, hence, the measurement is not sensitive to changes in concentration any longer	Good sensitivity can be obtained Depending on the scattering cross-section it can be in the order of ~0.1%
Acquisition time and repetition rate	The technique allows fast measurements at a high repetition rate. The measurement time can be as short as a few milliseconds. However, it must be kept in mind that the shorter the measurement/acquisition time, the lower the sensitivity and accuracy as the noise level increases	The technique allows fast measurements at a high repetition rate. The measurement time can be sub-second. However, it must be kept in mind that the shorter the measurement/acquisition time, the lower the sensitivity and accuracy as the noise level increases. Pulsed laser sources are suitable to bring acquisition times down to nano-seconds should extremely high temporal resolution be required
Process monitoring	Fiber-coupled ATR probes facilitate *in situ* measurements in liquid systems. Such probes can be installed in the same way as thermocouples or pressure transducers. Hence, there is no need for optical access to the sample	Fiber-coupled probes allow *in situ* measurements without the requirement for a large optical access to the sample

(Continued)

Table 9.2 (Continued)

	Infrared	**Raman**
Accessible species	Most molecular species are detectable. Homonuclear diatomic molecules (such as hydrogen, oxygen, and nitrogen) are not IR-active and hence cannot be detected	Most molecules, in particular those in typical crude oil, are Raman-active and hence can be detected simultaneously. This includes the homonuclear diatomics, which cannot be measured using IR spectroscopy
Interferences	Background black-body radiation may be detected as an interference signal when the fluid or parts of the analytical device exhibit elevated temperature. Moreover, water is a strong absorber in the IR spectral range and may represent an interference, making the evaluation of the signal difficult	Interference from laser-induced fluorescence may be a problem in crude oil applications. In order to avoid such effects a number of approaches have been developed, including NIR Raman (Meyer, Lupoi, and Smith, 2011), deep-UV Raman (Liu and Berg, 2013), polarization-resolved detection Raman (Egermann, Seeger, and Leipertz, 2004), and shifted-excitation Raman difference spectroscopy (SERDS) (Shreve, Cherepy, and Mathies, 1992; Zhao, Carrabba, and Allen, 2002; Maiwald *et al.*, 2006, Noack *et al.*, 2013). An overview can be found in Wei, Chen, and Liu (2015). Moreover, the presence of phase boundaries, e.g. when the sample contains small particles or droplets, can result in interference from elastically scattered light (Rayleigh scattering and Lorentz–Mie scattering). This scattering can be orders of magnitude stronger than the Raman signal. Therefore, suitable spectral filters may be required, for example holographic notch filters or long-pass filters, or a combination of the two

9.5 Evaluation of Vibrational Spectra

This section introduces methods for evaluating spectroscopic data. The most straightforward method to extract quantitative information from a vibrational spectrum is to calibrate the intensity of a single peak against the concentration of the corresponding species. This approach, however, is unlikely to work in the analysis of crude oil, owing to the chemical complexity that results in a spectral overlap of different peaks. Another straightforward but also simplistic technique is spectral "soft modeling" (note that the term soft modeling is sometimes used in the literature for other approaches as well). In spectral soft modeling the spectrum of a mixture is considered a linear combination of the weighted spectra of the pure components in the mixture (Zehentbauer and Kiefer, 2012). The weighting factors of the individual species are determined in a simple fitting (e.g. minimizing the residual between the experimental spectrum and a synthetic spectrum calculated from the weighted pure species spectra). After calibration, the weighting factors of the individual species can be converted to concentration values. This approach does only work as long as there are no spectral line shifts or changes in the signal intensity, owing to non-ideal mixture behavior. Therefore, the method is mainly used in gases (Kiefer *et al.*, 2008) and simple liquid mixtures (Struthers *et al.*, 2011). The spectroscopy of crude oil will normally not fulfill the prerequisites for the application of soft modeling. Therefore, this approach is not discussed further here.

More sophisticated approaches to spectral analysis are deconvolution, peak fitting, and indirect spectral hard modeling. These methods are more universally applicable and can deal with complex spectra of mixtures. In all three, the spectrum is considered a sum of individual peaks represented by Gaussian, Lorentzian, or Voigt profiles. Deconvolution and peak fitting are basically techniques for identifying peaks and their spectral parameters, such as center wavenumber, intensity, line shape, and bandwidth. When "peak fitting" is applied, the experimental spectrum is fitted to a sum of individual lines (some of the spectral parameters may be fixed during this procedure) in order to obtain a good representation of the measured spectrum. In contrast, "deconvolution" algorithms determine these parameters computationally as a first step. For instance, the first- and second-derivative spectra are derived and the position of a peak in the original spectrum can be identified at the extreme values of the second-derivative spectrum. This works even for overlapping peaks. The deconvolution is particularly useful, when the signal exhibits a high signal-to-noise ratio. When the noise level is high, however, the analysis via derivative spectra becomes problematic, as statistical fluctuations may incorrectly be identified as peaks by automatic deconvolution algorithms. Eventually, the peak parameters can be calibrated against the mixture composition and hence, when these parameters are determined in a spectrum of an unknown mixture, the compositional information can be obtained. This procedure is known as "indirect spectral hard modeling" (Alsmeyer, Koß,

and Marquardt, 2004; Viell and Marquardt, 2012). In order to reduce the computational cost, it is reasonable to reduce the spectral window of interest to a minimum. In other words, a limited spectral region with contributions from all species of interest is chosen before a detailed analysis is carried out.

Chemometrics represent the most universal approach to spectral analysis. Chemometric techniques are mathematical and statistical methods. They allow chemically relevant information out of the vibrational spectra to be obtained, displaying this information and putting it into a form of data that can be interpreted. These methods were first introduced in the 1980s by Wold (Wold, Esbensen, and Geladi, 1987) and Kowalski (Sharaf, Illman, and Kowalski, 1986). One of the most important and powerful tools of chemometrics is the principal components analysis (PCA). PCA is a data reduction method used to re-express the original data set depending on a large number of variables with fewer dimensions. The original variables are projected in a new Cartesian system in the order of decreasing variance and only the variables with high variance are retained. In order to correlate the information in the original data set to the investigated property (e.g. the amount of a component in a mixture) chemometrics algorithms for performing regression are used. Among those algorithms, the most common ones are principal component regression (PCR) and partial least squares regression (PLSR). The first step of PCR is a PCA, which is described in more detail below, and then a linear regression of the response variables on the principal components is performed. In PLSR, differently from PCR in which the response variables are not considered to create the principal components, these responses are taken into account. This often leads to more precise models. Within chemometrics there are also non-linear higher-order approaches such as support vector machines (SVMs) and artificial neuronal networks (ANNs). SVMs are learning machines based on statistical learning theory, trained through a supervised learning algorithm. ANNs are models inspired by the interconnection system of neurons, which communicate between each other and are capable of learning. Differently from the result of SVMs, the result of ANNs is dependent on the initial parameters and this sometimes makes it necessary to repeat the network training.

As aforesaid, PCA is a very common tool and it represents a kind of gold standard in the field of chemometrics. The first paper on PCA appeared in 1901 (Pearson, 1901), but it was Harold Hotelling who formulated in 1933 the PCA theory as it is known today (Hotelling, 1933). PCA is a change of variable space with the aim of reducing the original variables into a lower number of non-correlated orthogonal factors (eigenvectors) or components that capture maximum possible information from the original variables. The matrix of the measured data X (matrix of intensities or absorbances) can be expressed by Equation 9.8:

$$X = S \cdot L' + E, \tag{9.8}$$

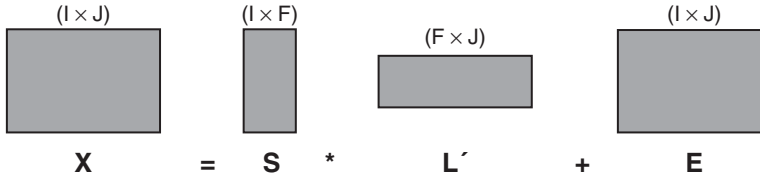

Figure 9.6 The matrix of the original data (X) can be expressed as the product of the matrix of the scores (S) and the matrix of the loadings (L) plus the matrix of the residuals (E).

where S is the matrix of the scores, L is the matrix of the loadings, and E is the matrix of the residuals. The scores are the eigenvectors, the loadings are their weights, and the residuals represent that part of the data not explained by the model. Equation 9.8 can be expressed graphically, as shown in Figure 9.6, in which F is the number of principal components.

Each principal component consists of one score and one loading vector and can be expressed as:

$$Z_i = s_i \cdot l_i' \tag{9.9}$$

with the number of components i. The goal of PCA is to find components that explain the most of the variation in the original data. The first principal component accounts for the maximum possible variance in the original data. The second component, which is orthogonal and uncorrelated to the first one, captures most of the information from the original data that is not in the first component. This would be the requirement for all the other components. In order to visualize the concept, the very simple plot in Figure 9.7 is considered. PCA has the goal of finding a new dimension, which is able to represent all the data points individually. First, the vector having the direction of maximum variance of the data points is considered and then the data points are projected on this vector. In this way, the points can be very easily represented and they are highly separated between each other. This vector is called the first principal component and it is indicated in Figure 9.7 as Z_1. Perpendicular to Z_1 is

Figure 9.7 Determination of the first and second principal components.

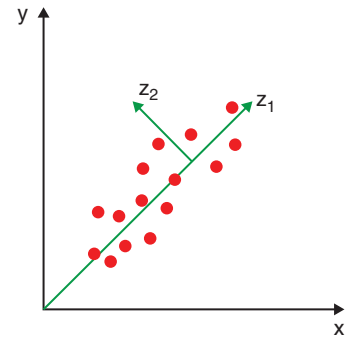

the second principal component Z_2. The first loading is the direction where the original data projected on that direction have the highest variance. The scores are the projections of the original data on the loadings.

Considering the vibrational spectra of a mixture containing different percentages of a species, the first loading gives the shape that best describes all the variations in all the samples. The loading would be in common for all the samples. The score value would take into account the amount of the spectrum of this common profile in each of the individual samples. In summary, the scores differ for every sample while the loading is what the samples have in common. By subtracting the first principal component from the original data, the residual, which is the part of the original data that has not been explained, is obtained. If this residual is high then one further principal component can be extracted. The second component would be orthogonal to the first one and it would be the one that best describes the remaining variation in the data. Also for this component, individual score values for each sample are obtained. The total number of components would be the one that best explains all the variation in the original data.

Mathematically, the procedure to find the principal components can be explained in three steps:

1) Find the covariance matrix of the original variables:

$$Cov(X) = \frac{1}{n-1}(X' \cdot X), \tag{9.10}$$

where X is the matrix of the original data and n is the number of observations.

2) Perform an eigenvalue decomposition (EVD) of the covariance matrix of the original variables. For this purpose, find eigenvalues (l_i) and the corresponding eigenvectors (u_i). The eigenvalues can be found by solving the equation

$$(Cov(X) - l_i)u_i = 0. \tag{9.11}$$

The eigenvector associated with the largest eigenvalue (variance) is the first principal component. The principal components are orthogonal because they are the eigenvectors of the covariance matrix, which is symmetric.

3) Component retention: PCA aims to retain the fewest possible number of components while explaining most of the variation in the data. This can be done by following Kaiser's rule, which recommends retaining only the components with eigenvalues exceeding unity. Alternatively, the ratio between each eigenvalue (variance in the original data explained by each principal component) and the sum of all the eigenvalues (total variance in the original data) can be considered. Only the principal components associated with eigenvalues giving high ratios, and then explaining the most of the variance in the original data, must be retained.

9.6 Applications

IR spectroscopy was used in most applications of vibrational spectroscopy to crude oil. The main reason for this is the robustness and simplicity of the attenuated total reflection technique. Figure 9.8 shows the IR spectra of different crude petroleum oil samples from South America and Africa as an example (Galtier *et al.*, 2011). It can be seen that the spectra appear very similar, owing to the similar functional groups contained in the fluids. Most of the features that are marked by wavenumbers are characteristic of aliphatic hydrocarbons. The strong peaks at 2952, 2922, and 2853 cm^{-1} are due to CH stretching vibrations. The corresponding CH bending modes can be found at 1376 and 1456 cm^{-1}. Signatures of aromatic compounds can be observed as well. The weak shoulder band at 3052 cm^{-1} can be assigned to CH stretching vibrations of CH groups that are part of an aromatic ring. In addition, the peak at 1602 cm^{-1} is due to C=C stretching.

As aforesaid, the spectra are typically evaluated using chemometrics in order to systematically identify any characteristic features that correlate with the information required. PCA is the main tool to do an initial analysis and to reduce the dimensionality of the data set. Depending on the number of PCs contributing to the variance of the data set, the results of a PCA are graphically displayed. In case of three or more PCs, three-dimensional plots showing the scores of different PCs are often presented. For clarity, however, it can be beneficial to reduce the graphical dimension to a set of two-dimensional plots that show the correlations between the PCs pairwise. An example is given in Figure 9.9, which illustrates the score plot of PC1 and PC2 after applying a PCA

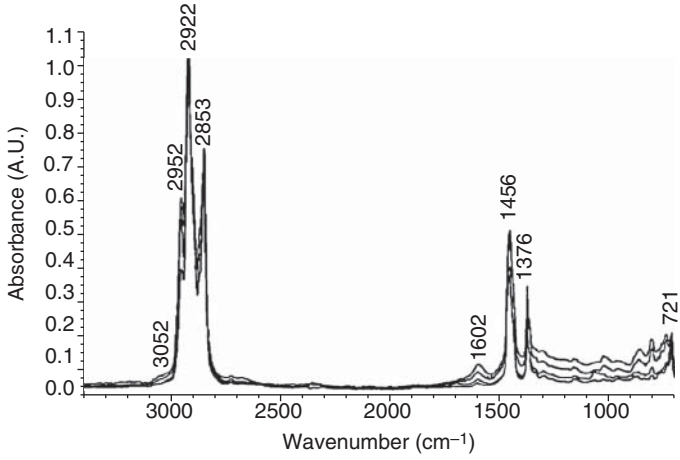

Figure 9.8 Normalized IR spectra of different crude petroleum oils. *Source:* Galtier *et al.* (2011). Reproduced with permission of American Chemical Society.

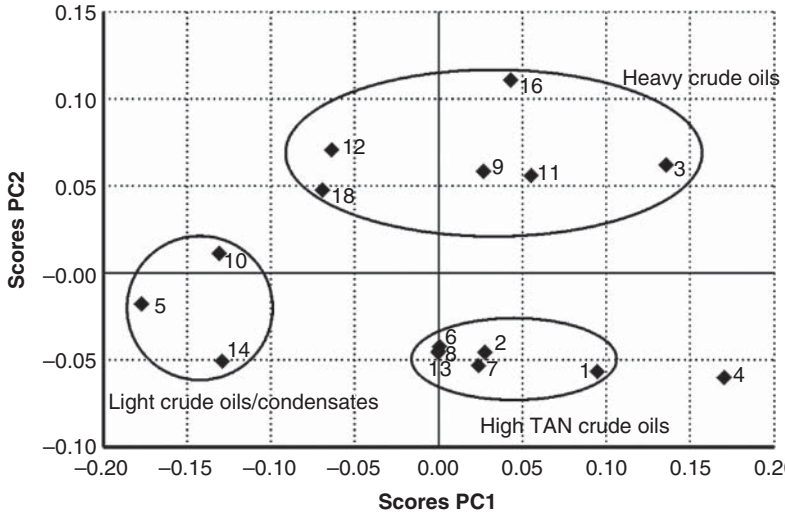

Figure 9.9 Score plot from the PCA of the IR spectra of 18 crude oils and condensates (two outliers removed). *Source:* Aske, Kallevik, and Sjöblom (2001). Reproduced with permission of American Chemical Society. (Note that the figure was redrawn based on the original graphic to improve the graphical quality.)

to the IR spectra of 18 crude oil samples from Europe and West Africa (Aske, Kallevik, and Sjöblom, 2001). The first two PCs explain 82% of the variation in the data set. It can be seen that the data points presenting the individual samples arrange themselves into groups, which are indicated by the circles. Samples close to each other in the score plot will have similar properties. The groups identified correspond to samples with a high total acid number (TAN), to light crude oils and condensates, and to heavy crude oils.

In a next step, regression algorithms can be applied in order to find correlations between the spectral signatures and the parameters of interest. Basically, these parameters can be anything from the concentration of a certain compound or class of compounds to physicochemical properties like density and viscosity. Figure 9.10 shows a series of correlation plots, where predicted values are plotted against measured values. Panels A and B show data from gas chromatography, while panels C–F have been derived from IR spectra. In this study (Tomren, Barth, and Folgerø, 2012), 20 different crude oils and condensates have been analyzed. The diagrams show impressively how well the measured and predicted values agree with each other, demonstrating the capability of the spectroscopic method to not only derive chemical composition but also provide information about the macroscopic properties.

It should be noted that spectroscopic analysis must not necessarily be applied to the crude oil itself. It can also be used after processing the original fluid

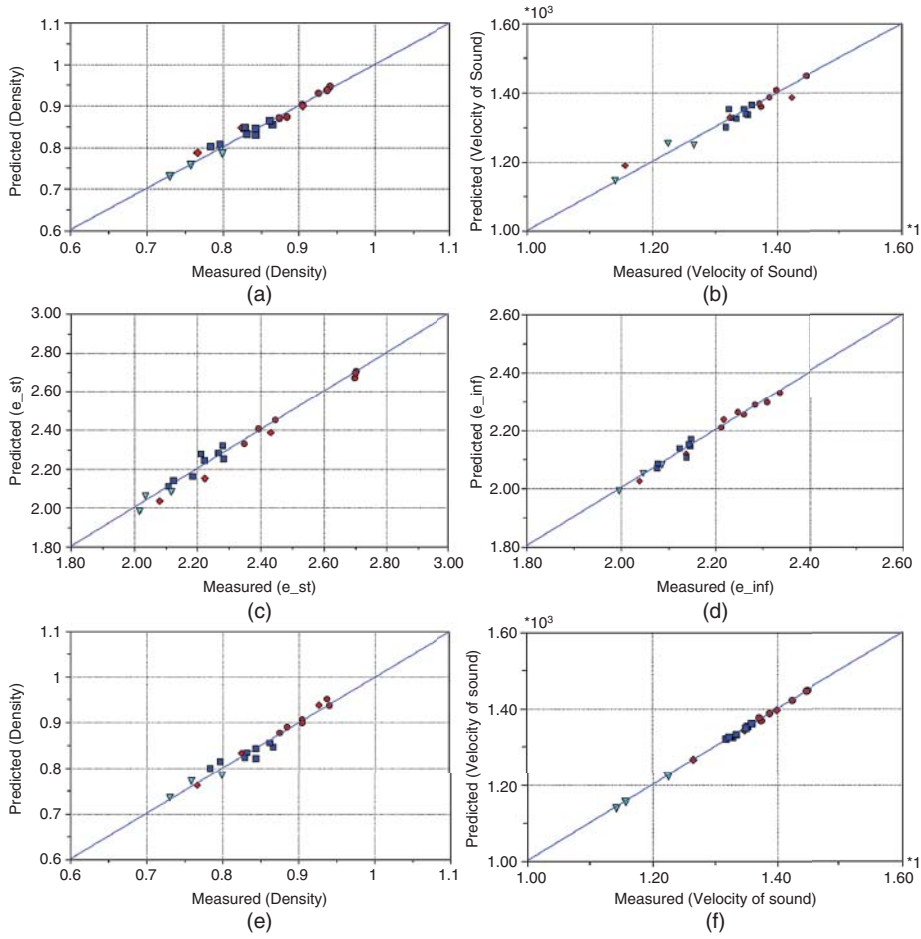

Figure 9.10 Results from PLSR. Predicted value plotted against measured for (a) density based on GC, (b) velocity of sound based on GC, (c) static permittivity (e_st) based on IR data, (d) high frequency permittivity (e_inf) based on IR data, (e) density based on IR data, and (f) velocity of sound based on IR data. *Source:* Tomren, Barth, and Folgerø (2012). Reproduced with permission of American Chemical Society.

(e.g. after separation into its individual fractions). For example, the applications of Raman in IR spectroscopy to gaseous and liquid fuels have been reviewed (Kiefer, 2015). Investigating the SARA fractions of crude oil is another option. The fingerprint IR spectra of a crude oil and its SARA fractions are shown in Figure 9.11 as an example. An interesting point is that the spectrum of the original crude oil agrees rather well with a theoretical spectrum that was composed of the weighted spectra of the individual fractions. Recalling the section on

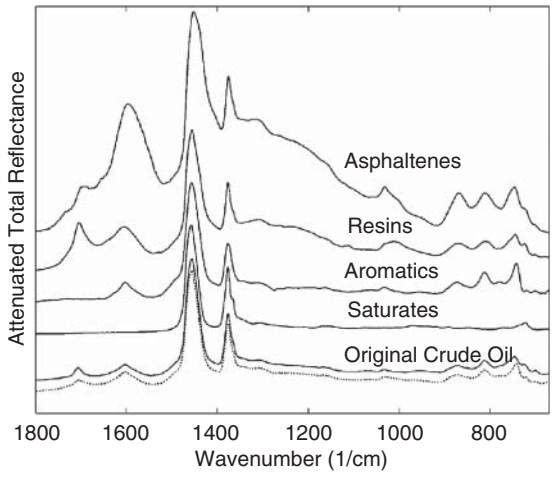

Figure 9.11 IR spectra of SARA fractions from a crude oil are shown together with a spectrum of the original crude oil. The broken line is a theoretical spectrum of the crude oil calculated from a linear combination (weighted with the experimental composition) of the individual SARA spectra. *Source:* Hannisdal, Hemmingsen, and Sjöblom (2005). Reproduced with permission of American Chemical Society.

signal evaluation, this comparison between an experimental spectrum and the corresponding spectrum determined from the component spectra is similar to the spectral soft modeling approach. The agreement of both spectra suggests that the components of one fraction do not establish strong molecular interactions with the components of another fraction. Otherwise, the changes in peak position and shape would be more significant.

For completeness, it should be noted that Raman spectroscopy is emerging in the analysis of the fractions of crude oils as well. There is an ever-increasing number of applications of Raman techniques (Dearing *et al.*, 2011; Kuptsov and Arbuzova, 2011; Abdallah and Yang, 2012; Riedemann *et al.*, 2016). The development of improved instrumentation, in particular regarding light sources and detectors in the NIR, is a key driver in this context. As an example for Raman spectra from a crude oil component, three spectra of an asphaltene sample are shown in Figure 9.12 (Abdallah and Yang, 2012). In this study, a Raman microscope was employed to acquire spectra in a confocal backscattering configuration. The Raman spectrum was collected from three different locations in order to obtain information about the sample homogeneity. Panel (b) shows the zoomed-in region of the so-called D1 and G bands. As we mention in Section 9.1, asphaltenes are mainly polycyclic aromatic compounds. Hence, they consist of mainly sp2-hybridized carbon atoms. The G band results from the stretching vibration of the sp2 carbon atoms within aromatic hexagonal sheets as well as from sp2 carbon atoms in chains. By contrast, the D1 band originates from the boundary of an ordered structure. In graphene sheets, the D1 band is commonly used to estimate the number of defects in a layer (Beams, Cancado, and Novotny, 2015). Consequently, Raman spectroscopy can yield an estimate of the size of the ordered structures and thus the molecule size in an asphaltene.

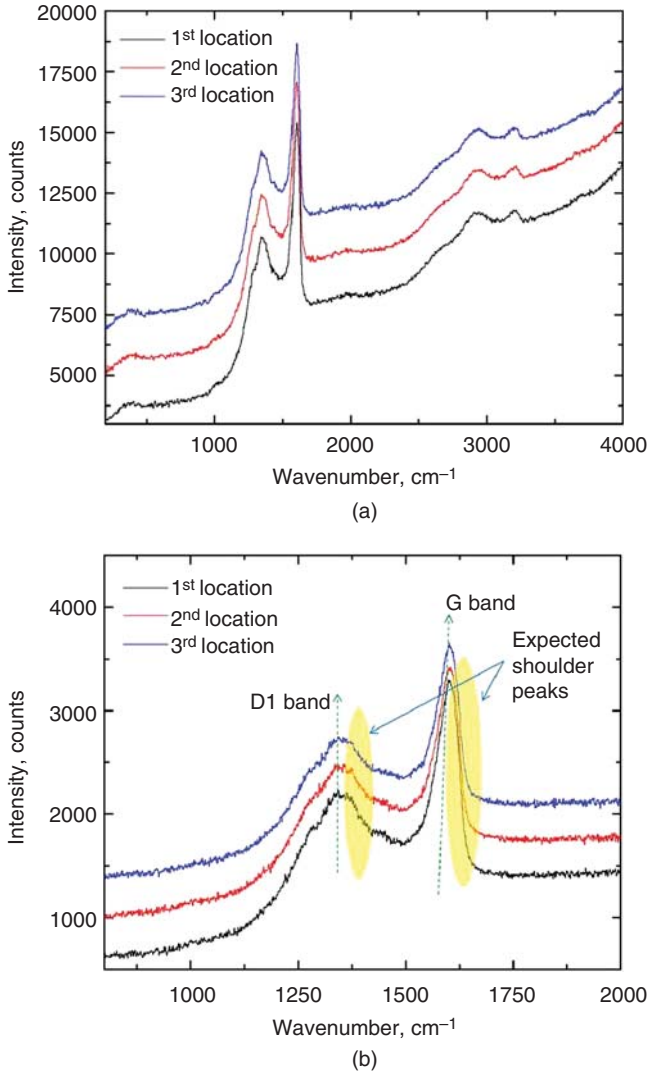

Figure 9.12 Raman spectra of an asphaltene sample: (a) shows the overall spectra recorded at tree different locations on the sample and (b) shows the zoomed-in region of the D1 and G bands. *Source:* Abdallah and Yang (2012). Reproduced with permission of American Chemical Society.

Moreover, besides the classical determination of particular properties, there are new interesting developments, for example utilizing the capability of optical methods for imaging with chemical contrast. Kazarian and co-workers have set up a high-pressure high-temperature cell for spatially resolved attenuated total

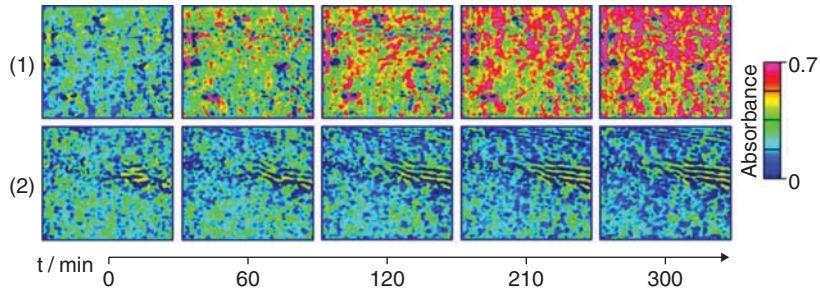

Figure 9.13 *In situ* macro ATR-FTIR spectroscopic images of the blends of two crude oils measured at 60 °C. The partial volumes are 50% (1) and 75% (2). The images were obtained based on the distribution of the integrated absorbance of the spectral band at 1550–1650 cm^{-1}. The measured area is ca. 610 µm × 530 µm. *Source:* Gabrienko, Martyanov, and Kazarian (2015). Reproduced with permission of American Chemical Society.

reflection IR spectroscopy (Gabrienko, Martyanov, and Kazarian, 2015). This cell was used to do temporally resolved imaging of crude oil blends at varied temperatures. Figure 9.13 shows two series of IR images recorded in different blends. Initially, the two blends appear rather homogeneous, which is reflected by a uniform distribution. In the upper sequence of images, the sample shows clear signs of a spatial re-distribution, while the lower images remain almost the same as time elapses. As the two-dimensional distribution was obtained from the spectral signature of the aromatic C=C stretches (see also discussion above), the change in the distribution can be interpreted in terms of asphaltene precipitation. Hence, IR spectroscopy allows new and detailed insights into the chemistry and phase behavior of crude oils and its constituents.

9.7 Conclusion

The application of vibrational spectroscopy in terms of IR and Raman spectroscopy to crude oil and its constituents is a quickly emerging area in analytical chemistry. This is particularly true for combinations of spectroscopy and multivariate data analysis. This chapter gave an overview of experimental methods and the most common means of data evaluation. It was shown that vibrational spectroscopy facilitates not only compositional analysis but also the direct measurement of physicochemical properties using appropriate regression models.

The development of robust and reliable instrumentation is a key driver of the growth of vibrational spectroscopy. Many decades of continuous improvement have established trust in academia and industry and, hence, the ever-increasing number of spectroscopic applications to fluid characterization and process monitoring. This also includes the implementation of vibrational spectroscopy as handheld and portable devices enabling field studies without the need for sampling and sample preparation. In conclusion, Raman and IR spectroscopy will have a bright future, especially in the field of petroleum fluids.

References

Abdallah, W. A. and Yang, Y. (2012) Raman spectrum of asphaltene. *Energy & Fuels*, 26, 6888–6896.

Alsmeyer, F., Koß, H.-J., and Marquardt, W. (2004) Indirect spectral hard modeling for the analysis of reactive and interacting mixtures. *Applied Spectroscopy*, 58, 975–985.

Aske, N., Kallevik, H., and Sjöblom, J. (2001) Determination of saturate, aromatic, resin, and asphaltenic components in crude oils by means of infrared and near-infrared spectroscopy. *Energy & Fuels*, 15, 1304–1312.

Averett, L. A. and Griffiths, P. R. (2008) Effective path length in attenuated total reflection spectroscopy. *Analytical Chemistry*, 80, 3045–3049.

Banwell, C. N. and McCash, E. M. (1994) *Fundamentals of Molecular Spectroscopy*, McGraw-Hill, London.

Beams, R., Cancado, L. G., and Novotny, L. (2015) Raman characterization of defects and dopants in graphene. *Journal of Physics: Condensed Matter*, 27, 083002.

Dearing, T. I., Thompson, W. J., Rechsteiner, C. E., Jr, and Marquardt, B. J. (2011) Characterization of crude oil products using data fusion of process Raman, infrared, and nuclear magnetic resonance (NMR) spectra. *Applied Spectroscopy*, 65, 181–186.

Egermann, J., Seeger, T., and Leipertz, A. (2004) Application of 266-nm and 355-nm Nd:YAG laser radiation for the investigation of fuel-rich sooting hydrocarbon flames by Raman scattering. *Applied Optics*, 43, 5564–5574.

Gabrienko, A. A., Martyanov, O. N., and Kazarian, S. G. (2015) Effect of temperature and composition on the stability of crude oil blends studied with chemical imaging in situ. *Energy & Fuels*, 29, 7114–7123.

Galtier, O., Abbas, O., Le Dreau, Y., *et al.* (2011) Comparison of PLS1-DA, PLS2-DA and SIMCA for classification by origin of crude petroleum oils by MIR and virgin olive oils by NIR for different spectral regions. *Vibrational Spectroscopy*, 55, 132–140.

Greer, J. S., Petrov, G. I., and Yakovlev, V. V. (2013) Raman spectroscopy with LED excitation source. *Journal of Raman Spectroscopy*, 44, 1058–1059.

Griffiths, P. R. and De Haseth, J. A. (2007) *Fourier Transform Infrared Spectrometry*, John Wiley & Sons, Ltd, Chichester.

Haken, H. and Wolf, H. C. (1995) *Molecular Physics and Elements of Quantum Chemistry*, Springer, Heidelberg, Germany.

Hannisdal, A., Hemmingsen, P. V., and Sjöblom, J. (2005) Group-type analysis of heavy crude oils using vibrational spectroscopy in combination with multivariate analysis. *Industrial & Engineering Chemistry Research*, 44, 1349–1357.

Harrick, N. J. and du Pré, F. K. (1966) Effective thickness of bulk materials and of thin films for internal reflection spectroscopy. *Applied Optics*, 5, 1739–1743.

Hotelling, H. (1933) Analysis of a complex of statistical variables into principal components. *Journal of Educational Psychology*, 24, 417.

Kiefer, J. (2015) Recent advances in the characterization of gaseous and liquid fuels by vibrational spectroscopy. *Energies*, 8, 3165–3197.

Kiefer, J., Rasul, N. H., Ghosh, P. K., and Von Lieres, E. (2014) Surface and bulk porosity mapping of polymer membranes using infrared spectroscopy. *Journal of Membrane Science*, 452, 152–156.

Kiefer, J., Seeger, T., Steuer, S., *et al.* (2008) Design and characterization of a Raman-scattering-based sensor system for temporally resolved gas analysis and its application in a gas turbine power plant. *Measurement Science and Technology*, 19, 085408.

Kuptsov, A. K. and Arbuzova, T. V. (2011) A study of heavy oil fractions by Fourier-transform near-infrared Raman spectroscopy. *Petroleum Chemistry*, 51, 203–211.

Liu, C. and Berg, R. W. (2013) Nonlinearity in intensity versus concentration dependence for the deep UV resonance Raman spectra of toluene and heptane. *Applied Spectroscopy Reviews*, 48, 425–437.

Maiwald, M., Erbert, G., Klehr, A., *et al.* (2006) Rapid shifted excitation Raman difference spectroscopy with a distributed feedback laser emitting at 785 nm. *Applied Physics B*, 85, 509–512.

Meyer, M. W., Lupoi, J. S., and Smith, E. A. (2011) 1064 nm dispersive multichannel Raman spectroscopy for the analysis of plant lignin *Analytica Chimica Acta*, 706, 164–170.

Noack, K., Eskofier, B., Kiefer, J., *et al.* (2013) Combined shifted-excitation Raman difference spectroscopy and support vector regression for monitoring the algal production of complex polysaccharides. *Analyst*, 138, 5639–5646.

Pearson, K. (1901) Principal components analysis. *The London, Edinburgh, and Dublin Philosophical Magazine and Journal of Science*, 6, 559.

Riedemann, J. S., Kadasala, N. R., Wei, A., and Kenttämaa, H. I. (2016) Characterization of asphaltene deposits by using mass spectrometry and Raman spectroscopy. *Energy & Fuels*, 30, 805–809.

Schmidt, M. A. and Kiefer, J. (2013) Polarization-resolved high-resolution Raman spectroscopy with a light-emitting diode. *Journal of Raman Spectroscopy*, 44, 1625–1627.

Schrader, B. (ed.) (1995) *Infrared and Raman Spectroscopy*, Wiley-VCH, Weinheim, Germany.

Sharaf, M. A., Illman, D. L., and Kowalski, B. R. (1986) *Chemometrics*, John Wiley & Sons, Ltd, Chichester.

Shreve, A. P., Cherepy, N. J., and Mathies, R. A. (1992) Effective rejection of fluorescence interference in Raman spectroscopy using a shifted excitation difference technique. *Applied Spectroscopy*, 46, 707–711.

Struthers, H. C., Zehentbauer, F. M., Ono-Sorhue, E., and Kiefer, J. (2011) Chemical composition monitoring in a batch distillation process using Raman spectroscopy. *Industrial & Engineering Chemistry Research*, 50, 12824–12830.

Tomren, A. L., Barth, T., and Folgerø, K. (2012) Multivariate analysis of crude oil composition and fluid properties used in multiphase flow metering (MFM). *Energy & Fuels*, 26, 5679–5688.

Viell, J. and Marquardt, W. (2012) Concentration measurements in ionic liquid-water mixtures by mid-infrared spectroscopy and indirect hard modeling. *Applied Spectroscopy*, 66, 208–217.

Wei, D., Chen, S., and Liu, Q. (2015) Review of fluorescence suppression techniques in Raman spectroscopy. *Applied Spectroscopy Reviews*, doi: 10.1080/05704928.2014.999936.

Wold, S., Esbensen, K., and Geladi, P. (1987) Principal component analysis. *Chemometrics and Intelligent Laboratory Systems*, 2, 37–52.

Zehentbauer, F. M. and Kiefer, J. (2012) Detection of unexpected species in soft modelling of vibrational spectra. *Chimica Oggi/Chemistry Today*, 30, 54–56.

Zhao, J., Carrabba, M. M., and Allen, F. S. (2002) Automated fluorescence rejection using shifted-excitation Raman difference spectroscopy. *Applied Spectroscopy*, 56, 834–845.

Index

Analytical Characterization Methods for Crude Oil and Related Products, First Edition.
Edited by Ashutosh K. Shukla.